FRM II
Forschungs-Neutronenquelle
Heinz Maier-Leibnitz

MLZ
Heinz Maier-Leibnitz Zentrum

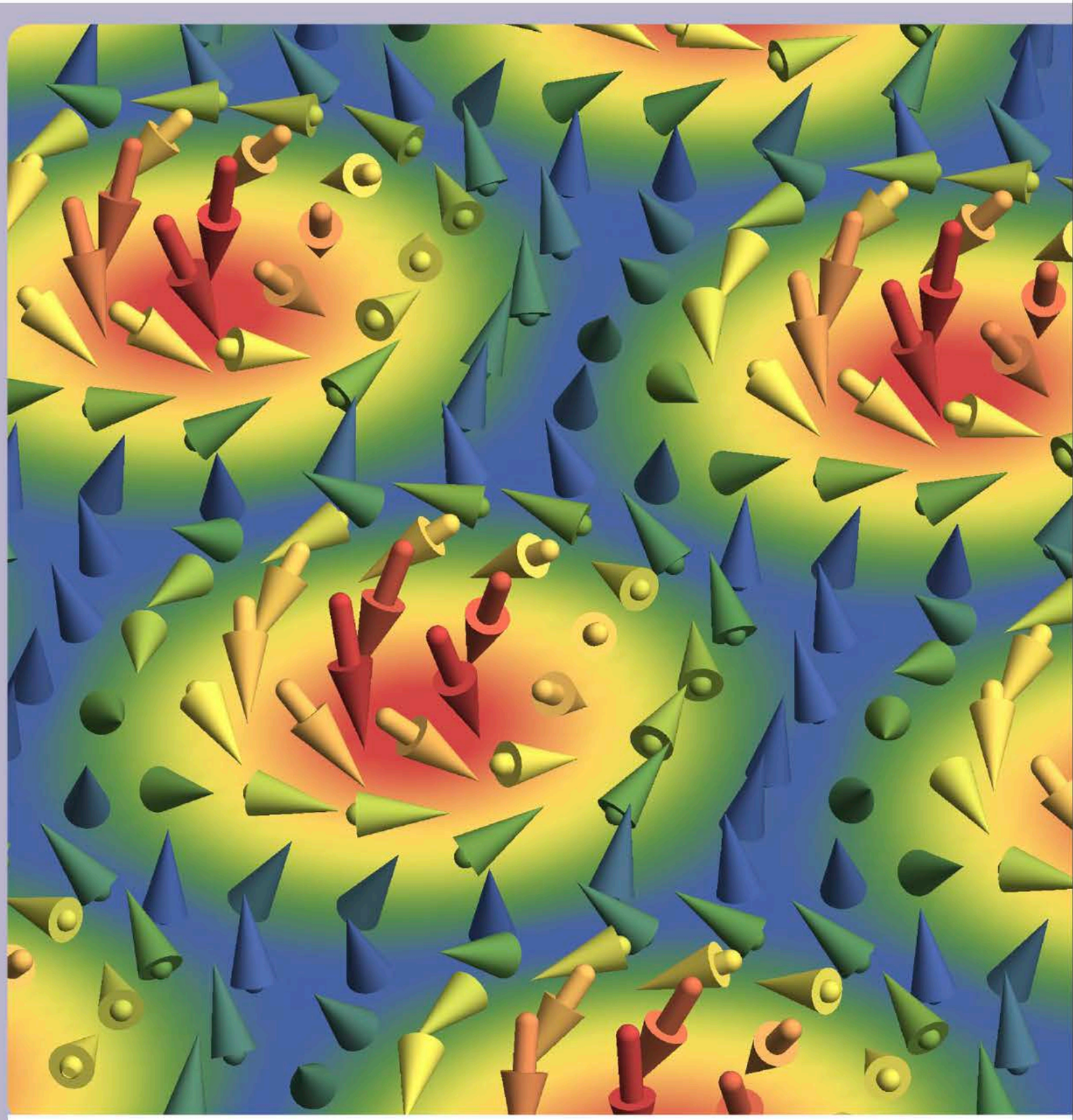

Annual Report 2018

MLZ is a cooperation between:

JÜLICH
Forschungszentrum

Helmholtz-Zentrum
Geesthacht
Zentrum für Material- und Küstenforschung

Technical
University
of Munich

Bavarian State Ministry of Science and the Arts

SPONSORED BY THE

Federal Ministry of Education and Research

The Heinz Maier-Leibnitz Zentrum (MLZ):

The Heinz Maier-Leibnitz Zentrum is a leading centre for cutting-edge research with neutrons and positrons. Operating as a user facility, the MLZ offers a unique suite of high-performance neutron scattering instruments. This cooperation involves the Technische Universität München, the Forschungszentrum Jülich and the Helmholtz-Zentrum Geesthacht. The MLZ is funded by the German Federal Ministry of Education and Research, together with the Bavarian State Ministry of Science and the Arts and the partners of the cooperation.

The Forschungs-Neutronenquelle Heinz-Maier-Leibnitz (FRM II):

The Forschungs-Neutronenquelle Heinz-Maier-Leibnitz provides neutron beams for the scientific experiments at the MLZ. The FRM II is operated by the Technische Universität München and is funded by the Bavarian State Ministry of Science and the Arts.

Joint Annual Report 2018

of the MLZ and FRM II

Vision for the future

We reflect on a year full of changes and many achievements. First of all, we are pleased to welcome two new scientific directors. As of April 2018, Prof. Dr. Peter Müller-Buschbaum, who has been deputising for Prof. Dr. Winfried Petry as Chair of the Institute for Functional Materials at the TUM Physics Department since 2006, took over both as Chair of the Institute and Scientific Director of the FRM II and MLZ. His predecessor, Prof. Petry, officially retired after 17 years as scientific director and was nominated Emeritus of Excellence of the Technical University of Munich in recognition of his outstanding achievements at the TUM.

The Forschungszentrum Jülich, a partner that cooperates closely with the Heinz Maier-Leibnitz Zentrum (MLZ), has also appointed a new scientific director. Prof. Dr. Stephan Förster has headed the Jülich Institute for Neutron Scattering (ICS-1/JCNS-1) since April 2017, and since the end of February 2018 also represents the Helmholtz institutions Forschungszentrum Jülich and Helmholtz-Zentrum Geesthacht within the scientific directorate of the MLZ.

Reinforced by two new MLZ directors, we further developed a vision for the MLZ beyond 2030. This roadmap, as well as the achievements of the MLZ during the years 2014 to 2017, was successfully presented in the MLZ Review 2018 in November. The MLZ aims to be a technologically pre-eminent, reliable, safe and efficient place for neutron research for the advancement of science and our society. This vision, among other things, includes supporting the MLZ users from the first idea for an experiment to the publication of the results, and to drive innovation in automation, digitalisation and robotics. In addition, the MLZ aims to provide a complete state-of-the-art suite of instruments to promote new science. To this end, the instrumentation of the MLZ is continuously in expansion. The new cold neutron three axes spectrometer KOMPASS, which is operated by the TUM and the University of Cologne, first detected neutrons in 2018. It is further proposed to install three scientific instruments from the Berlin neutron source BER II, following the planned shut down in 2019.

Furthermore, other neutron research reactors in Europe will cease operation in the coming years. Therefore, after 2019 the MLZ will take up the mantle as the German neutron centre within a changing European neutron landscape. In order to strengthen European neutron science via enhanced collaboration among the facilities, the MLZ, together with seven partners within the European research infrastructure, founded the League of Advanced European Neutron Sources (LENS) in September 2018.

Ahead of us lies the 15th year of reactor operation at the FRM II. The year 2019 will be decisive for the transport of spent fuel elements to the Ahaus interim storage facility. The first of three milestones has already been achieved with the licensing of the transport and storage cask CASTOR MTR-3, which will be able to accommodate five spent fuel elements from the FRM II. The next steps include the approval of licenses for storing the casks in the interim storage facility Ahaus and, finally, for the transport of the spent fuel elements to Ahaus.

Another major task in 2019 will be the completion of our new office and laboratory buildings, bringing all our work force closer together in order to further enhance collaboration and communication between the partners of the MLZ.

Let us go forward and tackle together all the challenges that lie ahead to make our vision of the MLZ a reality.

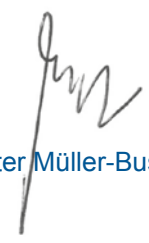

Peter Müller-Buschbaum

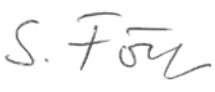

Stephan Förster

Johannes Nußbickel

Anton Kastenmüller

Scientific Highlights & Reports

Materials Science

Quantum Phenomena

Soft Matter

Structure Research

Neutron Methods

Instrumental Upgrades & Services

Reactor & Industry

Facts & Figures

Instrument scientist Dr. Hao Deng at the single crystal diffractometer HEiDi which is fed by hot neutrons.

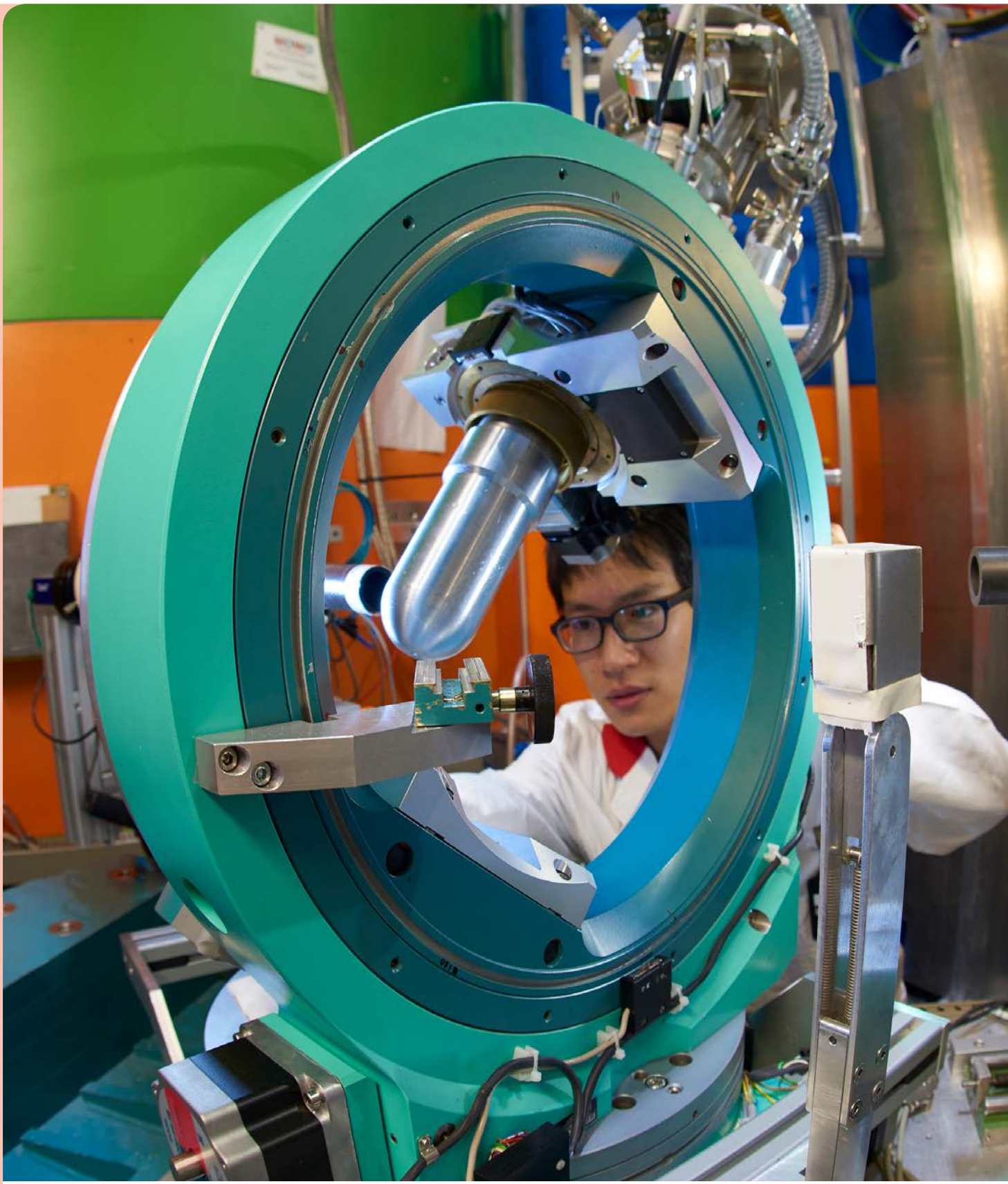

Scientific Highlights & Reports

Magnetic vortices: twice as interesting

The circular vortex of a whirlpool that appears when water in a bathtub is drained is an everyday experience. Their magnetic siblings, denoted skyrmions, provide a showcase where magnetic objects exhibit particle-like properties due to their topology or winding. These little whirls of the magnetisation could prove crucial for the development of future magnetic storage because of their stability and their tiny dimensions.

One of the key questions is the mechanism behind the stabilisation of skyrmions. A team of researchers from the Technical University of Munich, Technical University of Dresden and the University of Cologne has shown for the first time that two independent magnetic skyrmion phases can form in the same material due to different mechanisms. Usually, skyrmions exist in a single thermodynamic parameter range, that is, a certain range of temperature and magnetic or electric field strength. The discovery of a second, thermodynamically disconnected skyrmion phase in Cu_2OSeO_3 suggests a new way for the discovery, design and manipulation of skyrmionic phases.

Alfonso Chacon (left) and Dr. Sebastian Mühlbauer (right) adjust the detector of the small angle neutron scattering instrument SANS-1.

Experiments were carried out at SANS-1.

A. Chacon, L. Heinen, M. Halder, A. Bauer, W. Simeth, S. Mühlbauer, H. Berger, M. Garst, A. Rosch, and C. Pfleiderer, Observation of two independent skyrmion phases in a chiral magnetic material, Nat. Phys. 14, 936 (2018)

Trapped at the surface

Colloidal semiconductor quantum dots (QDs) are potential building blocks for next-generation photovoltaic devices. Solar cells based on QDs have achieved promising efficiencies above 10%. Relative to the bulk solid, QDs possess a very high surface-to-volume ratio. Their surface atoms are passivated via suitable ligand molecules in order to prevent defect states in the band gap. As imperfect passivation can severely limit the efficiency of QD solar cells, a deeper understanding of the electronic and surface structure of QDs is necessary.

Positron-annihilation spectroscopy is a very sensitive tool with which to analyse both the electronic and surface structure of materials. However, the cause of the high surface sensitivity and a theoretical understanding of the underlying positron state were still lacking. Scientists have been able to resolve a long-standing controversy concerning the nature of the positron state in QDs: the positron is not confined inside the QDs but, rather, localised at their surfaces.

Experiments were carried out at the PLEPS instrument of the positron source NEPOMUC.

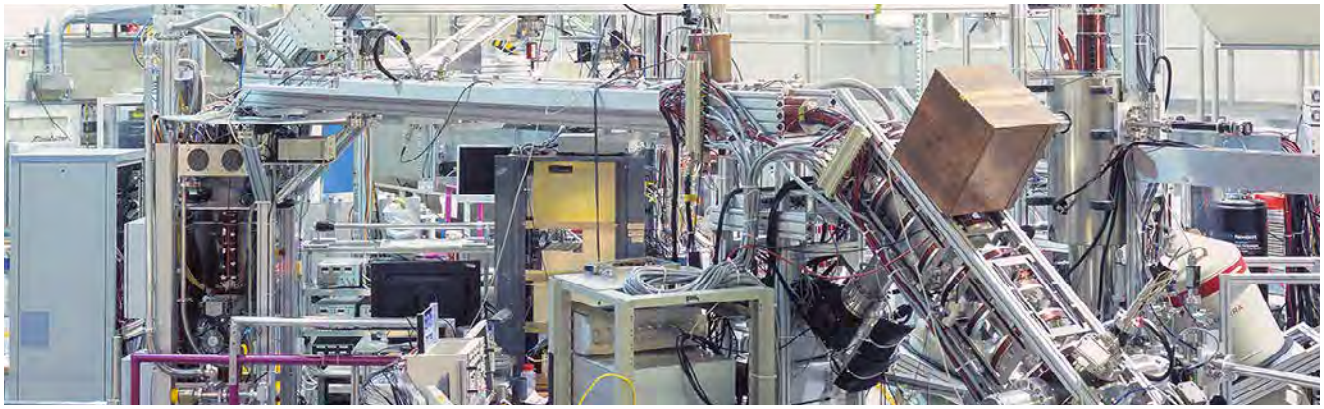

The neutron induced positron source at MLZ provides the highest intensity monoenergetic positron beam worldwide.

W. Shi, V. Callewaert, B. Barbiellini, R. Saniz, M. Butterling, W. Egger, M. Dickmann, C. Hugenschmidt, B. Shakeri, R. Meulenberg, E. Brück, B. Partoens, A. Bansil, and S. Eijt, Nature of the Positron State in CdSe Quantum Dots, Phys. Rev. Lett. 121, 057401 (2018)

With a little help from a lipid

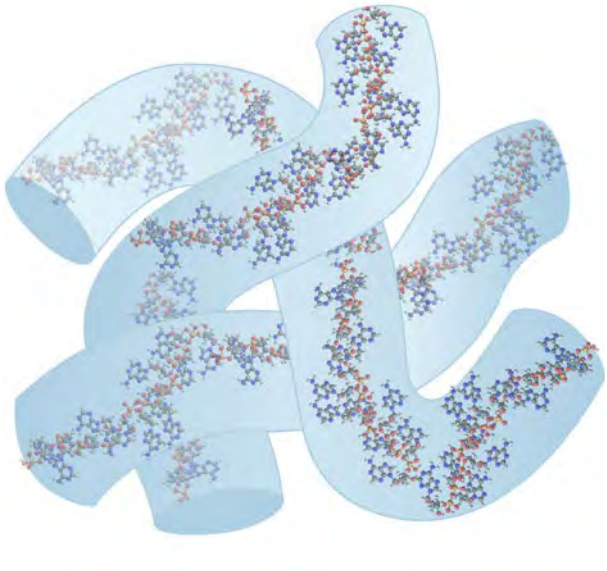

Schematic representation of the proposed inverse wormlike micellar phase inside the mRNA-containing LNPs core.

When the human genome (DNA) is translated into proteins, the so-called messenger RNA (mRNA) plays an intermediate role. mRNA treatments represent an exciting approach to curing diseases that cannot be tackled with current therapeutics, for example cancer. However, the delivery of mRNA to target cells remains a challenge, but lipid nanoparticles (LNPs) can be used as transport vehicles.

Using small angle neutron scattering, the scientists determined the structure of LNPs encapsulating mRNA. They showed that the lipids are not homogeneously distributed across the LNP, and that one of the lipids is localised, mainly at its surface. Armed with this information regarding the structure, the pharmaceutical scientists designed LNPs to transport mRNA and successfully modify intracellular protein production in two clinically relevant human cell types.

Experiments were carried out at KWS-2.

M. Arteta, T. Kjellman, S. Bartesaghi, S. Wallin, X. Wu, A. Kvist, A. Dabkowska, N. Székely, A. Radulescu, J. Bergenholtz, and L. Lindfors, Successful reprogramming of cellular protein production through mRNA delivered by functionalized lipid nanoparticles, PNAS 115, 3351 (2018)

New material for medical imaging

Piezoelectric material elongates or contracts under an electric field and can also convert pressure into voltage. It is for example used in ultrasound imaging, translating voltage into vibration and thus creating sound. In the automotive sector, it is used for the controlled injection of fuel in the engine.

An important performance parameter of such materials is the electrostrain, which is a measure of how much the material's length changes in proportion to its original dimension under an electric field. Single crystal piezoelectric materials have set the new benchmark to 1.7% of electrostrain, whereas the highest value in polycrystalline materials was up to 0.7% by now. A new polycrystalline ceramic discovered by Indian researchers showed a value of 1.3%. A close examination of the structure of $BiFeO_3$-$PbTiO_3$-$LaFeO_3$ on the atomic scale helped the researchers in explaining the mechanism of the extremely large electrostrain in this material.

Experiments were carried out at SPODI.

Dr. Rajeev Ranjan and Dr. Anatoliy Senyshyn (r.) during their measurements at the structure powder diffractometer SPODI.

B. Narayan, J. Malhotra, R. Pandey, K. Yaddanapudi, P. Nukala, B. Dkhil, A. Senyshyn, and R. Ranjan, Electrostrain in excess of 1% in polycrystalline piezoelectrics, Nat. Mater. 17, 427 (2018)

Spin glass can mimic quantum spin liquid

Quantum spin liquids represent a novel state of matter in which the spins do not arrange themselves in an ordered pattern as in a conventional magnet. They can find applications in quantum computation. The Nobel laureate, Philip W. Anderson, proposed a model on a triangular lattice for such a state but, up to now, this has not been realised experimentally.

Two candidate compounds for such spin liquids, $YbMgGaO_4$ and its sister compound $YbZnGaO_4$, were measured using neutrons. From inelastic neutron scattering, researchers observed the quasi-continuous excitation spectrum, considered to be conclusive evidence for a spin-liquid state. By combining results from susceptibility, specific heat, and thermal conductivity measured at temperatures around 0.05 Kelvin, as well as theoretical calculations, they found that the true ground state is indeed a spin-glass. The team showed that a spin glass mimics a quantum spin liquid in many ways, but is induced by the disordered arrangements of the atoms rather than of the quantum fluctuations needed for the latter.

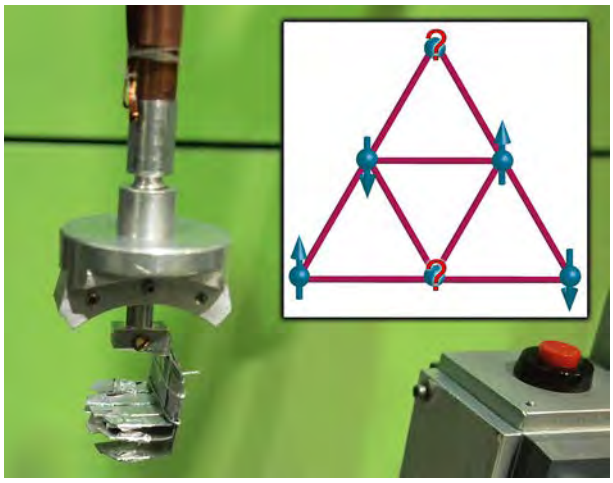

$YbZnGaO_4$ sample mounted onto the ^3He cryostat on PANDA. Inset: schematic of Philip W. Anderson's model on a two-dimensional triangular structure with atoms (spheres) and spins (arrows). Question marks represent undetermined spin arrangements.

Experiments were carried out at PANDA.

Z. Ma, J. Wang, Z.-Y. Dong, J. Zhang, S. Li, S.-H. Zheng, Y. Yu, W. Wang, L. Che, K. Ran, S. Bao, Z. Cai, P. Čermák, A. Schneidewind, S. Yano, J. S. Gardner, X. Lu, S.-L. Yu, J.-M. Liu, S. Li, J.-X. Li, and J. Wen, Spin-Glass Ground State in a Triangular-Lattice Compound $YbZnGaO_4$, Phys. Rev. Lett. 120, 087201 (2018)

Neutrons explain higher efficiency of solar cells with additives

Organic solar cells consist of hydrocarbon compounds. They are cheaper to produce than conventional photovoltaic cells and have so far achieved efficiencies up to 13% when converting solar into electrical energy. Neutrons are the tool of choice for looking deeper into its inner morphology and finding out why the solvent additive 1,8-octanedithiol (ODT) increases the efficiency by modifying structures. The researchers added various concentrations of ODT, analysing them with grazing incidence small angle neutron scattering.

The results showed that the surface and interior of the intermediate layer were similar without the additive ODT and some isolated nano-islands had formed. The charge carriers were trapped in these islands. In contrast, the structure with the additive ODT is quite different: there are fewer traps, the interconnections are much better developed and, thus, charge carriers can be transported more efficiently.

However, neutrons also showed that there is a limit beyond which an additional additive does not increase efficiency: The ODT induces a compact layer of acceptors on the surface. In this case, surface and inner structures differ.

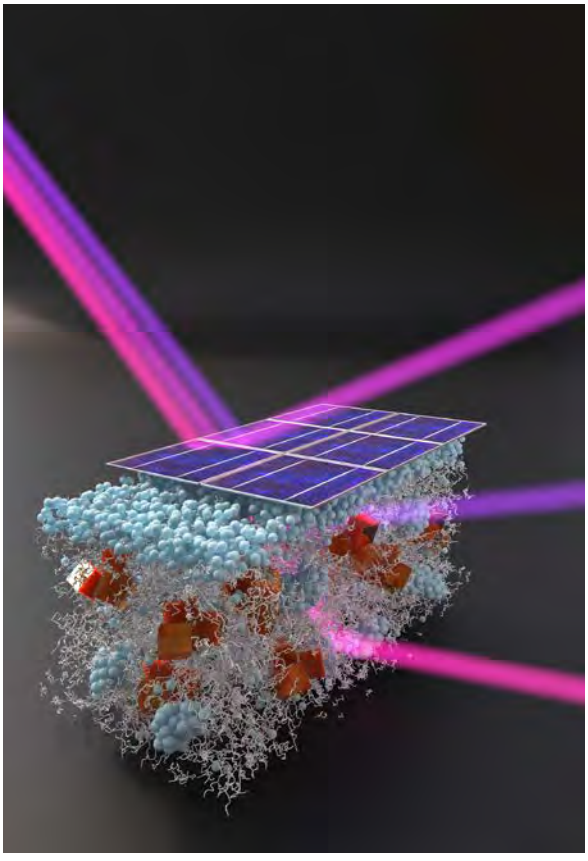

Organic solar cells can be sprayed in thin layers on surfaces.

Experiments were carried out at REFSANS.

W. Wang, L. Song, D. Magerl, D. Musegui González, V. Körstgens, M. Philipp, J.-F. Moulin, and P. Müller-Buschbaum, Influence of Solvent Additive 1, 8-Octanedithiol on P3HT:PCBM Solar Cells, Adv. Funct. Mater. 28, 1800209 (2018)

Superconductor with a twist

Researchers used neutron diffraction to reveal tiny distortions among the otherwise symmetrical atomic order of an iron pnictide superconductor at temperatures near the point of optimal superconductivity. The key to the material's superconductivity seems to lie within a property that is unique to this class of materials: a structural transition in the arrangement of its atoms, from tetragonal to orthorhombic. In a tetragonal crystal, the atoms are arranged as cubes that have been stretched in one direction. An orthorhombic structure is shaped like a brick.

Sodium-iron-arsenic pnictide crystals are known to be tetragonal until cooled to a transition temperature that forces the lattice to become orthorhombic, a step toward superconductivity that appears at lower temperatures. However, the researchers were surprised to see anomalous orthorhombic regions well above that structural transition temperature. They reported that this occurred in samples that were minimally doped with nickel and persisted when the materials were over-doped.

The ability to manipulate that point of optimum doping may help to increase the temperature at which iron pnictides become superconductors.

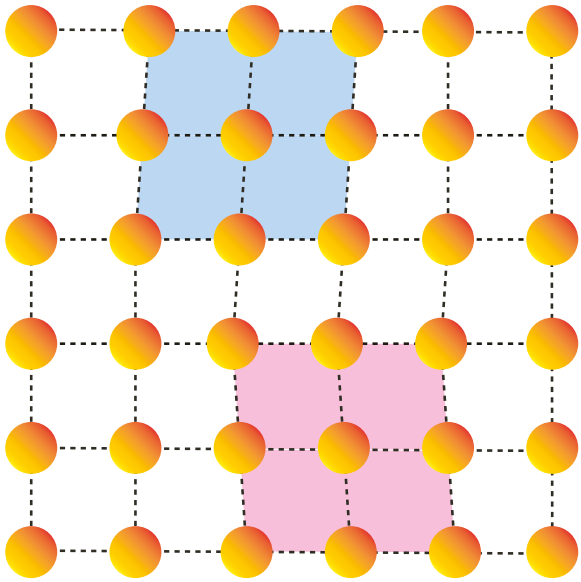

The square-shaped arrangement of atomes in a pnictide superconductor is locally distorted (red, blue).

Experiments were carried out at TRISP.

W. Wang, Y. Song, C. Cao, K.-F. Tseng, T. Keller, Y. Li, L.W. Harriger, W. Tian, S. Chi, R. Yu, A. H. Nevidomskyy, and P. Dai, Local orthorhombic lattice distortions in the paramagnetic tetragonal phase of superconducting $NaFe_{1-x}Ni_xAs$, Nat. Commun. 9, 3128 (2018)

Fast storage material in neutron light

Phase change memories store data by altering the state of the matter of the individual bits between liquid-like, glassy and crystal states. The technology has the potential to provide inexpensive, high-speed, high-density storage. There is still a lack of clarity as to how the material manages the phase changes on such short time scales, and how to control the changes with the necessary precision. Now, scientists have analysed an alloy of germanium, antimony and tellurium mixed in a specific ratio, which will cause both the density maxima and the associated metal-to-semiconductor transitions to occur below the melting point, making the transition much more distinct than in other such compounds.

Above the phase transition, the liquid has a low viscosity and crystallisation occurs quickly. Below, however, the liquid solidifies rapidly and retains the poorly conductive, amorphous state. In "nanoscopic bits", this state is preserved practically indefinitely. Applying a short pulse of heat causes the temperature to rise quickly locally, thereby transitioning the bit into the conducting state within nanoseconds.

Dr. Zachary Evenson at the TOFTOF time of flight spectrometer.

Experiments were carried out at TOFTOF.

S. Wei, Z. Evenson, M. Stolpe, P. Lucas and C. Austen Angell, Breakdown of the Stokes-Einstein relation above the melting temperature in a liquid phase-change material, Sci. Adv. 4, eaat8632v (2018)

Evolution of residual stresses in laser beam melting – A neutron diffraction study

F. Bayerlein[1], M. Hofmann[2]

[1]Institute for Machine Tools and Industrial Management (iwb), Technical University of Munich, Garching, Germany; [2]Heinz Maier-Leibnitz Zentrum (MLZ), Technical University of Munich, Garching, Germany

Additive manufacturing (AM) is increasingly used in the production of functional parts. In order to ensure product reliability in challenging load cases and environments, a sound knowledge of the residual stress state and its evolution through the building process is essential.

We therefore conducted neutron diffraction measurements at STRESS-SPEC on different stages of the build-up of an Inconel 718 sample via laser beam melting (LBM, fig. 1). A simple cuboidal sample geometry was used in order to facilitate alignment and to minimise additional geometrical effects on the resulting residual stresses. Strains were measured in three perpendicular directions, coinciding with the symmetry axes of the structure, so that the stresses in these directions could be calculated using Hooke's Law. Thus, by providing quasi-transient data of the evolution of residual stresses in both the base plate and the part, simulation models can be investigated and tested for their structural validity.

By way of an example of the results obtained, fig. 2 shows the longitudinal residual stresses for the part when completely built, as determined by the neutron diffraction measurements. For the purpose of comparison, the results of a sequentially coupled thermal and mechanical FEM simulation are also plotted in the figure, showing good agreement with the experimental data.

The measurements during the entire build-up sequence provided some unique and fundamental insights into the residual stress development in Inconel 718 within the LBM process. They can be used to predict tendencies for residual stress development with respect to different regions of simple geometrical shapes, and to the build-up process [1].

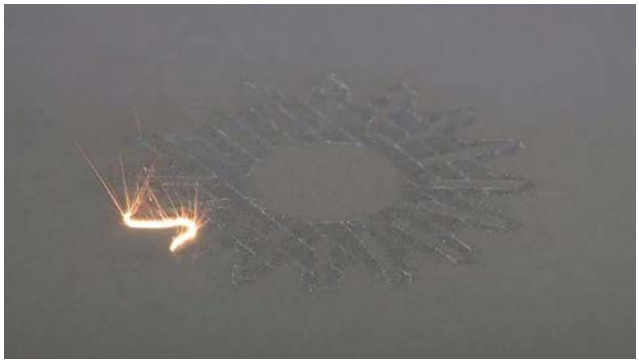

Figure 1: Snapshot of the building process of IN718 samples using laser beam melting (LBM). On the left the trace of the laser melting the powder can be seen.

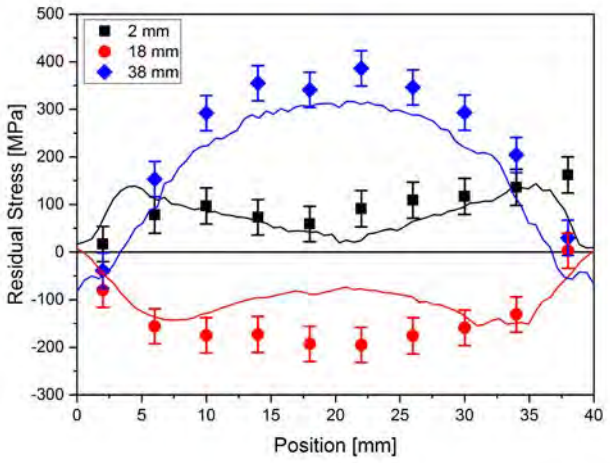

Figure 2: Longitudinal residual stress distribution at three different heights in the LBM manufactured IN718 sample. The symbols represent the experimentally derived values while the lines are results from the FEM simulations.

In particular, we were able to show in this study that an exposure of a single layer already introduces significant stresses into the base plate, even for a relatively small part-to-plate-ratio. Also, the stress distribution in the base plate is more symmetrical along the longitudinal, as compared to the perpendicular, cross-section of the part. This may be attributable to the asymmetrical positioning of the part on the base plate in this direction. The addition of every extra new layer produces tensile stresses in the material directly below. They appear mainly in the build-up plane (longitudinal-transversal). This behavior can be observed from the very beginning of the build-up process. The process continuously introduces residual stresses, which are mainly compressive, into the base plate. In later stages, however, tensile stresses of the same magnitude develop close to the edges. Finally the quasi-transient development is in line with the expectation of a continuously growing self-similar distribution with zero or compressive to tensile stresses from the center to the edges of the part-plate-system.

[1] F. Bayerlein, et al., Transient development of residual stresses in laser beam melting – A neutron diffraction study, Addit. Manuf. 24, 587 (2018)

Lattice strain of high ductility layered Ti/Al composites under in-situ tensile deformation

G. H. Fan[1], M. Huang[1], C. Xu[1], W. M. Gan[2], L. Geng[1]

[1]School of Materials Science and Engineering, Harbin Institute of Technology, Harbin, China; [2]German Engineering Materials Science Centre (GEMS) at MLZ, Helmholtz-Zentrum Geesthacht GmbH, Garching, Germany

High strength and ductility are required for metal structural materials, but they are always mutually exclusive, i.e. strengthening is often accompanied by a decrease in ductility. The structure design of the composites, such as a layered structure, has attracted much attention in recent years since it leads to simultaneous improvement in both strength and ductility. Accordingly, the deformation and fracture mechanisms of Layered Metallic Composites (LMCs) has been the focus of scientific interest. Although many deformation mechanisms have been proposed to explain their plastic deformation behavior, elastic deformation behavior is still unclear, being difficult to characterise due to the entire elastic recovery. Moreover, the effect of the elastic stage on the plastic deformation of LMCs has generally been neglected. It is crucial to understand these fundamental mechanisms in order to steer the design of high-performance layered materials. Neutron diffraction measurement can overcome this elastic recovery and obtain its lattice strain evolution. In this work, the Ti/Al LMCs were prepared by the hot-rolling and annealing of pure Ti and Al sheets, and show much higher ductility than any individual Ti or Al sheets. The lattice strain evolution of the Ti/Al LMCs during tensile deformation was analysed to investigate the effect of the elastic stage on plastic deformation.

Figure 1 shows the lattice strain evolution of the Ti/Al LMCs, indicating that the deformation of the Ti/Al LMCs can be divided into three stages: elastic stage, elastic-plastic stage, and plastic stage. At the elastic stage, Ti and Al layers with different Young's modulus (E) maintain equal elastic strains, loading a certain internal stress formed at the interface. With further tensioning, the Al layer starts to deform plastically while the Ti layer is still elastically deforming, thus reaching the so-called elastic-plastic stage. It is known that the Al layer cannot be freely deformed and will be restrained by adjacent Ti layers. At this elastic-plastic stage, stress-transfer behavior occurs, and the Ti layer will withstand additional internal stress to promote plastic deformation of the Ti layer and facilitate the compatible deformation between the Ti and Al layers. But, at the same time, this stress partitioning causes an accumulation of internal stress at the Ti/Al interface,

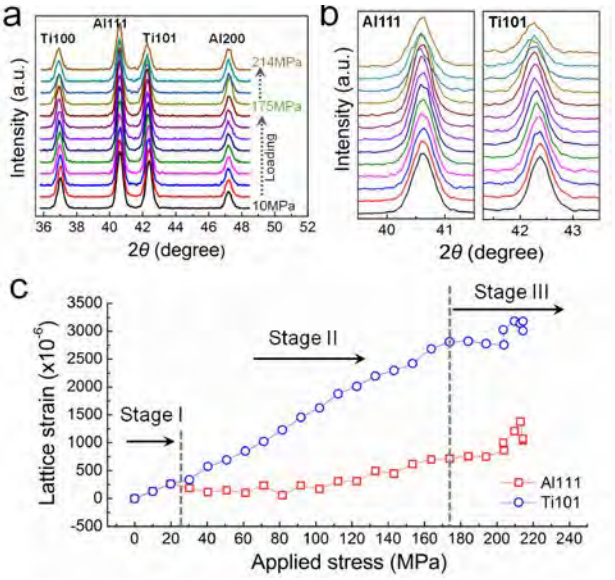

Figure 1: (a) The diffraction pattern profiles at various stress levels along the tensile direction of Al and Ti via in-situ tension at STRESS-SPEC; (b) magnified view of (111) for Al layer and (10.1) for Ti layer. (c) Lattice strain evolution in LMC consisting of (111) for Al layer and (10.1) for Ti layer. The lattice strain-applied stress curve is classified into three stages: Stage I (elastic stage), Stage II (elastic-plastic stage) and Stage III (plastic stage).

and further promotes the strain localisation of the LMCs and the nucleation of the interface crack. However, on the one hand, the layered structure can alleviate the strain localisation through strain-transfer, which improves the ductility of the Ti layer; and on the other hand, the layered structure can restrain the propagation of the interface cracks, which is mainly attributed to two aspects: (i) the tips of the interfacial cracks are blunted by the adjacent Ti and Al layers via their plastic deformation, which reduces the driving force of crack propagation; (ii) the constraint effect of the layered structure changes the stress state of the Ti/Al LMCs, which increases the resistance to crack propagation. The nucleation and propagation of cracks indirectly affect the internal stress state of the Ti/Al LMCs and the redistribution of strain localisation, which influences the overall plastic deformation behavior. Thus, ultra-high ductility can be demonstrated for the current Ti/Al LMS.

[1] M. Huang, et al., Role of layered structure in ductility improvement of layered Ti-Al metal composite, Acta Mater. 153, 235 (2018)

PALS analysis of subnanometer cavities in cellulose and graphene coatings

R. S. Brusa[1,4] , W. Egger[2], C. Hugenschmidt[3], R. Checchetto[1]

[1]Department of Physics, University of Trento, Povo-Trento, Italy; [2]Universität der Bundeswehr (München) und Institut für Angewandte Physik und Messtechnik, LTR 2, Neubiberg, Germany; [3]Heinz Maier-Leibnitz Zentrum (MLZ) and Physics Department E21, Technical University of Munich, Garching, Germany; [4]Trento Institute for Fundamental Physics and Applications, National Institute for Nuclear Physics (TIFPA-INFN), Povo-Trento, Italy

The deposition of a functional coating layer on the surface of polymer and biopolymer materials is an effective way of improving the gas barrier properties for applications in packaging technology. Here, we review recent results that indicate that the gas transport properties of bilayer membrane systems can be explained thanks to structural information on the coating cavity structure obtained by Positron Annihilation Lifetime Spectroscopy (PALS).

The first system consists of a Graphene Laminated (GL) coating formed by stacked few layer graphene (FLG) nanocrystals on low-density polyethylene (LDPE) supports, see fig. 1 (left): here, penetrant infiltration occurs through nano-channels formed between the stacked FLG. Permeation experiments using CO_2, N_2 and D_2 revealed that molecular transport through the bilayer membrane has an anomalous character: the kinetics was reproduced assuming that the penetrant concentration in the GL coating, $c_{int}(t)$, reached its saturation value c_s following compressed exponential kinetics $c_{int}(t) = c_s[1 - e^{-(\lambda_{rel}t)\beta}]$. The relaxation time $\tau_{rel} = 1/\lambda_{rel}$ revealed a thermally activated character and its value increased with the kinetic diameter of the penetrant molecules. Depth-resolved PALS analysis, see fig. 1 (right), revealed that the average cross-section of these cavities is comparable in size to the kinetic diameter of the penetrant molecules, suggesting that the anomalous transport character was connected to a distribution of nano-channels path lengths where molecular infiltration in the GL structure occurs [1].

The second system consists of dense coatings made of self-assembled cellulose nanofibrils (CNF) on a poly(lactic acid) (PLA) support. Gas transport analysis revealed that coatings a few micrometers thick act as impermeable gas barriers for CO_2, O_2, and N_2 and reduce the D_2 and He permeation flux by a factor larger than 10^3 with respect to the PLA support, see fig. 2 (left). Experimental data revealed that D_2 and He diffusivity values were in the 10^{-10} and 10^{-9} cm^2s^{-1} range, respectively, and that penetrant migration occurs by thermally activated process. PALS analysis has revealed that the diffusive paths in the coating consist of elongated cavities with cross-sectional size ~ 0.31 nm between the packed nanofibrils, corresponding to τ_3 = 1.4 ns in fig. 2 (right). Thanks to this information, it was possible to explain the observed configurational regime in the transport of small penetrant transport and the extremely high D_2 and He selectivity which was, in fact, due to sieving effects [2].

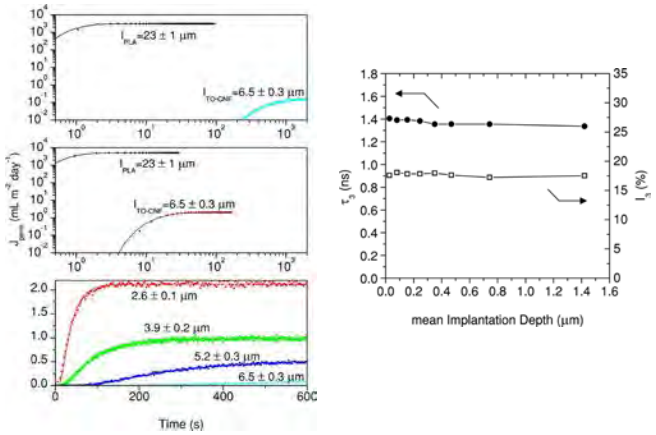

Figure 2: (Left) Permeation curves of uncoated PLA film and TO-CNF/PLA bilayer membranes pertinent to deuterium (upper panel) and helium (middle panel) obtained at T = 301 ± 2 K. In the lower panel, we show the deuterium permeation curves of TOCNF/PLA membranes with different TO-CNF coating thickness. (Right) o-Ps lifetime and intensity of the o-Ps annihilation signal as a function of the positron mean implantation depth.

[1] R. Checchetto, et al., Anomalous molecular infiltration in graphene laminates, Phys. Chem. Chem. Phys. 20, 24671 (2018)

[2] D. Roilo, et al., Cellulose Nanofibrils Films: Molecular Diffusion through Elongated Sub-Nano Cavities, J. Phys. Chem. C 121, 15437 (2017)

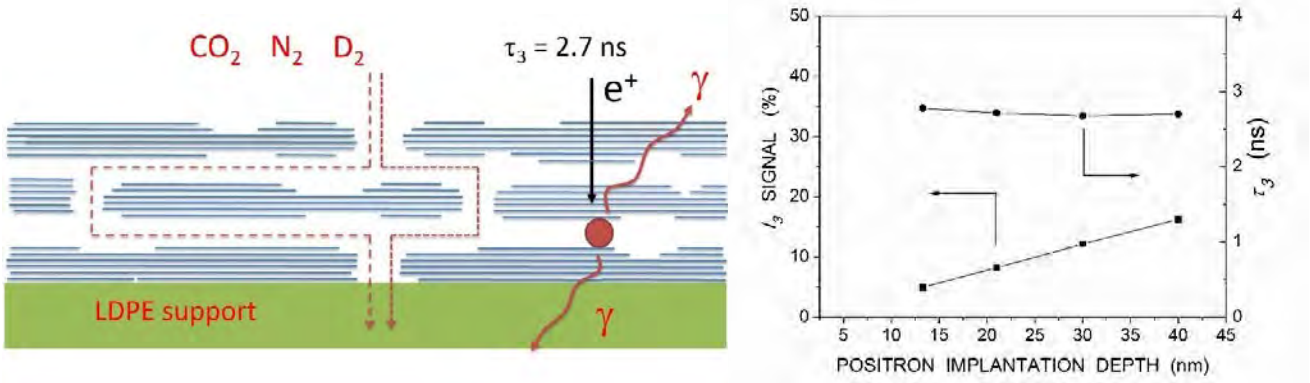

Figure 1: (Left) GL coating on the LDPE support. Dashed red arrows indicate nano-channels with distributed path lengths. (Right) o-Ps lifetime and intensity of the o-Ps annihilation signal in the GL coating as a function of the positron mean implantation depths. Indetermination in the vertical scales are smaller than the symbol size.

Vacancy-type defects in ion implanted GaN probed by monoenergetic positron beams

A. Uedono[1], S. Takashima[2], M. Edo[2], K. Ueno[2], H. Matsuyama[2], W. Egger[3], C. Hugenschmidt[4], K. Kojima[5], S. F. Chichibu[5], S. Ishibashi[6]

[1]Division of Applied Physics, Faculty of Pure and Applied Science, University of Tsukuba, Tsukuba, Ibaraki, Japan; [2]Advanced Technology Lab. Fuji Electric Co., Ltd., Hino, Tokyo, Japan; [3]Universität der Bundeswehr München, Institut für Angewandte Physik und Messtechnik, Neubiberg, Germany; [4]Heinz Maier-Leibnitz Zentrum (MLZ) and Physics Department E21, Technical University of Munich, Garching, Germany; [5]Institute of Multidisciplinary Research for Advanced Materials, Tohoku University, Sendai, Japan; [6]Research Center for Computational Design of Advanced Functional Materials, National Institute of Advanced Industrial Science and Technology, Tsukuba, Ibaraki, Japan

GaN is a material ideally suited to high-power and high-speed electronics owing to its beneficial physical properties, such as high saturation electron velocity and high breakdown voltage. Since ion implantation is the technique most commonly used to control carrier concentration, the use of this technique is a critical requirement for advancing GaN device technology. A drawback of ion implantation is the introduction of defects. Therefore, expanding our knowledge of the annealing behavior of the defects is crucial. In the present study, we used monoenergetic positron beams to study the annealing behavior of vacancies in Mg-implanted GaN [1].

Using a positron beam line constructed at the University of Tsukuba, Doppler broadening spectra of the annihilation radiation were measured as a function of the incident positron energy E in darkness and while the sample was illuminated with a 325 nm He-Cd laser. The measured spectra were characterised by the S parameter. The lifetime spectra of positrons were also measured using the pulsed monoenergetic positron beam PLEPS at NEPOMUC.

Figure 1 shows the S parameter of Mg-implanted GaN with [Mg] of 1 × 10^{17} cm^{-3} before and after annealing at 1300 °C as a function of E. For as-implanted GaN, the S values were larger than the defect free value (0.441), suggesting the trapping of positrons by vacancies. Using the positron diffusion model, the depth distributions of S were obtained. Figure 2 shows the results of the analysis and Mg distributions measured by SIMS. For the as-implanted sample, the

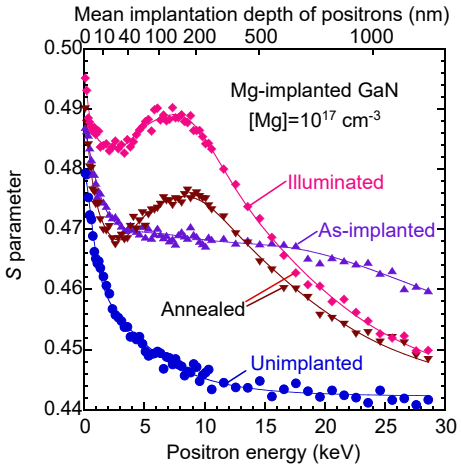

Figure 1: S parameters as a function of the incident positron energy E for Mg-implanted GaN with Mg concentrations of 1 × 10^{17} cm^{-3}. The measurement for the as-implanted sample was performed in darkness, and that for the sample annealed at 1300 °C was performed both in darkness and under illumination.

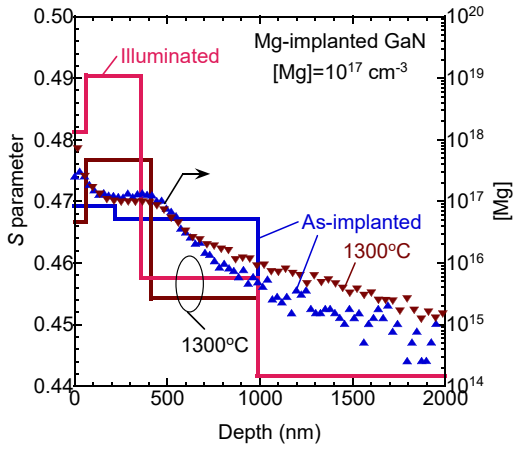

Figure 2: Depth distributions of S obtained from the analysis of the S-E curves shown in fig. 1. The distributions of Mg measured by SIMS are also shown.

damaged region (0 - 1000 nm) extended the block profile of Mg (≤ 500 nm), which is due to the defect introduction by Mg implanted below 500 nm. After annealing at 1300 °C, although the S value below 400 nm decreased, the value at 50 - 400 nm increased, suggesting the agglomeration of vacancy-type defects.

The lifetime spectra were measured at E = 8 keV. The spectrum of the as-implanted sample was analysed assuming one annihilation mode, and the derived positron lifetime was 248 ps. This lifetime is in agreement with the calculated positron lifetime for a divacancy, $V_{Ga}V_N$ (246 ps), suggesting that the major defect species in the as-implanted sample was $V_{Ga}V_N$. The spectrum of the sample annealed at 1300 °C was decomposed assuming three components. The second-longest lifetime obtained was 320 - 330 ps (relative intensity = 35%), which was attributed to the annihilation of positrons trapped by vacancy clusters such as $(V_{Ga}V_N)_3$. Under illumination, its intensity increased up to 42%, which is due to the electron trapping of the vacancies and a resultant increase in the trapping rate of positrons. This is the origin of the increase in S measured under illumination (fig. 1 and 2). We have shown that positron annihilation is a sensitive tool in the detection of vacancy-type defects and their carrier trapping process, and that this technique can be used to better understand the annealing behavior of the point defects in ion implanted GaN.

[1] A. Uedono, et al., Carrier Trapping by Vacancy-Type Defects in Mg-Implanted GaN Studied Using Monoenergetic Positron Beams, Phys. Stat. Sol. B 255 (4), 1700521 (2018)

Mixing effects in a ternary Hf-Zr-Ni metallic melt

B. Nowak[1], D. Holland-Moritz[1], F. Yang[1], Z. Evenson[2], A. Meyer[1]

[1]Institut für Materialphysik im Weltraum, Deutsches Zentrum für Luft- und Raumfahrt (DLR), Köln, Germany; [2]Heinz Maier-Leibnitz Zentrum (MLZ) and Physics Department, Technical University of Munich, Garching, Germany

We studied the impact of substituting Zr by Hf on the melt dynamics in a Hf-Zr-Ni metallic glass-forming liquid [1]. The boundary binary alloys $Zr_{34}Ni_{64}$ and $Hf_{35}Ni_{65}$ exhibit very similar packing fractions and topological short-range orders in the molten state. However, the Ni self-diffusion is about a factor of 2 slower in the Hf-bearing melt compared to that in the Zr-based melt. This leads to the question to what extent the dynamical behavior of the melt is influenced by alloying effects if the overall packing fraction remains constant. This question is particularly relevant for glass formation in metallic alloys, as the glass-forming ability (GFA) seems to be generally enhanced by increasing the number of different atomic components.

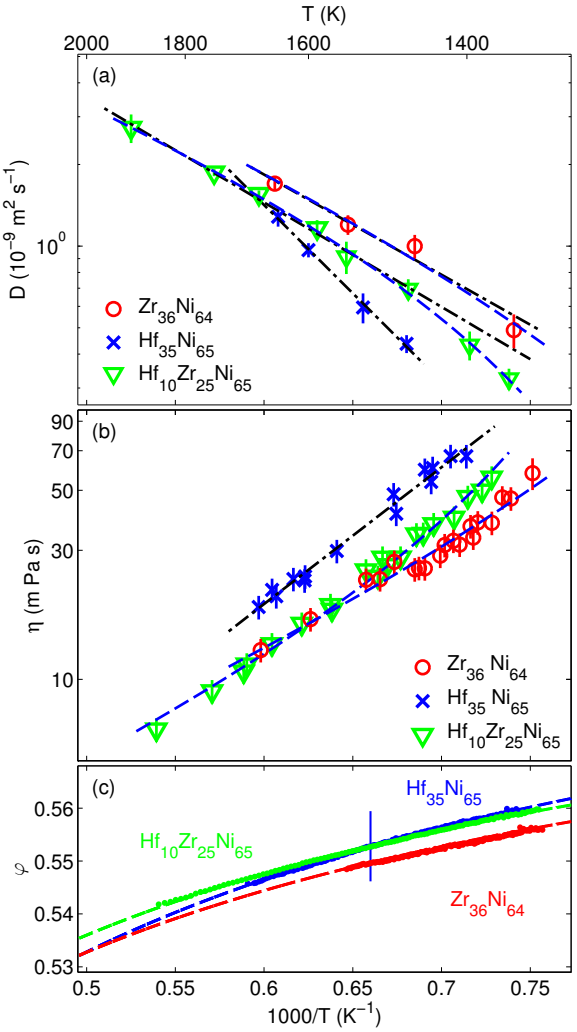

Figure 1: (a) Self-diffusion coefficients in $Hf_{35}Ni_{65}$, $Zr_{36}Ni_{64}$, and $Hf_{10}Zr_{25}Ni_{65}$ measured by QENS. The black dashed-dotted lines represent the Arrhenius fit and the blue dashed lines the scaling-law fit predicted by MCT. (b) Measured viscosity for $Zr_{36}Ni_{64}$, $Hf_{35}Ni_{65}$ and $Hf_{10}Zr_{25}Ni_{65}$ by in an electrostatic levitator. (c) Packing fraction for $Zr_{36}Ni_{64}$, $Hf_{35}Ni_{65}$ and $Hf_{10}Zr_{25}Ni_{65}$. Experimental uncertainties are shown by the vertical line.

To investigate this effect in details, we focused on the atomic dynamics and melt viscosity of the ternary $Hf_{10}Zr_{25}Ni_{65}$ alloy. The microscopic dynamics was studied at the time-of-flight instrument TOFTOF. One special aspect of the experiment is that the Zr- and Hf- containing melts are chemically highly reactive. Thus, we combined the quasielastic neutron scattering (QENS) method with containerless processing techniques. In this case, in order to access large temperature intervals, both electrostatic and electromagnetic levitations were used. With this, we were able to determine the Ni self-diffusion coefficient in the liquid from 1355 K to 1905 K. As shown in fig. 1 (a), we found that substituting Zr by Hf in the binary alloy $Zr_{36}Ni_{64}$ results in a smaller Ni self-diffusion coefficient. In addition, over a temperature range of 550 K, deviations from the Arrhenius-like temperature dependence have been observed in the ternary melt. This can be described by a scaling-law like behavior as predicted by mode-coupling theory (MCT), which is very often observed for relaxation dynamics in glass-forming liquids.

We also studied the macroscopic melt viscosity of the binary and the ternary. As it can be seen in fig. 1 (b), both the atomic dynamics and the melt viscosity exhibit the same composition trends: substituting Zr by Hf results in more sluggish dynamics, or higher melt viscosities. We can even show for the ternary alloy that over the entire studied temperature range, the atomic dynamics and the melt viscosity obey the same temperature dependence.

On the other hand, the derived packing fraction from the measured liquid density remains almost unchanged (fig. 1 (c)). Since the atomic size of Zr and Hf is nearly equal, this indicates that the changes of the dynamics by the substitution should be mainly attributed to different chemical interactions in the melt. The more sluggish dynamics in the ternary melt also favors the glass formation.

[1] B. Nowak, et al., Mixing effects in a ternary Hf-Zr-Ni metallic melt, Phys. Rev. B: Condens. Matter 97, 094202 (2018)

New Ni-base superalloy for higher service temperatures

C. Solís[1], J. Munke[1], M. Hofmann[1], M. Bergner[2], A. Kriele[3], M.J. Mühlbauer[1,4], D.V. Cheptiakov[5], S. Mühlbauer[1], B. Gehrmann[6], J. Rösler[2], R. Gilles[1]

[1]Heinz Maier-Leibnitz Zentrum (MLZ), Technical University of Munich, Garching, Germany; [2]Institut für Werkstoffe, Technische Universität Braunschweig, Braunschweig, Germany; [3]German Engineering Materials Science Centre (GEMS) at MLZ, Helmholtz-Zentrum Geesthacht GmbH, Garching, Germany; [4]Institute for Applied Materials (IAM), Karlsruhe Institute of Technology (KIT), Eggenstein-Leopoldshafen, Germany; [5]Laboratory for Neutron Scattering and Imaging, Paul Scherrer Institut, Villigen, Switzerland; [6]VDM Metals International GmbH, Altena, Germany

A new high temperature Ni-base superalloy VDM 780 Premium has been developed for higher service temperatures (above 650 °C) in stationary gas turbine applications, preserving the good processing characteristics of the commonly used alloy 718. Due to its promising industrial applications, the morphology and microstructure of this newly developed superalloy have been studied for the first time within the framework of a BMBF project by means of neutron diffraction (SPODI, STRESS-SPEC, HRPT at PSI), X-ray diffraction (MatSci Laboratory at MLZ) and small-angle neutron scattering (SANS-1) [1].

Samples after three different ageing treatments performed to set up different microstructures have been studied. The neutron diffraction (ND) results show the presence of the γ-matrix and γ'-hardening phases as well as a high temperature phase with a structure that is compatible with the δ and η phases, while no traces of the γ'' hardening phase are observed, regardless of the heat treatment (fig. 1). Furthermore, recent synchrotron and transmission electron microscopy measurements have confirmed the presence of both high-temperature phases in the material, despite the very small amount. As these phases will strongly influence the mechanical properties of the material at high temperature, a detailed study of both high-temperature phase structures by means of high resolution transmission electron microscopy (HRTEM) and neutron techniques will allow further optimisation of this new superalloy.

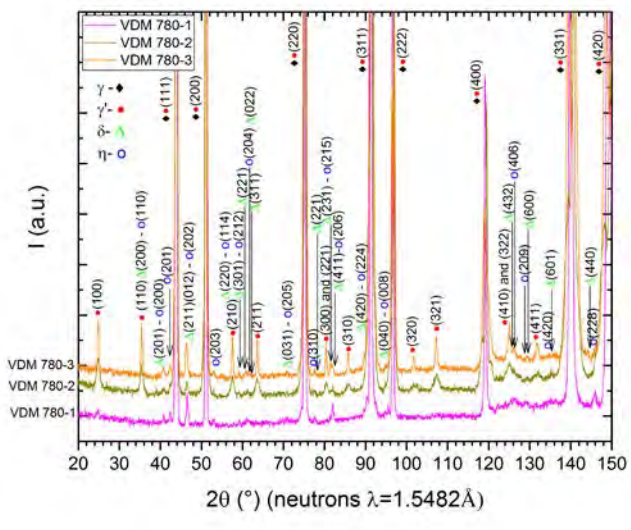

Figure 1: ND patterns at ambient temperature (SPODI) of the VDM 780 Premium alloy samples after three different aging treatments.

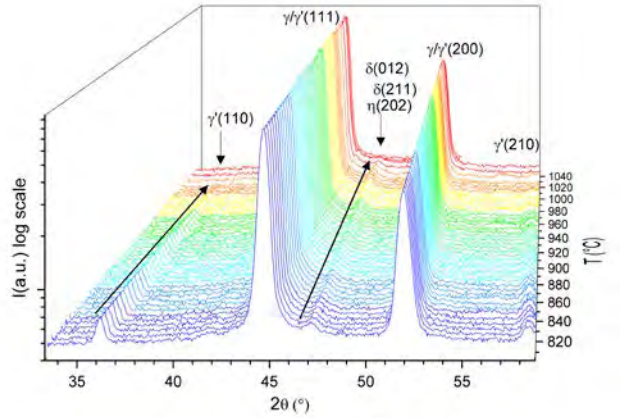

Figure 2: In-situ ND patterns (STRESS-SPEC) measured during heating from 820 °C up to 1040 °C to determine the solvus temperatures.

Rietveld refinements allow phase identification, determination of the lattice constants and the weight fractions of the constituent phases, and show that the presence of the different phases, number and morphology are highly dependent on the ageing treatments. In situ neutron diffraction studies (fig. 2) at high temperature have made it possible to determine the solvus temperatures of the different phases present in each sample following the corresponding aging treatment, as well as the study of the evolution of the lattice parameters with temperature. Moreover, in situ small-angle neutron scattering measurements allow the evolution of the morphology and size of the precipitates with temperature change to be followed. Also, the Vickers hardness of the different samples has been correlated with the amount and particle size of the γ'-hardening phase present in each sample.

Future investigation of this alloy will focus on measurements to discern the presence of the two different high-temperature phases, to stabilise one of them and follow its evolution with temperature.

[1] C. Solís, et al., In situ characterization at elevated temperatures of a new Ni-based superalloy VDM-780 Premium, Metall. Mater. Trans. A 49, 4373 (2018)

In situ neutron diffraction study of phase relaxation in lithium-ion batteries

J. Wilhelm[2], S. Seidlmayer[1], S. Erhard[2], M. Hofmann[1], R, Gilles[1], A. Jossen[2]

[1]Heinz Maier-Leibnitz Zentrum (MLZ), Technical University of Munich, Garching, Germany; [2]Institute for Electrical Energy Storage Technology (EES), Technical University of Munich, München, Germany

Reduced capacity and rate capability at low temperature operation is a limiting factor in the application of lithium-ion batteries in electro-mobility. The visualisation of electrode inhomogeneity resulting from low-temperature lithium transport limitations illustrates the shortcomings in current electrode designs. Our study of lithiation gradients and relaxation processes in graphite anodes was carried out at the STRESS-SPEC instrument, using time-resolved in situ neutron diffraction. The measurements were performed with commercial high power $LiCoO_2$/Graphite pouch bag batteries operated in the temperature range of -20 °C to 40 °C. According to the specifications, this battery type is designed for high power use and allows for 1C continuous charging and 12C continuous discharging in a temperature window of 0 °C to 60 °C. The scattering gauge volume was defined by a 5 × 20 mm^2 entrance slit and a 5 mm radial collimator in front of the detector. For our experimental focus on lithiated graphite phases during discharge, we limited the data collection to the 2θ-range of 28° < 2θ < 42°. This allows fast data collection at 3 min intervals with sufficient signal quality. With decreasing temperature, strong anode polarisation is observed due to the phase coexistence of LiC_{12} and less lithiated phases such as LiC_{18} and $Li_{1-x}C_{54}$ during and after discharge. Phase coexistence is maintained only briefly at 25 °C, but lasts for more than 6 hours at -10 °C before equilibration. The long-term relaxation phenomena are attributed to slow lithium transport within particles at low temperature. Analysis of the relaxation times and particle size distribution yields effective diffusion constants for lithium transport in graphite of 1.7 × 10^{-10} cm^2s^{-1} at room temperature and 0.7 × 10^{-11} cm^2s^{-1} at -10 °C. We find that a moderate discharge rate is already sufficient to cause considerable anode polarisation at low temperature, while at higher discharge rates up to 5C, self-heating reduces polarisation and relaxation time.

A combination of neutron diffraction, electrochemical cycling, and impedance measurements was applied to study the performance of a high power $LiCoO_2$/graphite pouch bag battery in the temperature range of -20 °C to 40 °C. The battery shows decreasing capacity and increasing charge transfer resistances as well as greater polarisation during discharge with decreasing temperature. In situ diffraction data of the anode during discharge and subsequent relaxation reveal the occurrence of inhomogeneous lithiation of the graphite with multiple coexisting phases. After discharge, equilibration of the graphite phases toward a single or two phases close to mean lithium content takes place. Expanding our previous work with high energy cylindrical cells, we were able to exclude SoC (state of charge) inhomogeneity due to internal temperature gradients. Additionally, SoC gradients due to potential drops along the current collector were strongly reduced due to the choice of the small format pouch bag battery. The observed effects are best explained by slow lithium diffusion in the solid phase. Through analysis of the relaxation times, we attribute the slow lithium transport to limitations of ion movement through grain boundaries between different phase domains or crystallites within the particles rather than to in-plane transport across the electrode. We suggest further investigation of batteries built with electrodes with narrow particle size distributions to clarify the extent of inhomogeneity between particles of different size and surface areas.

[1] J. Wilhelm, et al., In Situ Neutron Diffraction Study of Lithiation Gradients in Graphite Anodes during Discharge and Relaxation, J. Electrochem. Soc. 165 (9), A1846 (2018)

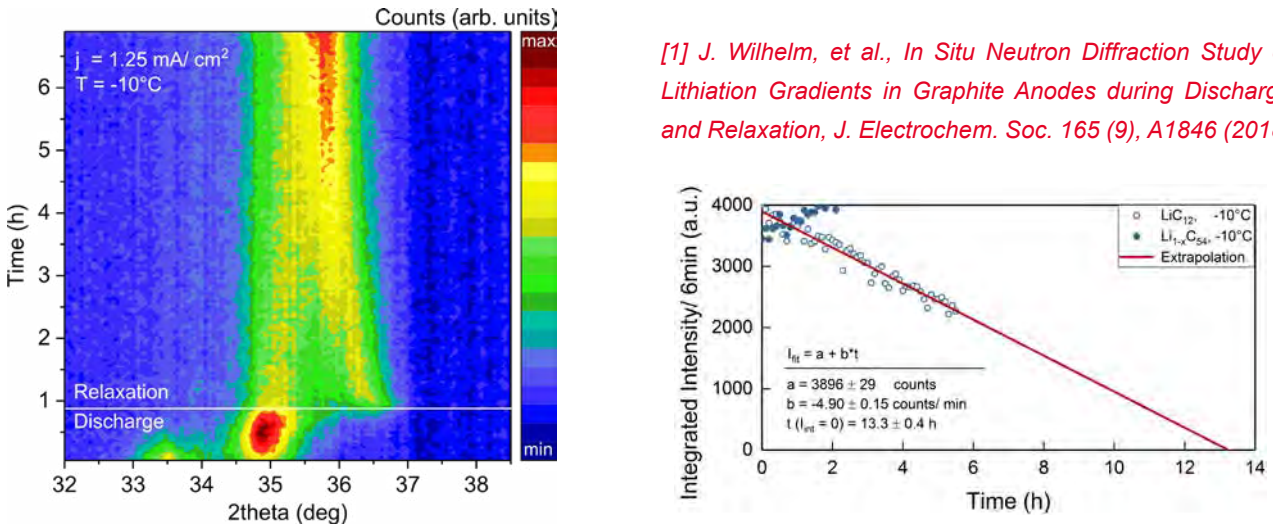

Figure 1: Left: scattering angle vs time and scattering intensity (color coded) at T = -10 °C. Right: linear extrapolation of decreasing integrated intensity share of LiC_{12} during relaxation after discharge at T = -10 °C.

Neutron Depth Profiling on battery electrodes at the N4DP setup

M. Trunk[1], M. Wetjen[2], L. Werner[1], R. Gernhäuser[3], B. Märkisch[1], Z. Revay[4], H. Gasteiger[2], R. Gilles[4]

[1]Physics Department ENE, Technical University of Munich, Garching, Germany; [2]Chemie Department, Lehrstuhl für Technische Elektrochemie, Technical University of Munich, Garching, Germany; [3]Physics Department, Zentrales Technologielabor, Technical University of Munich, Garching, Germany; [4]Heinz Maier-Leibnitz Zentrum (MLZ), Technical University of Munich, Garching, Germany

Neutron Depth Profiling (NDP) is a non-destructive, isotope specific, high-resolution nuclear analytical technique, which is sensitive to several light nuclides such as ^{3}He, ^{10}B, ^{6}Li, ^{14}N, ^{17}O. Upon neutron capture, the nuclei undergo nuclear reactions and emit charged particles. The energy loss of the charged particles through matter is correlated to the emission depth and a concentration profile as a function of the depth can be obtained. Recently, the Neutron Depth Profiling setup 'N4DP' was installed at the PGAA facility at the Heinz Maier-Leibnitz Zentrum. The facility provides a homogeneous cold neutron beam (1.83 meV) and a maximum thermal equivalent neutron flux of 4 x 10^{10} neutrons/cm^{2}s. The optimised N4DP chamber, shown in fig. 1, enables PGAA and NDP simultaneously, and also makes it possible to reduce the background.

Here, the concentration profiles of immobilised lithium in silicon-graphite-based electrodes for lithium-ion batteries were investigated. Silicon is one of the anode materials that offer the greatest promise for lithium-ion batteries to achieve

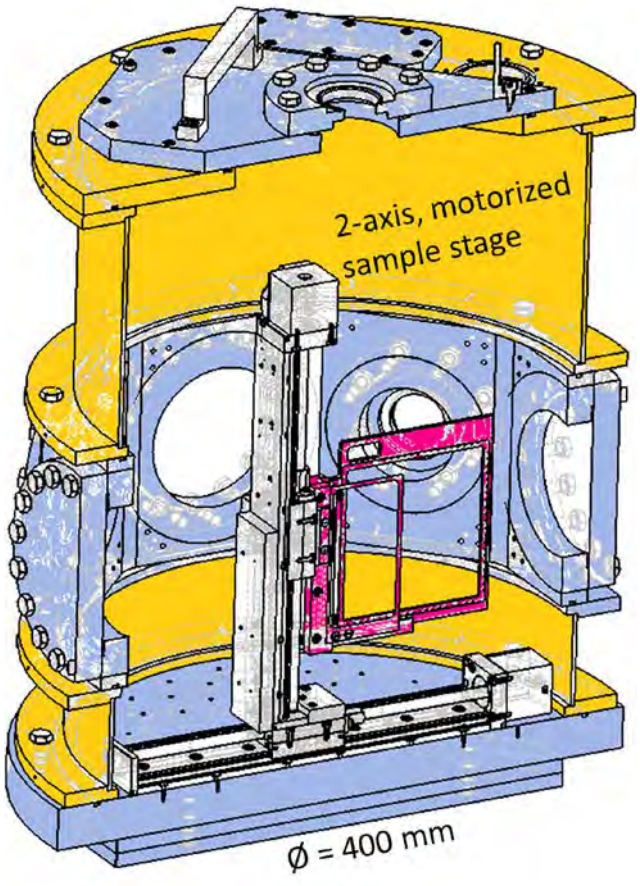

Figure 1: Scheme of the N4DP vacuum chamber.

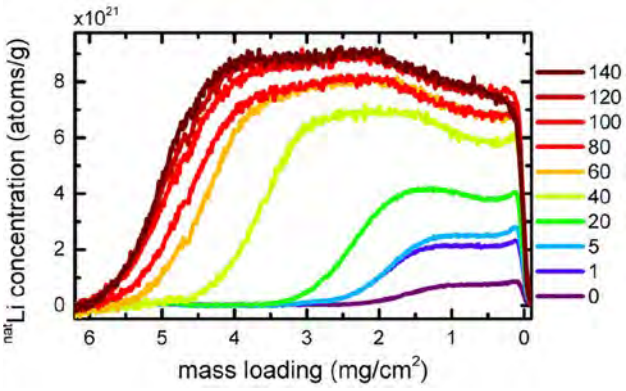

Figure 2: Concentration profiles of lithium in silicon-graphite-based electrodes, measured ex situ using NDP [1].

cell-level energy densities > 350 Wh/kg in the future. Nonetheless, its commercialisation is still hampered because of large morphological changes which the silicon particles undergo upon repeated insertion and extraction of lithium, also resulting in a significant swelling of the entire electrode. Here, the concentration profiles of the electrolyte decomposition products containing lithium were investigated ex situ, using NDP across the thickness of the silicon-based electrode, as a function of the charge/discharge cycle number and these are shown in fig. 2 [1]. The data show a significant increase in the immobilised lithium in the electrodes over cycling, and the electrode mass growth can also be directly studied. Both trends increase until a saturation level (at about 100 cycles) is reached. Furthermore, a change in the shape of the concentration profile after several charge/discharge cycles is observed by NDP, revealing depth-dependent ageing processes. Interestingly, the data indicate that no sections that are isolated completely electrically are formed with respect to depth. Even if some of the silicon particles become electrically isolated upon prolonged charge/discharge cycling, this process seems to occur uniformly across the electrode without a preferential disconnection, e.g. at the bottom of the electrode due to the blocking of conducting pathways. This project is supported by BMBF 05K16WO1.

[1] M. Trunk, et al., Materials Science Applications of Neutron Depth Profiling at the PGAA of the Heinz Maier-Leibnitz Zentrum, Mater. Charact. 146, 127 (2018)

The texture of prehistoric gold artefacts studied via neutron diffraction

F. E. Wagner[1], R. Gebhard[2], W. M. Gan[3], M. Hofmann[4], M. Mönnich[5]

[1]Physics Department E15, Technical University of Munich, Garching, Germany; [2]Archäologische Staatssammlung München, München, Germany; [3]German Engineering Materials Science Centre (GEMS) at MLZ, Helmholtz-Zentrum Geesthacht GmbH, Garching, Germany; [4]Heinz Maier-Leibnitz Zentrum (MLZ), Technical University of Munich, Garching, Germany; [5]Akademie der Bildenden Künste, München, Germany

Gold has been used to make objects of ornamental and representative character since late neolithic times. Our knowledge of early manufacturing techniques is scant and based largely on archaeological finds of ancient tools and on pictures found in ancient Egyptian tombs.

The working of the gold has, however, left traces in the material itself, from which one can draw conclusions as to the methods of production. One such feature, the metallurgical texture, has so far attracted little attention. A polycrystalline metal such as gold consists of individual grains, i.e., tiny single crystals with different orientations of their crystal axes. Depending on the manner in which the metal was deformed during its production, these orientations acquire preferred directions in the object. This is known as " texture" or "preferred orientation", and may conserve a memory of the casting, deformation or heat treatment processes.

Texture determination is usually performed using X-ray diffraction. In the case of gold, the X-rays are strongly absorbed and therefore probe only the uppermost micrometres. Here, thermal neutrons are superior, since they can penetrate millimetres deep into gold. We have used the STRESS-SPEC neutron diffractometer to study prehistoric gold objects in order to non-destructively determine their texture and draw conclusions as to how the objects were made.

In our studies we focussed on flat specimens. The first objects studied (fig. 1) were from a find of 21 gold objects discovered in 1998 at a Bronze Age fortification near Bernstorf, about 40 km north of Munich [1]. These finds are of very pure gold, which is why their authenticity has been questioned by some archaeologists. Subsequently, several other prehistoric gold objects from the Bullenheimer Berg in Lower Francony and from Hammersdorf near Erding in Upper Bavaria were studied. Surprisingly, the Bernstorf objects were found to exhibit a very pronounced cube texture. This is a preferred orientation in which the {001} planes of the fcc unit cell of the gold crystallites lie in the plane of the sheet, while the other two face in two mutually orthogonal directions in the plane of the foil. It is known that such a texture arises when fcc metals such as gold are rolled and then annealed. The three other prehistoric gold objects we have studied so far showed no pronounced texture.

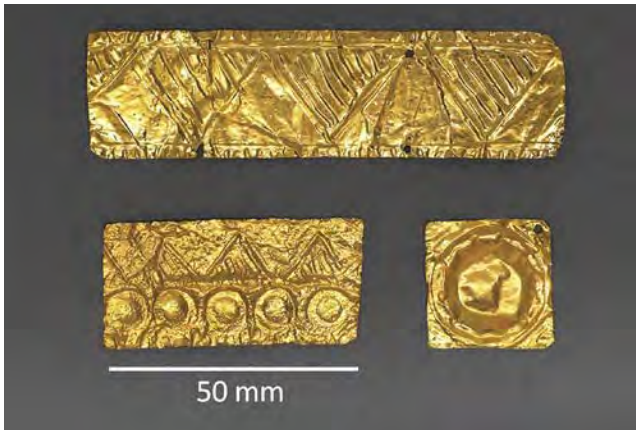

Figure 1: The Bernstorf gold artefacts studied from the collection of the Archäologische Staatssammlung München.

We have also performed reference experiments with samples made by rolling and annealing, as well as by hammering and annealing in different ways. The essence of these experiments is that a cube texture such as that of the Bernstorf gold can be obtained by rolling and subsequent annealing, but also by a special technique of hammering with a hammer with a cylindrical peen in such a way that the gold expands in only one direction. The cube texture of the reference specimens was, however, never as pure as that of the Bernstorf objects. We are still trying to find a reason for this. Hammering with a flat hammer on a flat anvil tends to produce a texture such as that observed in the gold objects from Hammersdorf and the Bullenheimer Berg. Such hammering textures are usually weak, which means that the deviations from a random distribution of the crystallites are not very strong. They also depend on details of the hammering and on intermediate annealing steps used by goldsmiths to make the metal soft again when it has become brittle after hammering.

The conclusions one can draw from the experiments performed so far are that the texture is an important feature of the metallurgical state of ancient gold artefacts and can give clues as to the manner in which the objects were made. However, the results we have obtained to date do not allow us to make definitive statements regarding the authenticity of the gold from Bernstorf, since hammering in one direction as well as rolling, both with subsequent annealing, result in a similar cube texture.

[1] F. E. Wagner, et al., The Metallurgical Texture of Gold Artefacts Found at the Bronze Age Rampart of Bernstorf (Bavaria) Studied by Neutron Diffraction, J. Archaeolog. Sci.: Rep. 20, 338 (2018)

Extrinsic in-gap states in samarium hexaboride

W.T. Fuhrman[1], J.R. Chamorro[1,2], P. A. Alekseev[3,4], J.-M. Mignot[5], T. Keller[6,7], J.A. Rodriguez-Rivera[8,9], Y. Qiu9, P. Nikolić[1,10], T.M. McQueen[1,2,11], C.L. Broholm[1,11]

[1]Institute for Quantum Matter and Department of Physics and Astronomy, The Johns Hopkins University, Baltimore, MD, USA; [2]Department of Chemistry, The Johns Hopkins University, Baltimore, MD, USA; [3]National Research Centre "Kurchatov Institute", Moscow, Russia; [4]National Research Nuclear University "MEPhI", Moscow, Russia; [5]Laboratoire Léon Brillouin, CEA-CNRS, CEA/Saclay, Gif sur Yvette, France; [6]Max Planck-Institut für Festkörperforschung, Stuttgart, Germany; [7]Max-Planck-Institute for Solid State Research at Heinz Maier-Leibnitz Zentrum (MLZ), Garching, Germany; [8]Department of Materials Sciences, University of Maryland, College Park, MD, USA; [9]NIST Center for Neutron Research, National Institute of Standards and Technology, Gaithersburg, MD, USA; [10]School of Physics, Astronomy and Computational Sciences, George Mason University, Fairfax, VA, USA; [11]Department of Materials Science and Engineering, The Johns Hopkins University, Baltimore, MD, USA

First prepared in the 1950's, samarium hexaboride (SmB_6) hosts exotic properties that blur the lines between metal and insulator. Over time, various low energy phenomena in SmB_6 have become associated with in-gap states, loosely defined as 15 - 35 meV via (e.g.) Raman spectroscopy (suppression of spectral weight below 35 meV), ARPES (4f binding energy of 15 - 20 meV), point contact spectroscopy (20 meV conductance peak), and STM measurements (20 meV gap in tunneling conductance DOS).

Recently, the advent of topological band theory led to the proposal of SmB_6 as a topological Kondo insulator, with experiments revealing metallic surface states as the origin of the low-temperature resistance plateau. Yet, experimental probes such as specific heat, optical conductivity, and quantum oscillations still indicate magnetic and metal-like properties originating in the bulk of SmB_6, while non-local transport measurements reveal its distinctly insulating nature. Exotic phenomena have been proposed to account for this peculiar low energy density of states, with no clear consensus emerging.

Magnetic neutron scattering, a direct probe of bulk magnetism, is well-suited to inform about this potentially exotic low-energy regime. However, our results in both zero field and 9 T reveal no indications of magnetism below the 13 meV spin-exciton [1]. Furthermore, we show that the lowest energy excitation probed by neutrons, the well-known spin-exciton, has a long intrinsic lifetime, indicating a lack of substantial low-energy decay channels. Given the nearly complete Sm^{3+} moment contained within the spin-exciton and the continued trend to lower heat capacity with improved sample quality, it is reasonable to assign most, if not all, of the low energy DOS observed in SmB_6 to extrinsic origins. We infer that extrinsic defects such as rare-earth impurities and vacancies, present in varying quantities in all samples of SmB_6, create a gapless continuum which dynamically screens impurity moments and introduces a low-energy DOS. The variety of metal-like properties induced by impurities is an important part of the phenomenology of this cornerstone Kondo insulator.

[1] W. T. Fuhrman, et al., Screened moments and extrinsic in-gap states in samarium hexaboride, Nat. Commun. 9, 1539 (2018)

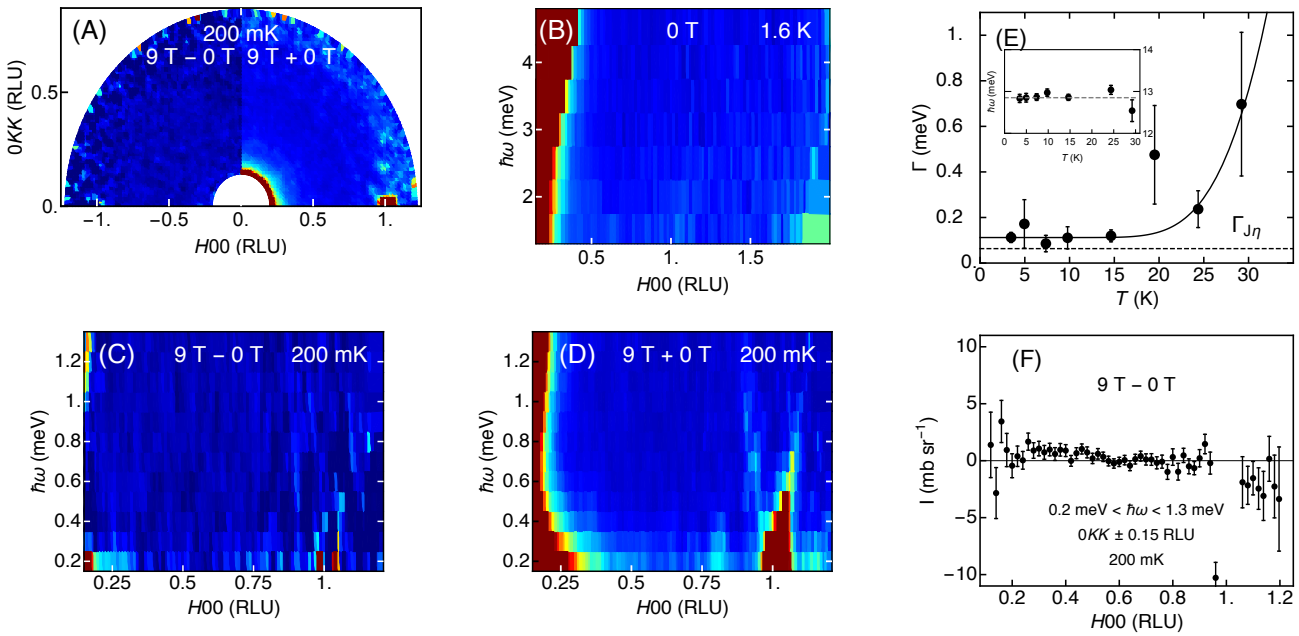

Figure 1: Low energy neutron scattering of SmB_6. Only residual Bragg and background scattering is apparent. (A) Energy integrated from 0.2 meV to 1.3 meV. Left shows 9 T - 0 T, right shows average (9 T + 0 T). (B) 0 T data from 1.5 meV to 5 meV. (C) 9 T - 0 T data. (D) Average of 9 T and 0 T data. (E) Spin-exciton lifetime and mode energy vs T. Solid line shows $\Gamma_0 + A^*\exp(-\Delta/k_BT)$, with non-thermal lifetime $\Gamma_0 = 0.11$ meV and exponential activation to the mode energy $\Delta = 12.8$ meV. Dashed line is estimate from coupling the collective mode to a presumed extrinsic DOS at E_F ($\Gamma_{J\eta} = 0.080$ meV). (F) 9 T - 0 T scattering integrated from 0.2 meV to 1.3 meV.

Spin plaquette entanglement in $SrCu_2(BO_3)_2$

M. E. Zayed[1] , A. Schneidewind[2]

[1]Carnegie Mellon University in Qatar, Education City, Doha, Qatar; [2]Jülich Centre for Neutron Science (JCNS) at MLZ, Forschungszentrum Jülich GmbH, Garching, Germany

Through a series of inelastic neutron scattering experiments combining high pressures and low temperatures, we show that the usual two-spin entanglement realised by Cu^{2+} dimers in $SrCu_2(BO_3)_2$ is replaced by a four-spin entanglement corresponding to a plaquette configuration at 21.5 kbar. These experiments resolve a long-standing open question in the field of quantum magnetism regarding the phase-diagram of the Shastry-Sutherland model.

The Shastry-Sutherland Model, a network of orthogonal spin dimers (fig. 1 insets), possess the unusual property of being an exactly solvable frustrated quantum spin model. The only known realisation of this model with spin S = 1/2 is $SrCu_2(BO_3)_2$. However, the exact ground-state solution, a direct product of singlets on the dimers, covers only the initial range of the phase diagram: upon increasing the value of the inter-dimer to an intra-dimer magnetic coupling ratio, one eventually finds a square lattice type of antiferromagnetic (AFM) order. How the transition between the singlet and the AFM phase occurs has led to a considerable amount of theoretical research. Our experimental work on $SrCu_2(BO_3)_2$, has shown that an intermediary state exists and that its signatures are compatible with a four-spin plaquette. In this new state, the unpaired Cu^{2+} electrons are entangled in a basic unit consisting of four electrons (the plaquette) instead of the original two-electron singlet pair (the dimer).

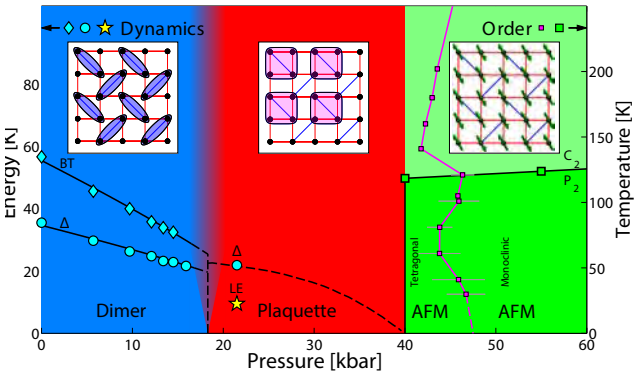

Figure 1: Experimental phase diagram of $SrCu_2(BO_3)_2$. The blue region is the dimer phase, the red region the newly identified plaquette phase, and the green region is the antiferromagnetic phase. The magenta line shows the tetragonal – monoclinic boundary. Two different space groups (C_2 and P_2) are present in the monoclinic region. Circles are the triplet gap Δ energies, diamonds are the corresponding two-triplet bound state (BT) energies and the star is a new low-energy excitation (LE) observed at Q = (1,0,1). Green squares, representing Q = (1,0,0) magnetic Bragg peaks, are observed only above 40 kbar. The insets represent the Shastry-Sutherland network realised by the Cu^{2+} ions of $SrCu_2(BO_3)_2$. The dimer, plaquette and AFM spin configurations are highlighted in each region.

Fig. 2 shows spectra collected on the IN14 and PANDA spectrometers. The evolution of the low-lying energy excitations can be extracted [1]. The results are summarised in fig. 1 which also shows the completed experimental pressure-temperature phase diagram. At zero pressure, the compound is in its original dimer phase. As pressure increases, the energy levels of the excitations, which are triplets (Δ) and bound-triplets (BT) states, soften quasi linearly up to 16 kbar. Between 16 and 21.5 kbar a discontinuity in the softening is observed and a new low-energy excitation (LE) suddenly appears. Increasing the pressure even further leads, at 40 kbar, to the expected AFM ordering. A structural distortion follows, with the compound losing its crystallographic tetragonal symmetry for a lower monoclinic symmetry.

Inelastic neutron scattering was performed on three different instruments: IN14 at ILL Grenoble France, TASP at SINQ-PSI Villigen Switzerland, and PANDA at the FRM II/ MLZ Garching Germany. The results at pressures 40 kbar and higher were obtained by a combination of neutron diffraction at ILL, and synchrotron X-ray diffraction at ESRF, Grenoble France.

M. E. Z. acknowledges the generous support of the Qatar Foundation through Carnegie Mellon University in Qatar's Seed Research program. The statements made herein are solely the responsibility of the author(s).

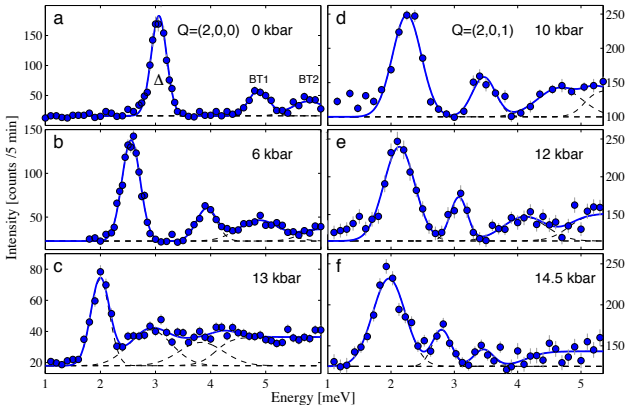

Figure 2: Energy spectra of $SrCu_2(BO_3)_2$ at different pressures. (a-c) Evolution of the spectrum for Q = (2, 0, 0), measured on IN14, ILL. (d-f) Evolution of the spectrum for Q = (2, 0, 1), measured on PANDA, MLZ. The singlet triplet excitation Δ and the two lowest bound triplet states BT1 and BT2 are indicated.

[1] M. E. Zayed, et al., 4-spins plaquette singlet state in the Shastry–Sutherland compound $SrCu_2(BO_3)_2$, Nature Physics 13, 962 (2017)

c-axis pressure induced AF order in optimally P-doped $BaFe_2(As_{0.70}P_{0.30})_2$ superconductor

D. Hu[1], R. Georgii[2], B. Pedersen[2], P. Dai[1]

[1]Department of Physics and Astronomy, Rice University, Houston, Texas, USA; [2]Heinz Maier-Leibnitz Zentrum, Technical University of Munich, Garching, Germany

In the isoelectronic-doped iron pnictides superconductor $BaFe_2(As_{1-x}P_x)_2$, where the parent compound $BaFe_2As_2$ has a collinear AF order below T_N preceded by a tetragonal-to-orthorhombic lattice distortion at T_s with $T_s \geq T_N$, optimal superconductivity with $T_c \approx 30$ K emerges upon complete suppression of the 3D AF order and T_s by increasing x to 0.3 or hydrostatic pressure. Although the origin of the quantum critical point and even the existence of QCP at x = 0.30 is still under debate, the wide range of strong non-Fermi liquid behavior appears in the normal state around optimal superconducting concentration. To understand the remarkable strange normal state electronic behaviors and high temperature superconductivity, we would manipulate and study the interplay between the nematic/magnetic order and superconductivity in optimally doped $BaFe_2(As_{0.70}P_{0.30})_2$ superconductor by using an external probe such as pressure.

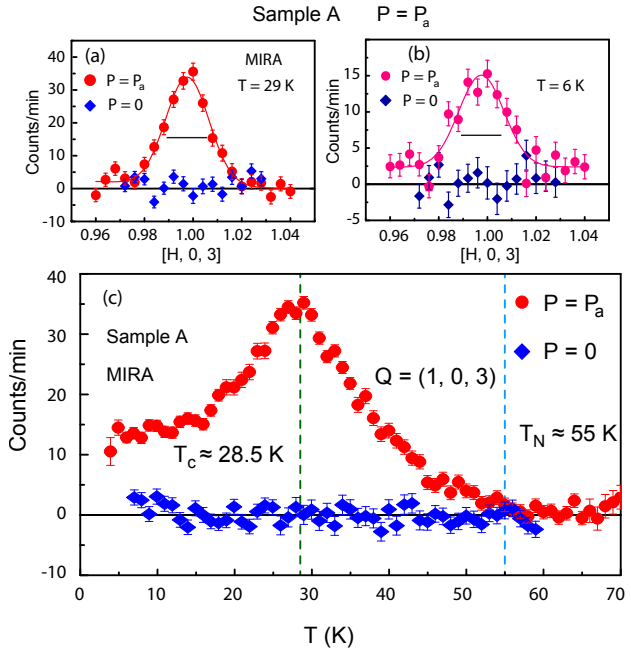

Figure 1: Summary of neutron scattering results on MIRA. (a - b) Q-scans through the (1, 0, 3) magnetic Bragg peak position at different temperatures for P = P_a and P = 0. (c) Temperature dependence of the magnetic scattering at Q_{AF} = (1, 0, 3) for P = P_a and P = 0.

By measuring the c-axis pressure dependence of the resistivity using a custom designed uniaxial pressure device with 0 < P_c < 480 MPa, a systematic reduction in T_c from 29.5 to 28.5 K was found. Meanwhile, the temperature dependence of the resistivity systematically deviates from the linear behavior, suggesting the reappearance of antiferromagnetic order, which is reminiscent of the situation in $BaFe_2(As_{0.71}P_{0.29})_2$ at ambient condition. To confirm the results of transport measurements, we have carried out neutron diffraction experiments on the MIRA-II spectrometer. At zero pressure, the sample has no static AF order at T = 29 K and 6 K as shown in wave vector scans along the [H, 0, 3] direction through the magnetic Bragg peak position (1, 0, 3). Upon application of a finite c-axis aligned uniaxial pressure ($P_a \approx 400$ MPa), we find temperature-dependent peaks at (1, 0, 3). The solid lines are Gaussian fits to the data, which give the static spin-spin correlation lengths of 220 ± 30 Å, indicating pressure-induced long-range magnetic order. Comparing the temperature dependence of the (1, 0, 3) scattering at zero and Pa pressure, the induced magnetic order with T_N = 55 K is observable after the application of c-axis pressure, which is similar to that of underdoped $BaFe_2(As_{1-x}P_x)_2$, where the reduction of magnetic scattering below T_c is due to the competition of superconductivity with static AF order. Further Rietveld analysis of the single crystal diffraction data revealed that the major effect of a $P_c \approx 400$ MPa is to suppress the c-axis and expand the in-plane lattice parameters without much affecting the average pnictogen height hAs/P.

Our neutron scattering results reveal that a moderate uniaxial pressure along the c-axis in the $BaFe_2(As_{0.70}P_{0.30})_2$ superconductor can spontaneously induce a three-dimensional stripe AF order with T_N > 30 K, while only slightly suppressing T_c. These results indicate a strong magnetoelastic coupling near optimal superconductivity, suggesting a uniaxial pressure-induced nematic phase stripe AF order competing with superconducting in $BaFe_2(As_{1-x}P_x)_2$.

[1] D. Hu, et al., c-axis pressure-induced antiferromagnetic order in optimally P-doped $BaFe_2(As_{0.70}P_{0.30})_2$ superconductor, npj Quantum Mater. 3, 47 (2018)

Impact of oxygen diffusion on superconductivity in $YBa_2Cu_3O_{7-\delta}$ thin films studied via positrons

C. Hugenschmidt[1,2], M. Reiner[2], T. Gigl[1,2], R. Jany[3], G. Hammerl[3]

[1]Physics Department, Technical University of Munich,Garching, Germany; [2]Heinz Maier-Leibnitz Zentrum (MLZ), Technical University of Munich, Garching, Germany; [3]Experimental Physics VI, Center for Electronic Correlations and Magnetism, University of Augsburg, Augsburg, Germany

The oxygen deficiency δ in $YBa_2Cu_3O_{7-\delta}$ (YBCO) plays a crucial role for affecting high-temperature superconductivity. We applied (coincident) Doppler broadening spectroscopy (CDBS) of the electron-positron annihilation line to an in situ study of the temperature dependence of the oxygen concentration and its depth profile in single crystalline YBCO films [1]. In $YBa_2Cu_3O_{7-\delta}$, positrons show a particularly high affinity to the oxygen-deficient plane of the CuO chains. The momentum of the annihilating pair measured using (C)DBS is highly sensitive to the oxygen deficiency δ and, in turn, to the local transition temperature Tc.

A 230 (10) nm thin single-crystalline YBCO film was epitaxially grown on a single crystalline (001) oriented $SrTiO_3$ (STO) substrate by pulsed laser deposition. The experiments were performed at the CDB spectrometer at the high-intensity positron beam NEPOMUC. A variable positron implantation energy E_+ in the range between 0.3 and 30 keV enables in situ depth-dependent investigations at temperatures up to 900 °C.

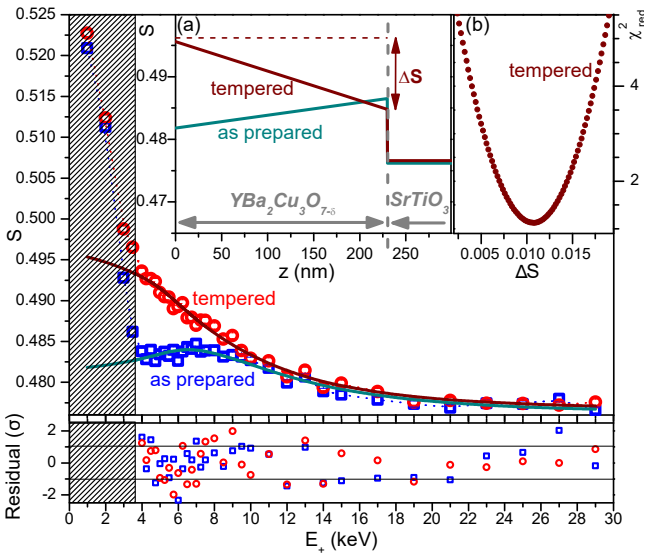

Figure 1: S parameter as a function of positron implantation energy E_+ before and after tempering. The solid lines represent fits yielding S(z) as plotted in inset (a) with the respective goodness of the fit $\chi^2_{red}(\Delta S)$ with ΔS = S(0 nm) − S(230 nm) in the tempered sample (b). For E_+ < 4 keV (grey shaded area) positron surface states affect the data.

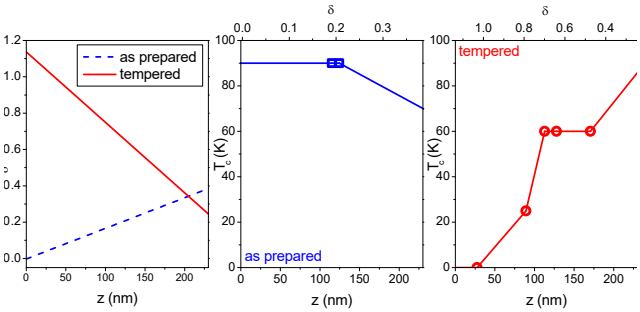

Figure 2: Oxygen deficiency δ and inferred critical temperature Tc as a function of depth z in the as prepared and tempered YBCO film.

As shown in fig. 1 the depth-dependent change in the oxygen deficiency is revealed by analysing the so-called S parameter as a function of the positron implantation energy $S(E_+)$ recorded before and after tempering. In the as-prepared state, a plateau between 4 and 8 keV indicates the predominant annihilation in the YBCO film. Applying a linear dependence of S on z yielded excellent agreement with the measured data for both the as prepared and tempered state (solid lines in fig. 1).

The oxygen diffusion during tempering is found to lead to a distinct depth dependence of δ, which is not accessible using x-ray diffraction. A steady state reached within a few minutes is defined by both the oxygen exchange at the surface and at the interface to the STO substrate. The depth-dependence of the critical temperature Tc found in the as prepared and tempered YBCO film is shown in fig. 2.

[1] M. Reiner, et al., Impact of oxygen diffusion on superconductivity in $YBa_2Cu_3O_{7-\delta}$ thin films studied by positron annihilation spectroscopy, Phys. Rev. B: Condens. Matter 97, 144503 (2018)

Ultrahigh-resolution neutron spectroscopy of low-energy spin dynamics in UGe_2

F. Haslbeck[1,2], S. Säubert[1,3], M. Seifert[1,3], C. Franz[3], M. Schulz[3], A. Heinemann[4], T. Keller[5,6], Pinaki Das[7,9], J. D. Thompson[7], E. D. Bauer[7], C. Pfleiderer[1], M. Janoschek[2,7,8]

[1]Physics Department, Technical University of Munich, Garching, Germany; [2]Institute for Advanced Study, Technical University of Munich, Garching, Germany; [3]Heinz Maier-Leibnitz Zentrum Garching, Technical University of Munich, Garching, Germany; [4]German Engineering Materials Science Centre (GEMS) at Heinz Maier-Leibnitz Zentrum (MLZ), Helmholtz-Zentrum Geesthacht GmbH, Garching, Germany; [5]Max-Planck-Institut für Festkörperforschung, Stuttgart, Germany; [6]Max Planck Society Outstation at the Heinz Maier-Leibnitz Zentrum (MLZ), Garching, Germany; [7]Los Alamos National Laboratory, Los Alamos, New Mexico, USA; [8]Laboratory for Scientific Developments and Novel Materials, Paul Scherrer Institut, Villigen PSI, Switzerland, [9]Present address: Division of Materials Sciences and Engineering, Ames Laboratory, U.S. DOE, Iowa State University, Ames, Iowa, USA

Ultraslow spin dynamics represent a key characteristic of quantum matter such as quantum spin liquids, electronic nematic phases, topological spin textures, non-Fermi liquid behavior, and unconventional superconductivity. Typically, their key characteristics emerge in the low milli-Kelvin range which requires excellent energy and momentum transfer resolution. In principle, neutron scattering is ideally suited to study the relevant spin excitations. However, the typical energy resolution of conventional neutron spectroscopy corresponds to Kelvin temperatures. Although techniques such as neutron spin-echo spectroscopy offer an ultrahigh energy resolution of sub-μeV, they are incompatible with conditions that depolarise neutron beams such as ferromagnetism (FM), superconductivity, or large magnetic fields.

We have overcome these limitations in our study of the FM superconductor UGe_2 by using the novel Modulated Intensity by Zero Effort (MIEZE) technique available at the instrument RESEDA, which is insensitive to depolarising conditions while, at the same time, providing ultrahigh resolution. Superconductivity mediated by Cooper pairs that form spin singlets is incompatible with FM because the associated large internal magnetic fields break the anti-parallel pairing of the electron spins. In turn, since UGe_2 exhibits microscopic coexistence of FM and superconductivity near a magnetic quantum phase transition, it is a candidate for spin-triplet superconductivity characterised by Cooper pairs with parallel spins. Spin-triplet superconductivity is believed to be mediated by an abundance of longitudinal spin fluctuations, as transverse spin fluctuations break spin-triplet pairs.

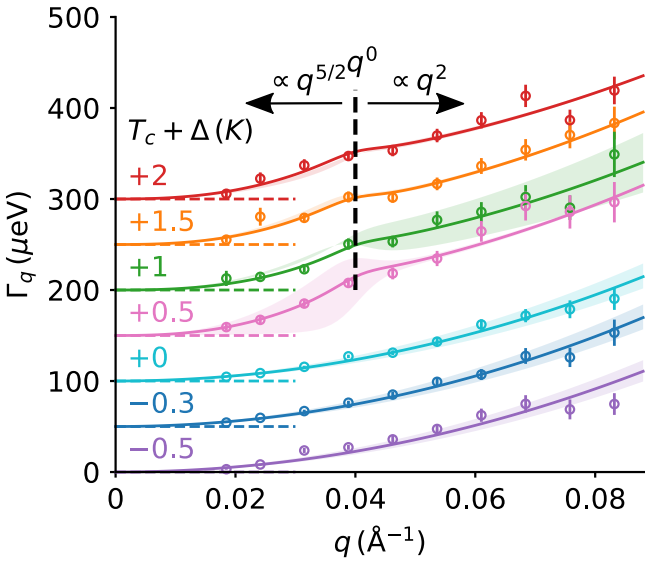

Figure 1: Spin fluctuation spectrum Γ_q of the putative spin-triplet superconductor UGe_2 as a function of momentum q and temperature T. We observe a crossover at q^0 where the character of the fluctuations changes from localised to itinerant.

Indeed, we find that the spin fluctuations in UGe_2 are purely longitudinal. Figure 1 shows the corresponding spin fluctuation spectrum Γ_q as a function of momentum q for temperatures above and below the Curie temperature T_C. For $T \leq T_C$, the data is perfectly fitted by $\Gamma_q \propto q^z$ with z = 2.0(1) which is in excellent agreement with predictions for a 3D Ising FM with local moments. For $T > T_C$, the fluctuation energy Γ_q is also well described by z = 2, however, only above a crossover value of by $q^0 = 0.04$ Å^{-1}. Below q^0, our data is best fitted with z = 2.53(4), consistent with calculations for itinerant FMs. Interestingly, the superconducting coherence length of UGe_2 is $\xi^{SC} = 200$ Å, which implies that the spin fluctuations relevant to the spin-triplet pairing are only present for $q < q^0$.

In summary, using MIEZE spectroscopy we reveal a dual character of the spin fluctuations in UGe_2 that is consistent with spin-triplet superconductivity. Here, localised spin degrees of freedom promote the strong Ising character of the spin fluctuations required to conserve spin triplet pairing, while itinerant spin fluctuations over the exchange-split Fermi surface mediate the pairing. This showcases that MIEZE is able to provide new quantitative insights into the ultra-slow spin dynamics that are characteristic of quantum matter.

[1] F. Haslbeck, et al., Ultrahigh-resolution neutron spectroscopy of low-energy spin dynamics in UGe_2, Phys. Rev. B 99, 014429 (2019)

Spinterface in fullerene: A polarised neutron reflectivity study

S. Mallik[1], S. Mattauch[2], M. Kumar Dalai[3], T. Brückel[4], S. Bedanta[1]

[1]Laboratory for Nanomagnetism and Magnetic Materials (LNMM), School of Physical Sciences, National Institute of Science Education and Research (NISER), HBNI, Jatni, India; [2]Jülich Centre for Neutron Science (JCNS) at MLZ, Forschungszentrum Jülich GmbH, Garching, Germany; [3]Institute of Minerals and Materials Technology, Bhubaneswar, Odisha, India; [4]PGI-4 Forschungszentrum Jülich GmbH, Jülich, Germany

For a decade, organic spintronics has been an evolving field due to its potential applications from quantum computation to biomedical imaging. Probing the hybridised magnetic interface between an organic semiconductor (OSC) and a ferromagnet (FM) offers the possibility of tuning the native properties of both the constituent layers. Charge/spin transfer from the FM to the OSC layer is expected when they are brought into contact with each other due to the orbital hybridisation between the FM and OSC molecule at the interface. Recently, the term 'spinterface' has been coined to describe such hybridised interfaces. As of yet, not much work has been done to investigate the effect of such OSC/FM interfaces on the magnetisation reversal and domain structure, which are the essential properties for any applications. We prepared a Fe(15 nm)/ C_{60}(40 nm) bilayer on a MgO(001) substrate to study these interfacial magnetic properties. Polarised neutron reflectivity (PNR) is the ideal tool to probe the layer- specific structural as well as magnetic properties in such bilayer samples. Specular PNR was performed on this bilayer at room temperature at the reflectometer MARIA at the Heinz Maier-Leibnitz Zentrum in Garching, Germany. The wavelength (λ) of the neutrons in the PNR measurements was 6.5 Å. Two scattering cross sections R^{++} (up - up) and R^{--} (down - down) have been measured, depending on the interaction of the neutrons with the magnetic spins in the sample (fig. 1 (a)). From these measurements we found that non-magnetic Fullerenes can exhibit a magnetic moment of ~ 2.95 μ_B/cage, within an interface layer of 1.9 nm thickness (fig. 1 (b)), at the Fe(15 nm)/C_{60}(40 nm) bilayer interface. This indicates the formation of a spinterface due to the p – d orbital hybridisation between the C and Fe atoms at the interface.

Further, we found that the magnetic C_{60} layer prefers to be aligned anti-parallel with the Fe layer at the remnant state. The latter observation was confirmed by domain imaging via magneto-optic Kerr microscopy. The formation of such a spinterface leads to a substantial effect on both the magnetic domain structure and the magnetisation reversal when compared to a single layer of Fe(15 nm).

The value for the magnetic moment found here is the highest induced magnetic moment in the Fe/C_{60} bilayer interface reported so far and therefore shows great potential for applications in organic spintronics.

[1] S. Mallik, et al., Effect of magnetic fullerene on magnetization reversal created at the Fe/C_{60} interface, Sci. Rep. 8(1), 5515 (2018)

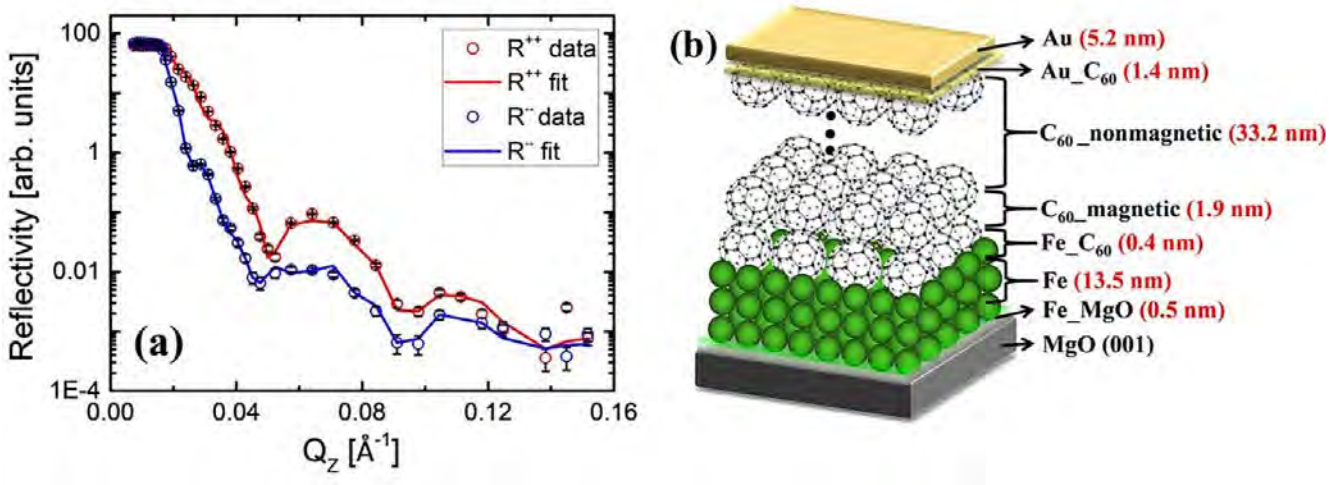

Figure 1: (a) PNR data and corresponding fits for the Fe/C_{60} bilayer sample measured at RT at saturation (μ_0H = 100 mT) using the reflectometer MARIA. (b) The model layer structure of the sample is shown with the thicknesses obtained from the fit to the PNR data shown in (a).

Order, disorder and chirality in the layered Kagome system $CaBaCo_2Fe_2O_7$

J. D. Reim[1,2], E. Rosén[2], O. Zaharko[3], M. Mostovoy[4], M. Valldor[5], J. Robert[6], W. Schweika[2,7]

[1]Institute of Multidisciplinary Research for Advanced Materials, Tohoku University, Sendai, Japan; [2]Jülich Center for Neutron Science JCNS and Peter Grünberg Institute PGI, JARA-FIT, Forschungszentrum Jülich, Jülich, Germany; [3]Laboratory for Neutron Scattering and Imaging, Paul Scherrer Institute, Villigen, Switzerland; [4]Zernike Institute for Advanced Materials, University of Groningen, Groningen, Netherlands; [5]Leibniz Institute for Solid State and Materials Research, Dresden, Germany; [6]Institut NEEL, CNRS, Grenoble, France; [7]European Spallation Source ERIC, Lund, Sweden

The geometric frustration of magnetic order is the origin of many complex non-collinear spin structures, leading to unusual and exciting phenomena. A well-known classical example is antiferromagnetic ordering on the Kagome lattice. The system $CaBaCo_2Fe_2O_7$ presented has a hexagonal Swedenborgite structure, in which magnetic ions form alternating Kagome and triangular layers. The magnetic interactions are strongly antiferromagnetic (AF) due to the superexchange between the half-filled t_{2g} orbitals of Co^{2+} and Fe^{3+} ions, leading to the building of units of double-tetrahedra of the nearest neighbor ions, which form a network of magnetic sites with strong geometric frustration. The actual interactions depend on the choice of magnetic and non-magnetic ions. Applying a simple Heisenberg model and varying the specific interaction ratio between ions in the Kagome layers (J_{in}) to out-of Kagome-layers (J_{out}) yields a complex phase diagram, which comprises the 2D Kagome spin-liquid state for decoupled layers, $J_{out} = 0$. With increasing interlayer coupling, 3D spin-liquid states even emerge as ground states. Further, one predicts partial 3D AF order with canted non-collinear spin structures, and beyond $J_{out} > 3/2J_{in}$, 3D AF order of $\sqrt{3} \times \sqrt{3}$ type.

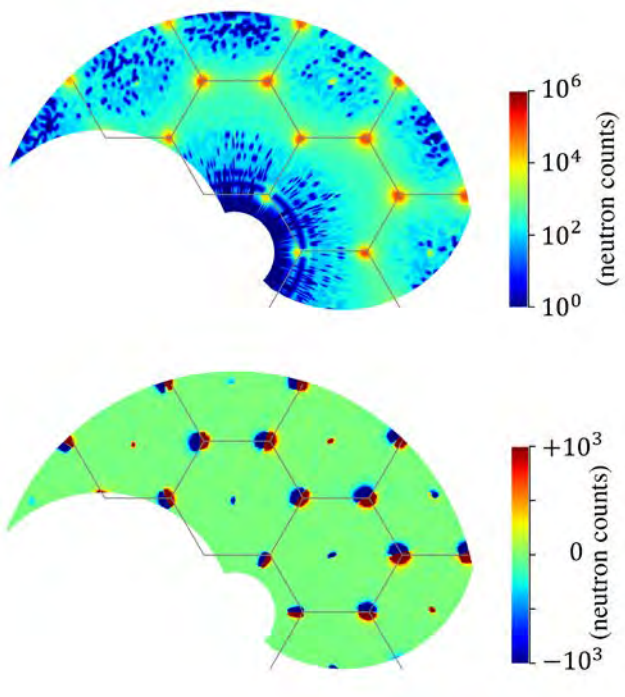

Figure 1: Magnetic scattering in the (hk0)-plane at T = 4 K. (a) total magnetic intensity (log-scale) reveals significant diffuse scattering. (b) chiral scattering (lin. scale) obtained by polarisation reversal || Q displays an anti-symmetry ⊥Q characteristic for cycloidal spin correlations.

We studied single crystals of $CaBaCo_2Fe_2O_7$ by polarised neutron diffraction on the DNS instrument and observed long-range $\sqrt{3} \times \sqrt{3}$ antiferromagnetic order below $T_N = 160$ K. The magnetic scattering at low temperatures of 4 K is shown in fig. 1 (a). Significant diffuse scattering near the magnetic peaks indicates a partially ordered ground state with residual entropy. A theoretical analysis yields a flat energy landscape near the K-points, the vortices of the Brillouin zone boundary, and a degeneracy for spiral correlations. In addition, the broken inversion symmetry in the structure gives rise to Dzyaloshinski-Moriya (DM) interactions, which may select a specific chirality. In the experiment, we explored the chirality by going beyond standard XYZ polarisation analysis, applying polarisation reversal parallel to the scattering vector. The difference between the two measurements separates the chiral scattering displayed in fig. 1b. Pronounced chiral patterns are seen near the K-points, the wave vector of the magnetic ordering. Intensities (on a linear scale) of this interference term range equally from negative to positive values. It is intriguing to see the specific anti-symmetry ⊥Q of the pattern, uniquely identifying cycloidal correlations with their rotation axes and propagation in the ab plane.

Modeling shows the selection for the cycloidal type of spiral ordering by adding the DM-interaction to the frustrated Heisenberg model. The energy landscape remains rather flat but shows three minima near the antiferromagnetic peaks corresponding to three spiral states connected with a 120° angle in the ab-plane. Symmetry analysis shows that the simultaneous presence of three spiral orders, taking place, e.g., in the skyrmion crystal, can also induce a weak ferromagnetic moment, as found in our magnetisation measurements. The present case resembles hedgehog-like spin correlations with an additional AF modulation between nearest neighbors.

As shown, Swedenborgites, which are both geometrically frustrated and chiral, provide a fertile playground for the search for unconventional magnetic order.[1]

[1] J. D. Reim, et al., Neutron diffraction study and theoretical analysis of the antiferromagnetic order and the diffuse scattering in the layered kagome system $CaBaCo_2Fe_2O_7$, Phys. Rev. B 97, 144402 (2018)

Non-reciprocal magnons in MnSi

T. Weber[1], J. Waizner[2], G. S. Tucker[3,4], L. Beddrich[5,6], M. Skoulatos[5,6], R. Georgii[5,6], A. Bauer[6], C. Pfleiderer[6], M. Garst[7], P. Böni[6]

[1]Institut Laue-Langevin (ILL), Grenoble, France; [2]Institut für Theoretische Physik, Universität zu Köln, Köln, Germany; [3]Laboratory for Neutron Scattering and Imaging, Paul Scherrer Institut (PSI), Villigen, Switzerland; [4]Laboratory for Quantum Magnetism, École Polytechnique Fédérale de Lausanne, Lausanne, Switzerland; [5]Heinz Maier-Leibnitz Zentrum (MLZ), Technical University of Munich, Garching, Germany; [6]Physics Department E21/E51, Technical University of Munich, Garching, Germany; [7]Institut für Theoretische Physik, Technische Universität Dresden, Dresden, Germany

The itinerant-electron magnet MnSi crystallises in the cubic $P2_13$ space group, which lacks inversion symmetry. The lack of a central symmetry introduces a Dzyaloshinskii-Moriya interaction term between the magnetic moments of the Mn electrons. Such a term tends to arrange the magnetic momenta perpendicular to one another. Together with other interaction terms, most prominently the exchange interaction, which favours parallel arrangements, a rich phase diagram is obtained, including helimagnetic, conical, field-polarised ferromagnetic, and skyrmion order.

The Dzyaloshinskii-Moriya interaction is furthermore responsible for asymmetries ("non-reciprocities") in the probabilities for either creating or annihilating magnons in the various magnetic phases of MnSi. These asymmetries are independent of, and not related to, the principles of detailed balance and the Bose factor for the mean magnon occupation number. The non-reciprocal nature of the dynamical structure factor S(q, E, B) is a result of a loss of time-inversion symmetry: S becomes asymmetrical with respect to a reversal of either the reduced momentum transfer q, the energy transfer E, or the applied magnetic field B. Symmetry is restored by reversing the signs of either two of these dependent variables.

Uniting the data gathered at the cold-neutron triple-axis spectrometers MIRA (MLZ) and TASP (Paul-Scherrer-Institut, Villigen, Switzerland) with theoretical linear spin-wave models, we have succeeded in fully and quantitatively describing the field-dependent evolution of the non-reciprocal magnon dispersion relations in all ordered magnetic phases of MnSi. In a first step [1], we investigated the conical and field-polarised phase, and extended the measurements towards the skyrmion phase in a second step [2] (fig. 1). In the magnetic phases, asymmetrical structure factors S can only be observed for reduced momentum transfers q along the direction of the external magnetic field B, but not perpendicular to it.

As these intriguing phenomena warrant further investigation, we have extended our measurement, as well as the theoretical models, towards polarisation-resolving of the non-reciprocal spectra in all phases. The new results will be published shortly.

[1] T. Weber, et al., Field dependence of nonreciprocal magnons in chiral MnSi, Phys. Rev. B 97 (22), 224403 (2018)
[2] T. Weber, et al., Non-reciprocal magnons in non-centrosymmetric MnSi, AIP Adv. 8, 101328 (2018)

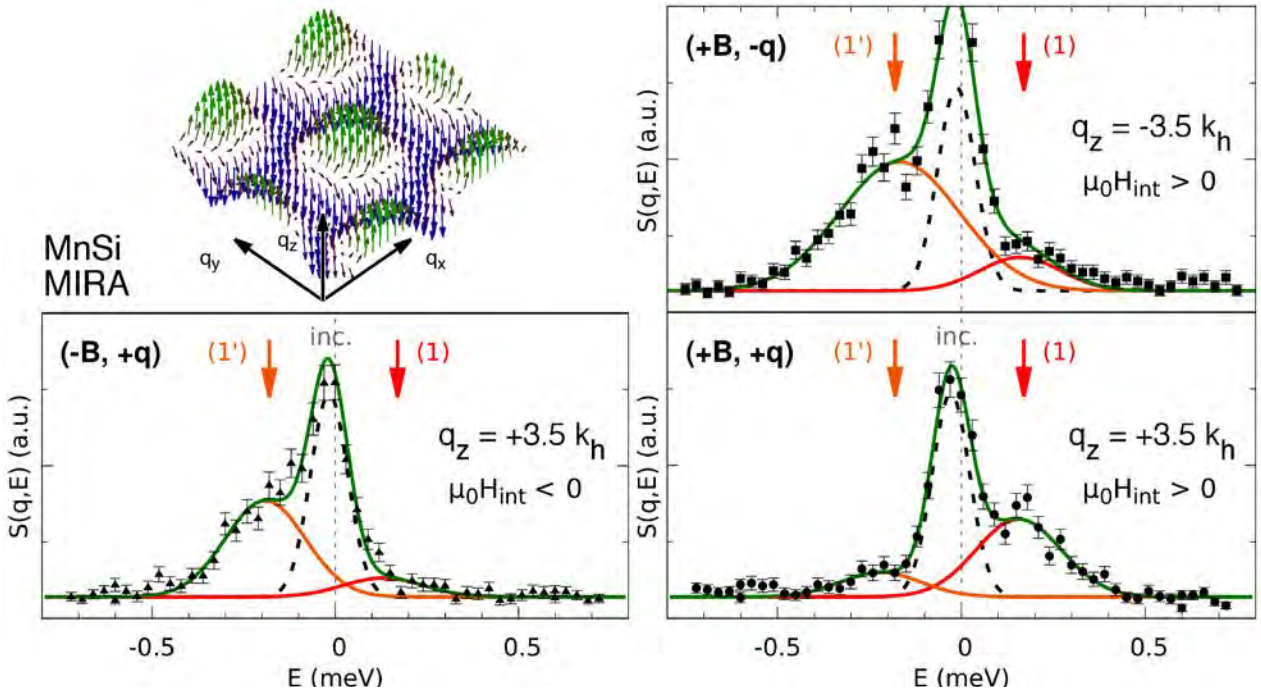

Figure 1: MnSi is well known for hosting a skyrmion lattice, which aligns the magnetic moments in a vortex-like fashion. Shown here are the non-reciprocal magnons in the skyrmion phase as measured at the triple-axis spectrometer MIRA. The observed asymmetries at the marked points (1) and (1') appear only for reduced momentum transfers along the skyrmion axis, q_z. Figure reproduced from Publication 2 (modified).

Magnetoelectric coupling in iron oxide nanoparticle-barium titanate composites

L.-M. Wang[1,3,4], O. Petracic[1], E. Kentzinger[1], S. Mattauch[2], Al. Koutsioumbas[2], X.-K. Wei[5], U. Rücker[1], M. Schmitz[1], M. Heggen[1], V. Leffler[6,7], S. Ehlert[6], T. Brückel[1]

[1]Jülich Centre for Neutron Science JCNS and Peter Grünberg Institut PGI, JARA-FIT, Forschungszentrum Jülich GmbH, Jülich, Germany; [2]Jülich Centre for Neutron Science (JCNS) at MLZ, Forschungszentrum Jülich GmbH, Garching, Germany; [3]Dongguan Neutron Science Center, Dongguan, People's Republic of China; [4]Institute of High Energy Physics, Chinese Academy of Sciences, Beijing, People's Republic of China; [5]Ernst Ruska-Centre for Microscopy and Spectroscopy with Electrons and Peter Grünberg Institute, Forschungszentrum Jülich GmbH, Jülich, Germany; [6]Jülich Centre for Neutron Science JCNS-1 and Institute of Complex Systems ICS-1, Forschungszentrum Jülich GmbH, Jülich, Germany; [7]Institute of Physical Chemistry, RWTH Aachen University, Aachen, Germany

Magnetoelectric (ME) composites containing self-assembled iron oxide nanoparticles (NPs) with a diameter of 20 nm on top of a Barium Titanate (BTO) crystal were prepared for this study. The ME coupling of these composites was investigated using AC susceptibility measurements as well as polarised neutron reflectometry (PNR) at different applied electric fields. PNR measurements were performed at the reflectometer MARIA at the Heinz Maier-Leibnitz Zentrum in Garching.

The iron oxide NPs dispersed in toluene solution were observed using high resolution TEM, as shown in fig. 1 (a). We find that the average diameter is 20 nm with a relatively monodisperse size distribution. The inset shows a close-up view of one NP. The structure of the ME sample viewed in cross-section as an HAAD image is shown in fig. 1 (b). Several layers can be identified. The upper white layer represents the Au layer. One third of the iron oxide NPs is covered by the Au layer. The other part is visible as a dark grey layer. The Ti + TiO_x is visible as a black layer. The upper part of the Ti layer is oxidised into a TiO_x layer following the oxygen plasma procedure. The oxidised Ti layer provides the necessary adhesion of the NPs to the substrate, which is a perquisite for facilitating the strain transfer from the BTO substrate to the NPs. Systems without the Ti layer show no ME coupling effect. The BTO substrate is found in the lower part as a mid-grey area.

Magnetometry measurements were performed using a superconducting quantum interference device magnetometer. Field cooling and field warming curves show magnetisation steps near the rhombohedral to orthorhombic transition at 190 K, and the orthorhombic to tetragonal transition at 287 K. We assume that strain mediated ME coupling is responsible for these magnetisation changes.

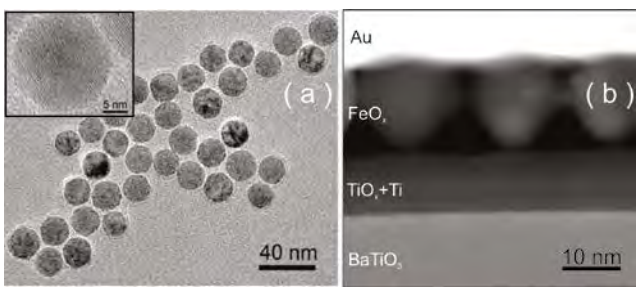

Figure 1: TEM images of the NPs, and a close-up view of a single NP in the inset. (b) High-angle annular dark-field (HAAD) image in cross section of the heterostructure Au / BTO / Ti / NP / Au.

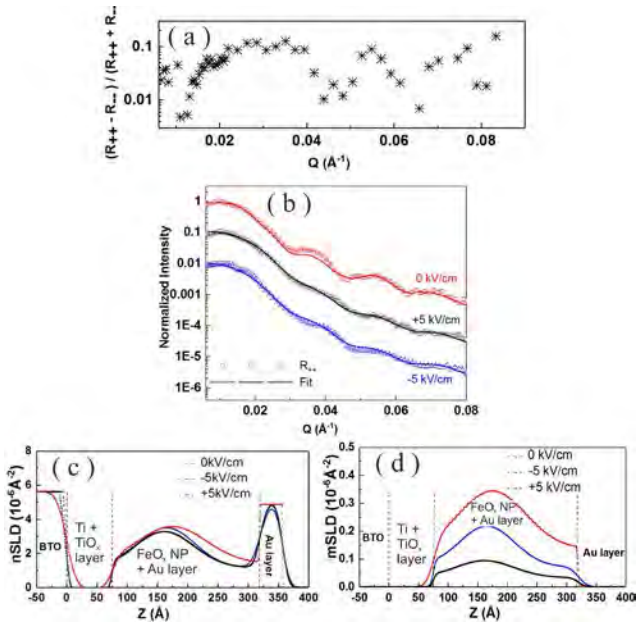

Figure 2: BTO/Ti/NP/Au sample measured at 300 K (a) Asymmetry plot versus Q in R++ and R−− channels with an applied saturation magnetic field of 0.98T and a zero E field. (b) PNR data (scatters) measured at coercive field and the corresponding fittings (solid lines).Fittings are performed on both R++ and R−− data but for simplicity, only R++ are shown. The R++ reflectivity at +5 kVcm^{-1} and -5 kVcm^{-1} is divided by 10 and 100 for a better visibility, respectively. (c) The nuclear scattering length density as a function of the thickness Z obtained from the fits (d) magnetic scattering length density as a function of the thickness Z obtained from the fits.

We have also demonstrated that the magnetisation can be influenced by a DC electric field at room temperature. A typical butterfly-shaped curve was obtained, as expected from in-plane strain mediated ME coupling in ME composites.

Polarised neutron reflectometry was employed at various electric and magnetic fields. The reflectivity curves were measured in the non-spin flip channels R++ and R−− (fig. 2 (b)) which indicate the sum and difference of the nuclear scattering length density (nSLD, fig. 2 (c)) and magnetic scattering length density (mSLD, fig. 2 (d)), respectively. Spin asymmetry (fig. 2 (a)) shows that almost 10% of the total signal is contributed by the magnetic signal from the iron oxide NPs. The mSLD shows that the change in roughness in each layer is the major reason for the differences in the reflectivities at different E-fields. In addition, the differences in the mSLD of the iron oxide NPs also show a contribution depending on the E-field.

[1] L.-M. Wang, et al., Magnetoelectric coupling in iron oxide nanoparticle – barium titanate composites, J. Phys. D: Appl. Phys. 52, 065301 (2019)

Proteins aggregate not

J. Siefker[1], R. Biehl[2], M. Kruteva[2], A. Feoktystov[3], M.-O. Coppens[1]

[1]Centre for Nature Inspired Engineering (CNIE) and Department of Chemical Engineering, University College London, London, United Kingdom; [2]Jülich Centre for Neutron Science (JCNS-1) and Institute for Complex Systems (ICS-1), Forschungszentrum Jülich GmbH, Jülich, Germany; [3]Jülich Centre for Neutron Science (JCNS) at Heinz Maier-Leibnitz Zentrum (MLZ), Forschungszentrum Jülich GmbH, Garching, Germany

The natural environment of proteins inside cells is a crowded solution, at high concentrations or immobilised on surfaces. However, proteins do not lose their activity. On the contrary, in highly concentrated bulk solutions, proteins tend to aggregate irreversibly. Now, we have shown that the aggregation of both myoglobin and lysozyme is also prevented inside the pores of two mesoporous silicas, SBA-15 and KIT-6 [1].

Mesoporous silicas pose a distinct challenge to direct methods, such as transmission electron microscopy and nuclear magnetic resonance, when it comes to adequately observing immobilised protein structures in these materials. Small-angle neutron scattering (SANS) can surmount these limitations and observe the spatial arrangement of protein within pores.

Measurements were conducted at KWS-1 at the MLZ with protein loaded mesoporous silica samples at different concentrations of protein inside the pores (fig. 1). For low concentrations, we observe a slight contribution from the protein to the scattered intensity, while at the highest concentration an additional protein peak at higher Q values appears (fig. 2). The observed peak corresponds to a fluid-like structure of the protein within the pores. The corresponding volume fractions reach 40% for myoglobin and 64% for lysozyme, close to the disordered packing limit. The proteins are able to be released from the pores and still show activity; thus, they are functional.

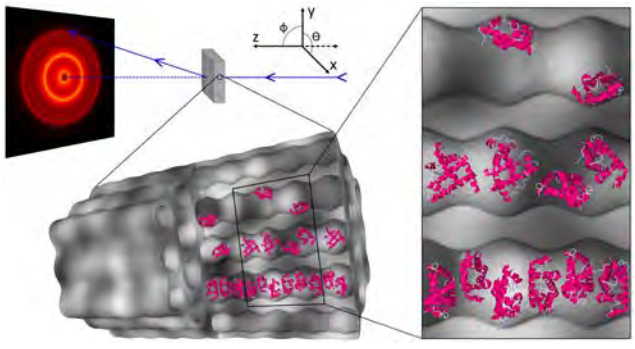

Figure 1: Depiction of the scattering geometry and spatial organisation of myoglobin in SBA-15 silica pores at different concentrations.

Consequently, we observe the stabilisation of a fluid-like protein arrangement, facilitated by geometry-dependent crowding effects in the cylindrical pores of the ordered mesoporous silica, SBA-15. Stabilisation is induced from a fluid-like structure factor, which is observed for samples at maximum protein loading in SBA-15 with pore diameters of 6.4 and 8.1 nm. Application of this effect to prevent irreversible aggregation in high concentration environments is proposed.

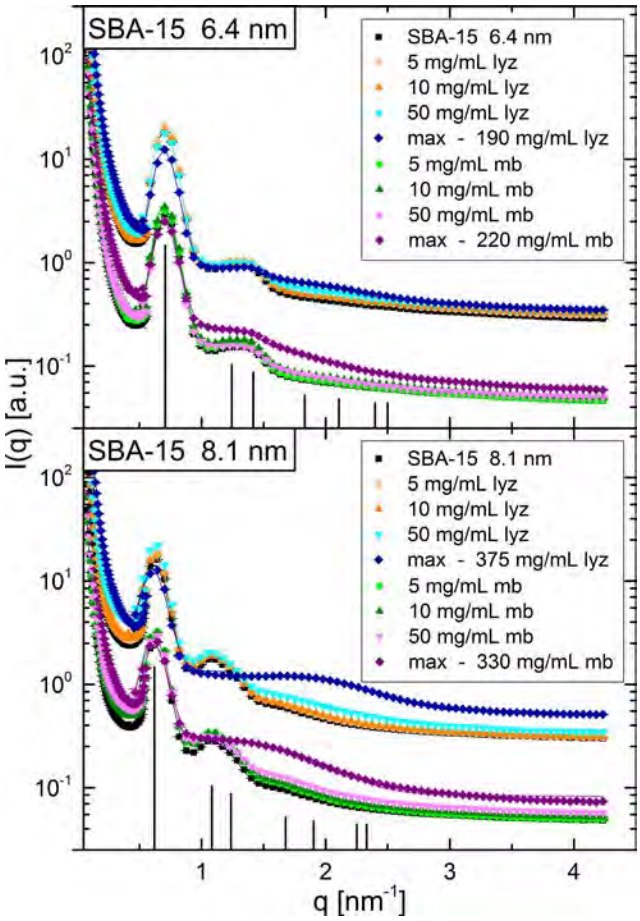

Figure 2: Scattering of myoglobin (mb) and lysozyme (lyz) loaded on SBA-15 with a mesopore diameter of 6.4 and 8.1 nm. Lysozyme data are shifted by a factor of 10. Black lines show the model of hexagonally arranged cylinders, including distortions, complemented by an additional protein contribution for maximal protein concentration samples (max). The protein scattering shows up in the diffusive scattering. Due to the confinement in a cylindrical pore, the protein formfactor needs to be convoluted with the cylinder formfactor. Protein spatial correlations are described by a fluid-like 3D Percus-Yevick structure factor. Bragg reflection peaks of the hexagonally arranged cylinders are marked with vertical lines (listed in sequence: (100), (110), (200), (210), (300), (220), (310)). All contributions are smeared by the resolution of the instrument, resulting in a break at approx. 0.4 nm^{-1} due to changing detector distance.

[1] J. Siefker, et al., Confinement Facilitated Protein Stabilization As Investigated by Small-Angle Neutron Scattering, J. Am. Chem. Soc. 140, 12720 (2018)

Invisible deuterium makes membrane proteins visible

I. Josts[1], J. Nitsche[1], S. Maric[2], H. D. Mertens[3], M. Moulin[4], M. Haertlein[4], S. Prevost[4], D. I. Svergun[3], S. Busch[6], V. T. Forsyth[4,5], H. Tidow[1]

[1]The Hamburg Centre for Ultrafast Imaging & Department of Chemistry, Institute for Biochemistry and Molecular Biology, University of Hamburg, Hamburg, Germany; [2]Biofilms-Research Center for Biointerfaces, Dept. of Biomedical Science, Faculty of Health and Society, Malmö University, Malmö, Sweden; [3]European Molecular Biology Laboratory Hamburg, Hamburg, Germany; [4]Institut Laue Langevin (ILL), Grenoble, France; [5]Life Sciences Department, Keele University, Staffordshire, England; [6]German Engineering Materials Science Centre (GEMS) at Heinz Maier-Leibnitz Zentrum (MLZ), Helmholtz-Zentrum Geesthacht, Garching, Germany

Integral membrane proteins (IMPs) play central roles in cellular life: They are essential for the transport of matter and signals across cell membranes and are key targets for drug development. Detailed knowledge of their structures and of the dynamics of different states is therefore highly desirable. However, structural studies of IMPs are complicated by the fact that many membrane proteins suffer loss of stability, activity and function outside a lipid environment.

Here, we describe an approach that makes use of a new method for analysing membrane proteins. We used the special nature of a hydrogen isotope: deuterium labelled 'stealth carrier' nanodiscs (sND) are effectively invisible in low-resolution neutron diffraction and enable structural studies of integrated membrane proteins in a lipidic native-like solution environment. We recently reported our findings in two publications in the journals Structure [1] and Communications Biology [2].

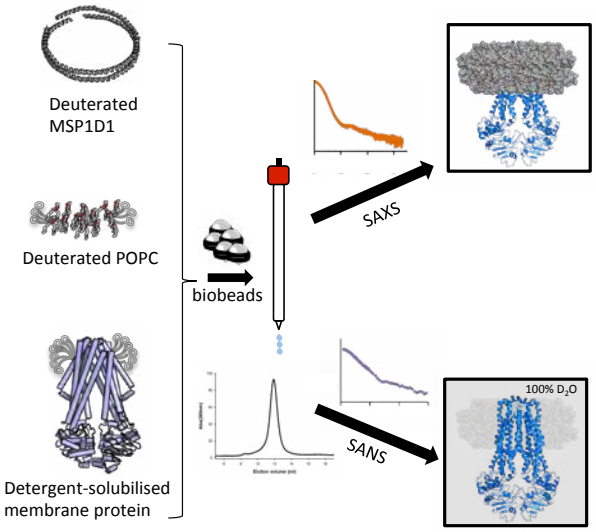

Figure 1: Overview of the stealth nanodiscs method for structural studies of integral membrane proteins in a native-like lipid environment using small-angle (X-ray/neutron) scattering. The integral membrane proteins were incorporated in selectively deuterated stealth carrier nanodiscs that are "invisible" under the chosen conditions in the SANS experiments. This method was used to determine the overall structure and detect differences between conformational states of the ABC transporter MsbA [1] as well as the structural basis for the activation of a PMCA-type Ca^{2+}-pump by calmodulin [2].

The complex multi-contrast scattering contribution of the scaffold disc makes data analysis and structural analysis of the incorporated IMP extremely challenging. However, nanodisc lipid bilayer scaffolds have emerged as an invaluable tool for solution-state studies of IMPs in a native-like lipid environment (see fig. 1).

Here, we made use of sND technology to incorporate a membrane protein – the ATP-binding cassette (ABC) transporter protein MsbA – into stealth carrier nanodiscs. The effective invisibility of the carrier system enabled us to obtain high quality small-angle neutron scattering (SANS) data from MsbA in a lipid environment. The SANS experiments were performed at the instrument SANS-1 and were accompanied by synchrotron small-angle X-ray scattering (SAXS) measurements. Thus, we were able to obtain structural models of different conformational states of MsbA in solution [1]. In a follow-up project we applied this method to investigate the structural basis for the activation of an essential Ca^{2+}-pump by its regulator calmodulin [2].

This methodology can be applied to other classes of integral membrane proteins and paves the way for low-resolution structure determination of IMPs in solution using both ab initio and rigid body analysis approaches.

The research was carried out in close collaboration between scientists of Universität Hamburg, EMBL Hamburg, Malmö University, MLZ Munich and ILL Grenoble.

[1] I. Josts, et al., Conformational States of ABC Transporter MsbA in a Lipid Environment Investigated by Small-Angle Scattering Using Stealth Carrier Nanodiscs, Structure 26, 1072 (2018)

[2] J. Nitsche, et al., Structural basis for activation of plasma-membrane Ca^{2+}-ATPase by calmodulin, Commun. Biol. 1, 206 (2018)

Supercritical CO_2 accompanied by droplet formation when passing the Widom line

V. Pipich[1], D. Schwahn[2]

[1]Jülich Centre for Neutron Science (JCNS) at MLZ, Forschungszentrum Jülich GmbH, Garching, Germany; [2]Heinz Maier-Leibnitz Zentrum (MLZ), Technical University of Munich, Garching, Germany

Supercritical CO_2 is used as a "green" solvent as it is non-poisonous, chemically stable, reusable, and is therefore employed as a substitution for organic solvents in industrial applications. The physical state lies somewhere between a liquid and a gas, without the distinct classical liquid-gas phase boundary. Only recently has it become known that supercritical fluids show two distinct regimes of gas-like and liquid-like behavior separated by the Frenkel line. Hitherto, the Frenkel line has been determined from slight differences in mass density and from the individual molecular dynamics. In the gas-like phase, molecules move solely by diffusion, whereas in the liquid-like phase vibration dynamics also comes into play. To date, the various theoretical models have not been able to determine Frenkel lines which are consistent both with each other and with experiment.

We explored thermal fluctuations of the CO_2 molecular density beyond the critical point of 31 °C, (i.e. in the supercritical regime along the isothermal pathway of 45 °C at pressure fields between 1 and 480 bars) using neutrons, employing small-angle scattering (SANS). The scattered intensity at the momentum transfer Q = 0, i.e. dΣ/dΩ(0) is depicted as red dots in fig. 1. dΣ/dΩ(0) is proportional to the susceptibility S(Q=0), which is a relevant experimental parameter determining the degree of thermal density fluctuations.

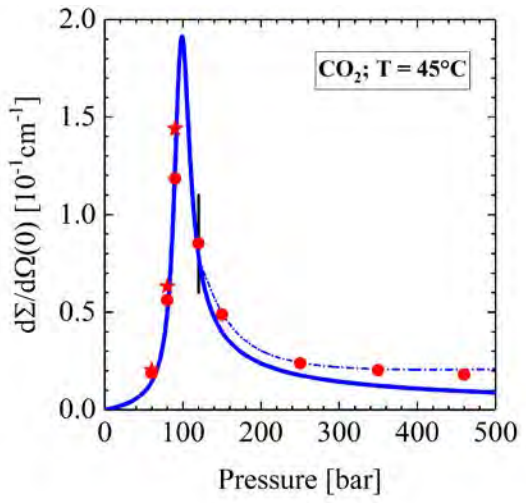

Figure 1: Susceptibility of thermal density fluctuations versus pressure. The solid line describing the susceptibility was evaluated on the basis of the number density n(P) determined from the equation of state (EOS) theory. The maximum of $\delta n/\delta P|_{V,T}$ and dΣ/dΩ(0) represent the Widom line at 45 °C. The dash-dotted lines represent corrections of n(P) above 120 bars on the basis of the SANS data, indicating a larger number density. The vertical line at 120 bars represents the Frenkel line at 45 °C.

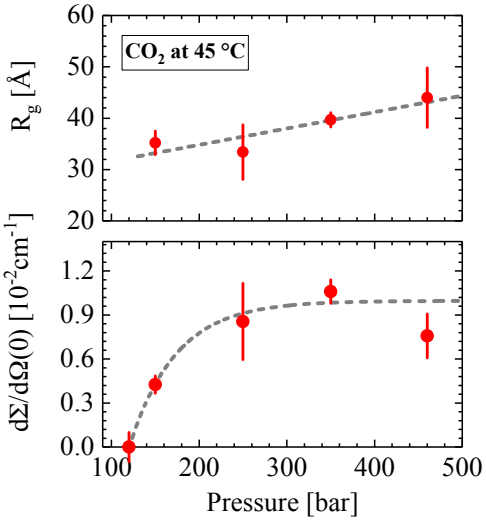

Figure 2: Radius of gyration (R_g) and scattering intensity at Q = 0 (dΣ/dΩ(0)) of the droplets versus pressure. The fit of dΣ/dΩ(0) with an exponential (dashed line) is a guide for the eye, showing fairly constant values beyond 250 bars. The zero intensity at 120 bars corresponds to the Frenkel line. R_g, on the other hand, shows rather constant values beyond 120 bars.

Figure 1 shows the expected maximum at the Widom line. S(0) can be evaluated via the fluctuation-compressibility relation from the first derivative of the CO_2 molecular density n(P) with respect to the pressure (P). These calculations were performed on the basis of the equation of state (EOS) measurements taken from the NIST Chemistry WebBook. The results are plotted as a solid blue line in fig. 1. At low pressure both susceptibilities are in excellent agreement, whereas at about 20 bars beyond the Widom line SANS determines a slightly larger n(P), indicating that the Frenkel line has been passed. Additionally, we observe the formation of droplets, whose radius of gyration (R_g) and scattering intensity at Q = 0 are depicted in fig. 2. This means that the "high-pressure" area, i.e. the liquid-like regime of supercritical fluids, represents a two-phase regime, which furthermore shows a slightly larger CO_2 mass density than that determined from EOS. Such observation is new and was surprising as textbooks on classical thermodynamics teach us that there is a continuous transition from the gas-like to liquid-like behavior along a supercritical pathway.

[1] V. Pipich, et al., Densification of Supercritical Carbon Dioxide Accompanied by Droplet Formation When Passing the Widom Line, Phys. Rev. Lett. 120, 145701 (2018)

Structure of mixed self-assembled monolayer on nanoparticles

Z. Luo[1], D. Marson[2], Q. K. Ong[1], A. Loiudice[3], J. Kohlbrecher[4], A. Radulescu[5], A. Krause-Heuer[6], T. Darwish[6], S. Balog[7], R. Buonsanti[3], D. I. Svergun[8], P. Posocco[2], F. Stellacci[1]

[1]Institute of Materials, École Polytechnique Fédérale de Lausanne, Switzerland; [2]Department of Engineering and Architecture and INSTM Trieste Unit, University of Trieste, Italy; [3]Institute of Chemical Sciences and Engineering, École Polytechnique Fédérale de Lausanne, Switzerland; [4]Laboratory for Neutron Scattering and Imaging, Paul-Scherrer Institute, Switzerland; [5]Jülich Centre for Neutron Science (JCNS) at MLZ, Forschungszentrum Jülich GmbH, Garching, Germany; [6]The National Deuteration Facility, Australian Nuclear Science and Technology Organization, Australia; [7]Adolphe Merkle Institute, University of Fribourg, Switzerland; [8]European Molecular Biology Laboratory, Hamburg Unit, EMBL c/o DESY, Germany

The complex organisations of amino acid residues on protein surfaces give rise to a wide range of functions. In the field of biology, a great deal of effort is devoted to understanding such structure-property relationships.

Nanoparticles (NPs) are core-shell materials with a (mostly inorganic) core coated with (mostly organic) ligands. They could be regarded as model compounds for proteins as they share similar sizes and, when coated with a mixture of different types of ligand molecules, present patchy surfaces that bear many similarities to protein surfaces. At present there are a number of approaches aimed at characterising the core of NPs. However, when it comes to the structures of the ligand shell, few reliable techniques have been developed. The available approaches, e.g. NMR, IR, STM, are qualitative in nature, i.e. they can only distinguish between patchy, Janus, and random morphologies.

In this report [1], we study metallic NPs coated with small molecule ligands, using SANS. We establish that the combination of SANS and the Monte Carlo calculations (along the lines of the procedure for proteins) leads to a robust and quantitative solution of 3D models for both the ligand shell and the core of the NPs. We used contrast variation to highlight different parts of the ligand shell and metal core of the NPs and fitted the SANS curves simultaneously. This approach can distinguish various morphologies of the ligand shell, even some with very similar structures (fig. 1). We highlight the versatility of this approach for characterising not only gold NPs but also – for the first time – mixed-ligand copper and silver NPs and ternary ligand coated NPs (no other technique achieves the latter). All the SANS results have been compared with molecular dynamic simulations that achieve quantitative agreement both on the spatial organisation and characteristic length scales of the ligand shell. We believe that this technique could become a general tool in nanoparticle research.

[1] Z. Luo, et al., Quantitative 3D determination of self-assembled structures on nanoparticles using small angle neutron scattering, Nat. Commun. 9, 1343 (2018)

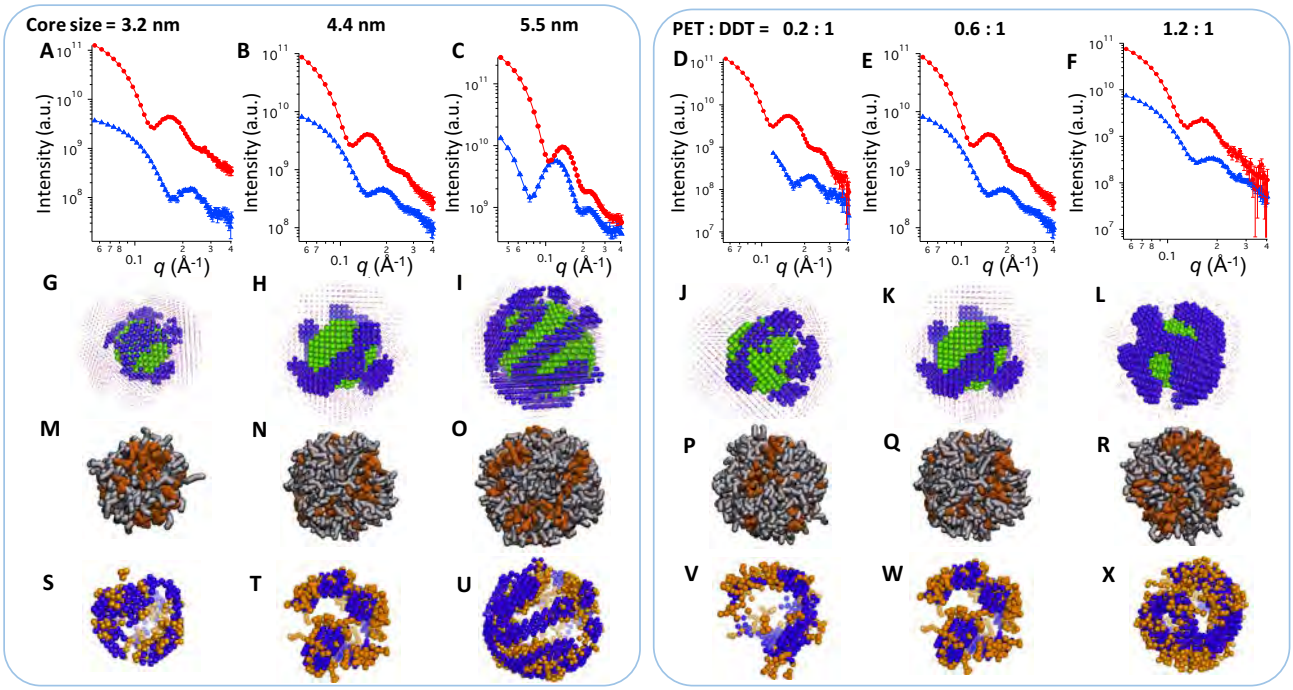

Figure 1: SANS data, collected at SANS1 (PSI) and KWS-2 (MLZ) instruments (A-E) and calculated 3D models (G-L) of various mixed ligand NPs; MD results (M-R) are compared with SANS models (S-X) achieving quantitative agreement.

Resolving component dynamics of a simplified industrial polymer system

T. Gambino[1,2], A. Alegría[1], A. Arbe[1], J. Colmenero[1], N. Malicki[2], S. Dronet[2], B. Schnell[2], W. Lohstroh[3], K. Nemkovski[4]

[1]Centro de Física de Materiales (CSIC, UPV/EHU) and Materials Physics Center MPC, San Sebastián, Spain; [2]Manufacture Française des Pneumatiques MICHELIN, Clermont-Ferrand, France; [3]Heinz Maier-Leibnitz Zentrum, Technical University of Munich, Garching, Germany; [4]Jülich Centre for Neutron Science JCNS, Forschungszentrum Jùlich GmbH, Garching, Germany

The optimisation of the performance of rubber in tyres requires reducing the rolling resistance and increasing the dissipation of energy during braking. Blending polymers is an efficient and cheap way to obtain materials with new properties, but the rational design of interesting mixtures for the tyre industry involves an understanding of the dynamics of both components at distinct frequency ranges (10 - 10^2 Hz for the rolling resistance and 10^4 - 10^7 Hz for the adherence).

Here, we have applied the concepts and methodologies developed 'academically' for the investigation of polymer blend dynamics to disentangle the component dynamics in a simplified industrial system consisting of a 50/50 mixture of a random copolymer, SBR, with an oligomer, PS. The main conceptual ingredients are dynamic heterogeneity (the two components retain their 'identity') and concentration fluctuations (leading to a variety of environments in the sample). The methodology involves the combination of different experimental techniques including DSC, dielectric spectroscopy (DS) and QENS. As an essential part of this methodology, QENS on isotopically labelled samples was a requirement in order to isolate the response of one of the components in the mixture. Given the broad distributions of mobilities (arising from the intrinsic dynamic heterogeneities in the atomic dynamics of the neat components and also provoked by concentration fluctuations), this has been realised by combining TOFTOF and SPHERES (see fig. 1 for the case where the SBR component is isolated).

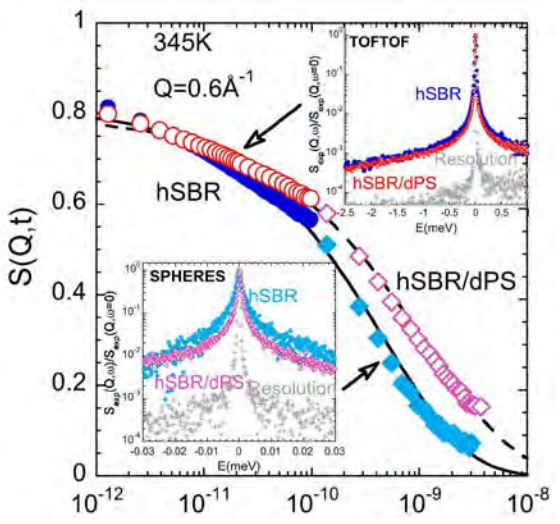

Figure 1: Intermediate scattering functions of pure SBR and the SBR component in the blend with deuterated PS. Lines are fits of stretched exponentials to the experimental results for t ≥ 2 ps. Insets show the normalised measured functions in the frequency domain, obeying the same symbol code.

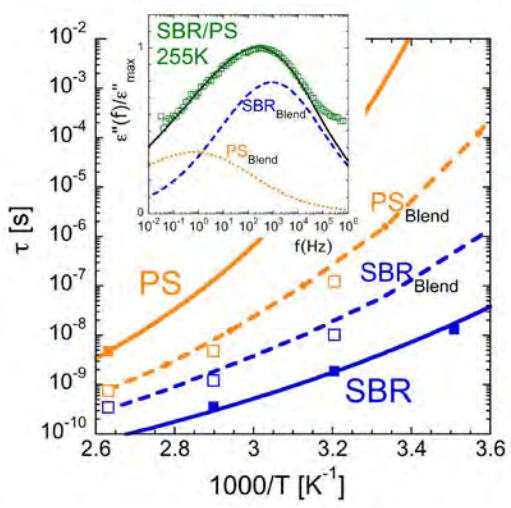

Figure 2: Relaxation map (lines: descriptions of the DS times; symbols: QENS characteristic times at the Q-value matching the latter) of the blend components (dashed lines and empty symbols) compared with the neat materials (solid lines and full symbols). The inset shows DS results at 255 K decomposed in the two contributions.

Thanks to the synergetic combination of QENS with DS data (where the isotopic labeling does not play a role) covering a broad frequency range, a complete description of the segmental dynamics of the two polymer components in such a complex mixture was possible in the full range of frequencies of industrial interest (see fig. 2). In this way, we resolved the fragility of the two components in the blend and identified the distribution of the effective glass-transition temperatures of each blend component, which nicely match the whole glass-transition range of the mixture as determined by DSC.

This work thus demonstrates that the concepts established for blend dynamics in systems composed of 'canonical' polymers can be transferred to other, more complex mixtures of industrial interest.

[1] T. Gambino, et al., Applying Polymer Blend Dynamics Concepts to a Simplified Industrial System. A Combined Effort by Dielectric Spectroscopy and Neutron Scattering, Macromolecules 51, 6692 (2018)

Triggered metastable micelles can be restored by a self-templating process

C. Dähling[1], J. E. Houston[2], A. Radulescu[2], M. Drechsler[3], M. Brugnoni[1], H. Mori[2], D. V. Pergushov[5], F. A. Plamper[1,6]

[1]Institute of Physical Chemistry, RWTH Aachen University, Aachen, Germany; [2]Jülich Centre for Neutron Science (JCNS) at Heinz Maier-Leibnitz Zentrum (MLZ), Forschungszentrum Jülich GmbH, Garching, Germany; [3]Bavarian Polymer Institute, University of Bayreuth, Bayreuth, Germany; [4]Department of Organic Materials Science, Yamagata University, Yonezawa, Japan; [5]Department of Chemistry, Lomonosov Moscow State University, Moscow, Russia; [6]Institute of Physical Chemistry, TU Bergakademie Freiberg, Freiberg, Germany

Controlling, adjusting and understanding the structure of polymeric micelles is an important aspect of colloidal science. It helps to efficiently engineer the properties of a final product. Many systems have been described, where stimuli-responsive (block) copolymers exhibit a structural switch in their micellar morphology following a conditional change. This switch is often reversible, allowing a return to the original structure when the original conditions have been restored. However, a precise and reproducible tailoring of micellar off-equilibrium structures is rarely at hand.

We describe a system with 4 polymeric components (polycation, polyanion, a permanently water-soluble polymer and a thermoresponsive polymer), which allows for repeated adjustment of different micellar structures under the same conditions. While the thermoresponsive component allows a temperature-dependent transition between spherical micelles and vesicles/worm-like micelles, the interaction between polycation and polyanion provides an easy way of controlling the dynamics of the system. This is true as both charged constituents form an insoluble interpolyelectrolyte complex, which can be plasticised in the presence of salt. Hence, close to equilibrium structures are expected in the presence of salt, while the micellar dynamics is restricted in the absence of salt. By lowering the salt concentration at a specific temperature, the micelles become kinetically frozen, preserving the structure at other temperatures too. Hence, different nonequilibrium morphologies are provided under the same final conditions.

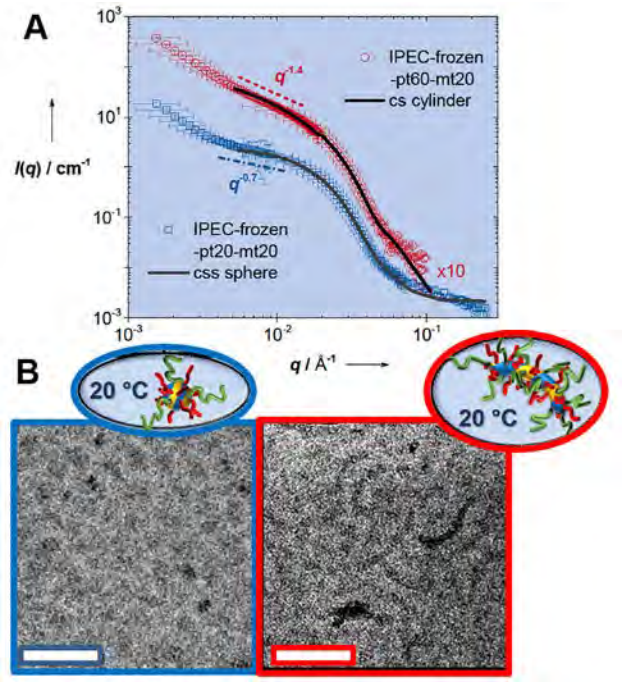

Figure 1: SANS pattern (A) and cryo-TEM images (B) of two samples of the same micellar interpolyelectrolyte complex under the same conditions such as concentration, temperature, pressure etc. but with different thermal and compositional history: intermediate heat treatment gives worm-like micelles (shown in red); they transform back into spherical micelles upon intermediate salt addition (shown in blue; scale bar 100 nm; SANS was performed at KWS-2 at MLZ).

A specific example is shown in the figure, where spheri-cal micelles were obtained by freezing the structure at room temperature, while a rather pure phase of worm-like micelles, which have undergone a different thermal history, is detected at the same temperature, concentration etc. The difference derives from the fact that freezing occurred for the latter sample at elevated temperature, where the thermoresponsive component is insoluble in water. These structures were analysed by SANS and cryo-TEM. Indeed, the SANS patterns can be well fitted with a spherical and a cylindrical form factor model (taking into account additionally loose aggregates which appear at low q-values). The SANS data are in line with the cryo-TEM results.

Importantly, these non-equilibrium worm-like structures can be released by the addition of salt at room temperature, again yielding spherical micelles. Sequential heating and subsequent freezing allow a restoration of the worm-like morphology in a repeated fashion. This recycling occurs by a self-templating effect due to the polymer-encoded micellar structure being translated differently under different conditions. Such a system holds promise for on-demand property changes, which could include e.g. triggered gelation (under otherwise constant conditions). At the same time, the original state can be restored.

[1] C. Dähling, et al., Self-Templated Generation of Triggerable and Restorable Nonequilibrium Micelles, ACS Macro Lett. 7, 341 (2018)

Water vapor absorption in polyelectrolyte-brush/multilayer-composites

O. Löhmann[1], S. Micciulla[2], O. Soltwedel[1, 3], E. Schneck[4], R. von Klitzing[1]

[1]Department of Physics, Technische Universität Darmstadt, Darmstadt, Germany; [2]Large scale structures, Institut Laue Langevin (ILL), Grenoble, France; [3]Heinz Maier-Leibnitz Zentrum (MLZ) and Physics Department, Technical University of Munich, Garching, Germany; [4]Biomaterials Department, Max Planck Institute of Colloids and Interfaces, Potsdam, Germany

Designing sensors with unique responses to outer stimuli is one of the key elements in a digital world. External stimuli such as temperature, electromagnetic fields, humidity, and light have an influence on the structure of polymer coatings and their life-time. Possible applications are in the field of touchless sensors, which exhibit high spatial sensitivity to the degree of environmental moisture, such as in the vicinity of the human finger. Polyelectrolytes (PE) are responsive to humidity and can be tailored on a sub nm-scale. Moreover, by combining individual PEs, thin coatings with the desired structure and responsiveness are obtained. In this context, composites made from polyelectrolyte multilayers (PEMs) adsorbed on end-grafted polymer brushes (PB) represent a valuable approach to the design of complex organic composite materials with tailored responsive properties. In our study, we address the correlation between the swelling properties and their internal structure as a function of various relative humidities (RH). The system investigated is a composite of an end-grafted 2-(methacryloyloxy)ethyl-trimethylammonium chloride brush covered with a poly(sodium styrenesulfonate) and poly(diallyldimethylammonium) chloride PEM. Both compartments, PB and PEM, as well as the composite are responsive to external humidity. Ellipsometry and neutron reflectometry (NR) are applied extensively to monitor the water uptake and the accompanying conformational changes in the PB/PEM-composite, respectively. The overall swelling behavior is observed as identical in both methods. Additionally, NR offers evidence of significant interaction between the two components. The plot shows the measured specular reflectivity data (symbols in A) with the respective best fits (colored lines in A) and their corresponding scattering length density profiles (same color code in B) for three representative RH. Sections C-E show the volume fraction profiles of all components when exposed to varying RH. At low humidity a strong interdigitation of the PB and PEM is observed. With increasing RH, a change in their spatial distribution is found, indicating considerable PEM mobility within the brush. The brush conformation is more stretched after PEM adsorption. A direct result is reduced water uptake by the brush. The swelling response of a PEM adsorbed on top of a brush is minimally influenced by its support. When the RH is increased, the PB/PEM interpenetration is gradually reduced and the PB is compressed. We found that the water accumulates in the interfacial region between the brush and PEM so that these two compartments become increasingly separated with increasing RH. The swelling process is almost reversible, which demonstrates the potential applicability of these composites as a matrix for chemical gas or moisture sensors.

[1] O. Löhmann, et al., Swelling Behavior of Composite Systems: Mutual Effects between Polyelectrolyte Brushes and Multilayers, Macromolecules, 51, 2996 (2018)

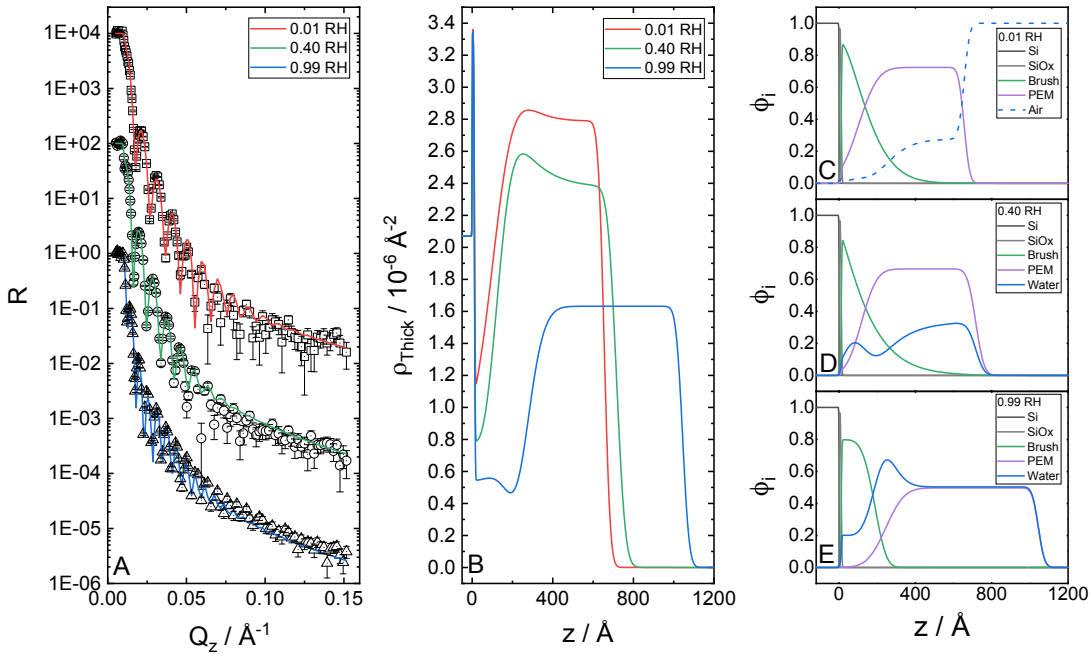

Figure 1: Three exemplary data sets for a PMETAC brush coated with a PSS/PDADMAC PEM of 17 single layers. (A) Reflectivity data and the corresponding fits at 1, 40, and 99% RH. (B) Corresponding SLD profiles. (C) Volume fraction profile at 1% RH. (D) Volume fraction profile at 40% RH. (E) Volume fraction profile at 99% RH.

Swelling of a polymeric network confined in doubly-thermosensitive microgels

M. Brugnoni[1], A. Scotti[1], A. A. Rudov[3,4], A. P. H. Gelissen[1], T. Caumanns[5], A. Radulescu[6], T. Eckert1, A. Pich[2,3], I. I. Potemkin[3,4,7], W. Richtering[1]

[1]Institute of Physical Chemistry, RWTH Aachen University, Aachen, Germany; [2]Institute of Technical and Macromolecular Chemistry, RWTH Aachen University, Aachen, Germany; [3]DWI - Leibniz Institute for Interactive Materials e.V., Aachen, Germany; [4]Physics Department, Lomonosov Moscow State University, Moscow, Russia; [5]GFE Central Facility for Electron Microscopy, RWTH Aachen University, Aachen, Germany; [6]Jülich Centre for Neutron Science (JCNS) at MLZ, Forschungszentrum Jülich GmbH, Garching, Germany; [7]National Research South Ural State University, Chelyabinsk, Russia

Microgels are soft polymeric networks able to adapt to changes in their environment e.g. swell and deswell in a solvent, depending on the temperature. By constraining a poly(N-isopropylmethacrylamide) (pNIPMAM) shell between a rigid silica core and an outer poly(N-isopropylacrylamide) (pNIPAM) shell, doubly thermoresponsive microgels are formed. Subsequent core removal leads to the formation of the corresponding hollow structure, namely double-shell microgels with two spatially separated polymer shells surrounding a solvent-filled cavity. The unique composition of these microgels makes it possible to investigate three distinct swelling states: both shells swollen; both shells collapsed; and an intermediate state with a collapsed outer shell and a swollen inner shell. Figure 1 shows snapshots obtained from Brownian molecular dynamics simulations of core-double-shell and hollow double-shell microgels at the different swelling states. The calculations predict that a high cross-linking density (10%) in the inner shell is crucial to maintaining the cavity of the hollow microgels.

Scattering techniques are an elegant way of probing the form factors of real microgels and exploiting the internal structure by using the appropriate form factor models. Small-angle neutron scattering (SANS) with contrast variation is crucial to an investigation of the architecture of microgels made of different materials, in this case, silica and polymeric networks. The higher scattering of the rigid silica cores precludes analysis of the polymeric shell via light or X-ray scattering. However, in SANS, the scattering length density of the silica core can be matched by using a mixture of H_2O/D_2O as a solvent, which allows the polymeric networks to be studied. Figure 2 illustrates the form factors of core-double-shell and hollow double-shell microgels at the swelling states referred to above. The radial density profiles are obtained from the fits with a core-double-shell model. It can be observed that in the presence of a rigid core, the swelling of the inner shell leads to an interpenetration of the two polymeric shells. Following core removal, this interpenetration vanishes. The inner shell swells preferentially into the cavity and does not penetrate into the outer shell. An additional swelling of the inner shell results once more in a re-increase in the cavity size. Finally, upon cooling, the hollow double-shell microgels undergo a push-pull effect. Hollow, responsive double-shell microgels have promising applications as e.g. in nanomedicine and catalysis. Obviously, SANS is crucial in determining how the cavity and the structural integrity of the nanocapsules can be preserved.

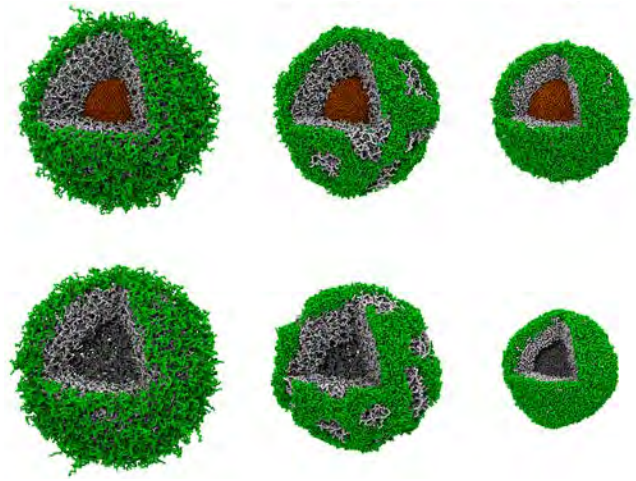

Figure 1: Snapshots representing the equilibrium structures of a core-double-shell (top) and the corresponding hollow double-shell microgel (bottom) at different swelling states obtained from molecular dynamics. The microgels gradually collapse from left to right; first the outer shell (green) collapses, followed by the inner shell (gray).

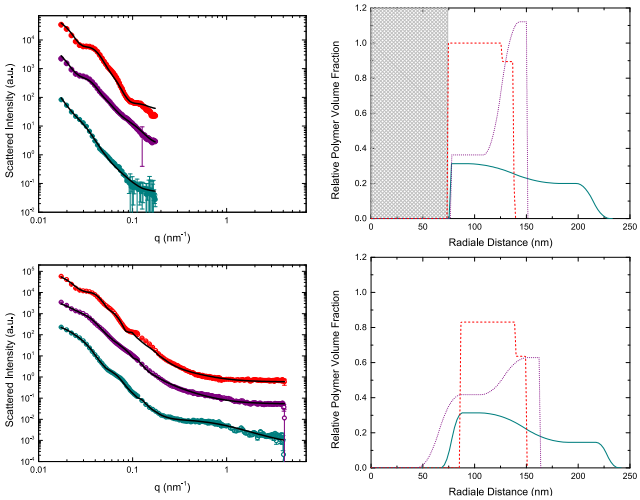

Figure 2: Left: Form factors of core-double-shell microgels in a D_2O/H_2O mixture (top) and hollow double-shell microgels in D_2O (bottom) probed by SANS at 20 °C (blue), 40 °C (purple) and 50 °C (red). The solid lines represent the fits. Right: Corresponding radial density profiles.

[1] M. Brugnoni, et al., Swelling of a Responsive Network within Different Constraints in Multi-Thermosensitive Microgels, Macromolecules, 51, 2662 (2018)

Structure of human telomere G-quadruplex in the presence of a model drug

F. Bianchi[1], L. Comez[2], R. Biehl[3], F. D'Amico[4], A. Gessini[4], M. Longo[5], C. Masciovecchio[4], C. Petrillo[1], A. Radulescu[5], B. Rossi[4], F. Sacchetti[1], F. Sebastiani[6], N. Violini[7], A. Paciaroni[1]

[1]Dipartimento di Fisica e Geologia, Università di Perugia, Perugia, Italy; [2]IOM-CNR c/o Dipartimento di Fisica e Geologia, Università di Perugia, Perugia, Italy; [3]Jülich Centre for Neutron Science (JCNS) & Institute of Complex Systems (ICS), Forschungszentrum Jülich, GmbH, Jülich, Germany; [4]Elettra-Sincrotrone Trieste, Basovizza, Trieste, Italy; [5]Jülich Centre for Neutron Science (JCNS) at MLZ, Forschungszentrum Jülich GmbH, Garching, Germany; [6]Lehrstuhl für Physikalische Chemie 2, Ruhr-Universität Bochum, Bochum, Germany; [7]Jülich Centre for Neutron Science (JCNS), Forschungszentrum Jülich GmbH, Jülich, Germany

G-rich DNA sequences are able to fold into structures called G-quadruplexes (G4), which have been the focus of a number of studies in both fundamental and applied research, from cancer biology and novel therapeutics through to nanotechnology. G4 may fold in a variety of different topologies, depending on various factors such as the oligonucleotide sequence, the particular cation used, the presence of crowding agents, the DNA concentration and the specific interaction with ligands. This last point is key to therapeutic applications, as different conformers can be formed during the binding of G4 with ligands. Here, we report on the results of Small Angle Neutron Scattering (SANS) experiments performed to elucidate how the structural features of the human telomeric G-quadruplex d[A(GGGTTA)3GGG] (Tel22) change upon complexation with Actinomycin D (ActD), an anticancer ligand with remarkable conformational flexibility (fig. 1). While the data of Tel22 are well-represented by the form factor of a squared parallelepiped, those of Tel22+ActD are fitted with a form factor consisting of a mixture of monomers (squared parallelepiped) and dimers (two adjacent squared parallelepipeds), representing Tel22 + ActD complexes with molecularity 1:1 and 2:1 respectively (fig. 2).

It turns out that the monomer characteristic sizes are very similar to those of unbound Tel22 (15 ± 2 Å and height 28 ± 2 Å), suggesting a rather small contribution from the ligand to the complex molecular volume. Moreover, we found that in the presence of ActD, the dimerisation process

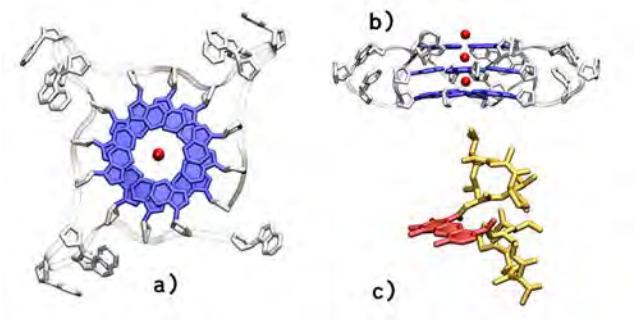

Figure 1: Schematic a) top- and b) side- view of G-quadruplex scaffold. In blue: G-tetrads, in red: potassium central ions. c) Molecular prospectus of actinomycin D molecule.

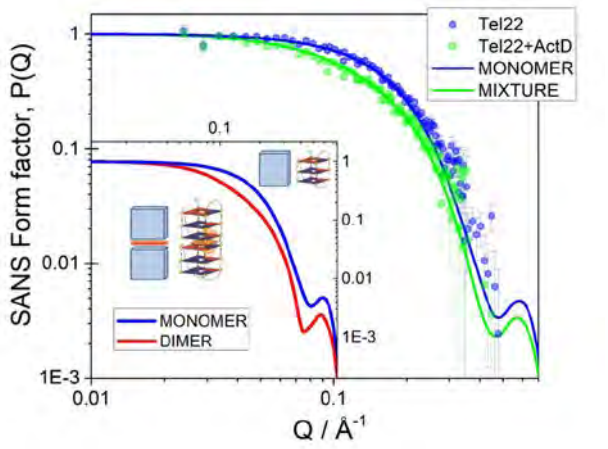

Figure 2: Form factors obtained from SANS measurements on KWS-2, for Tel22 (closed blue hexagons) and Tel22+ActD (closed green circles). The form factors of a parallelepiped representing the Tel22 monomer (blue line) and a mixture of parallelepiped monomers and dimers fitted to the complex data (green line) are also reported. Inset: Form factors of parallelepiped monomer (blue line) and parallelepiped dimer (magenta line).

involves a fraction of 0.5 ± 0.1 G-quadruplexes. The radius of gyration calculated within the Guinier approximation, is 10.6 ± 0.4 Å and 12.2 ± 0.3 for Tel22 and Tel22 + ActD, respectively. The molecular volumes, estimated from the Porod invariant, turn out to be V_{Tel22} = (6.8 ± 0.3) × 10^3 Å^3 and V_{Tel22} + ActD = (10.1 ± 0.4) × 10^3 Å^3. The value of V_{Tel22} is in quite good accord with the estimate of 6400 Å^3 one can derive from a knowledge of the molecular weight and the partial specific volume, which is usually assumed to be 0.55 ml/g for G-quadruplexes. Therefore, these SANS data measured at the instrument KWS-2 provided the first direct structural evidence for the drug-driven dimerisation of Tel22. Complemented with circular dichroism spectroscopy, ultraviolet resonance Raman spectroscopy and Small Angle X-Ray Scattering, the SANS results provided a piece of information crucial to disclosing the molecularity of the Tel22 + ActD complex.

[1] F. Bianchi, et al., Structure of human telomere G-quadruplex in the presence of a model drug along the thermal unfolding pathway, Nucleic Acids Res. 46, 11927 (2018)

Capillary condensation and gelling of microemulsions with clay additives

M. Gvaramia[1,2], G. Mangiapia[1,3], P. Falus[4], M. Ohl[5], O. Holderer[1], H. Frielinghaus[1]

[1]Jülich Centre for Neutron Science (JCNS) at MLZ, Forschungszentrum Jülich GmbH, Garching, Germany; [2]Department of Inorganic and Analytical Chemistry, University of Geneva, Geneva, Switzerland; [3]German Engineering Materials Science Centre (GEMS) at MLZ, Helmholtz-Zentrum Geesthacht GmbH, Garching, Germany; [4]Institut Laue Langevin (ILL), Grenoble, France; [5]Jülich Centre for Neutron Sciences JCNS-1, Forschungszentrum Jülich GmbH, Jülich, Germany

Microemulsions are thermodynamically stable mixtures of oil and water that are mediated by the surfactant. Locally, there are oil and water domains, separated by the surfactant film, that are observable via scattering experiments. The domain sizes are usually a few nanometers and display shapes from spherical droplets, through elongated droplets to the bicontinuous sponge phase. In the following, we restrict ourselves to the bicontinuous microemulsion. When exposing the microemulsion to hydrophilic surfaces, a lamellar order is locally induced next to the interface. From spectroscopic measurements, we know that the membrane fluctuations in microemulsions are faster in the lamellar state. This is connected to the lubrication effect, since the lamellae can slide off more easily and the motions are faster. In spectroscopic measurements with hydrophilic clay particles, we have been able to show that the platelet diameter causes a cutoff of the undulation modes, and larger platelets lead to a better order with longer wavelength modes. The capillary condensation in bicontinuous microemulsions is expected to take place when two parallel surfaces are narrowed, resulting in a completely lamellar microemulsion (fig. 1). So far, all experiments have been confined to relatively low clay concentrations, when the system is still liquid. The lamellar fraction in microemulsions with 1% clay is around 25% in volume. We have subsequently tried to observe the capillary condensation with increasing clay concentration, using small angle neutron scattering (at KWS-1) and neutron spin echo (NSE) spectroscopy (at J-NSE) [1].

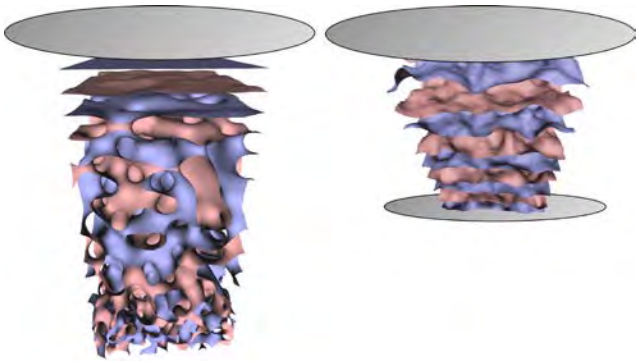

Figure 1: A sketch for the phase transition of the capillary condensation of a microemulsion between clay platelets.

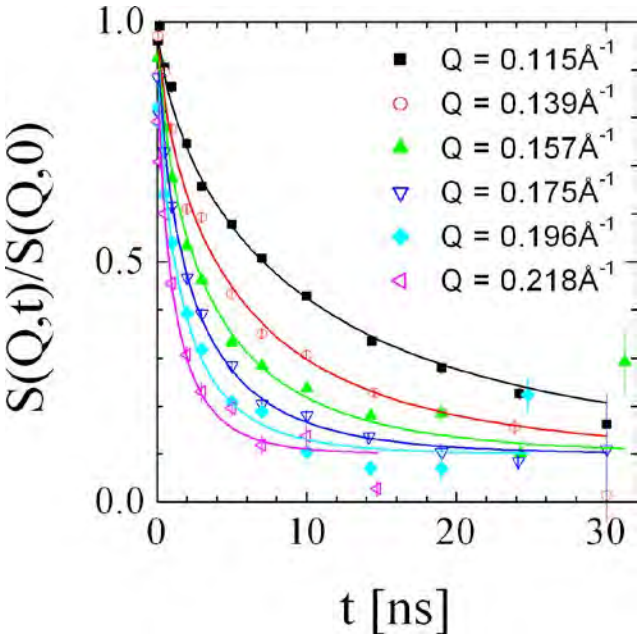

Figure 2: Relaxation curves of one clay system at 1.5% vol clay with a film contrast microemulsion. The lines result from a fit of a stretched exponential with an elastic contribution of 0.1 for all Q-values.

Using small angle neutron scattering, the structure of microemulsions was observed as a function of the clay content. The correlation peak of the microemulsion changed discontinuously in terms of the repeat unit and the correlation length which is closely connected to the lamellar ordering of the microemulsion. The large-scale surface (Porod) scattering indicated that the clay platelet ordering is induced by the microemulsion ordering. The critical clay concentration depends on the platelet diameter and is explained by the free energy of the platelets competing with the fluctuating medium. The gel phase transition is observed in the spectroscopic NSE measurements (fig. 2) where the diffusion motion is widely suppressed in the gel phase, but otherwise superimposes with the membrane undulations.

[1] M. Gvaramia, et al., Capillary condensation and gelling of microemulsions with clay additives, J. Colloid Interface Sci. 525, 161 (2018)

Structure and dynamics of folded and unfolded BSA

F. Ameseder[1,2], A. Radulescu[3], M. Khaneft[3], O. Holderer[3], W. Lohstroh[4], P. Falus[5], D. Richter[1], A. Stadler[1,2]

[1]Jülich Centre for Neutron Science JCNS and Institute for Complex Systems ICS, Forschungszentrum Jülich GmbH, Jülich, Germany; [2]Institute of Physical Chemistry, RWTH Aachen University, Aachen, Germany; [3]Jülich Centre for Neutron Science (JCNS) at MLZ, Forschungszentrum Jülich GmbH, Garching, Germany; [4]Heinz Maier-Leibnitz Zentrum, Technical University of Munich, Garching, Germany; [5]Institut Laue-Langevin (ILL), Grenoble, France

We used neutron scattering experiments to elucidate the structural and dynamical properties of native folded bovine serum albumin (BSA) and its denatured state in solution [1,2].

The structural aspects were investigated using small-angle neutron scattering (SANS) on the instrument KWS-2, see fig. 1 [1]. BSA was denatured by 4 M and 6 M guanidinium hydrochloride (GndCl), which results in denatured BSA that is collapsed and cross-linked by intact disulphide bonds. In contrast, breakage of the disulphide bonds in denatured BSA by the addition of the strong reducing agent β-mercaptoethanol (6 M GndCl, 150 mM β-met) leads to a swollen and expanded structure of denatured BSA, see fig. 1.

We investigated localised dynamics on the ps to ns time-scale and Å length-scale using neutron time-of-flight and backscattering spectroscopy on TOFTOF and SPHERES at the MLZ [2]. A significant dynamical heterogeneity in the native folded BSA was observed. Chemical denaturation has a profound effect on the ps to ns motions of the protein. Anomalous diffusion in denatured BSA on the ps to ns time-scale was found to show properties similar to those of polymers in solution. By using neutron spin-echo (NSE) experiments performed on J-NSE at the MLZ and IN15 at the ILL, we were able to probe slow collective dynamics up to 150 ns of denatured BSA, see fig. 2 [1]. We observed a high molecular flexibility of denatured BSA, depending significantly on the solvent conditions. The internal motions of denatured BSA measured using NSE were described using theoretical models derived from polymer theory. The fully reduced and denatured BSA was interpreted via the Zimm model with internal friction, and internal friction was found to depend significantly on the GndCl concentration. On the other hand, disulphide bonds acting as cross-links in denatured BSA restrict internal motions substantially, leading to large-wavelength Zimm mode suppression.

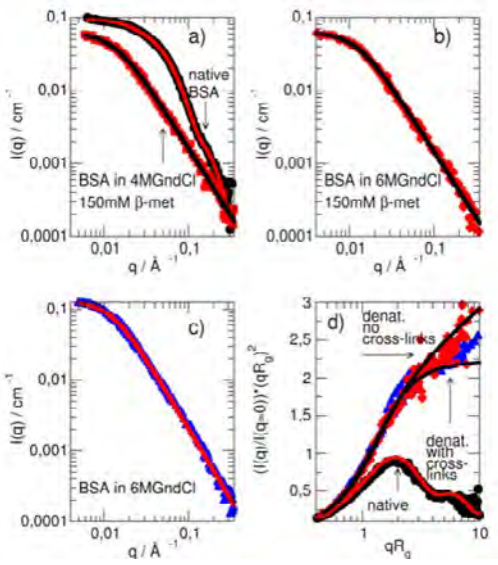

Figure 1: SANS data of denatured and native BSA in different solvent conditions measured on KWS-2. Solid lines are theoretical fits based on the crystal structures for native BSA and generalised Gauss functions for the denatured states of BSA.

Our experiments demonstrate the huge potential of neutron scattering for the investigation of disordered proteins and their polymer-like properties. Concerning future work, our results will be of high relevance for the investigation of intrinsically disordered proteins, a special class of proteins that is unfolded under physiological conditions.

[1] F. Ameseder, et al., Relevance of Internal Friction and Structural Constraints for the Dynamics of Denatured Bovine Serum Albumin, J. Phys. Chem. Lett. 9, 2469 (2018)

[2] F. Ameseder, et al., Homogeneous and heterogeneous dynamics in native and denatured bovine serum albumin, Phys. Chem. Chem. Phys. 20, 5128 (2018)

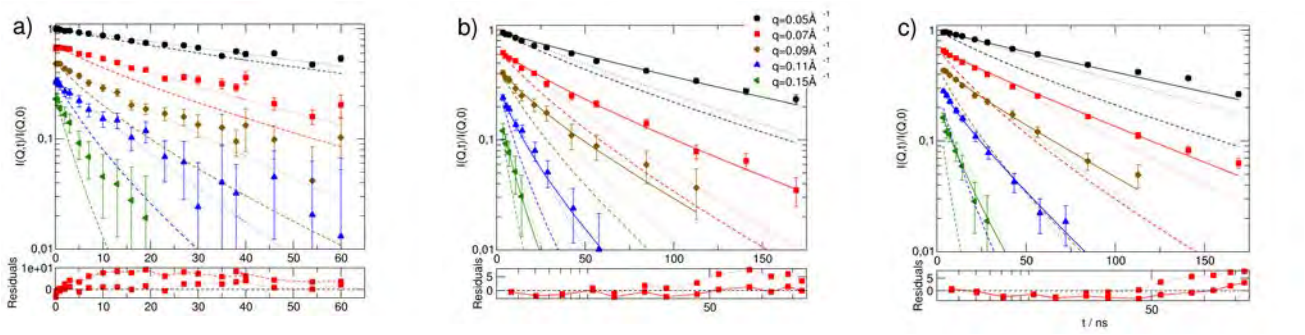

Figure 2: Experimental NSE data of denatured BSA and fits based on polymer theory. Zimm model (dashed lines), ZIF model (dotted lines), and Zimm model with reduced mode amplitudes (solid lines). Data measured on (a) J-NSE at MLZ, (b) and (c) on IN15 at ILL. (a) Expanded BSA in 4 M GndCl & 150 mM β-met, (b) expanded BSA in 6 M GndCl & 150 mM β-met without sulphur bonds and (c) collapsed BSA in 6 M GndCl with active sulphur bonds.

Human dystrophin structural changes upon binding to anionic membrane lipids

R. Dos Santos Morais[1,2,3], O. Delalande[2], A. Martel[4], M.-S. Appavou[5], J. Pérez[3], S. Combet[1], J. F. Hubert[2]

[1]Laboratoire Léon-Brillouin (LLB), UMR 12 CEA-CNRS, Université Paris-Saclay, CEA-Saclay, Gif-sur-Yvette CEDEX, France ; [2]IGDR CNRS UMR 6290, Université de Rennes 1, Rennes, France; [3]Synchrotron SOLEIL, L'Orme des Merisiers, BP 48, Saint-Aubin, Gif-sur-Yvette, France; [4]Institut Laue-Langevin (ILL), Grenoble, France; [5]Jülich Centre for Neutron Science (JCNS) at Heinz Maier-Leibnitz Zentrum (MLZ), Forschungszentrum Jülich GmbH, Garching, Germany

Scaffolding proteins play an important role in supporting the plasma membrane (sarcolemma) of muscle cells. Among them, the filamentous peripheral membrane protein dystrophin strengthens the sarcolemma through protein-lipid interactions. Its absence due to gene mutations leads to severe Duchenne muscular dystrophy (DMD), a hitherto incurable disease. The major part of the dystrophin consists of a central domain composed of 24 coiled-coil repeats (R1 to R24), whose 3D-structure is not accessible by classical high resolution methods (fig. 1). Using SANS and the contrast variation technique, we specifically probed the solution structure of the three first consecutive repeats (R1–3), a part of dystrophin known to physiologically interact with membrane lipids. Its free structure in solution was compared to that found in the presence of contrast-matched phospholipid-based bicelles. SANS data (obtained on KWS-1 at the MLZ, PACE at the LLB, and D22 at the ILL) of the protein/lipid complexes were obtained either with zwitterionic, or anionic bicelles, at two different temperatures, in order to probe the role of electrostatic interactions and membrane fluidity. Our results highlight that, when bound to zwitterionic bicelles, no important conformational modification of the protein fragment is detected. On the contrary, when R1-3 is bound to anionic bicelles, SANS data demonstrate large modifications of its 3D-structure, as revealed by a significant increase in the protein gyration radius from 42 ± 1 to 60 ± 4 Å. The R1-3/anionic bicelle complex was further analysed by classical coarse-grained molecular dynamics (CG-MD) simulations and the innovative interactive CG-MD method. The final models proposed for R1-3 bound to membrane lipids are in total agreement with the experimental SANS data (fig. 2). Finally, we report on accurate

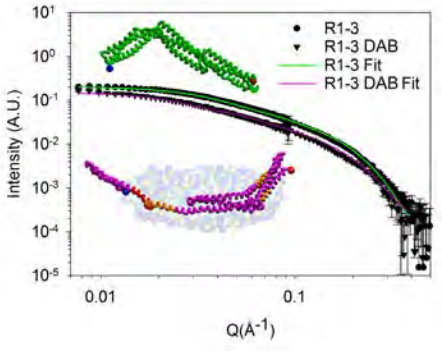

Figure 2: Experimental SANS intensities (circles and triangles for R1–3 alone or bound to contrast-matched, deuterated anionic bicelles (DAB), respectively) are shown fitted with the theoretical CRYSON curves generated from the R1–3 model free in solution (green) and the R1–3 model bound to anionic bicelles (purple). The inset shows the corresponding all-atom models represented with the same color code. Blue and red dots represent the N- and C-termini, respectively.

mapping of the protein/lipid interactions obtained by coupling click-chemistry with mass spectrometry, in line with the in silico data. We highlight that the coiled-coil in repeat one specifically opens upon binding to anionic bicelles. We propose that such coiled-coil opening could occur during the contraction/elongation process of muscles to ensure dystrophin membrane anchoring in the sarcolemma. Understanding these structural changes may help with the design of rationalised efficient shortened dystrophins devoted to gene therapy for DMD patients. Finally, our approach opens up new possibilities for the structure determination of peripheral and even integral membrane proteins not compatible with different high resolution structural methods.

[1] R. Dos Santos Morais, et al., Human dystrophin structural changes upon binding to anionic membrane lipid, Biophys. J. 115, 1231 (2018)

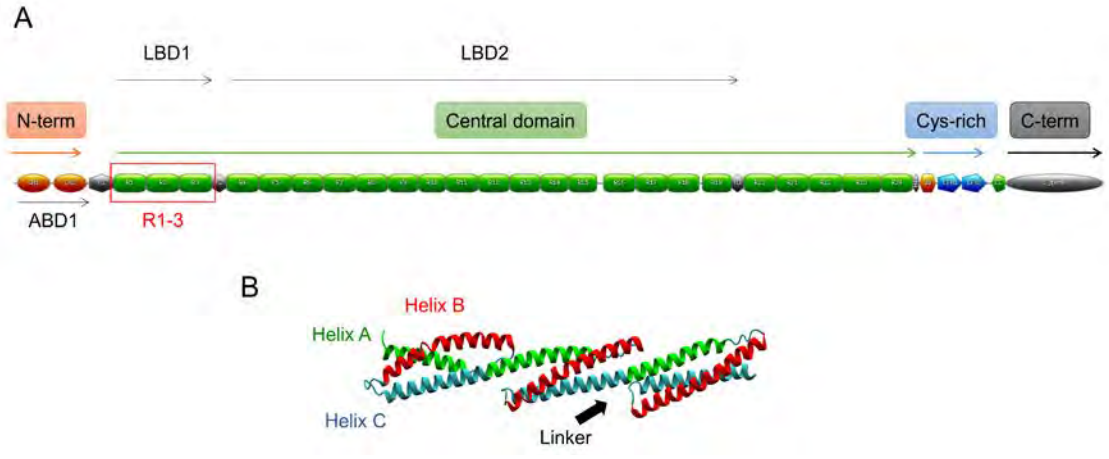

Figure 1 : (A) Schematic representation of dystrophin and its four domains, including the central domain composed of 24 spectrin-like repeats (R). The R1–3 protein fragment is framed in red and can interact with membrane phospholipids. LBD, lipid binding domain; ABD, actin binding domain. (B) The 3D structure of three spectrin repeats folded in triple coiled-coil (PDB: 1U4Q) showing the organisation of the dystrophin central domain is shown. The linker region is the junction between the helix C of one repeat and the helix A of the subsequent one.

Leaflet coupling in asymmetric lipid vesicles

B. Eicher[1,2], D. Marquardt[3], F. A. Heberle[4,5,6], I. Letofsky-Papst[7], G. N. Rechberger[8,9], M.-S. Appavou[10], J. Katsaras[4,5,6], G. Pabst[1,2]

[1]University of Graz, Institute of Molecular Biosciences, Biophysics Division, NAWI Graz, Austria; [2]BioTechMed-Graz, Graz, Austria; [3]Department of Chemistry and Biochemistry, University of Windsor, Windsor, Ontario, Canada; [4]Shull Wollan Center, Oak Ridge National Laboratory, Oak Ridge, Tennessee, USA; [5]The Bredesen Center for Interdisciplinary Research and Graduate Education, University of Tennessee, Knoxville, Tennessee, USA; [6]Biology and Soft Matter Division, Oak Ridge National Laboratory, Oak Ridge, Tennessee, USA; [7]Institute for Electron Microscopy and Nanoanalysis and Center for Electron Microscopy, Graz University of Technology, NAWI Graz, Austria; [8]Institute of Molecular Biosciences, University of Graz, Austria; [9]Omics Center Graz, BioTechMed-Graz, Graz, Austria; [10]Jülich Centre for Neutron Science (JCNS) at Heinz Maier-Leibnitz Zentrum (MLZ), Forschungszentrum Jülich GmbH, Garching, Germany

We have applied small-angle neutron scattering (SANS), in combination with other complementary techniques, to a study of the leaflet-specific structure of asymmetric lipid vesicles composed of palmitoyl-oleoyl-phosphatidylethanolamine (POPE) and palmitoyl-oleoyl-phosphatidylcholine (POPC). Asymmetric large unilamellar vesicles (aLUVs) with an average size of ~ 100 nm were engineered using cyclodextrin-mediated lipid exchange, which resulted in two types of aLUVs: (i) inner leaflet POPC and outer leaflet enriched POPE ($POPC^{in}/POPE^{out}$), and (ii) aLUVs with reversed asymmetry, i.e. ($POPE^{in}/POPC^{out}$). Differential scanning calorimetry and wide-angle X-ray scattering experiments showed that the leaflets of $POPE^{in}/POPC^{out}$ aLUVs are coupled below the melting transition, with an average area per lipid, which is intermediate between that of each leaflet in symmetric uncoupled vesicles. In turn, interleaflet coupling was absent in $POPC^{in}/POPE^{out}$. The coupling in the gel phase is most likely to be due to the molecular shape of POPE (small cross-sectional headgroup area vs. large area at the hydrocarbon chain terminus), which leads to a significant negative intrinsic curvature and an energetically preferred location of POPE in the inner leaflet. Interestingly, this is consistent with the location of phosphatidylethanolamines in mammalian plasma membranes.

In order to check whether this coupling also persists in the fluid phase, we performed SANS experiments at KWS-1 (MLZ, Garching) combined with contrast variation using either protiated POPE or chain perdeuterated POPE-d31. Data were jointly analysed using small-angle X-ray scattering data to achieve high structural fidelity. However, we found no evidence for transbilayer structural coupling above the melting temperature for both aLUVs. In particular, the lateral area per lipid in each leaflet was, within experimental uncertainty, equal to that of an uncoupled bilayer, with a symmetric lipid distribution. The loss of this coupling in the fluid bilayers is most likely the result of entropic contributions. We currently envisage experiments which will specifically address this point.

[1] B. Eicher, et al., Intrinsic curvature-mediated transbilayer coupling in asymmetric lipid vesicles, Biophys. J. 114, 146 (2018)

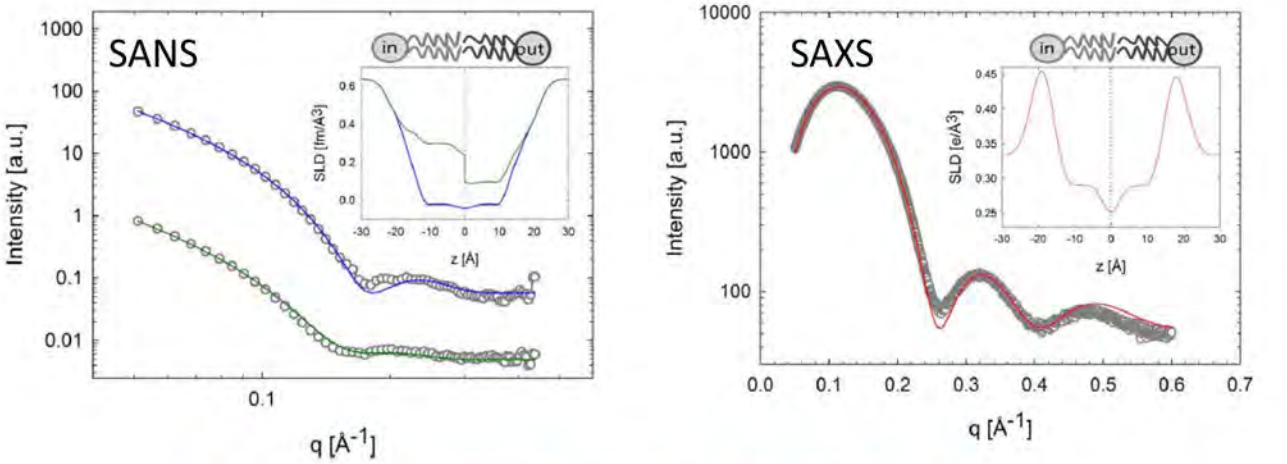

	A_L^{in} (Å²)	A_L^{out} (Å²)
$POPC^{out}/POPE^{in}$	59.7 (59.3)	64.7 (63.0)
$POPE^{out}/POPC^{in}$	64.7 (64.9)	59.9 (60.7)

Figure 1: Joint analysis of SANS/SAXS experiments on $POPE^{in}/POPC^{out}$ aLUVs at 35 °C. Solid lines show best fits (blue, $POPE^{in}/POPC^{out}$; green, $POPEd31^{in}/POPC^{out}$). Insets show the corresponding scattering length density profiles. The table gives the lateral area per lipid obtained for each leaflet. Numbers in brackets correspond to values calculated from leaflet composition. These data are within experimental uncertainty (3%) equal to the A_L values determined for aLUVs indicating the absence of transbilayer coupling.

The intriguing role of water in protein-ligand binding

J. Schiebel[1,2], R. Gaspari[2], T. Wulsdorf[1], K. Ngo[1], C. Sohn[1], T. E. Schrader[3], A. Cavalli[2], A. Ostermann[4], A. Heine[1], G. Klebe[1]

[1]Institut für Pharmazeutische Chemie, Philipps-Universität Marburg, Marburg, Germany; [2]Computational Sciences, Istituto Italiano di Tecnologia, Genova, Italy; [3]Jülich Centre for Neutron Science (JCNS) at MLZ, Forschungszentrum Jülich GmbH, Garching, Germany; [4]Heinz Maier-Leibnitz Zentrum, Technical University of Munich, Garching, Germany.

In vivo, proteins and their ligands are surrounded by water molecules. Thus, the solvent water necessarily has a major impact on the ligand binding event and energetics. The role of water molecules during ligand recognition is believed to be multifactorial and highly complex, explaining why binding affinity is often difficult to predict even when structural information is available.

The displacement of water molecules from protein-binding pockets during ligand association impacts affinity and governs enthalpy/entropy partitioning according to the properties of the individual water molecules in the binding pocket as compared to those in the bulk phase. In particular, it has been proposed that the expulsion of thermodynamically unfavourable water molecules during complex formation enhances the ligand's affinity. Although the importance of water molecules during ligand binding is generally accepted, experimental and, in particular, structural data that decipher how water molecules act exactly during protein-ligand complex formation is unfortunately rare. Information regarding the orientation and rotational states of the three atoms that form a water molecule usually remain unresolved when macromolecular X-ray crystallography is used. In contrast, neutron crystallography delivers structures that contain substantial information concerning hydrogen atoms.

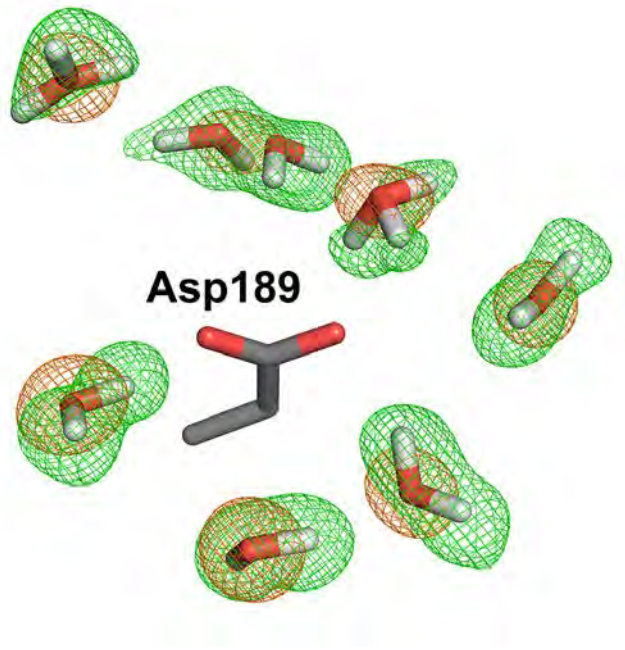

Figure 1: Water network including alternate orientations surrounding Asp189 in the binding pocket of the unliganded state of trypsin. Other residues in contact with the water molecules are not shown for clarity. X-ray 2mFo-DFc maps at 1.5 σ (orange meshes). Neutron mFo-DFc omit maps at 4 σ (green meshes) obtained after removal of deuterium atoms from all depicted water molecules for map calculation.

In order to substantially improve our understanding of ligand binding events, it is not sufficient to determine the structure of a protein-ligand complex via neutron diffraction at the required high resolution. It is also key to provide a high-quality neutron structure of the unliganded state of the protein, which describes the binding pocket in its hydration state prior to ligand association. In an attempt to accomplish this goal, we chose the digestion enzyme trypsin for our studies as a representative of the important class of serine proteases. Here, we determined neutron structures of bovine trypsin at BioDiff with exceptional resolutions better than d_{min} = 1.5 Å in the unliganded state and subsequently in the bound state with two selected inhibitors. These data have been augmented by X-ray and thermodynamic data as well as computer simulations. Our structures show the precise geometry of H-bonds between protein and the inhibitors along with the dynamics of the residual solvation pattern. Prior to binding, the ligand-free binding pocket is occupied by water molecules characterised by a paucity of H-bonds and high mobility, resulting in an imperfect hydration of the critical residue Asp189 (see fig. 1). It is likely that this phenomenon constitutes a key factor in fuelling ligand binding via water displacement and helps improve our current view on water influencing protein–ligand recognition.

[1] J. Schiebel, et al., Intriguing role of water in protein-ligand binding studied by neutron crystallography on trypsin complexes; Nat. Commun. 9, 3559 (2018)

Undecided even at very low temperature – H disorder in a short intramolecular O-H···O bond

K.-N. Truong[1], M. Meven[2], Ulli Englert[1]

[1]RWTH Aachen University, Institute of Inorganic Chemistry, Aachen, Germany; [2]Institute of Crystallography, RWTH Aachen University and Jülich Centre for Neutron Science (JCNS) at Heinz Maier-Leibnitz Zentrum (MLZ), Garching, Germany

Organic molecules with two different donor sites, the so-called ditopic ligands, represent attractive linkers for mixed-metal coordination polymers. In the crystal, the N- and O,O' donor 3-(2-(pyridin-4-yl)ethyl)-pentane-2,4-dione, **1** (see figure, top left) exists as an enol tautomer with a short intramolecular hydrogen bond.

In-house X-ray diffraction experiments showed disorder for this proton, but suffered from two obvious limitations:
a) preferential occupancy of one of the alternative sites is only detected with large standard uncertainties because of the small H form factor and the associated contrast problem.
b) the commonly used open-flow cooling systems for in-house diffraction do not allow the experiments to be extended to very low temperatures.

The high quality large crystals of **1** (see figure, bottom left) were obtained by re-crystallisation from dichloromethane. Our single crystal neutron diffraction experiment at the HEiDi instrument at 2.5 K extended to high resolution ($\sin\Theta/\lambda = 0.8$ Å^{-1}). It combined data collected at two different wavelengths ($\lambda = 0.793$ and 1.170 Å, $\Delta\lambda/\lambda \approx 5 \times 10^{-3}$); a displacement ellipsoid plot based on this data set is shown in the upper right part of the figure. These intensity data made it possible to refine precise site occupancies and interatomic geometries, including O-H distances (figure, bottom right). The interatomic distances in the acetylacetone moiety of **1** do not show alternating single and double bonds as expected for a well-ordered enol; O2-C4 and O1-C2 on the one and C4-C3 and C3-C2 on the other hand rather adopt very similar values, in agreement with the disorder suggested by the proton site occupancies. A subset of neutron data collected at 170 K and X-ray intensities obtained at the same temperature lead to the conclusion that the disorder in the short intramolecular hydrogen bond is essentially static. The proton remains undecided even at very low temperature, in clear contrast with our results on a related system, which we communicated in the MLZ 2017 report!

[1] K.-N. Truong, et al., Proton disorder in a short intramolecular hydrogen bond investigated by single-crystal neutron diffraction at 2.5 and 170 K, Acta Crystallogr. C74, 1635 (2018)

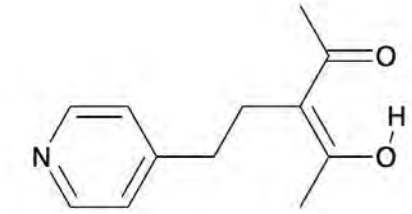

1

1a neutron data at 2.5 K
1b neutron data at 170 K,
X-ray constrained

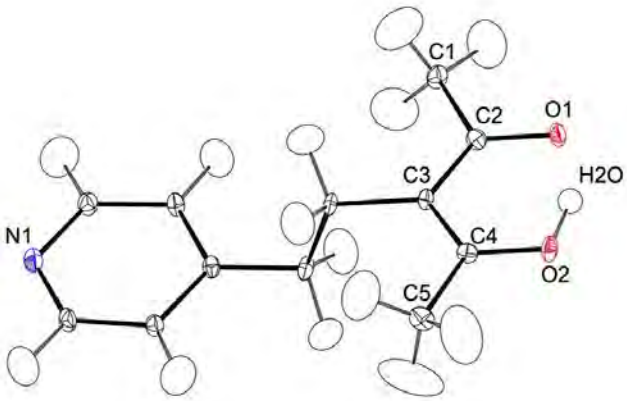

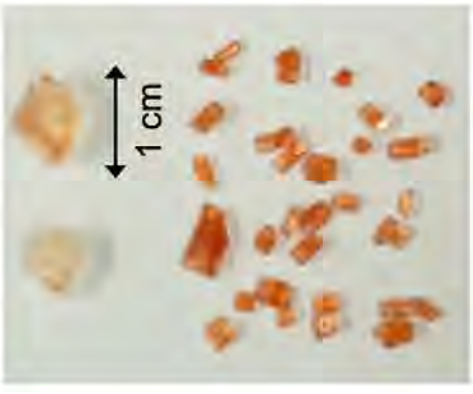

Interatomic distances in **1a** [Å]:
O2-H2O 1.067(8), O2-C4 1.305(2),
C4-C3 1.405(2), C3-C2 1.424(3),
O1-C2 1.288(2), O1-H1O 1.065(10)

Hydrogen atom occupancies, major : minor site
in **1a**, 2.5 K: 0.602(17) : 0.398(17)
in **1b**, 170 K: 0.59(7) : 0.41(7)

Figure 1: Lewis diagram of the title compound (top left); displacement ellipsoid plot (90%) for **1a**; minor site in the intramolecular H bond not shown (right); crystals of the title compound (bottom left).

Neutron diffraction analysis of the drug target protein CK2

C. Shibazaki[1], S. Arai[1], R. Shimizu[1], A. Ostermann[2], T. E. Schrader[3], R. Kuroki[4], M. Adachi[1]

[1]Tokai Quantum Beam Science Center, Quantum Beam Science Research Directorate, National Institutes for Quantum and Radiological Science and Technology (QST), Tokai, Japan; [2]Heinz Maier-Leibnitz Zentrum (MLZ), Technical University of Munich, Garching, Germany; [3]Jülich Centre for Neutron Science (JCNS) at MLZ, Forschungszentrum Jülich GmbH, Garching, Germany; [4]Japan Atomic Energy Agency (JAEA), Tokai, Japan

Casein kinase 2 (CK2) has broad phosphorylation activity against various regulatory proteins, which are important survival factors in eukaryotic cells. CK2 is a drug target protein as there is a strong correlation between malignancy and an abnormally high activity of CK2 in cancer. In order to clarify the hydration structure and catalytic mechanism of CK2 to aid an advanced drug design, we have determined the crystal structure of a ligand-free CK2 α subunit, including the hydrogen atom positions, using neutron diffraction.

We prepared a large crystal of recombinant human CK2, approximately 2 mm^3 in size. The crystal was soaked in deuterated (^2H) mother-liquor to decrease background due to incoherent scattering from hydrogen atoms (^1H). Neutron diffraction data were collected to 1.9 Å resolution at the instrument BIODIFF at the FRM II, and subsequently X-ray diffraction data were collected to a resolution of 1.1 Å at KEK-PF in Japan. The crystal structure of CK2 was solved to an R-factor of 18.8% and a free R-factor of 24.7% for the neutron diffraction data, and to an R-factor of 18.6% and a free R-factor of 21.2% for X-ray diffraction data with good statistics through a joint refinement (fig. 1 (a)).

The analysis revealed the structure of key elements in CK2 and other members of the protein kinase family: (1) a water molecule important for interaction with different inhibitors at the active site, (2) a highly conserved salt bridge inside the kinase C-lobe (fig. 1 (b)), (3) an intriguing penta network of water molecules (fig. 1 (c)), (4) a potential expanded hydrogen bond network originating from the catalytic residue Asp156 and running through the C-terminal domain (fig. 1 (d)). In particular, the long hydrogen bonding network is of interest to us. In the active site, Asp156 is well-known to enhance the nucleophilicity of the substrate OH-group to the γ-phospho group of ATP by elimination of the proton. His148 and Asp214, which are conserved in the protein kinase family, are located in the middle of the network. The water molecule forming a hydrogen bond with Asp214 appears to be deformed, since the position of omit map features for the deuterium atom in DOD718 is significantly different from the ideal geometry (fig. 1 (e)). Additionally, a mutational analysis of His148 in CK2 showed significant reductions of 40 - 75% in the catalytic efficiency with a similar affinity for ATP, indicating that the hydrogen bonding network may play an important role in conveying the proton from serine or threonine in substrate to Asp156.

This is the first study to directly determine proton positions in a protein kinase using neutron crystallography. Our findings of key elements, including the hydrogen atom positions, will contribute to a deeper understanding of the underlying catalytic mechanism. In addition, our results will lead to a new and interesting discussion on the role of a hydrogen bonding network for drug design in protein kinases.

[1] C. Shibazaki, et al., Hydration structures of the human protein kinase CK2α clarified by joint neutron and X-ray crystallography, J. Mol. Biol. 430, 5094 (2018)

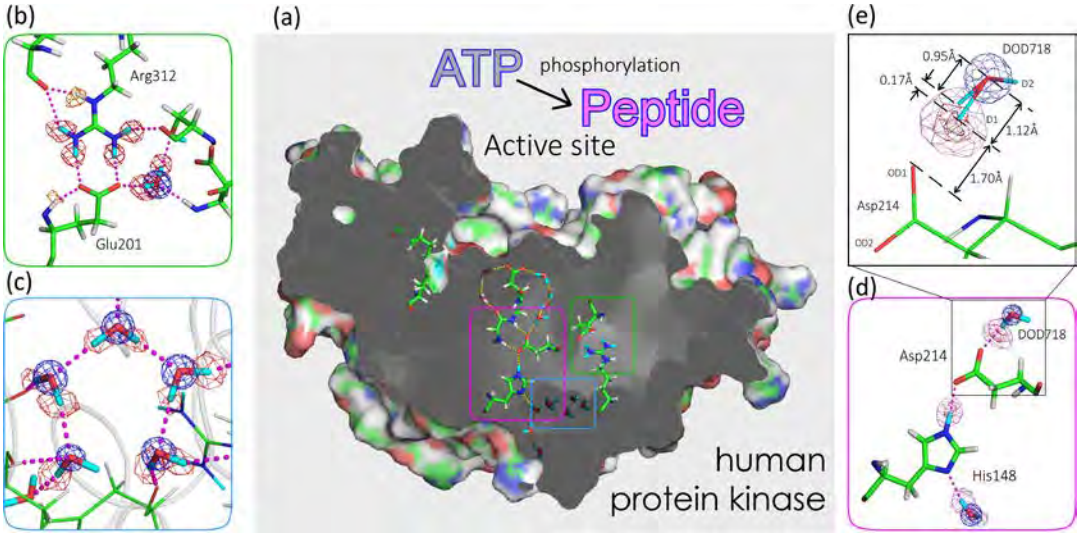

Figure 1: (a) Sectional view of CK2 determined by neutron crystallography. (b) Conserved salt bridge formed between Glu201 and Arg312. (c) Pentagonal network of five water molecules. (d) A part of the long hydrogen bonding network in the C-lobe of CK2. (e) Magnified drawing of Asp214 and DOD718 in (d). Neutron scattering length omit maps with positive and negative densities are represented in red and yellow, respectively. Electron density maps obtained by X-ray crystallography are shown in blue.

Lithium insertion mechanism of $Na_2Ti_6O_{13}$ anode material for Li-ion batteries unraveled

A. Kuhn[1], J.C. Perez-Flores[1], M. Hoelzel[2], C. Baehtz[3], I. Sobrados[4], J. Sanz[4], F. Garcia-Alvarado[1]

[1]Departamento de Química y Bioquímica, Facultad de Farmacia, Universidad CEU San Pablo, Madrid, Spain; [2]Heinz Maier-Leibnitz Zentrum (MLZ), Technical University of Munich, Garching, Germany; [3]Institute of Ion Beam Physics and Materials Research, Helmholtz-Zentrum Dresden-Rossendorf, Dresden, Germany; [4]Instituto de Ciencia de Materiales de Madrid (CSIC), Madrid, Spain

The exact mechanism of lithium insertion in sodium hexatitanate $Na_2Ti_6O_{13}$, an attractive alternative anode material in lithium-ion cells, has not been known so far. To obtain a full understanding of the properties of this titanate, a combination of in situ synchrotron X-ray diffraction, neutron diffraction and ^{7}Li MAS solid-state NMR spectroscopy has been used in the present work.

Lithium-ion batteries are an indispensable part of our daily lives. The negative electrodes are typically based on graphite. As the potential of Li insertion into graphite is close to that for the formation of metallic lithium, the deposition of metallic lithium on the graphite anode, so-called Li plating, can occur. Possible consequences are lithium dendrite formation and concomitant capacity loss, cell aging or even safety problems. Nowadays, several materials are being investigated which are not based on graphite, thereby avoiding all the previously stated issues for safe and long-life Li-ion cells. One of these materials is sodium hexatitanate.

$Na_2Ti_6O_{13}$ has high structural stability and is a promising material for long-life Li-ion cells. In batteries made with these anodes, lithium plating on the anode can be completely prevented. $Na_2Ti_6O_{13}$ has a very special open structure and creates a tunnel for lithium ions, enabling lithium storage as well as the mobility of lithium ions during charging and discharging. But how exactly does the mechanism for lithium storage work here?

Operando synchrotron XRD experiments (not shown) revealed only subtle structural changes in $Na_2Ti_6O_{13}$ during the entire lithiation process explored. Zero expansion is directly related to the long-life properties of this anode.

Lithiated compounds with x = 0.8 and 1.7 were studied at the high-resolution neutron powder diffractometer SPODI (λ = 1.5483(1) Å). Lithium was tracked down using difference Fourier synthesis maps of the $Na_2Ti_6O_{13}$ structure (fig. 1 (a)), in which Li atoms were not included for x = 0.8 (fig. 1 (b)) and

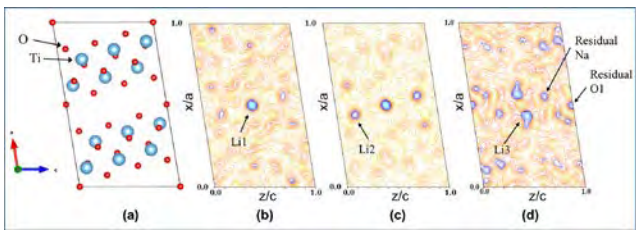

Figure 1: Two-dimensional difference Fourier synthesis maps from NPD patterns with the $Na_2Ti_6O_{13}$ framework (a), revealing Li1 (y/b=0.5), Li2 (y/b=0.5) and Li3 (y/b=0.0) positions.

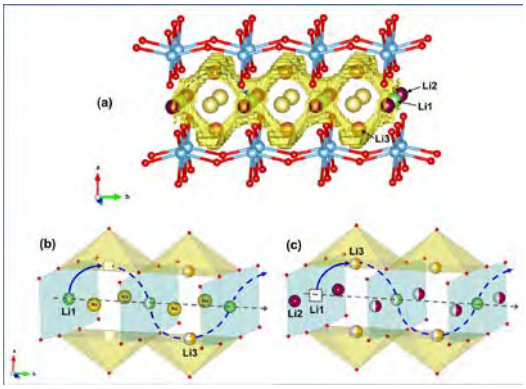

Figure 2. Lithium motion in $Li_xNa_2Ti_6O_{13}$. The Li sites and diffusion pathway as deduced from BVS isosurfaces of mobile lithium ions (yellow) overlaid on the structure along [010] (a). Schematic view of correlated Li motions produced in x = 0.8 (b) and x = 1.7 (c). Na atoms have been omitted in (c) for clarity. Key: Octahedral Ti (blue); O (red); Li1 (green); Li2 (red); Li3 (gold).

x = 1.7 phases (fig. 1 (c) and (d)). For $Li_{0.8}Na_2Ti_6O_{13}$ a single lithium Li1 was detected in the y/b = 0.5 section at special position 2c (½, ½, ½). For $Li_{1.7}Na_2Ti_6O_{13}$ apart from Li1 additional lithium Li2 and Li3 were observed at 4i sites in the y/b = 0.5 and 0.0 section, respectively.

During the first insertion stage (centered at 1.3 V) lithium is allocated in square planar LiO_4 2c (Li1) sites, minimising electrostatic repulsion with Na ions. During the second lithium uptake (centered at 1.1 V), Li ions pass from 2c to empty 4i (Li2) sites of y/b = 0.5 planes, near Ti^{3+} cations as inferred from 7Li MAS NMR spectroscopy (not shown). Li ions occupy three fourfold coordinated sites with reasonable Li^+ - O - Ti^{3+} bond distances, while Na cations remain at eightfold coordinated positions near Ti^{4+} cations. ^{7}Li MAS-NMR recorded at increasing temperatures suggests that Li ions move along sinusoidal paths to reduce Li-Na electrostatic interactions. Li mobility along the b-axis is favored by partial occupation of interstitial 4i sites (Li3) located at both sides of Na cations in y/b = 0 planes (fig. 2).

The most probable - Li1(2c) → Li3(4i) → Li1(2c) - conduction paths were deduced in lithium inserted samples. However, the formation of Li pairs at y/b=0 planes (Li2 sites), where Li ions are located near Ti^{3+} cations, reduce the number of mobile Li ions that participate in the conduction processes. The resultant Li-Li and Li-Na proximity limits insertion to ca. 2 Li ions per structural formula

[1] A. Kuhn, et al., Comprehensive investigation of the lithium insertion mechanism of the $Na_2Ti_6O_{13}$ anode material for Li-ion batteries, J. Mater. Chem. A 2, 443 (2018)

Phase transitions and thermal displacements in superionic Li_2Te and Li_2Se

J. Schneider[1], T. Schröder[2], M. Hoelzel[2], O. Kluge[3], W. W. Schmahl[1], O. Oeckler[4]

[1]Department of Geo- and Environmental Sciences, Crystallography Section, Ludwig Maximilian University Munich, Munich, Germany; [2]Heinz Maier-Leibnitz Zentrum (MLZ), Technical University of Munich, Garching, Germany; [3]Institute for Inorganic Chemistry, University of Leipzig, Leipzig, Germany; [4]Institute for Mineralogy, Crystallography and Materials Science, Leipzig University, Leipzig, Germany

Fast Li-ion conductors have been extensively studied for possible applications in batteries. However, the high-temperature behavior of Li-ion conductors has received less attention. In the series of ionic anti-fluorite-type Li_2X compounds (X = O, S, Se, Te), superionic phase transitions were reported for Li_2O and Li_2S, which inspired our investigation of Li_2Se and Li_2Te. Neutron diffraction at elevated temperatures makes it viable to investigate possible superionic phase transitions that are accompanied by anomalies in atomic motions. In particular, diffraction studies reveal lattice parameters, atomic positions and the atomic displacement parameters (spatial distribution parameters) as a function of temperature. Neutron diffraction has important advantages compared to X-ray diffraction in this instance as the X-ray scattering power of Li is weak and as nuclear scattering lengths for neutrons are not angle-dependent and thus do not correlate with atomic displacement parameters.

As Li_2Te and Li_2Se react rapidly with moist air, the samples were enclosed in niobium cans sealed under argon atmosphere. Powder diffraction patterns were collected using a vacuum high-temperature furnace at the instrument SPODI over a scattering angle range up to 160° 2θ at a wavelength of 1.5482 Å. Measurements were carried out up to 800 °C for Li_2Te and 1000 °C for Li_2S.

The data were analysed by Le Bail profile fitting followed by Rietveld refinement. The thermal evolution of the probability density functions of the atoms was described by three different model approaches. First, isotropic atomic displacement parameters were refined, revealing clear discontinuities in their evolution with temperature. At ~ 600 °C (Li_2Te) and ~ 780 °C (Li_2Se), the displacement parameters for Li cations increase abruptly, indicating a superionic transition and a “melting of the Li substructure” (fig. 1). Difference Fourier syntheses in the space group $Fm\bar{3}m$ show strongly anisotropic spatial distribution densities around the Li positions of the cubic site symmetry $m\bar{3}m$. Secondly, the observed relaxation towards an anisotropic 3 m site symmetry was better described by a 4-fold split-atom model, where anisotropic spatial distribution parameters were refined. Abrupt changes in their evolution with temperature are observed. Significantly improved profile refinement residuals support this flexible structure model. Joint probability density function maps demonstrate a thermally increasing delocalisation of Li atoms and yield potential energy distributions (fig. 2). The potential barrier between adjacent Li positions shows an abrupt drop at the superionic phase transition temperature, indicating a significant increase in Li-atom mobility in the corresponding directions. This structure model outperforms a third one that involves an anharmonic Gram-Charlier expansion of thermal displacement parameters up to fourth-order tensors. However, this approach confirms the results of the harmonic split-atom model.

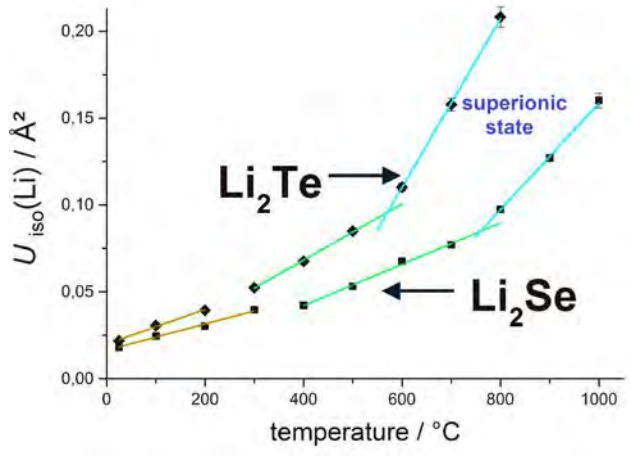

Figure 1: Isotropic atomic displacement parameters for Li in Li_2Te and Li_2Se as a function of temperature.

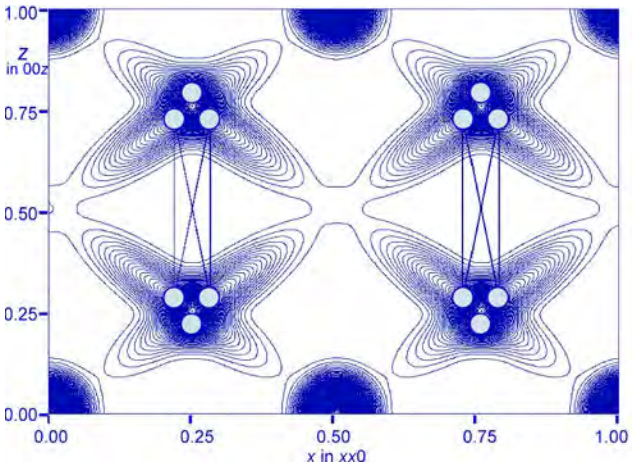

Figure 2: Joint probability density maps for Li_2Te at 800 °C.

[1] J. Schneider, et al., Phase transitions to superionic Li_2Te and Li_2Se – A high-temperature neutron powder diffraction study, atom displacements, probability density functions and atom potentials, Soild State Ionics 325, 90 (2018)

The new hydrogen-bond network and the ferrimagnetic order found in rockbridgeite

S.-H. Park

Department für Geo- und Umweltwissenschaften, Sektion Kristallographie, Ludwig-Maximilians-Universität München, München, Germany

Our interest in 3d transition metal (3d TM) phosphatic oxyhydroxides arises not only from the presence of diverse hydrogen bond (HB) networks, but also their magnetic structures and properties which are, for the most part, unknown. In our recent study, one such 3d TM phosphatic oxyhydroxide (rockbridgeite-type) was extensively characterised using high-resolution neutron powder diffraction (HRNPD) techniques (Instrument SPODI at MLZ) combined with Mössbauer, dielectric spectroscopy, and magnetic measurements [1]. By finding four crystallographically independent hydrogen positions, we were able to suggest the new structural formula $Fe^{2+}Fe^{3+}_{3.2}(Mn^{2+},Zn)_{0.8}(PO_4)_3(OH)_{4.2}(HOH)_{0.8}$ for this compound. The subtle structural analyses obtained revealed a honeycomb-like HB network (fig. 1) as possible pathways for conducting H^+. This is supported by the bond valance energy landscapes of H^+. HBs are highly polarisable and susceptible to stimulated ion hopping through the application of electric fields in the kHz range. Indeed, the real part of dielectric permittivity and the loss factor of rockbridgeite dramatically increase above 300 K. The relaxation process in 250 - 300 K may be attributed to fast local motion of H^+ over the split sites H3 in a short distance of 0.64 Å. The steep increase in dielectric loss from 300 K points to the H^+ conductivity over the entire HB network. Such a high protonic dynamic disorder under ambient conditions plays an essential role in electrolysers for fuel cells, pseudo-supercapacitors, as well as photocatalyses for water splitting.

On the other hand, the title structure is built up by unusual octahedral doublet, triplet, and quartet clusters of Mn^{2+}, Fe^{2+}, and Fe^{3+}, responsible for complicated magnetic ordering and interactions. Two anomalies in the heat capacity curve (C/δT) were clearly seen near 7 K and 81 K. The negative Curie-Weiss (CW) point at -122.5 K from magnetic

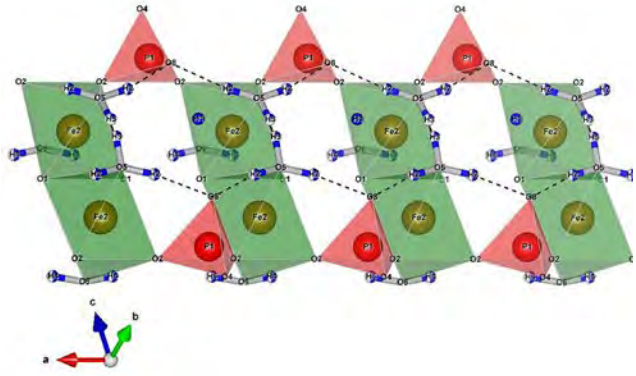

Figure 1: A honeycomb-like HB network (dashed line) of rockbridgeite runs through half-occupied [$Fe3O_6$] octahedral chains.

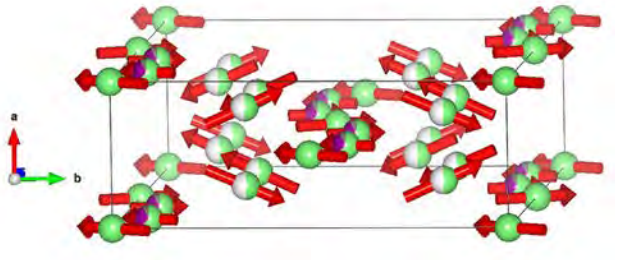

Figure 2: The ferrimagnetic spin order (red arrows) of three sublattices Fe1 (filled), Fe2 (mixed occupation), and Fe3 (half-filled) in rockbridgeite.

susceptibility measurements is typical for a paramagnetic to ferrimagnetic transition. Rietveld refinements of nuclear and magnetic structures with HRNPD data at 25 K with the propagation vector k = (0,0,0) confirmed the correct magnetic space group Cm'c'm (fig. 2). As a result, we obtained a new extremely complex ferrimagnetic order with net magnetisation in [001].

This study demonstrates that rockbridgeite-type compounds and further 3d TM oxyhydroxides deserve intensive investigation in the quest to develop noble protonic conductors and correlated matter (fig. 3). Thus, the use of HRNPD is indispensable in an investigation of complex prototype geomaterials as they rarely occur in ideal forms of high-quality, large single crystals.

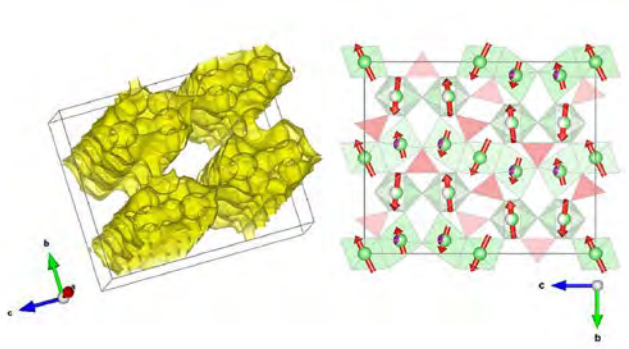

Figure 3: HRNPD data analyses (SPODI) gave rise to new findings about rockbridgeite with a honeycomb-like hydrogen bond network to provide pathways for conducting protons, as shown by isosurface of bond valance energy landscapes of H^+ at $V_{pot.E}$ = -1.2 eV (left). Besides, an extremely complex ferrimagnetic order in the title compound could be determined for the first time (right).

[1] B. Röska, et al., Determination of the hydrogen-bond network and the ferrimagnetic structure of a rockbridgeite-type compound, $Fe^{2+}Fe^{3+}_{3.2}(Mn^{2+},Zn)_{0.8}(PO_4)_3(OH)_{4.2}(HOH)_{0.8}$, J. Phys.: Condens. Matter 30, 235401 (2018)

Opening and closing the “bars” of an antimatter “cage”

E. V. Stenson[1,2,3], J. Horn-Stanja[1], S. Nißl[1,2], U. Hergenhahn[1,4], M. Singer[2], H. Saitoh[1,5], T. Sunn Pedersen[1,6], J. R. Danielson[3], M. R. Stoneking[7], M. Dickmann[2], C. Hugenschmidt[2]

[1]Max Planck Institute for Plasma Physics, Greifswald and Garching, Germany; [2]Heinz Maier-Leibnitz Zentrum (MLZ) and Physics Department E21, Technical University of Munich, Garching, Germany; [3]University of California, San Diego, La Jolla, California, USA; [4]Leibniz Institute of Surface Engineering (IOM), Leipzig, Germany; [5]The University of Tokyo, Kashiwa, Japan; [6]University of Greifswald, Greifswald, Germany; 7Lawrence University, Appleton, Wisconsin, USA

The nucleation and trapping of small-Debye-length electron-positron (e-/e+) plasmas would enable novel studies of “pair plasmas”, in which all particles have the same mass. Such plasmas dominated the early Universe 1 - 10 s after the big bang, are still found in astrophysical settings, and are predicted to have significantly different properties from electron-ion plasmas. A fundamental challenge is to develop a scheme that allows efficient injection and subsequent confinement of both species.

Toroidal traps with closed magnetic field lines are commonly used to confine positive and negative charges simultaneously, in the same volume, at plasma densities. However, injection from outside is inhibited by the same physics that traps particles inside. (Electron-ion plasmas are typically ionised within the device.) Furthermore, the relatively small margin between the available e+ flux and the amount needed to form a plasma necessitates techniques that strictly minimise losses. Therefore, e-/e+ plasma experiments require efficient injection methods to be developed and verified. It must also be established how long injected positrons will remain trapped and what factors limit their confinement. Both of these key issues were recently addressed at the NEutron-induced POsitron source MUniCh (NEPOMUC) at FRM II.

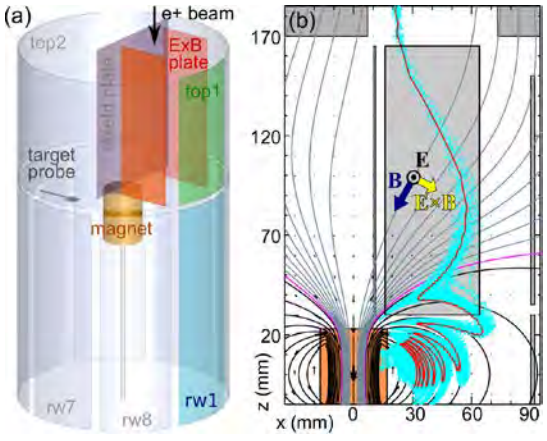

Figure 1: (a) The experiment set-up includes a supported neodymium magnet, a cylindrical outer wall divided into segments, and rectangular electrodes on either side of where the positrons enter. (b) A typical simulation of lossless transport from magnetic field lines connecting to the beam line (top), across field lines that intersect the wall, and into the confinement region (i.e., field lines that intersect only the magnet). Points along the trajectories of 100 particles – launched from the same starting point with a realistic range of velocities and propagated for 0.6 µs – are projected onto the xz plane (cyan dots), as is a single trajectory for a particle whose perpendicular and parallel velocities are near the median of the distribution (red line). Arrows indicate the direction of the single-particle drift (ExB) across the magnetic field (B) due to application of the electric field (E).

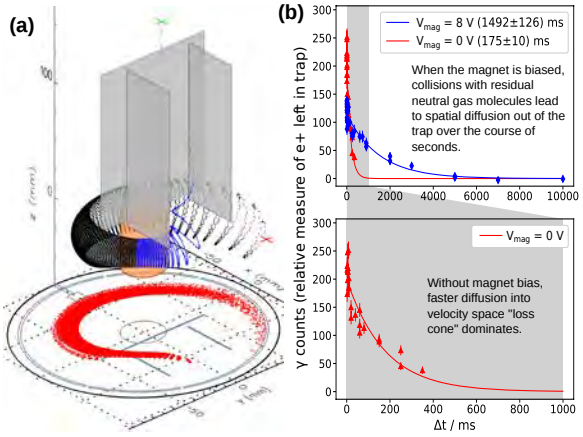

Figure 2: In panel (a), a simulation shows the trajectory of a single positron (blue/black dots) that has been successfully injected from the beam line into the prototype magnetic dipole trap, as well as the projection onto the bottom of the simulation box of the midplane crossings (red dots) of the entire positron beam. When the injection settings are left on steady-state, a positron is confined for a little less than a full orbit around the magnet (typically 10 - 20 µs), as shown here. Panel (b) shows, however, that positrons that are in these temporarily trapped orbits when the injection potentials are switched off (at Δt = 0) can remain trapped for seconds – corresponding to hundreds of thousands of toroidal transits.

Ultimately, we will confine pair plasmas in the dipole magnetic field of a levitated superconducting coil; for initial proofs of principle, we used a prototype trap based on a permanent magnet (fig. 1 (a)). By strategically biasing electrodes near the edge of the confinement region, we tailor the electrostatic potential so that positrons drift inward, across magnetic field lines (fig. 1 (b), 2 (a)). We then turn off the injection potentials to trap positrons inside (fig. 2 (b)). Both of these processes are well understood, thanks to single-particle simulations that reproduce and extend the experimental results, and both work remarkably well. The NEPOMUC beam can be guided into the trap with 100% efficiency, and confinement after injection has been switched off lasts for hundreds of thousands of toroidal transits. Identification of the primary loss channels (diffusion in both position and velocity spaces, due to scattering off residual gas) indicates that confinement time can be expected to improve by 1-2 orders of magnitude in the levitated dipole trap. Thus, essential methods for producing a confined e-/e+ plasma in a laboratory magnetosphere have been established.

[1] E. V. Stenson, et al., Lossless positron injection into a magnetic dipole trap, Phys. Rev. Lett. 121, 235005 (2018)

[2] J. Horn-Stanja, et al., Confinement of positrons exceeding one second in a supported magnetic dipole trap, Phys. Rev. Lett. 121, 235003 (2018)

Small-angle neutron scattering and in situ UV/Vis absorption spectroscopy

J. E. Houston[1], E. A. Kelly[2], R. C. Evans[3]

[1]Jülich Centre for Neutron Science (JCNS) at MLZ, Forschungszentrum Jülich GmbH, Garching, Germany; [2]School of Chemistry and CRANN, University of Dublin, Trinity College, Dublin, Ireland; [3]Department of Materials Science and Metallurgy, University of Cambridge, Cambridge, United Kingdom

The ability to observe chemical processes simultaneously via small-angle scattering is highly desirable for a deeper understanding of biological and soft matter systems. This is particularly crucial for dynamic systems in order to ensure sample stability, purity, chemical conditions, and for those cases where it is not possible to perform further measurements or characterisation on intermediate states ex situ. However, while such environments are becoming almost mainstream at large scale X-ray sources, they remain rare at neutron facilities.

Consequently, as part of a larger sample environment development project at KWS-2, which already includes in situ dynamic light scattering and Fourier infrared spectroscopy, we have recently developed a set-up for in situ UV/Vis absorption spectroscopy and light irradiation. A proof-of-concept investigation was undertaken to provide mechanistic and kinetic insights into the photoisomerisation and self-assembly of a novel photoresponsive azobensene-containing surfactant (AzoPS), see fig. 1. We investigated the time-dependent self-assembly of the different photoisomers of AzoPS using small-angle neutron scattering (SANS). The light sources for photoisomerisation were high powered UV (λ = 365 nm) and blue (λ = 450 nm) light emitting diodes. It was shown that the incorporation of in situ UV-Vis absorption spectroscopy with SANS allows the scattering profile, and hence micelle shape, to be correlated with the extent of photoisomerisation in real-time. It was observed that AzoPS could switch between wormlike micelles (trans-native state) and fractal aggregates (under UV light), with changes in the self-assembled structure arising simultaneously with changes in the absorption spectrum. Wormlike micelles were able to be recovered within 60 seconds of blue light illumination.

To the best of our knowledge, this is the first time the degree of AzoPS photoisomerisation has been tracked in situ through combined UV-Vis absorption spectroscopy-SANS measurements.

This combined UV-Vis/SANS approach could be extended to various other systems to allow monitoring of their self-assembly process, where the only requirement is the presence of a characteristic absorption spectrum.

[1] E. A. Kelly, et al., Probing the dynamic self-assembly behaviour of photoswitchable wormlike micelles in real-time, Soft Matter 15, 1253 (2019)

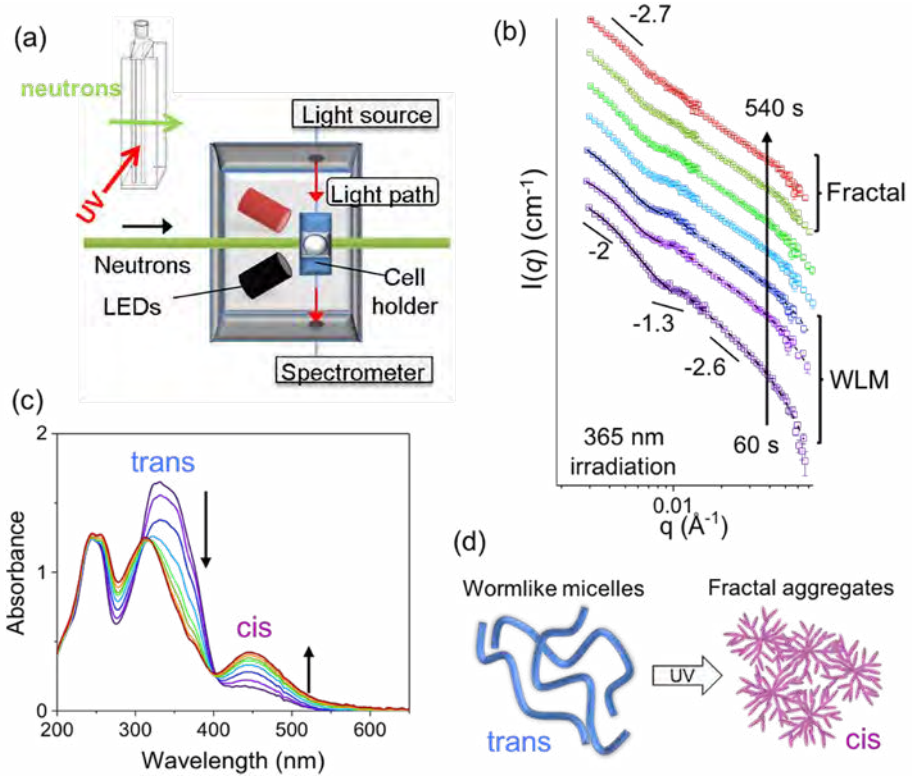

Figure 1: Self-assembly behaviour of AzoPS in D_2O (0.2 mmol L^{-1}) upon trans-cis photoisomerisation. (a) Schematic representation of the SANS/spectrometer set-up. (b) SANS scattering profiles as a function of UV irradiation time. (c) In-situ UV-Vis absorption spectra upon UV-irradiation. (d) Schematic representation of the wormlike micelle to fractal aggregate transition.

Thermal neutron imaging at NECTAR

T. Bücherl[3], H. Ehrenberg[1], M. Knapp[1], M. Makowska[2,5], M. Schulz[4], R. Schütz[4], S. Zimnik[1]

[1]Institute for Applied Materials - Energy Storage Systems (IAM-ESS), Karlsruhe Institute of Technology (KIT), Eggenstein-Leopoldshafen, Germany; [2]Heinz Maier-Leibnitz Zentrum (MLZ), Garching, Germany; [3]Technical University of Munich, ZTWB Radiochemie München RCM, Garching, Germany; [4]Heinz Maier-Leibnitz Zentrum (MLZ), Technical University of Munich, Garching, Germany; [5]University of Bayreuth, Bayreuth, Germany

The upgrade of NECTAR for thermal neutron imaging is making great progress. NECTAR was originally set-up as a radiography and tomography facility using fission neutrons for scientific and industrial applications. It shares the available beam time with the beam line for medical applications (MEDAPP), located on the same beam tube SR10. In 2016, a major upgrade was initiated by a project funded by BMBF (project number 05K16VK3) extending the range of applications through a thermal neutron spectrum.

Hitherto, the converter plates, in combination with a permanent 10 mm thick B_4C-filter, have provided a fission neutron spectrum with a minimised contribution from thermal neutrons for measurements. As a first step, this filter was dismantled and reinstalled on a moveable unit. This provides the option of fission neutrons (i.e. with converter and filter) or thermal neutrons (i.e. without converter and filter) for the experiments. For the latter, a preliminary removable fast shutter and a beam tube lined with B_4C rubber material minimise the possible activation of components in the MEDAPP-room when guiding the thermal neutrons to the NECTAR facility. In 2019, both will be replaced by refined components specially designed for quick and easy installation.

A motor driven beam limiter at the NECTAR facility allows the beam area to be adjusted to the sample size, thus avoiding unnecessary activation of the sample and equipment by up to 8 x 10^6 cm^{-2}/s^{-1} thermal neutrons at the sample position.

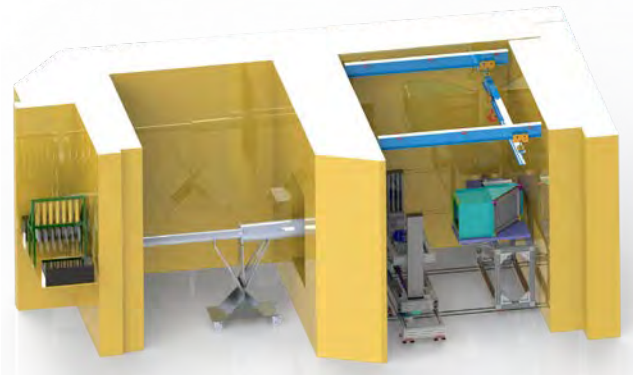

Figure 1: CAD-sketch of the updated NECTAR facility for additionally using thermal neutrons. From left to right: Chamber for filters for manipulating and collimating the neutron beam; Room for medical applications with an optional beam tube for guiding thermal neutrons to the NECTAR facilitiy; NECTAR facility.

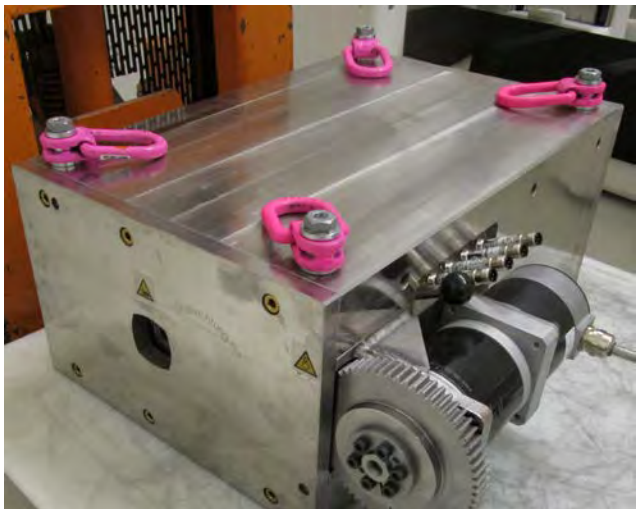

Figure 2: Collimator, ready for installation in the filter chamber, the so-called “Beckenwandnische”.

A newly designed collimator was installed after the last cycle in 2018. The compact design has four collimation units, allowing for adjustment of the L/D value between 200 and 800. Borated steel was the material of choice as it provides good shielding properties for neutrons and gammas whereas the activation of the material is low.

A new detector system, adapted to the new collimator, was designed, offering different fields of view varying between 70 x 70 mm² and 300 x 300 mm². The setup facilitates the quick exchange of cameras, lenses and scintillators to meet the respective requirements for each measurement. The construction has almost been completed and resolutions far below 100 µm will be achievable.

With these parameters, NECTAR will offer a state-of-the-art thermal neutron imaging option. In combination with the possibility of switching easily between thermal and fission neutrons for measurements without moving the sample and/or detector, a unique imaging facility will become available for experiments.

The first friendly-user experiments investigating hydrogen storage in ammonia, visualising root water uptake in heterogeneous soils and petrified eggs of the Cretaceous period have already delivered impressive results.

[1] M. J. Mühlbauer, et al., Neutron imaging with fission and thermal neutrons at NECTAR at MLZ, Physica B 551, 359 (2018)

Single-crystal neutron diffraction in diamond anvil cells at HEiDi

A. Grzechnik[1], M. Meven[1,2], K. Friese[3]

[1]Institute of Crystallography, RWTH Aachen University, Aachen, Germany; [2]Jülich Centre for Neutron Science (JCNS) at MLZ, Forschungszentrum Jülich GmbH, Garching, Germany; [3]Jülich Centre for Neutron Science-2 (JCNS-2), Forschungszentrum Jülich GmbH, Jülich, Germany

A diamond anvil cell (DAC) is the most versatile tool in high-pressure technology. It makes it possible to combine numerous experimental techniques to study various states of matter under compression. Its major limitation for neutron scattering on single crystals is the sample volume, which has to be much smaller than 1 mm^3. We have successfully demonstrated that it is possible to perform single-crystal measurements in a DAC at a modern neutron source such as the FRM II that provides instruments with a monochromatic beam of short wavelength neutrons with high flux [1].

The experiments reported here were performed at the hot neutron diffractometer HEiDi. We constructed a panoramic DAC in which the incident and diffracted beams pass through the gasket material (fig. 1), and not through the diamonds as in the transmission DAC. The major advantage of the panoramic cell is that the data completeness is almost 70%, far superior to the completeness in the transmission DAC. The design and performance were optimised using finite element analysis. The cell is equipped with inexpensive, commercially available diamonds and permits pressures above 10 GPa to be reached, depending on the size of the diamond culets. The cell is compact to ensure its optimal use on a four-circle diffractometer and is compatible with the cryostats available at HEiDi and POLI. It is thus useful for studies of quantum materials, minerals, and hydrogen-bonded compounds at high pressures and low temperatures. The optical access to the sample allows for in situ pressure calibration using ruby luminescence. This cell can also be used for combined neutron diffraction and Raman spectroscopy studies. The pressure can be increased remotely using a He membrane, when only selected reflections are measured at room temperature.

Currently, HEiDi is equipped with a point detector that requires finding reflections to determine the orientation matrix prior to the measurement. We showed that it is possible to determine the orientation matrix using the standard routines for searching for reflections in the reciprocal space even when the DAC is used. An algorithm was developed to correct for absorption from the gasket which is made of a weakly attenuating material such as CuBe, 40HNU-VI, or other alloys. As shown by a benchmark measurement on magnetocaloric $MnFe_4Si_3$, the corrected data are of excellent quality and allow a full structure refinement, including the simultaneous refinement of partial occupancies of different elements indistinguishable by X-ray scattering (e.g., Mn and Fe) and their anisotropic thermal displacement parameters. The maximum pressures, which can be reached in the DAC, are limited by the minimum size of the crystal and the scattering power of the material studied. The smallest crystals, from which the intensity data are currently collected at HEiDi, have a volume of about 0.1 - 0.2 mm^3, depending on the structure factor in the zero-order case F(000). It will be possible to study even smaller crystals when the upgrades to the monochromator and neutron guide at HEiDi have been completed. This will also increase the pressure limit that can be reached in the experiments.

[1] A. Grzechnik, et al., Single-crystal neutron diffraction in diamond anvil cells with hot neutrons, J. Appl. Cryst. 51, 351 (2018)

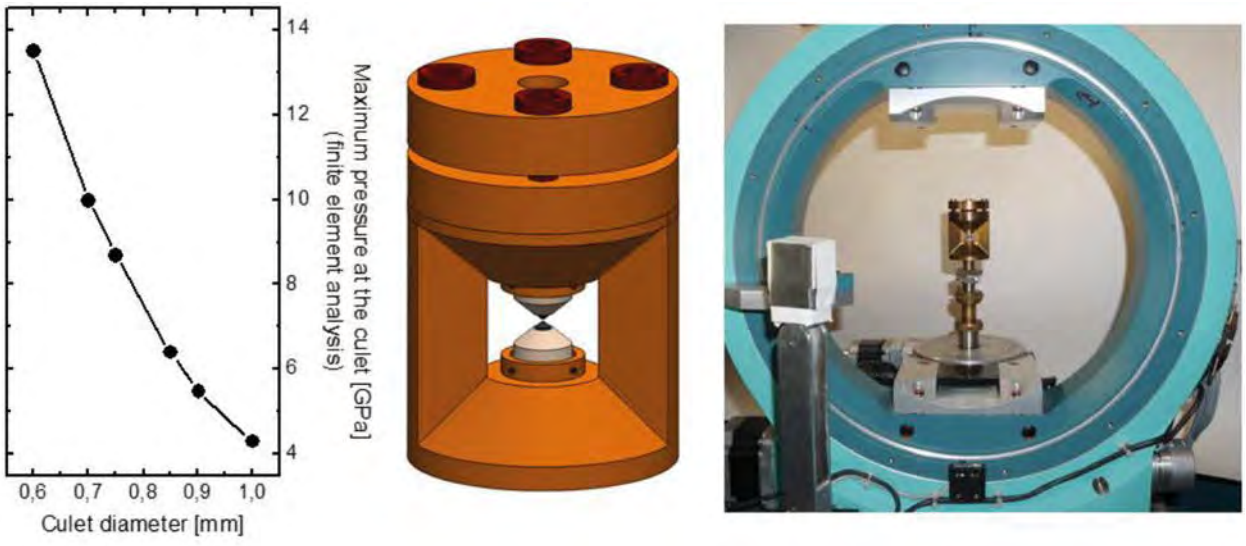

Figure 1: Panoramic diamond anvil cell at HEiDi.

Neutron depolarisation microscopy of the ferromagnetic transition in $HgCr_2Se_4$ under pressure

P. Jorba[1], M. Schulz[2], D. S. Hussey[3], M. Abir[4], M. Seifert[1,2], V. Tsurkan[5,6], A. Loidl[5], C. Pfleiderer[1], B. Khaykovich[4]

[1]Physics Department, Technical University of Munich, Garching, Germany; [2]Heinz-Maier-Leibnitz Zentrum (MLZ), Technical University of Munich, Garching, Germany; [3]Physical Measurement Laboratory, National Institute of Standards and Technology, Gaithersburg, MD, USA; [4]Nuclear Reactor Laboratory, Massachusetts Institute of Technology, Cambridge, MA, USA; [5]Experimental Physics V, Center for Electronic Correlations and Magnetism, University of Augsburg, Augsburg, Germany; [6]Institute of Applied Physics, Chisinau, Republic of Moldova

The novel technique of neutron depolarisation imaging offers the unique possibility to investigate the magnetic properties of bulk materials, even under high pressure and at low temperatures. Hitherto, the spatial resolution of this method has been limited to approx. 500 µm due to the large distance between the sample and the detector required to fit the polarisation analyser into the setup. We have now overcome these shortcomings by installing the first polarised neutron microscope at ANTARES with which a spatial resolution of 100 µm has been achieved.

As shown in fig. 1 (a), the neutron beam was polarised via a V-cavity polariser, after which a parabolic focusing neutron guide was installed to focus the neutron beam on the sample, yielding a strongly increased flux density. Subsequently, the neutron polarisation was analysed using a ^{3}He spin filter and a Wolter optic was used to magnify the image of the sample onto the detector, which was located 3.2 m away from the sample position. This novel approach makes it possible to decouple the spatial resolution from the distance between sample and detector while at the same time magnifying the image of the sample by a factor 4. Currently, a non-optimised setup has been used and the spatial resolution was limited to ~ 100 µm due to imperfections in the Wolter optic which may however be improved by at least an order of magnitude.

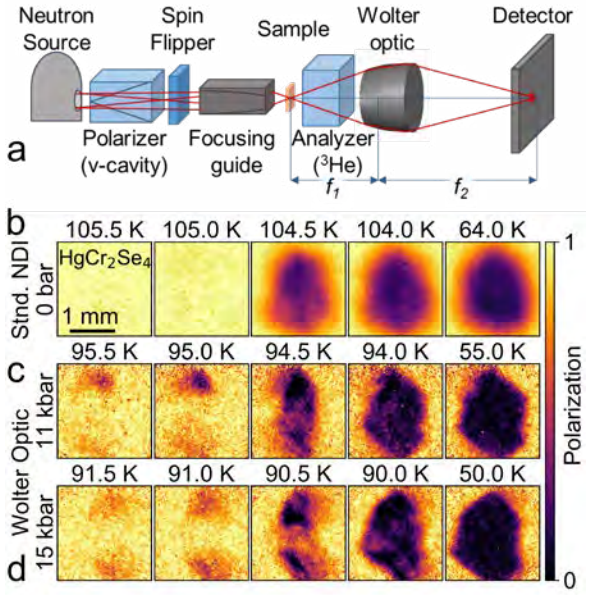

Figure 1: (a) Schematic of the neutron depolarisation microscopy setup; (b) Standard neutron depolarisation imaging data at 0 kbar; Depolarisation microscopy data at 15 kbar (c) and 11 kbar (d).

To demonstrate the potential of the technique, we have investigated the ferromagnetic transition of the chromium spinel $HgCr_2Se_4$ under high pressures up to 15 kbar. The pressure was applied via a CuBe clamp-type pressure cell with a thickness of 12 mm. The sample size was ~ 2 mm. Fig. 1 (b) shows the polarisation images obtained at different temperatures around T_C with a conventional neutron depolarisation setup at ambient pressure. Fig. 1 (c) and (d) show the data obtained with the polarised neutron microscope at 15 kbar and 11 kbar, respectively. The microscopy images clearly show better spatial resolution compared to the standard setup. Despite the additional material of the pressure cell in the beam, the exposure time for the microscopy images was decreased by almost a factor 2. While at ambient pressure a homogeneous transition temperature over the sample is found, inhomogeneities in the depolarisation signal can be observed for the images under high pressure around T_C on a length scale of ~ 100 µm, which was hitherto not possible. At much lower temperatures we again observe a homogeneous depolarisation signal. This inhomogeneity is most likely caused by pressure inhomogeneities induced by the freezing of the pressure medium Fluorinert under high pressure. Moreover, the linear decrease of T_C with pressure at a rate of 0.95 K/kbar from an initial transition temperature of 105 K was confirmed for pressures up to 15 kbar.

These first neutron depolarisation microscopy experiments clearly demonstrate the potential of combining condensing (focusing guide) and image-forming (Wolter optic) devices in polarised neutron imaging to decrease the acquisition time, while at the same time increasing the spatial resolution by up to a factor 10.

[1] P. Jorba, et al., High-resolution neutron depolarization microscopy of the ferromagnetic transitions in Ni_3Al and $HgCr_2Se_4$ under pressure, J. Magn. Magn. Mater. 475, 176 (2019)

Low-loss electrical steels for energy efficient electrical machines

H.A. Weiss[1], S. Steentjes[2], P. Tröber[1], N. Leuning[2], T. Neuwirth[3], M. Schulz[3], K. Hameyer[2], R. Golle[1], W. Volk[1]

[1]Chair of Metal Forming and Casting, Technical University of Munich, Garching, Germany; [2]Institute of Electrical Machines, RWTH Aachen University, Aachen, Germany; [3]Heinz Maier-Leibnitz Zentrum (MLZ), Technical University of Munich, Garching, Germany

When developing and designing efficient electrical machines, a detailed knowledge of the magnetic material behavior of the built-in components is crucial. Manufacturing non-grain oriented electrical steels for the stacked rotor and stator cores of electrical machines has a negative effect on the resulting magnetic material properties. The deteriorated magnetic behavior results from mechanical stress induced by punching the electrical steel laminations. Using the neutron grating interferometry (nGI) setup at the ANTARES beamline of the FRM II, magnetic properties next to the cutting line can be investigated. The information on how punching influences the magnetic behavior helps to reduce costly oversizing and to increase an electrical machine's energy efficiency.

nGI makes it possible to access information about the ultra-small-angle scattering of neutrons in a sample. This information is calculated from dark-field images (DFI) that allow the amount and size of magnetic domains to be spatially mapped, due to the scattering of neutrons on domain walls. In fig. 1, this is shown, by way of an example, for an electrical steel separated by wire-cutting (a) and punching (b). Within the images, a contrast of one is synonymous with no neutron beam scattering, whereas a contrast value of zero implies excessive scattering. Comparing the punched to the wire-cut specimen, a small area along the punched

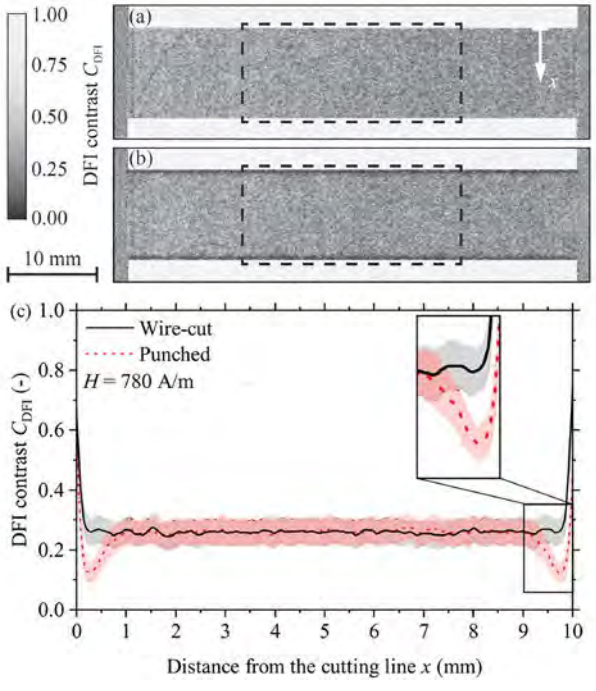

Figure 1: Dark field contrast image for a wire-cut (a) and a punched (b) electrical steel specimen for a field strength of 780 A/m; (c), DFI contrast CDFI plot over the distance from the cutting line x for a wire-cut and punched electrical steel specimen.

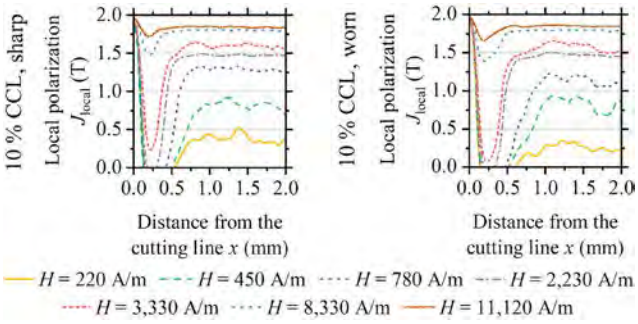

Figure 2: Maximum local polarisation J_{local} over the distance from the cutting line x for electrical steel manufactured with different punching parameters at various field strengths H.

edges with a decreased DFI contrast can be observed. The increased domain wall density next to the cutting line results from a magnetically anisotropic material behavior due to induced stress.

By investigating the DFI contrast CDFI distribution over the specimen width, a quantitative evaluation of the local domain wall configuration and, thereby, the local magnetic state, is possible. In fig. 1 (a) and (b) the dashed boxes indicate the evaluation range in which the DFI contrast profile is calculated. fig. 1 (c) displays the two profiles of the wire-cut and punched specimens discussed above. While the contrast profile of the wire-cut specimen is homogenous over the specimen width, the DFI contrast profile of the punched specimen has a local minimum next to the cutting line. With increasing distance, the contrast profile of the punched specimen approximates the profile of the wire-cut specimen. Obviously, the manufacturing method used has a significant influence on the local domain wall configuration and, hence, on the global magnetisation.

Calibrating the nGI setup using standardised magnetic measurements allows a local polarisation distribution to be calculated from the DFI. In fig. 2 the extent of elevated tool wear on the magnetic behavior next to the cutting line is shown for several field strengths. Increasing tool wear deteriorated the magnetic properties more substantially, regardless of the specimen magnetisation state. Taking this local magnetic property distribution within the electrical machine design and production process into consideration helps to increase the energy efficiency.

[1] H. A. Weiss, et al., Neutron grating interferometry investigation of punching-related local magnetic property deteriorations in electrical steels, J. Magn. Magn. Mater. 474, 643 (2019)

Low-roughness, transparent, hydrogen-tight sample container for UCN experiments

S. Döge[1,2], J. Hingerl[1,2], C. Morkel[2]

[1]Institut Laue-Langevin (ILL), Grenoble, France, [2]Physics Department, Technical University of Munich, Garching, Germany

The loss mechanisms in ultracold neutron (UCN) converters based on solid deuterium are still poorly understood. In order to enhance our knowledge of them, neutron transmission measurements need to be carried out on deuterium.

We have conceived, constructed and tested a sample container for cryogenic liquids and solids that addresses the issue of surface scattering, see fig. 1. Its highly polished amorphous silica windows, which are the key feature, make it possible to grow a sample with a smooth surface, thereby suppressing the scattering of ultracold neutrons from the sample surface as much a possible. Due to the high rigidity of silica compared to commonly used aluminum windows, the container does not bulge under pressure differentials of 1 to 2 bar. Furthermore, amorphous silica has the advantage of not producing any small-angle scattering of neutrons. This reduces the influence of the container on the deuterium measurement to a minimum. The main challenge in constructing the container was to make it hydrogen-tight at low temperatures. This was achieved by using an indium seal and chamfered aluminum clamps. Careful assembly and leak testing at room temperature ensure a reliable performance at cryogenic temperatures.

Figure 1: Sample container for cryogenic liquids and solids featuring highly polished and transparent windows.

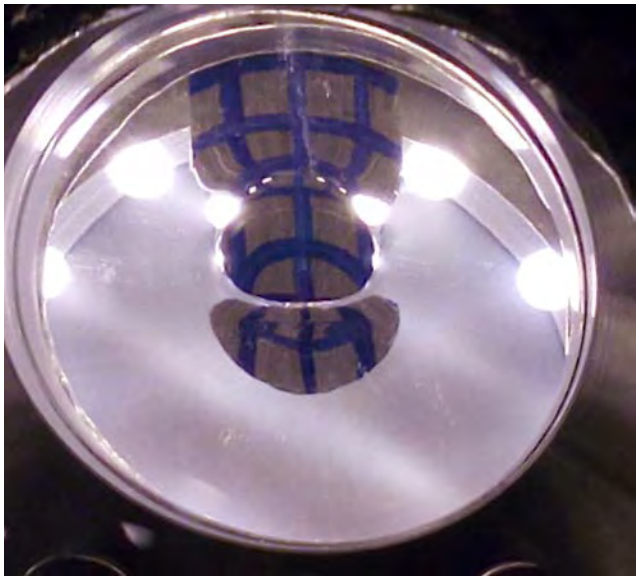

Figure 2: Direct view of a back-lit deuterium crystal at 15 K inside the sample container described here. The cadmium absorber flap in the middle blocks neutrons from traversing the vacuum bubble and prevents false results.

Any sample condensed into or grown inside this sample container can be verified optically before the neutron measurement is started, see fig. 2. To this end, a suspended mirror can be lowered into the neutron beam path in the sample preparation phase. The mirror is then held at a 45° angle to the neutron beam path and can be observed through a vacuum-tight viewport perpendicular to the beam path.

We have used this sample container in recent UCN transmission measurements of liquid and solid deuterium. The scattering cross sections of liquid deuterium are in very good agreement with a model we published in 2015. From the results for solid deuterium, we were able to determine the concentration and size of defects in solid deuterium crystals, which are the subject of a forthcoming publication. These findings will help gain a realistic understanding of the processes inside UCN sources based on solid deuterium.

This new type of sample container will also help other experimenters to obtain scattering data for cryogenic liquids and solids using long-wavelength neutrons without the troubling side effects hitherto commonly encountered with aluminum windows.

[1] S. Döge, et al., A hydrogen leak-tight, transparent cryogenic sample container for ultracold-neutron transmission measurements, Rev. Sci. Instrum. 89, 033903 (2018)

The new detector of the small angle scattering instrument KWS-2 after lifting the detector tube.

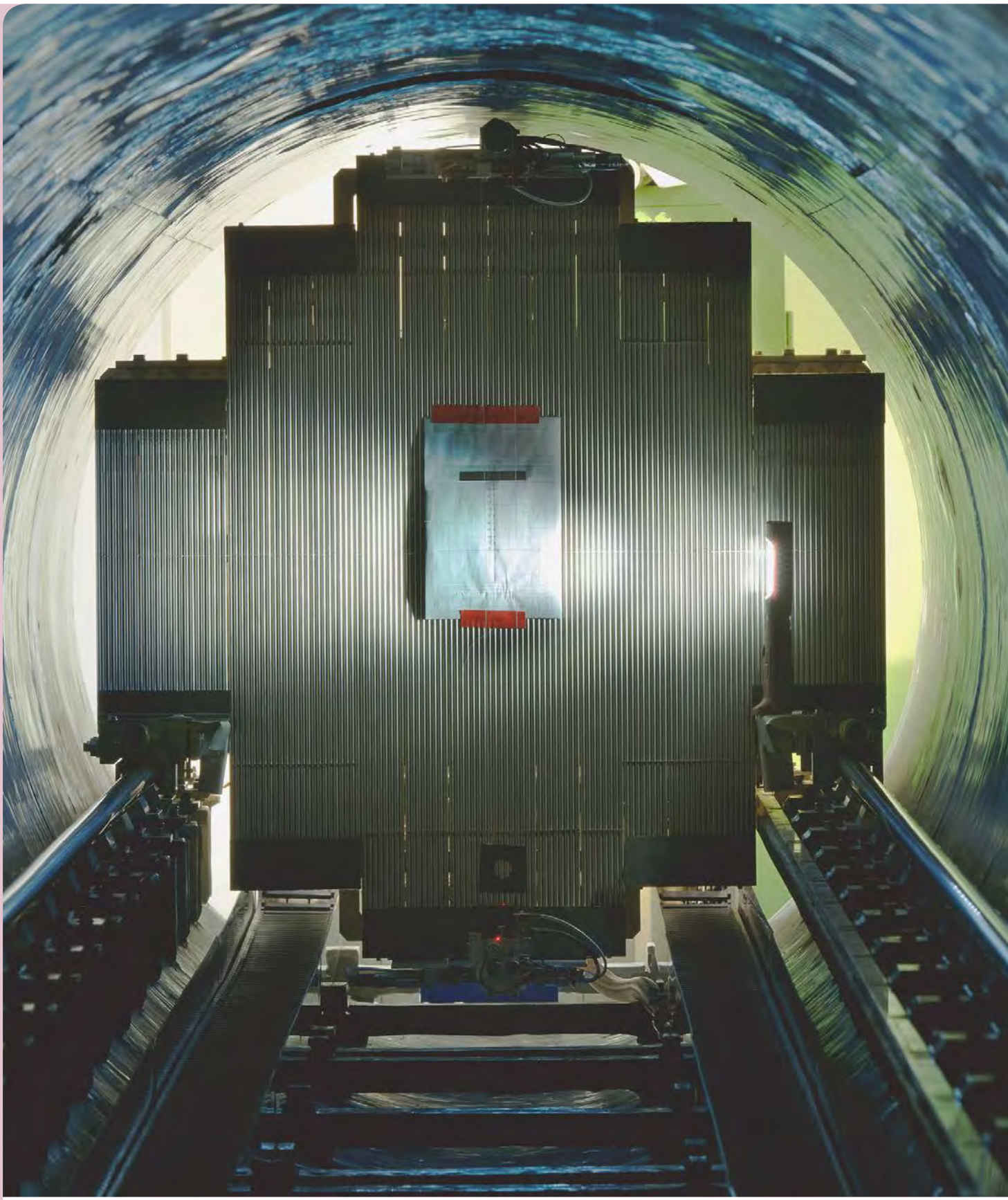

Instrumental Upgrades & Services

News from the instruments

A. Bertin[1,2], A.V. Feoktystov[2], C. Franz[3], D. Gorkov[3,4], M. Hofmann[3], C. Hugenschmidt[3], P. Link[3], M. Meven[2,5], T. Müller[2], V. Pipich[2], Z. Revay[3], M. Seifert[3], L. Werner[3], M. Zamponi[2]

[1]Institut für Festkörperphysik, TU Dresden, Dresden, Germany; [2]Jülich Centre for Neutron Science (JCNS) at MLZ, Forschungszentrum Jülich GmbH, Garching, Germany; [3]Heinz Maier-Leibnitz Zentrum (MLZ), Technical University of Munich, Garching, Germany; [4]II. Physikalisches Institut, Universität zu Köln, Köln, Germany; [5]Institute of Crystallography, RWTH Aachen at MLZ, Garching, Germany

Our instrument suite is continuously evolving, always striving to provide the best performance for its users. The constituents for achieving this are new detectors, neutron optical components such as polarisers and slit systems or sample environments reaching out towards new frontiers in the areas of temperature, pressure or magnetic field parameters.

New ^{3}He bottom-loader cryostat at ANTARES

Ferromagnetic quantum critical materials driven by hydrostatic pressure such as the Kondo lattice CePt or the chromium spinel $HgCr_2Se_4$ are challenging to probe due to the requirement for a complex sample environment (low temperatures, high pressures). The neutron depolarisation imaging setup at ANTARES was specifically designed to investigate these systems and enables us to perform experiments at several different pressures during one beam time. However, for pressure changes the sample has to be removed from the cryostat. Therefore, an efficient cryogenic system is required, which minimizes instrument downtime caused by cooling to base temperature or partial disassembly of the setup.

Recently, a new dedicated ^{3}He bottom-loader cryostat, which is adapted to the requirements for neutron imaging, was prepared by the FRM II sample environment group. For the sample change the cryostat can be mounted on two horizontal beams, as shown in fig. 1. In this position the dewar tail and the heat shields can be removed and the ^{3}He cold head can easily be accessed without disassembling any set-up components. The cryostat has been designed to fit into the 80 mm borehole of the normal conducting magnet available at ANTARES. Cooling a sample such as the pressure cell shown in fig. 1 from 300 K down to base temperature (500 mK) takes approximately 3 h.

Figure 1: The new ^{3}He bottom-loader cryostat in the sample change position at ANTARES. For a test of the cooling performance, a pressure cell was mounted on the sample holder.

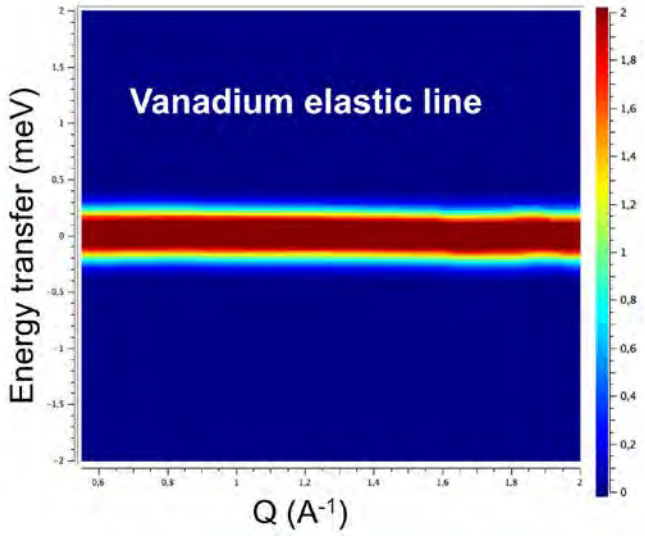

Figure 2: Inelastic neutron scattering spectra of Vanadium, obtained with 250 Hz chopper frequency and 4.2 Å incident neutron wavelength.

New 300 Hz disc chopper at DNS

DNS is a polarised high intensity cold-neutron time-of-flight spectrometer for the study of complex magnetic correlations in frustrated quantum magnets, strongly correlated electron systems, and nanoscale magnetic systems.

The commissioning of the 300 Hz disc chopper system was completed in 2018 and first time-of-flight inelastic user experiments were successfully performed. The received energy resolution of the Vanadium elastic line, achieved with 250 Hz chopper frequency and 4.2 Å incident neutron wavelength, is around 0.25 meV (fig. 2).

To extend the usable wavelength range down to 2 Å, a new radial bender polariser based on Fe/Si m = 3.5 supermirrors was installed, which is expected to increase the flux by a factor of two, with only marginal decrease in polarisation.

Mantid based data reduction for inelastic experiments has been developed by the scientific computing group and its implementation for the position-sensitive detector array covering 1.9 sr will soon reveal the full power of DNS.

STRESS-SPEC - New beam defining optics and sample environment

A new type of radial collimator (FOV = 1 mm) to define the neutron beam dimension impinging onto the sample was recently installed at STRESS-SPEC. This collimator was commissioned in autumn 2018, and both improves and extends the possibilities for defining the gauge volume dimensions at STRESS-SPEC. The advantages of using a radial collimator, as opposed to slits, in the incoming beam are improved flexibility when measuring bulky samples and minimisation of the effects from the divergent neutron beam that cause erroneous strain measurements close to a sample surface.

A quenching & deformation dilatometer funded by HZG has been adapted and commissioned at STRESS-SPEC and SANS-1 (fig. 3). It offers simultaneous high-precision measurements of length changes while heating/cooling or deforming the sample, and thus adds an additional measurement

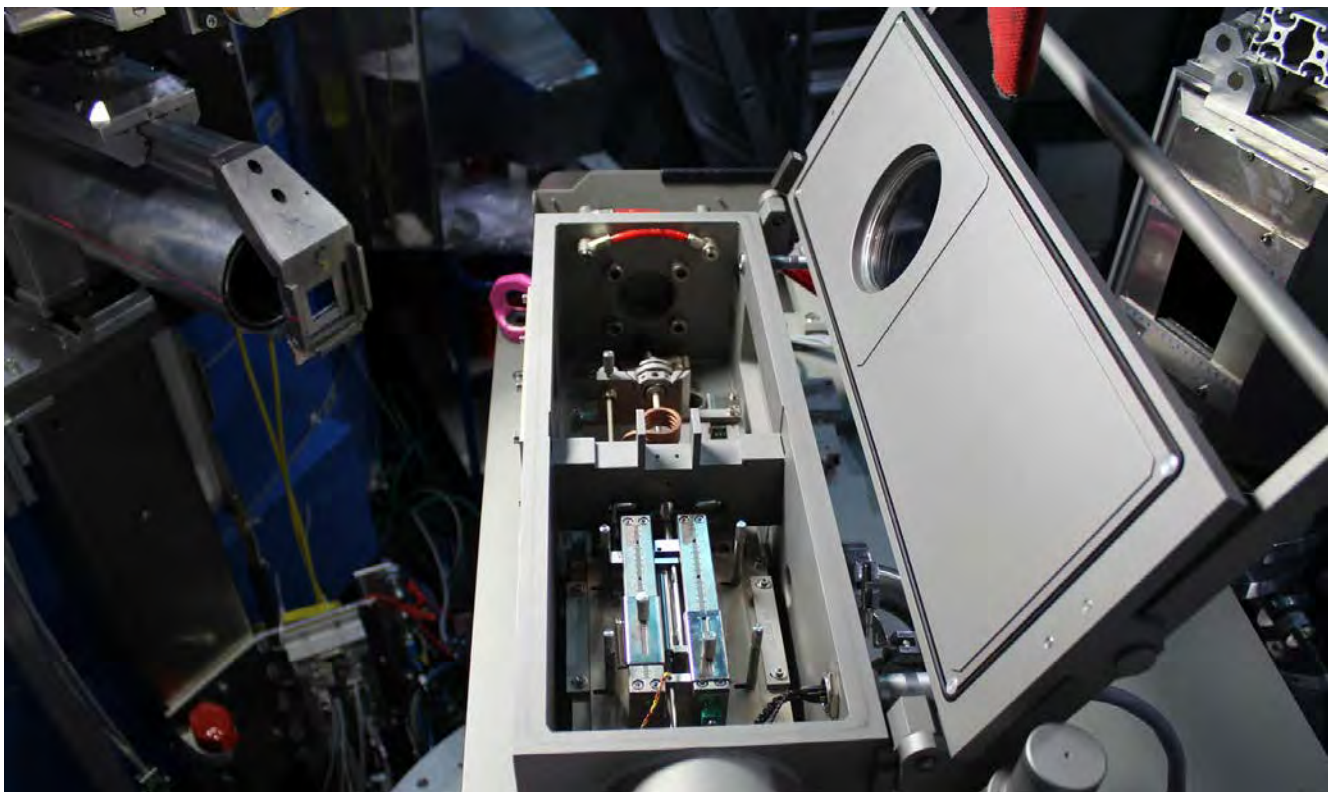

Figure 3: The new quenching & deformation dilatometer at STRESS-SPEC.

quantity that is sensitive to phase transformations. The combination of neutron and dilatometry measurements yields a unique perspective of the microstructural evolution during thermomechanical treatment. The typical cylindrical samples of Ø 5 × 10 mm are inductively heated and gas cooled according to a user-defined linear or exponential cooling rate. The temperature currently ranges from ambient up to 1500 °C with a heating rate up to 4000 °C/s, while the deformation rates for tension and compression tests are between 0.01 and 200 mm/s.

Recent upgrades at the backscattering spectrometer SPHERES

The SPectrometer for High Energy RESolution (SPHERES) at the MLZ is a third generation backscattering spectrometer with focusing optics and a phase-space transform (PST) chopper. It provides high energy resolution with a good signal-to-noise ratio [1]. Several components of the instrument have been upgraded over the years to further improve performance. The PST chopper was renewed in the recent past. The new, more compact one-wing chopper can be operated at the desired speed close to the optimum velocity for the phase space transformation and has new graphite deflector crystals on its circumference with higher reflectivity and mosaicity. Thanks to the increased velocity and improved deflector crystals, the intensity in most detectors had been doubled.

This year, the linear convergent “anti-trumpet” neutron guide was replaced by a focusing guide that is double elliptical in shape (vertical and horizontal). It has been optimised based on McStas simulations, which also took into account the new PST chopper. With the new elliptic guide, a further intensity gain of about 30% was obtained at the sample position.

In addition to the exchange of the focusing guide, a new background chopper has been installed about 2 m upstream of the PST chopper to further reduce background. This will then also allow for a high signal-to-noise setup by eliminating every second pulse, albeit at the cost of the intensity.

New field subtraction coils at RESEDA

One outstanding feature of LNRSE and LMIEZE is the large dynamic range in time resolution. As the lower frequency of the resonant flipper coils is limited to f_{min} = 35 KHz due to the Bloch-Siegert shift for all resonance methods, low Fourier times (and high energy transfers) have to be realised by the field subtraction method [2]. The method is unique to the new longitudinal resonant techniques and consists of an additional solenoid between the radio frequency (rf) flipper coils. Even though the field direction is unchanged and, therefore, beam polarisation is maintained, the coil acts as an effective field subtraction. To minimise the field homogeneity across the beam cross section, the subtraction coils underwent a complete redesign during the course of Wolfgang Gottwald’s Bachelor thesis. Following a simulation of the field profile, keeping RESEDA´s boundary conditions in mind, a design offering good homogeneity in combination with manageable size and weight was chosen. The final layout follows the optimal field shape (OFS) introduced by Zyen & Rem. With a total length of 1 m and five subcoils, in all over 1.3 km of wire were used and more than 2000 windings per coil had to be performed. Both coils on the primary and secondary spectrometer arm are now in active use at RESEDA.

Figure 4: Conventional air-cooled solenoid as a field subtraction coil surrounded by two longitudinal guide field coils on the primary spectrometer arm of RESEDA. The second longitudinal radio-frequency (rf) flipper is shown on the right-hand side.

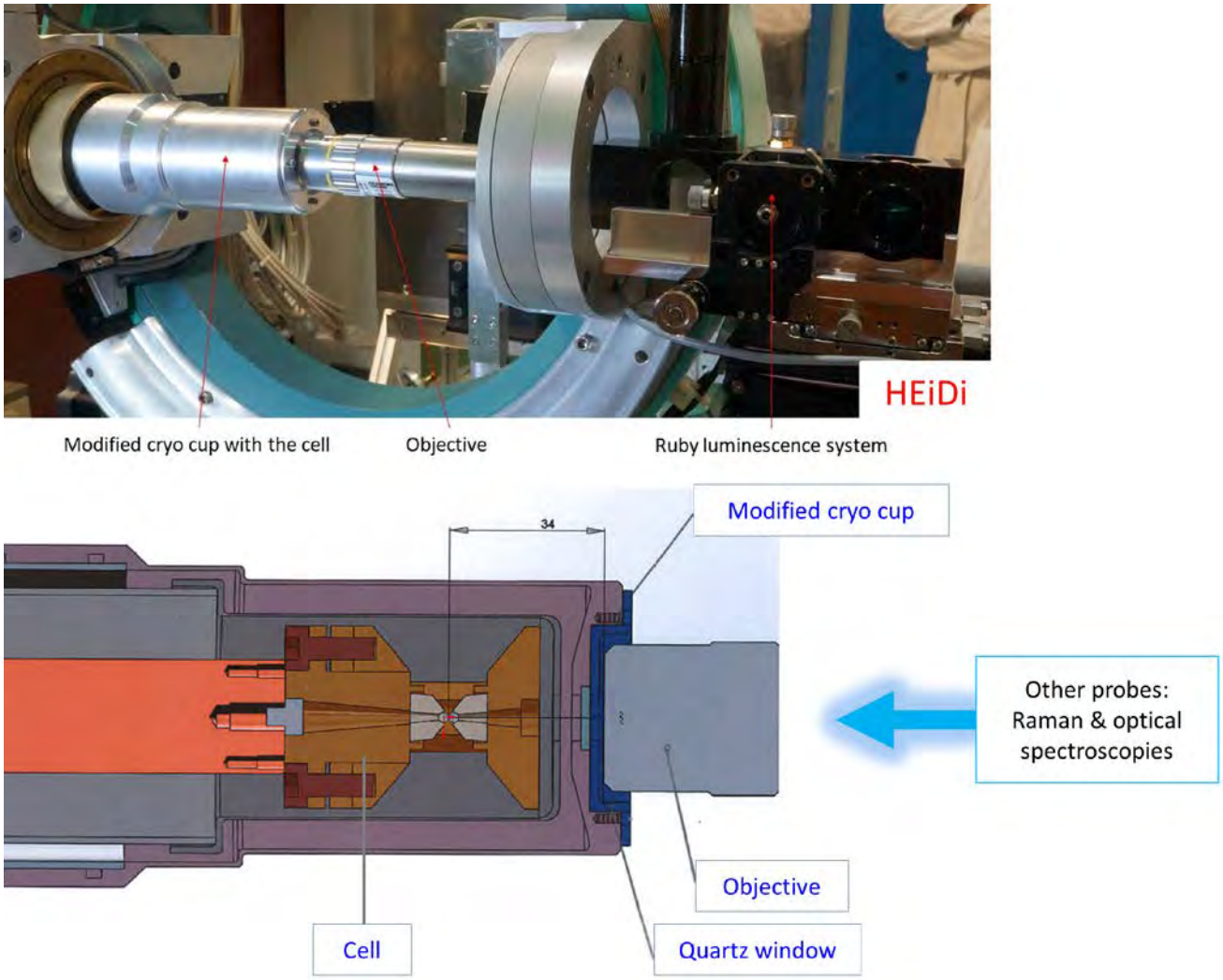

Figure 5: Photo and schematic drawing of the high pressure, low temperature setup at HEiDi.

High temperature and high pressure at HEiDi

The sample environment of the hot single crystal diffractometer HEiDi, operated by RWTH Aachen University and JCNS has recently been extended in two ways. Firstly, for single crystal studies at high temperatures up to > 1000 °C, a new mirror furnace (designed by the TUM sample environment group) has been equipped with a sample chamber which makes it possible to define gas load and pressure, e.g. for studies on ionic conductors relevant in the field of energy research, and has been able to be used routinely since this year.

Secondly, the ongoing BMBF project on high pressure equipment at HEiDi (project no. 05K16PA3) has made a significant step forward as a new Cu220 monochromator was able to be assembled for a short wavelength of λ = 0.8 Å with an expected flux gain of > 50%. In addition, the technical feasibility of combined low temperature – high pressure experiments on HEiDi down to < 5 K has been proven. Further details on that project are available in another contribution to this Annual Report and [3].

KOMPASS answers the first scientific questions using polarisation analysis

KOMPASS is a new polarised cold neutron triple-axis-spectrometer using advanced polarisation and focusing techniques. The instrument works exclusively with polarised neutrons and is specifically designed to study complex magnetic structures and associated dynamics via a zero-field 3D polarisation analysis option. High initial polarisation produced by a unique triple cavity [4], an optional velocity selector yielding high spectral beam purity together with the optimised, compact and flexible design of the instrument render KOMPASS applicable to a variety of scientific problems. Key topics include the investigation of all types of weak magnetic orders, complex (chiral) magnetic structures (e.g. rare-earths, skyrmions, multiferroics), quantum magnets, unconventional superconductors, systems of reduced dimensions and itinerant magnetic systems. At present, KOMPASS is undergoing the initial commissioning phase in the diffraction mode with polarised neutrons. To this end, the detector-unit was directly connected to the sample table, as shown in fig. 6.

After preliminary tests in September 2018, the instrument was equipped with a set of Helmholtz coils for longitudinal polarisation analysis, making it possible to conduct the very

Figure 6: Present status of KOMPASS under commissioning in the polarised diffraction mode.

first scientific diffraction experiments which yielded publishable results on multiferroic materials, frustrated magnets, and unconventional superconductors. Currently, we are focusing on finalising the analyser tower and incorporating the Cryo-PAD and other spherical polarisation analysis options.

The development and installation of KOMPASS is funded by the BMBF through the Verbundforschungsprojekt 05K16PK1.

KWS-1: new detector and polarisation analysis

We have undertaken a number of important upgrades at the KWS-1 small-angle neutron scattering diffractometer. In September 2018, we successfully commissioned a new ^{3}He detector (fig. 7). The new detector consists of an array of 144 ^{3}He tubes interfaced with fast electronics (GE Reuter Stokes, USA). Short, long and medium packs of ^{3}He tubes are stacked to better conform to the KWS-1 detector tube, increasing the active detection area by 20%. Dead-time measurements revealed a loss in detection of around 3% at 1.5 MHz, while resolution remains better than 8 mm. The new system is insensitive to background gamma radiation and its fast response allows us to routinely use a larger source aperture, resulting in a 2.8 factor improvement in counting time. The available q-range comprises 0.007 - 0.7 Å^{-1}.

In line with our development of KWS-1 for the magnetic SANS community, we report on our new, routinely available option of polarisation analysis. An analyser cell with polarised ^{3}He allows one to detect all four scattering cross-sections up to the q_{max} of 0.06 Å^{-1}. The latter can be further extended by moving the analyser stage off center. The cell lifetime achieved in the vicinity of a 3 T horizontal magnet is more than 90 hours.

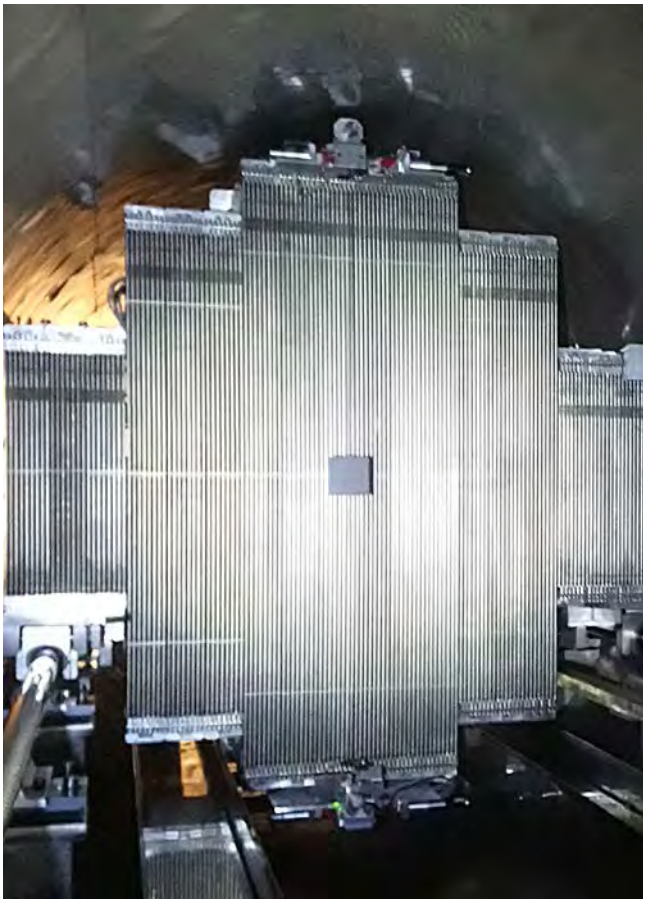

Figure 7: The new ^{3}He detector system in the tube.

Polarised neutron beam and polarisation analysis at the focusing VSANS diffractometer KWS-3

The polarised neutron scattering and polarisation analysis of the scattered beam for very small momentum transfer, down to Q = 3 x 10^{-5} Å^{-1}, is successfully implemented at the focusing VSANS diffractometer KWS-3 operated by JCNS at the MLZ. The operation principle of this instrument – one-to-one imaging of a small entrance aperture onto a 2D position sensitive detector via neutron reflection from the double-focusing toroidal mirror – allows for the effective use of transmission neutron polarising devices: the flipping ratio in the whole polarisation tract (supermirror polariser - adiabatic RF spin flipper - guiding fields – supermirror analyser) approaches 190 (polarisation 99%). As KWS-3 covers almost three decades of momentum transfer, 3 x 10^{-5} Å^{-1} < Q < 2 x 10^{2} Å^{-1}, the polarised VSANS can be used for the analysis of magnetic structures within the characteristic length scale from 30 nm to 20 µm. The polarisation setup is commissioned and ready for user operations. Details regarding new option are shown in fig. 8.

BAMBUS – A new inelastic neutron multiplexed spectrometer for PANDA

Cold neutron triple-axis spectrometers (TAS) are dedicated to the investigation of low-energy excitations in a wide area of condensed matter physics, from quantum magnetism to unconventional superconductors. New engineering solutions are being developed to increase the useful signal on TAS. In

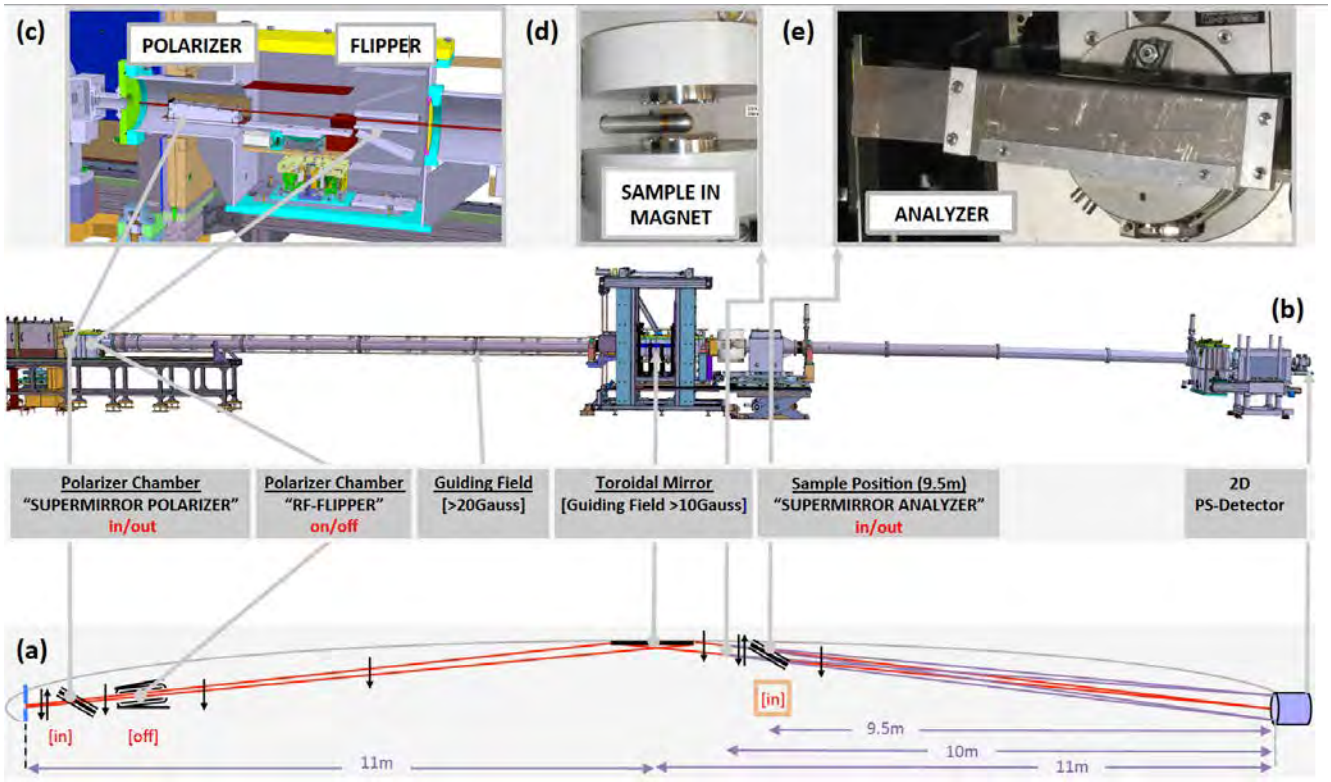

Figure 8: Polarisation and polarisation analysis option description: layout of the VSANS instrument KWS-3: (a) with elements related to polarisation option; (b) 3D model of the instrument; (c) detailed 3D model of the polariser chamber with the super-mirror polariser in the magnetic yoke, radio-frequency flipper and positioning/adjustment system; (d) photo of the 2.2 T electromagnet with cryo-finger as an example of a magnetism–related sample environment; (e) photo of the super-mirror analyser inside the vacuum sample chamber.

order to maintain PANDA as a cutting-edge instrument, the multianalyser Bambus is being constructed at the MLZ, in cooperation with TU Dresden (BMBF grants 05K13ODA and 05K16OD2) and JCNS. The concept is to collect data at a certain energy transfer along a curved path in Q space (total angular range of 40°), with the aim of constructing reciprocal space maps at multiple energy transfers in a reliable, easy-to-use setup without movable axes. This spectrometer is thought to be a complementary option to the normal TAS mode. Thanks to the transmission of the PG analysers, each cassette will be equipped with 5 consecutive vertically focusing analysers with Ef ranging from 3 to 5 meV, each analyser array scattering alternatively up and down. A combined collimator/filter will sit in front of the multianalyser entrance. Two prototypes have been tested, first with the aim of determining the detector types and configuration, and secondly, understanding the source of background and optimising the shielding configuration, respectively. The latter prototype also aimed to prove the capability of Bambus by successfully mapping MnF_2 spin wave excitations. Bambus is expected to be delivered during the summer of 2019. Commissioning of the instrument is planned for the second part of 2020. In parallel, user friendly software for data visualisation and analysis will be developed in collaboration with other TAS multiplexing teams (Camea, Bifrost,…).

Current developments of the N4DP setup

At the PGAA beamline of the Heinz-Maier-Leibnitz Zentrum (MLZ), a Neutron Depth Profiling (NDP) setup, N4DP, is currently being commissioned. The cold neutron beam has the highest flux currently available at any NDP-instrument worldwide.

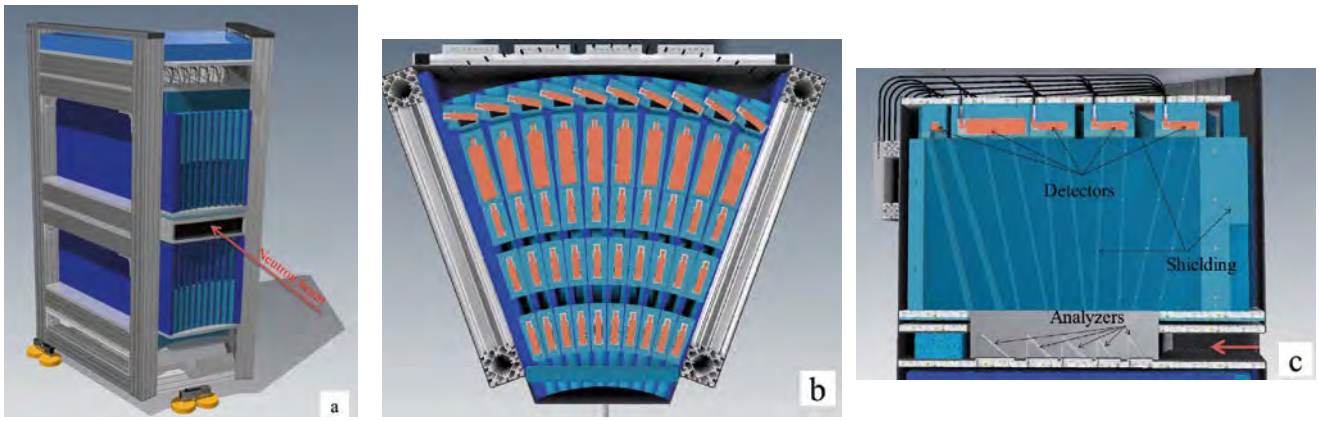

Figure 9: (a) Illustration of the Bambus multianalyser. (b) Detector configuration: the 4.5 meV energy channels equipped with 2 inch diameter detectors will favor intensity, and the 5 meV energy channels with 1 inch diameter detectors perpendicular to the cassette (and tilted by 20°) will favor energy resolution. (c) Side view of one cassette.

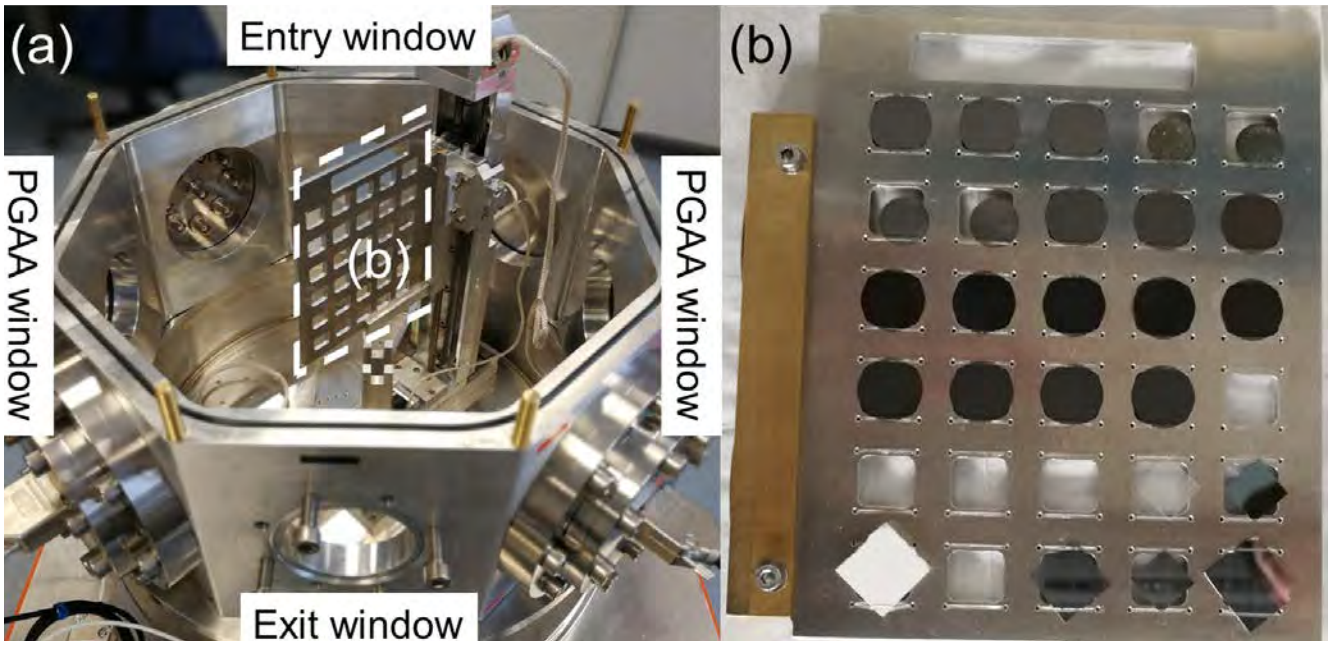

Figure 10: Photograph of the open chamber and of a sample holder.

The current setup already enables high quality NDP [5], and consists of an octagonal vacuum chamber in which detectors, samples and sample positioning are implemented. Samples are mounted as an array in the target plane on highly modular sample holders. Changing samples is facilitated by two remote controlled stepping motors, which make it possible to illuminate every point within an area of 250 x 250 mm^2. A photograph of the open chamber and a sample holder can be seen in fig. 10.

The charged particles produced and emitted by the sample are detected using silicon surface barrier detectors. While, in the past, 300 µm thick detectors were used, in the current version detectors with a thickness of just 100 µm are mounted within the chamber. This reduced thickness increases the signal-to-background ratio immensely. This is due to the fact that most background events are induced by gamma or beta radiation within the chamber.

Not only was the signal-to-background ratio improved in the latest upgrades of the N4DP setup, but the energy resolution was also significantly improved, resulting in possible depth resolutions below 5 nm. This has been achieved using CAEN 1422-AH preamplifiers. The preamplifiers are powered by a custom made circuit board, which also houses a secondary amplification stage. In this secondary stage, signals are amplified further, and are changed from single-ended to differential signals. This greatly reduces signal quality loss when transferring the preamplifier signals to the shaper module.

A typical measurement using the electronics described is shown in fig. 11. The measured sample consists of 10 nm of boron carbide deposited on an aluminum substrate. Since the neutron capture reaction of a boron-10 nucleus has two possible reaction paths, four peaks stemming from the boron are clearly visible. The peaks are near-Gaussian, with a low energy tail, which is due to the energy-loss distribution. The different width of the two low energy peaks at ca. 750 keV and 950 keV, when compared to the high energy peaks at ca. 1420 kev and 1750 keV, is also expected. This is due to the higher specific energy-loss of lithium nuclei, which form the low energy peaks, compared to alpha particles, which produce the high energy peaks. This helps to highlight the good energy resolution achievable with the current system.

Future plans include the implementation of multidimensional NDP using position-resolved silicon microstrip detectors. This will enable full 3D-reconstruction of the isotope distributions in the probed samples. With increased automation of the measurement and control processes at the instrument, implementation of the N4DP setup as a user-facility will become possible in the near future. [5]

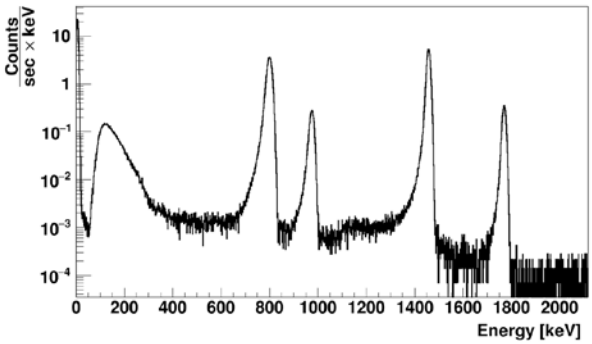

Figure 11: Energy-spectrum of a boron-carbide sample. At 0 keV one can see the electronic noise. The background distribution starts at the trigger threshold at roughly 100 keV. The four higher energy peaks are signals originating from the boron`s neutron capture reaction.

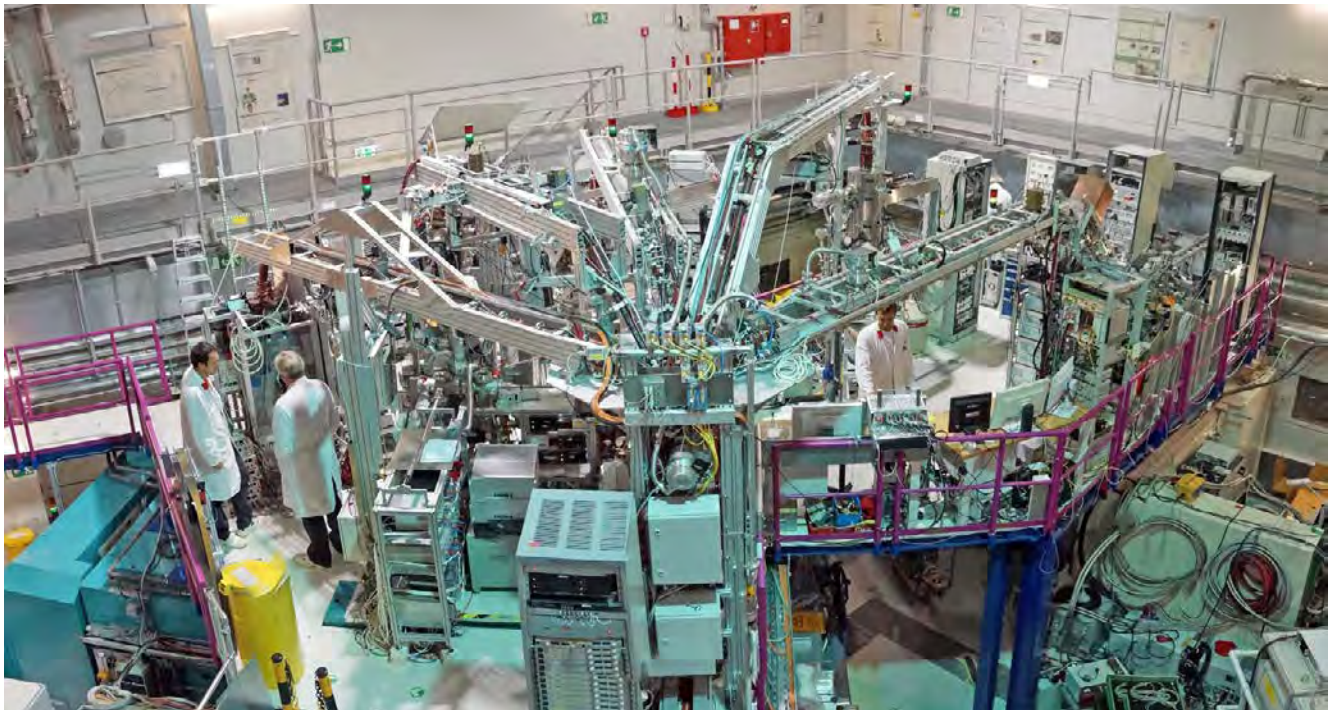

Figure 12: Positron beam facility with five instruments at NEPOMUC.

News from NEPOMUC

The positron beam facility (see fig. 12) at the high intensity positron source NEPOMUC (Neutron induced positron source Munich) provides either a high-intensity primary beam of 1 keV positrons (10^9 positrons per second) or a brightness enhanced 20 eV positron beam with 5 x 10^7 positrons per second. The positron beam is magnetically guided via a positron remoderator and a beam switch to five different positron instruments. For this purpose, 54 solenoid or Helmholtz-like coils generate a static longitudinal field and 56 saddle coils are mounted to create transverse magnetic fields. In total, 110 power supplies are in operation for the magnetic beam transport from the in-pile positron source to the main switch; another 16 items are needed to guide the positrons to e.g. the Coincident Doppler Broadening Spectrometer (CDBS). In 2018, a number of first generation remote controlled power supplies (56 items) were replaced by new, reliable ones with a much lower response time and reduced ripple (~ 3 mA). In addition, more stable high-voltage supplies have been replaced for positron extraction and acceleration at the in-pile positron source.

In order to enhance brightness, a tungsten single crystal W(100) in backreflexion geometry is applied inside the remoderation stage. As part of a measurement campaign, single crystals of SiC, which is being discussed as promising material for positron moderation, have been tested. We succeeded in observing an improved remoderation efficiency (factor of three higher). The high efficiency observed, however, dropped by about one order of magnitude within two days. This effect was attributed to surface contamination of the rest gas in the beam line. In 2019, it is planned to continue systematic studies using different moderating materials and with an improved crystal holder at the remoderation unit of NEPOMUC.

The instrument suite for positron beam experiments at NEPOMUC will be further extended as part of a new TUM project (BMBF 05K16WO7). A new piece of apparatus for Total Reflection High-Energy Positron Diffraction (TRHEPD) experiments is currently set up in an external lab. Before it is transferred to the experimental hall of the FRM II, several tests are being performed, such as complementary Reflection High-Energy Electron Diffraction (RHEED). Rather than replace the positron-electron plasma experiment at the open beam port (OP), it was decided to connect the TRHEPD device to the positron beam line near the present surface spectrometer. For future experiments, this arrangement has the advantage, among others, that the positron beam can simply be switched between these two operational instruments without the need to replace UHV-components. In 2018, the relevant section of the positron beam line was redesigned and adapted in order to connect the TRHEPD device to the high-intensity positron source NEPOMUC.

[1] J. Wuttke, et al., Rev. Sci. Instrum. 83, 075109 (2012)
[2] M. Krautloher, et al., Rev. Sci. Instr. 87, 12 (2016)
[3] A. Grzechnik, et al., J. Appl. Crystallogr. 51, 351 (2018)
[4] A.C. Komarek, et al., Nucl. Instr. and Meth. A 647, 63 (2011)
[5] L. Werner, et al., Nucl. Instrum. Methods Phys. Res. Sect. A 911, 30 (2018)

Committed to successful experiments – the MLZ service groups

G. Brandl[1], J. Krüger[2], P. Link[2], A. Weber[1], J. Peters[2], J. Voigt[1], J. Wuttke[1], K. Zeitelhack[2]

[1]Jülich Centre for Neutron Science (JCNS) at MLZ, Forschungszentrum Jülich GmbH, Garching, Germany; [2]Heinz Maier-Leibnitz Zentrum (MLZ), Technical University of Munich, Garching, Germany

The central service groups constitute the backbone of a successful user operation at the MLZ instruments. Technical instrument upgrades in shape neutron delivery systems, user friendly control systems, efficient detectors and state of the art sample environments are their bread and butter; and all that tailor-made to the indivual needs of 25 operational instruments.

Gas-center-stick for high temperature furnace

In situ measurements in specific gas atmospheres at high temperatures and the fast cooling of samples are in high demand at the MLZ. But even with standard applications, the rapid cooling of the furnace speeds up the sample change time and thus saves measurement time.

The present approach to a fast cooldown of a FRM type high temperature furnace (HTF) has been the norm for many years and involves flushing the furnace body using an inert gas. The main reason for this is a significant decrease in cooldown time compared to the intrinsic cooling rate, resulting in a speed up of sample change time. The disadvantage of this method is a rather low initial temperature of about 500 °C and the restriction to inert gases to protect both the

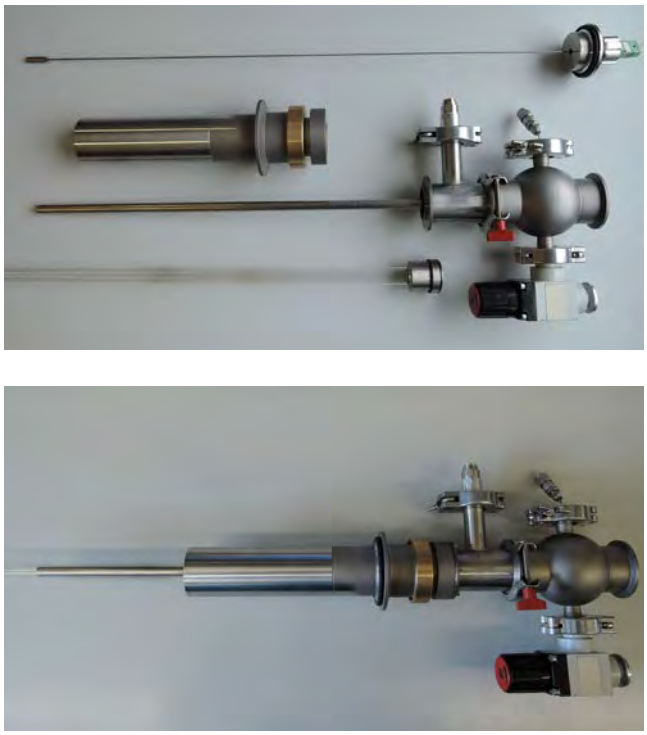

Figure 1: a) gas center stick and b) its modular setup

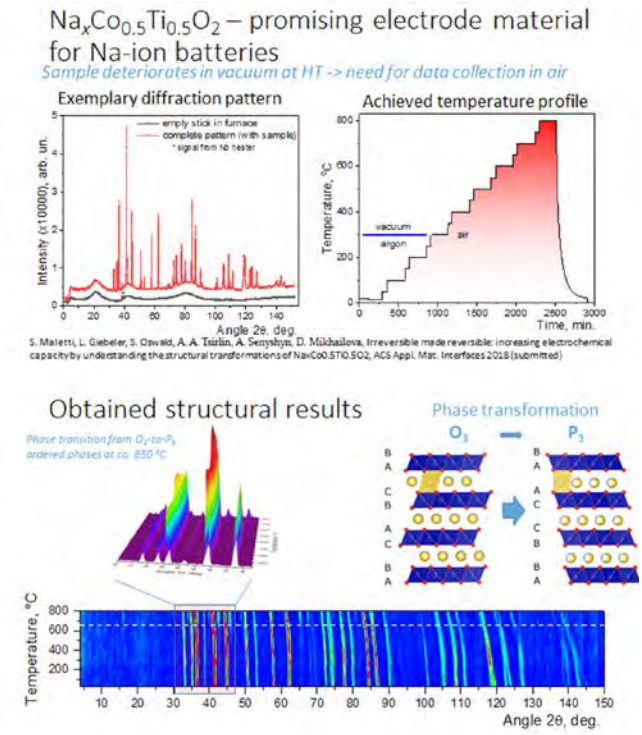

Figure 2: High-temperature structural studies of O_3-$Na_{0.85}Co_{0.5}Ti_{0.5}O_2$ (figures by A. Senyshyn).

Niobium resistive heater element and other furnace components such as radiation shields, turbo molecular pumps, sensors etc. Moreover, there are other applications which make a fast cooldown, or in situ measurements in specific gas atmospheres at high temperatures, desirable.

An example is the study of the precipitation kinetics of malleable alloys throughout the thermo-mechanical processing chain, from formation to the subsequent heat treatment steps. In this case, the experiment aims for rapid and controlled in situ cooling of the alloy. Another application are measurements on ionic conductors, which are widely used as material selective membranes and pumps, sensors and separators for different gases. The crystal structure of these materials is the key that defines their stability and performance. For modern industry-relevant solid state ionic conductors there is an emergent need for studies under experimental conditions close to real operation, e.g. high temperature studies and different gas atmospheres.

In order to make this type of experiment viable, when operating any HTF, our goal was not to modify the standard HTF, but to develop a dedicated center stick (fig. 1 (a)). In addition, a modular setup (fig. 1 (b)) and a suitable choice of material (quartz glass, sapphire, niobium, vanadium) allows

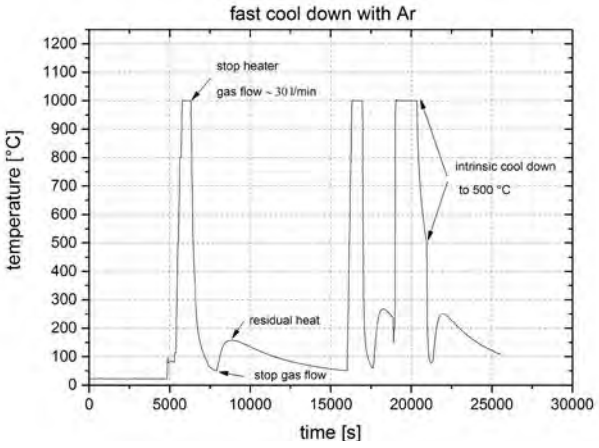

Figure 3: Fast cooldown experiments using Argon gas flow.

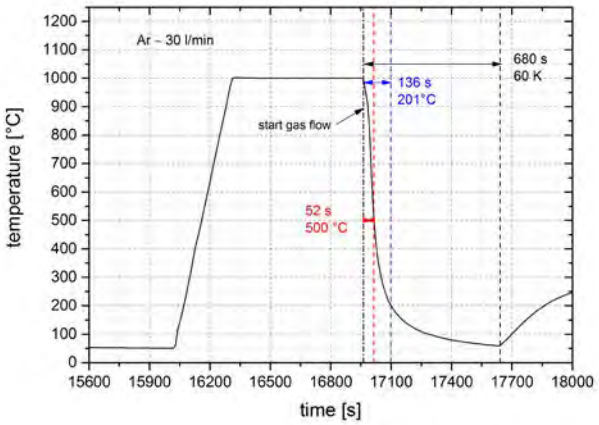

Figure 4: Detail of figure 3: note the short cooldown times realised with 30 l/min Ar flow.

for a set up adaptable to different applications (temperature, static gas, gas flow, quench). A remote controlled gas atmosphere and quench handling is another goal. Two separated volumes, isolation vacuum of the HTF and sample volume which allow an (uncoupled) sample temperature change of the HTF temperature (e.g. the removal of a sample while the furnace is at elevated temperature).

A first user experiment (fig. 2) at the instrument SPODI using a prototype center stick showed promising performance. A 2nd generation center stick was then constructed and used for rapid cooldown (quench) test measurements using Argon gas.

The gas flow capillary and sample space are made from quarz glass. The sample was heated to 1000 °C. The gas flow was enabled when heating had stopped. A rather high flow rate of about 30 liters/min was applied (proof of principle) and cooled the sample within 52 s to 500 °C. A temperature of about 200 °C was reached in 136 s and of about 60 °C in 680 s (see fig. 3 and fig. 4). Fig. 5 shows the comparison between a gas flow rate of 30 liter/min and 1,6 liter/min.

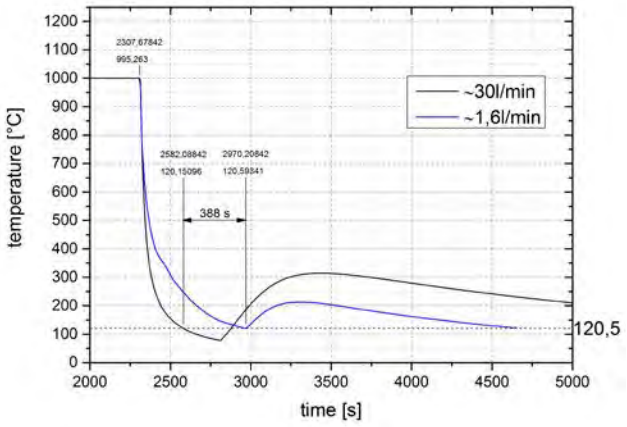

Figure 5: Comparison of different gas flow rates.

Further tests will follow to study the dependence of cooldown time on the mass flow of different gases to improve the performance and integrate the device into the user operation.

Neutron guides in perfect shape – the Neutron Optics Group

Reliable and efficient neutron beam delivery to the instruments is the central task of the neutron optics group. In addition to much routine work, a particular case was neutron guide NL4. It provides the primary beams for SANS-1 (NL4a) and PGAA (NL4b). Upon visual inspection and a subsequent cleaning procedure of the guide, we were able to boost the performance of these instruments by a factor of ~ 2. This was finally confirmed by gold foil activation measurements. A dust layer containing boron on the mirror faces of the guide, probably originating from shielding material containing B_2O_3, was identified as the cause. The material was removed from the vacuum sections.

Besides servicing the existing guided system, the neutron optics group runs a full neutron guide element production line. In view of the upcoming projects, we extended our portfolio to truly curved double elliptic or parabolic guide shapes. Tests of the assembly technique showed very good geometrical agreement of the final mirror surfaces with the specified elliptic shapes. For a 2 m long guide element, the optically measured average deviation of the surface normal from the theoretical value was less than 0.6×10^{-4} rad (r.m.s.). This enables us to produce guide elements for neutron guides with parabolic and elliptic shapes, such as that for the instrument TRISP, when it is transferred to the Neutron Guide Hall East. Self-vacuum-carrying neutron guides are an elegant and space effective way of transporting neutron beams. Nevertheless, such guides with larger cross sections have been subject to failure in the past. Their breaking into numerous shards then also damages the neighboring guide elements, leading finally to the need to exchange the full neutron guide,

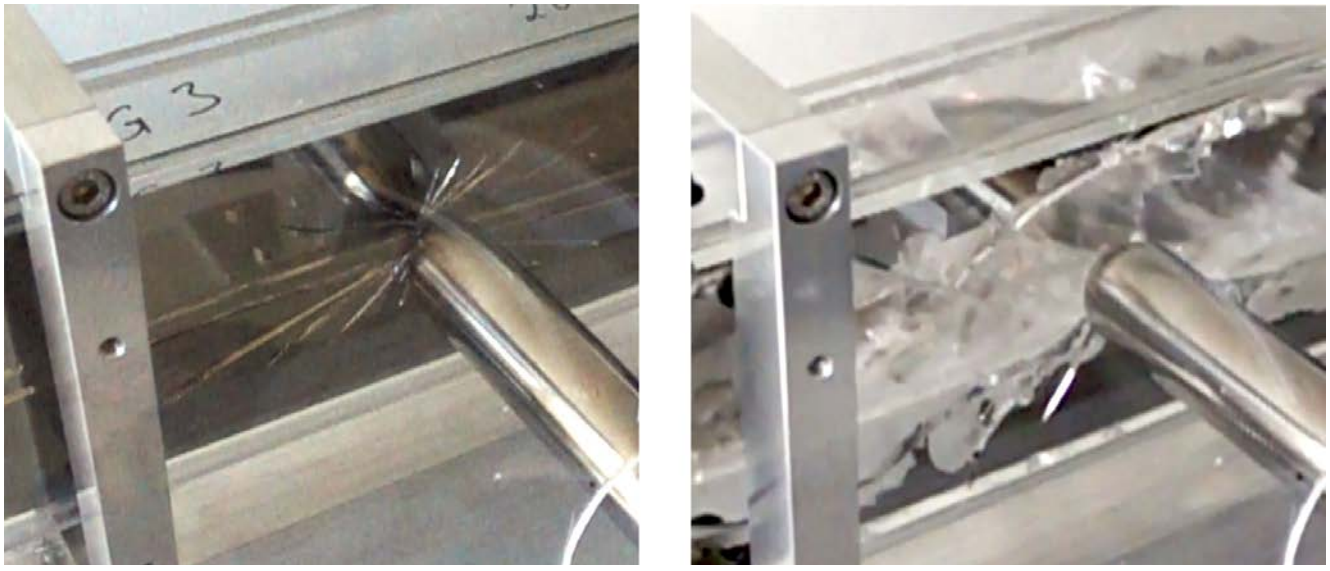

Figure 6: On the right-hand side standard neutron guide element with provoqued implosion, on the left-hand side laminated glass guide element under equivalent conditions.

as was done for NL5, for example. Increasing the glass thickness or using external vacuum housings are the standard ways to avoid this, although weight and space requirements are thereby enhanced. As an alternative potential solution for this problem, we developed neutron guide elements built from laminated glass. A test stand has been built to simulate the implosion of vacuum-carrying guide elements. The right-hand side of fig. 6 shows the moment of implosion of a standard guide element observed by a high speed camera. Under identical conditions, a guide element built from laminated glass remained vacuum tight, although visible cracks appeared (fig. 6 right-hand side). In conclusion, we found that laminated glass is a pathway to safer self-vacuum-carrying neutron guides where space restrictions hinder the usage of external vacuum housings.

Instrument control

The most important result of the work of the instrument control group in 2018: There was no noteworthy instrument downtime due to problems with the instrument control soft- and/or hardware.

The basis for this success was the concerted effort to increase the stability of the hardware and software. In particular, a large number of changes in the NICOS and Entangle systems were made (~1700) to improve software stability. Due to the extension of our testing and continuous integration system, the quality of the software reached a very high level.

Since most instruments have now been switched to NICOS, we started to reap some rewards from the unified infrastructure. A centralised monitoring system, collating the system status from multiple instruments, has been implemented to better provide technicians and the sample environment with essential “one-glance” information. On the other hand, we are now able to focus on the implementation of complementary methods, such as a dynamic light scattering (DLS) system that will be able to collect data at KWS-1, KWS-2 and J-NSE at the same time as neutron scattering is measured.
2018 was another successful year in the story of NICOS. International collaboration was strengthened and extended. In addition to collaboration with the ESS, closer collaboration with the PSI was initiated. A workshop involving the instrument control group of the SINQ and the instrument scientists of the first PSI instrument using NICOS was held in December 2018 at the SINQ. A further collaboration, together with B. Schillinger (ANTARES) and A. Craft (Idaho National Lab), was launched to install a NICOS/entangle based Tomography station at the Idaho National Lab. At ISIS, the NICOS daemon is integrated into the IBEX control software as a script execution component. Many features and improvements have resulted from this collaboration.

Contributing to SINE2020

As part of the SINE2020 work package 7, the MLZ instrument control group is developing the Sample Environment Communication Protocol (SECoP) in close cooperation with partners from PSI, HZB, ESS and ILL. The SECoP allows European facilities to reduce their development costs and share expensive equipment across various beamlines, respectively controlling shared equipment amongst different instrument control frameworks used at the facilities. An instrument control box developed at the MLZ has been successfully integrated into the ILL NOMAD instrument control system to improve the system.

Project Group

Improved reliability and new capabilities have also been the driving force behind the hardware and automation work in the project group. Besides the ongoing maintenance of the electric and electronic installation, larger upgrades have been implemented on several instruments.

The PLC of the J-NSE has been successfully migrated from the aging Siemens S7-300 product family to the modern S7-1500, which will be in industrial use for the years to come. This development thereby ensures that we will be able to incorporate developments for a wide range of new devices.

The work on J-NSE also included the exchange of the magnet power supplies and the development of new PLC software, which forms the basis for future instrument upgrades. The classic PROFIBUS fieldbus was migrated to the Ethernet-based PROFINET communication with an improved interface to NICOS. The new system was successfully put into operation in the summer and pasted a smile on the face of the person responsible for the instrument, who now operates a fully up to date spin-echo spectrometer with the latest magnet technology, motion control and user interface that provides world class experimental capabilities.

The backscattering spectrometer SPHERES has been equipped with a background chopper to improve the signal to noise ratio. The chopper disc and drive that use technology similar to the chopper at the DNS are based on an industrial solution. The chopper control has been completely overhauled to incorporate a new S7-1500 PLC. This allows the monitoring of a variety of properties describing the oscillation state of the chopper and a synchronous operation together with the PST-chopper of the instrument.

At the cold three axis spectrometer PANDA, the renewal of the entire instrument electronics began with the exchange of the Siemens S7-300 PLC that controls the monochromator rotation. In future, all remaining motion control components of this instrument will use Beckhoff PLCs which have also been chosen by the motion control group of the ESS. The PLC software was developed as part of the collaboration with the ESS and has become part of the library the ESS is compiling with their in-kind partners. Hence, we are also participating in the level of motion software to the standardisation at the ESS.

Detector Group: Two curved ^{3}He-based Multi-Wire Proportional Chambers for ErwiN

The new high intensity powder diffractometer ErwiN at the MLZ will be equipped with two curved 2-dimensional position sensitive ^{3}He-based Multi-Wire Proportional Chambers (MWPC), which are presently under construction in the FRM II detector laboratory. Both devices can be operated in parallel, the small size detector providing 30° and the large area detector providing 130° horizontal acceptance.

The identical modular design of both devices consists of two and nine individual MWPC segments, for the small and large detectors respectively, mounted seamlessly inside a common pressure vessel. This concept is derived from a design presented by the BNL detector group. However, individual

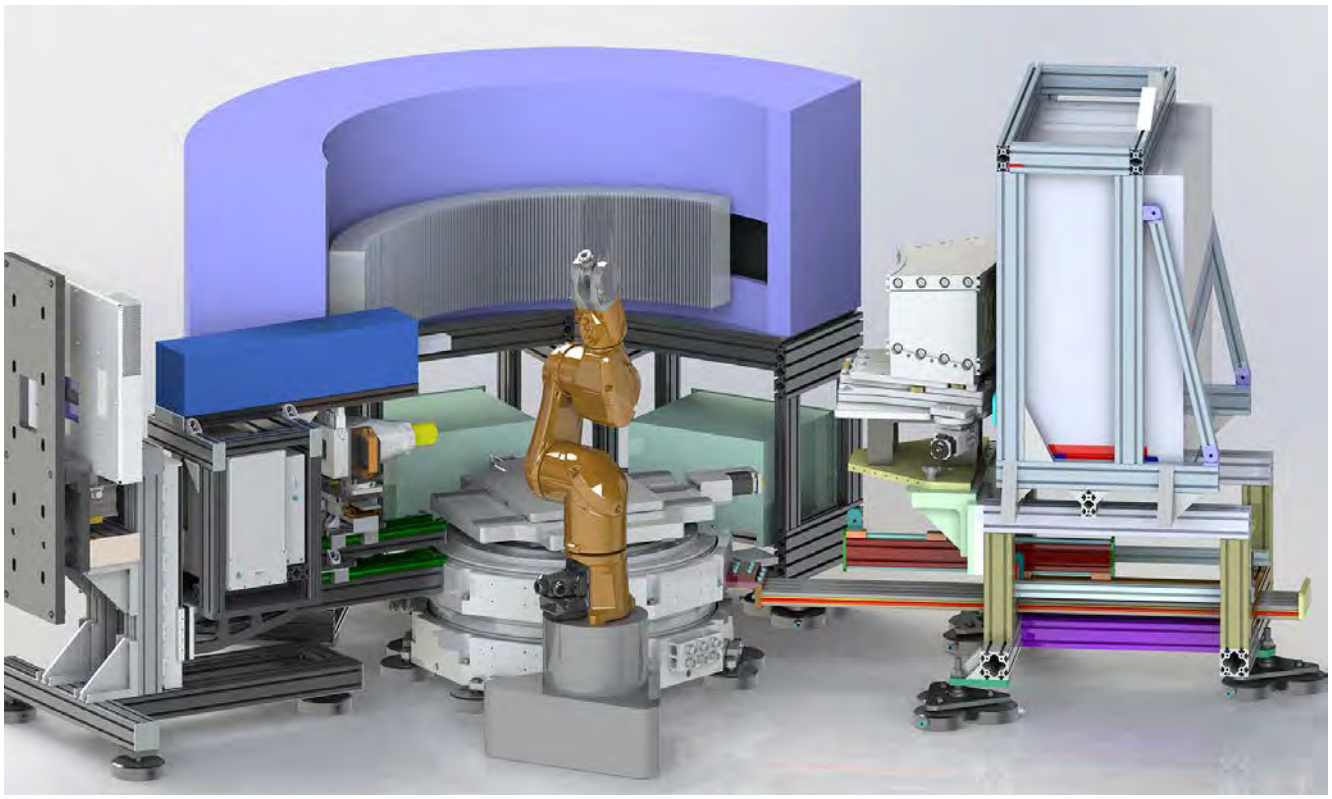

Figure 7: Artists view of the ErwiN instrument including the large area detector based on the MWPC modules.

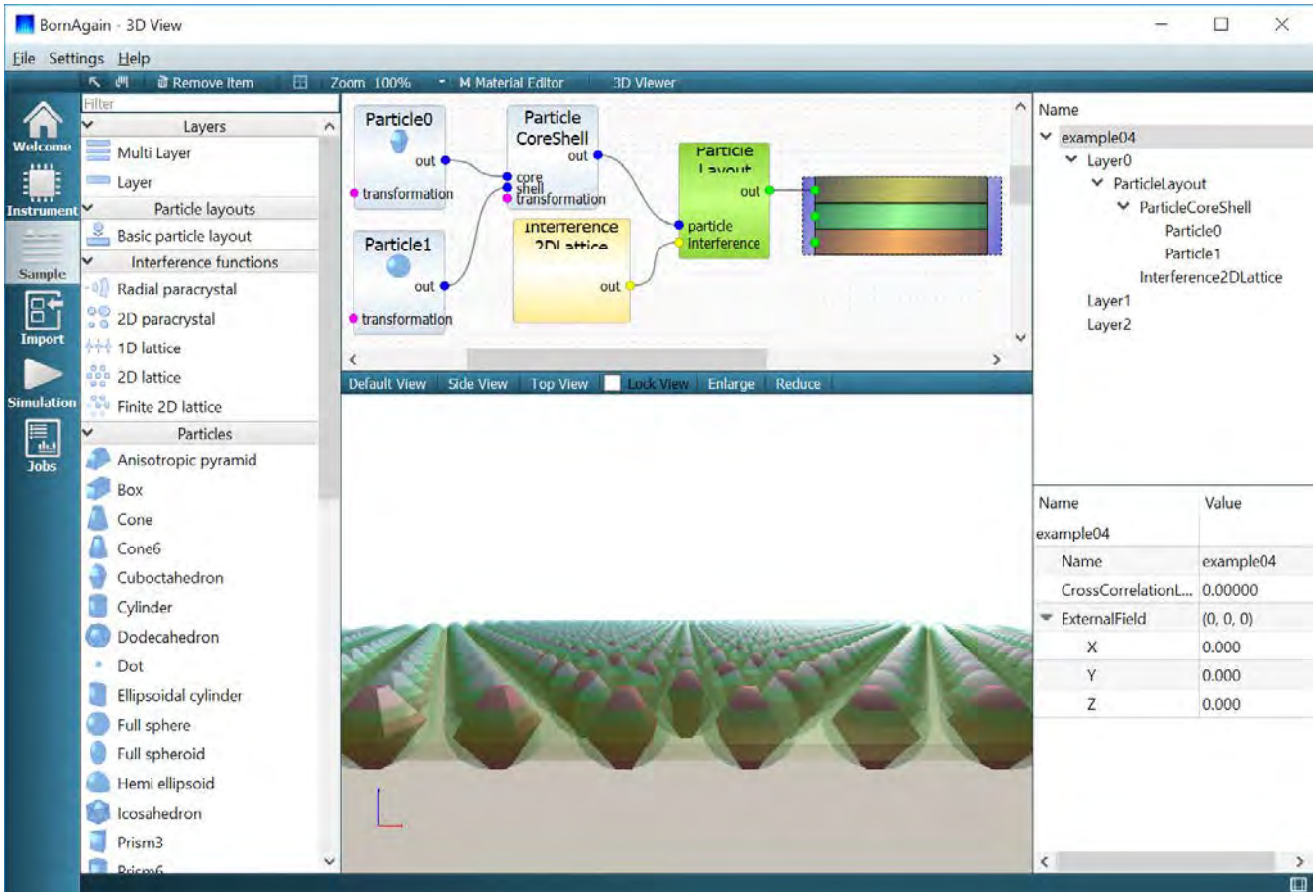

Figure 8: Screenshot of the BornAgain GUI, with a real-space representation of the sample model. By using with the mouse, a user can view the model from different perspectives.

channel readout with a centre-of-gravity algorithm based on the Time-over-Threshold method is applied to precisely determine the neutron impact position. Both devices provide 14° vertical acceptance, 0.115° angular resolution (FWHM) in both directions and a count rate capability of 200 kHz per MWPC segment. Filled with 6.5 bar ^{3}He + 1.5 bar CF_4, the detectors aim at a detection efficiency of 75% for thermal neutrons.

The construction of the smaller device, built in a joint venture with the Paul Scherrer-Institut (PSI) and the Institute Laue-Langevin (ILL), was completed in late 2017 and since then the focus has been set to the realisation of the individual channel readout and FPGA-based signal processing electronics developed in-house. The commissioning of the complete device in the detector laboratory is foreseen for early 2019.

Based on the promising results achieved with the small device, the FRM II and PSI began to build in tandem two identical large area detectors to be installed at ErwiN and DMC-2 at PSI. While PSI is taking care of the production and certification of the pressure vessels, the FRM II detector group is responsible for producing all MWPC segments and the corresponding readout electronics. The completion of the large detector intended for ErwiN is planned for the second half of 2019.

Scientific Computing

Personnel changes

In the course of 2018, Jan Burle and Jonathan Fisher left the Scientific Computing Group to take up posts in industry. We thank them for their excellent work on our software projects Steca (materials diffraction) and NSXTool (single-crystal diffraction), respectively. Despite a competitive job market, we succeeded in recruiting two new research software engineers, Juan Carmona Loaiza and Alexander Schober.

Data reduction

Development, improvement and the maintenance of data reduction software is a core responsibility of the Scientific Computing Group, and of critical importance to the user experience at the neutron instruments of the MLZ. In 2018, work continued on the stress and texture calculator Steca. Release 2.1 features a more consistent and intuitive user interface, and runs much faster than its predecessors. Steca is routinely used at our materials diffractometer StressSpec, and may in the future be ported to the ILL.

The project NSXTool for single-crystal peak integration came to a temporary halt as it happened that, for different reasons, both developers resigned their position at the MLZ and ILL, respectively. Since nothing has changed regarding the need to equip BioDiff with reliable software, we remain committed to bringing this project to a happy conclusion, in continued collaboration with the ILL. A new team will resume work on the code in 2019.

Together with the RESEDA team, we revised the data reduction package MIEZEPY and added a modern looking GUI. This software is indispensable for making use of the MIEZE technique, a variant of resonance spin echo with no optical components between the sample and the high-speed detector. The MLZ is a bastion of this experimental method that is available on RESEDA and MIRA.

Work continued on adapting Mantid to our time-of-flight instruments. The TOFTOF GUI was further improved and updated to Mantid 4.0. For single-crystal measurements on DNS, a new data reduction workflow based on multidimensional workspaces has been implemented. First tests have shown substantial improvements in speed and accuracy of the data reduction in comparison to the legacy code. This workflow is suitable for TOF and diffraction data, and will also be used for event-mode data from the position-sensitive detector.

Data analysis

On the data analysis side, our efforts concentrate on BornAgain. For small-angle scattering under grazing incidence (GISAS), this software is now well- established. With support from SINE2020 and from the European Spallation Source, we are currently extending BornAgain to off-specular scattering and reflectometry. While basic functionality is already available, more work is needed to compete with the flexibility and topical coverage of existing reflectometry software. A novel, very useful and unique feature of BornAgain is the real-space visualisation of the sample model. Despite the somewhat inauspicious date, the second BornAgain School and User Meeting at GATE Garching on December 19 - 21 was attended by 25 colleagues from the MLZ, the TUM, and other institutions in Germany and Europe.

Support for MLZ from Jülich: Engineering and Detectors

J. Daemen[1], R. Hanslik[1], H. Kämmerling[1], C. Tiemann[1], M. Herzkamp[2], K. Bingöl[3], R. Bruchhaus[3]

[1]Central Institute for Engineering, Electronics and Analytics, Engineering and Technology (ZEA-1), Forschungszentrum Jülich GmbH, Jülich, Germany; [2]Central Institute for Engineering, Electronics and Analytics, Electronic Systems (ZEA-2), Forschungszentrum Jülich GmbH, Jülich, Germany; [3]Jülich Centre for Neutron Science (JCNS) at MLZ, Forschungszentrum Jülich GmbH, Garching, Germany

Experts from the Central Institute for Engineering, Electronics and Analytics (ZEA) based at the Forschungszentrum Jülich provide considerable manpower and expertise to support and drive neutron scattering instrument improvement and operation at the MLZ. In 2018, the diffuse scattering neutron time-of-flight spectrometer DNS was fitted with a new polariser. A challenging task came up following the installation of the new high-performance detector at KWS-2: How to move and lift a complete detector tube more than 20 m long for the purpose of adjustment. The work to build the high-throughput time-of-flight neutron diffractometer POWTEX is progressing and the instrument is taking shape in Jülich. A device show-casing a new generation of pixelated scintillator detector using an array of silicon photomultipliers (SiPM) was built at the ZEA-2 in Jülich and tested at the MLZ in Garching.

A considerable workforce dedicated to supporting and driving neutron scattering instrument improvement and operation at the MLZ is located at the Forschungszentrum Jülich GmbH in Jülich. The Central Institute for Engineering, Electronics and Analytics, Engineering and Technology (ZEA-1) includes groups of expert engineers engaged in design and construction. These experts work closely with the engineers at the JCNS in Jülich to develop and build tailored solutions to improve the neutron scattering instruments at the MLZ in Garching. In addition, ZEA- 1 operates workshops in which parts ranging from tiny µm-sized up to heavy weights of several tons can be precisely machined, handled and assembled. The Central Institute for Engineering, Electronics and Analytics, Electronic Systems (ZEA-2) is active in preparing customised detector solutions for the neutron scattering instrument suite at the MLZ. These groups of skillful experts and the large scale infrastructure are key players in enhancing the performance of the neutron scattering instruments to meet the requirements that arise out of the challenges in the various scientific fields. In 2018, several projects involving the instruments DNS, SAPHiR, KWS-2, POWTEX and TOPAS were brought to fruition in close cooperation with the JCNS staff on site at the MLZ in Garching.

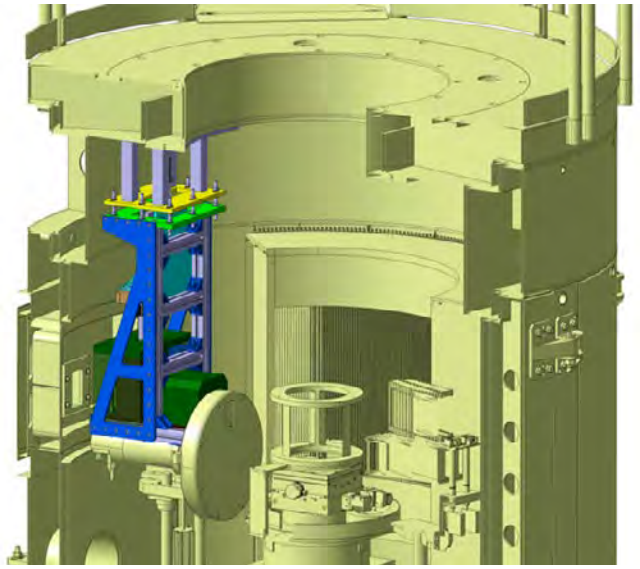

Figure 1: 3D-model of the polariser unit inside DNS.

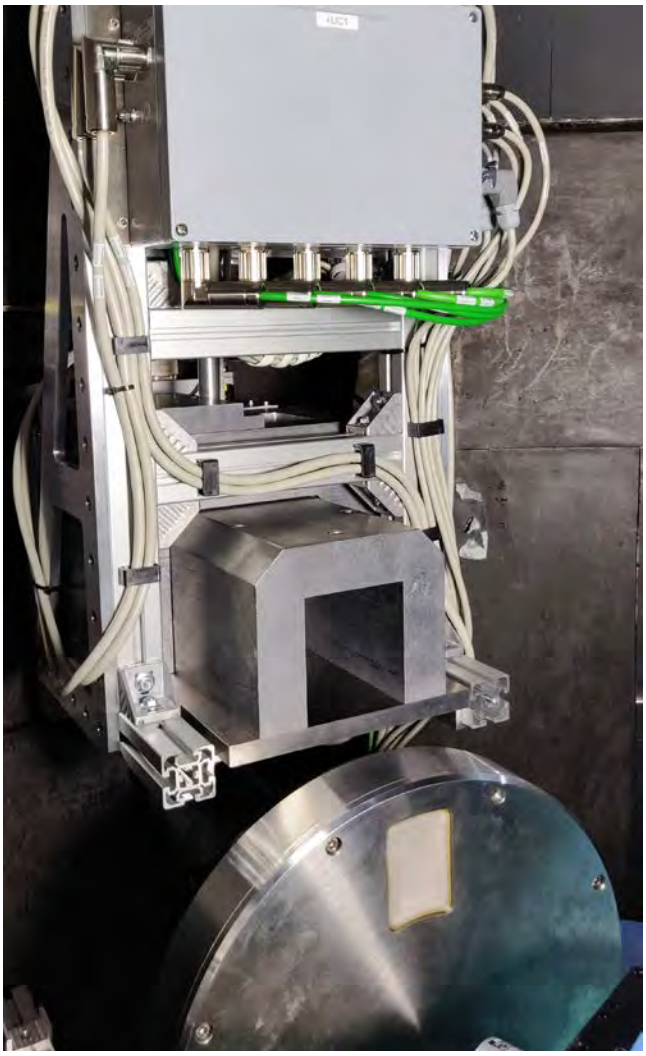

Figure 2: DNS polariser unit mounted within the instrument.

Figure 3: The shielding consists of 150 mm thick steel plates.

Figure 4: The shielding assembled at the ZEA-1 workshop in Jülich.

ZEA-1: New polariser for DNS

In order to increase the degree of neutron polarisation and the neutron flux at DNS, a new polariser based on thorough simulations was designed and manufactured. Due to the very limited space in the instrument housing, the construction of the frame and shielding to move the polariser in and out of the neutron beam was challenging, fig. 1. In addition, three motors served to adjust and rotate the polariser along three axes to achieve an optimal position within the neutron beam.

A motorised entrance slit was integrated and a shielded flight path tube with magnetic guide field mounted behind the polariser. The whole device is radiation shielded using a sandwich-like arrangement of the shielding materials. This guarantees low activation levels over the whole lifetime of the device. The entire equipment was designed by the engineering department of the ZEA-1 Institute, manufactured in their workshop in Jülich and then assembled and carefully tested together with the control unit before the complete setup was moved to the MLZ in Garching. Meanwhile, the polariser has been installed within the instrument and stands ready for hot commissioning with neutrons, fig. 2.

ZEA-1: Neutron guide shielding for SAPHiR

In the new guide hall east, the instruments POWTEX and SAPHiR will be arranged one after the other with both using the neutrons from one of the three ports in the beam plug of beam tube SR5. Neutrons pass through POWTEX and will be guided to the six anvil press instrument SAPHiR at the end position of this beam. A guide with radiation shielding was designed, manufactured and built up for testing in the workshop in Jülich, fig. 3 and fig. 4, as the result of close co-operation between the instrument teams of both instruments and the experts from ZEA-1. Meanwhile, the installation has been approved and is now being disassembled and transported to Garching.

ZEA-1: How to lift a complete detector tube of a SANS-instrument?

The new high-performance ^{3}He-detector at KWS-2 is a great success. An improvement by a factor of 25 compared to the old detector opens up new scientific opportunities. Scientists benefit from this improved KWS-2 for their research. However, the new detector has a different geometry and larger area. As a result, the center of the neutron beam was off-center of the detector and realignment was needed. As the detector covers the full cross-sectional area of the detector tube, an adjustment by moving the detector within the tube was not possible. Thus, the task was to move a complete detector tube more than 20 meters long, including the detector and a weight of several tons, by 100 millimeters upwards and 10 millimeters to the side relative to the incoming neutron beam.

Careful planning, redesign, engineering and manufacturing of several parts were the key elements in the success of the project. Crucial help came from a German company specializing in lifting and moving extremely heavy objects such as bridges.

Figure 5: Hydraulic posts were used to carefully lift the KWS-2 detector tube.

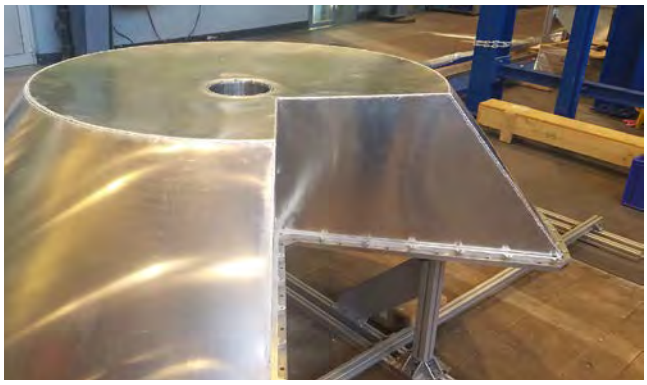

Figure 6: Aluminum cases which protect the detector surface after assembly.

Figure 8: Preparation for detector tube tests in the JCNS detector laboratory.

Sixteen hydraulic posts equipped with precise displacement transducers were placed beneath the detector tube support and the heavy tube was lifted synchronously in a smooth and supremely controlled manner, fig. 5. Now, both tube and detector are perfectly aligned for the benefit of scientific users.

ZEA-1: The powder diffractometer POWTEX takes shape

The set-up of the high-intensity time-of-flight neutron diffractometer POWTEX made considerable progress in 2018. A challenge was the precise manufacturing of the protection cases produced by welding thin aluminum sheets, fig. 6. Meanwhile, the impressive motor-driven doors of the instrument can be opened and closed by simply pressing the appropriate button, fig. 7. The next steps include adding and connecting the units for instrument control and running the final tests. It is expected that POWTEX will be one of the eye-catchers for the public interested in joining the open day of the Forschungszentrum Jülich in summer 2019. After that, the instrument will be dismounted and moved to the JCNS at the MLZ in Garching. The impressive doors of the instrument give an overview of the area in the ZEA-1 workshop where the instrument is assembled for testing.

Figure 7: POWTEX takes shape in the ZEA-1 workshop area in Jülich.

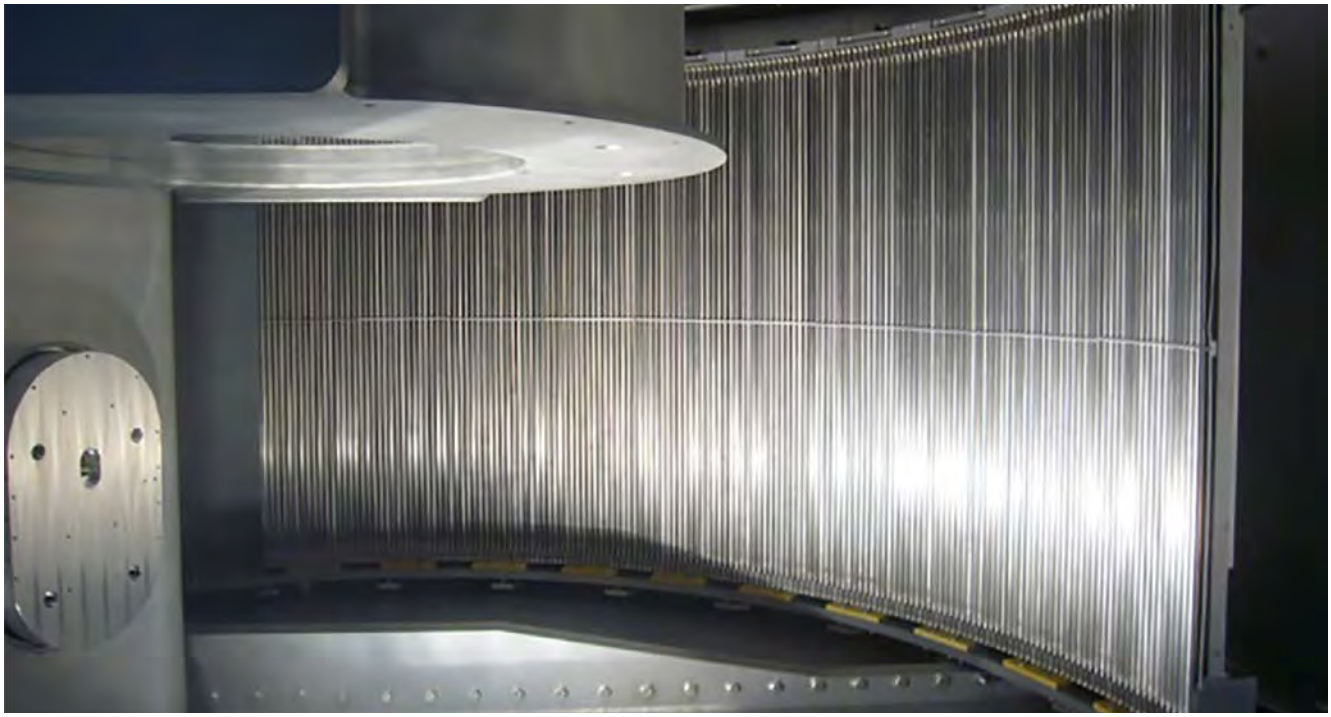

Figure 9: A series of 10 detector boxes are mounted in the vacuum chamber of TOPAS.

ZEA-1: Detector installation for TOPAS takes shape tube by tube

Meanwhile, all 288 ^{3}He detector tubes for TOPAS have been tested in the JCNS-laboratories using a Californium neutron source, fig. 8. Unfortunately, it turned out that more than 100 tubes did not meet the specifications and had to be returned to the manufacturer for repair.

Despite this, the mounting and cabling of the detector boxes was continued. All detector boxes with 16 detector tubes each were successfully tested at the Californium source in the laboratory. In the meantime, 10 out of 18 detector boxes have been installed and adjusted in the TOPAS vacuum chamber that stands in the guide hall east at the MLZ in Garching, fig. 9.

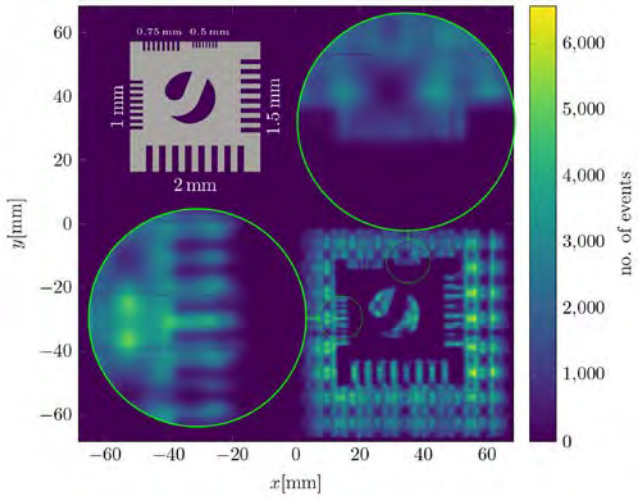

Figure 10: Reconstructed image from the measurement at TREFF. A mask, as depicted in grey, was fixed to the detector surface and is clearly visible in the image at the lower right part of fig. 10. The green circles show the details of the structures with 1 mm and 0.5 mm width in 5-fold magnification.

ZEA-2: Development of a prototype neutron scintillation detector using digital silicon photomultipliers

Based on a previously developed demonstrator, a prototype neutron detector with a 13 x 13 cm² surface area was developed. It uses a 1 mm thick monolithic GS20 scintillator glass as a neutron converter and a Philips Digital Photon Counter (PDPC) SiPM to detect the scintillation light. In order to reach the target resolution of 1 x 1 mm² with the PDPC pixel pitch of 4 mm, the light of each event needs to be distributed among multiple pixels to facilitate Anger camera reconstruction capability. To this end, an additional 1 mm thick glass sheet was inserted between the scintillator and the PDPC modules. An aluminum cap encloses the optical setup to prevent stray light from entering. Two Peltier elements keep the PDPC modules at a constant temperature because of the strong dark count rate dependency of the PDPC modules. The hot end of the Peltier elements are connected to an air-cooled fan/heat sink combination. Since the PDPC modules already provide digital data, the readout consists of a single concentrator board, which sorts packages and forwards them to the measurement PC.

First measurements were conducted at the TREFF instrument at the MLZ in Garching, albeit with some functional limitations. However, it was possible to achieve first reconstruction images of a boron carbide mask (see fig. 10). These show a very clear resolution of 1 mm structures, while 0.5 mm structures are faintly recognizable. Further work on the prototype will focus on improving the homogeneity of the detection efficiency and position resolution of the detector prior to finalisation.

Irradiation operator Jens Molch taking a freshly doped silicon ingot out of the reactor pool. In 2018, the FRM II irradiated 687 silicon ingots with a total mass of more than eight tons.

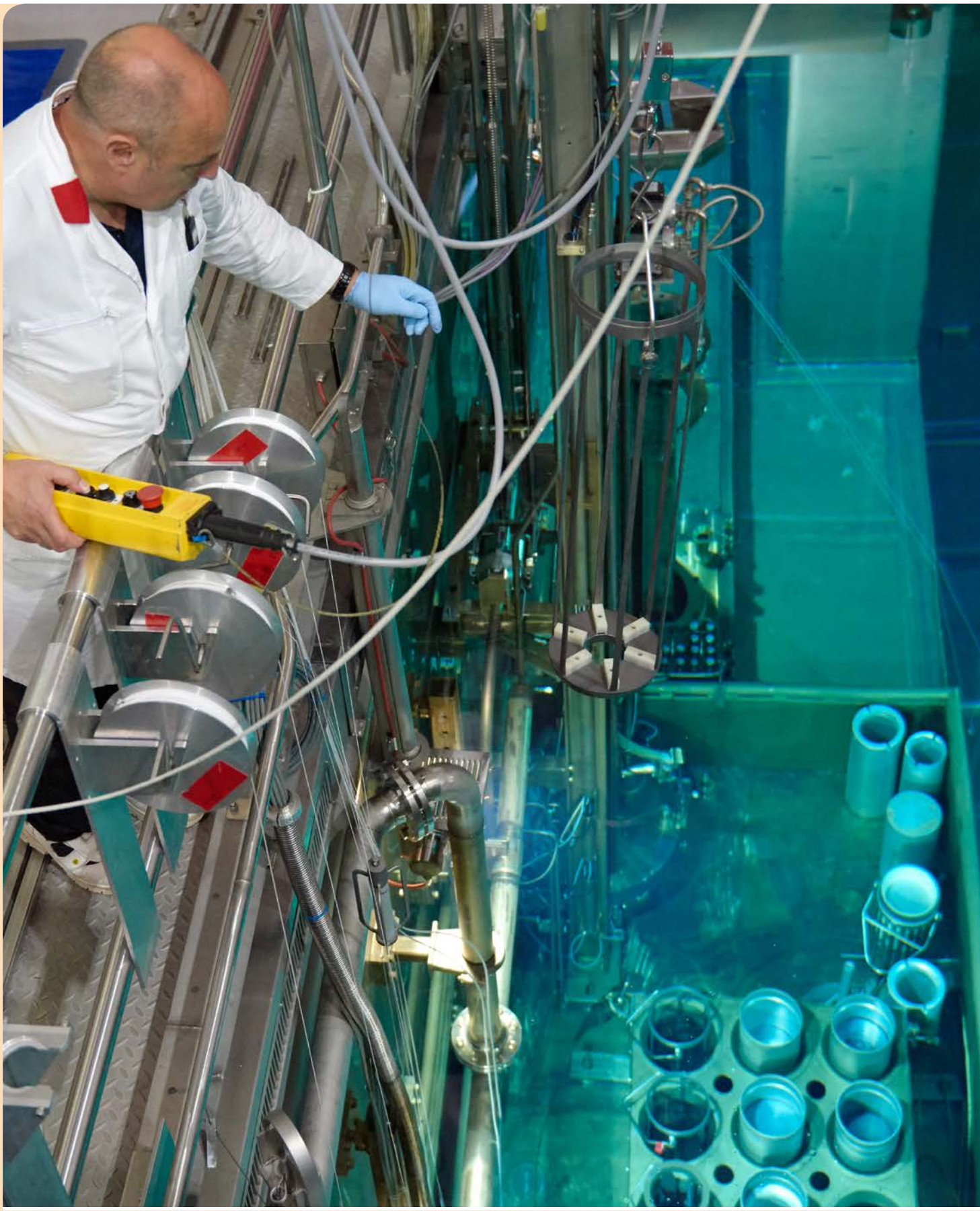

Reactor & Industry

Reactor operation facing challenges

A. Kastenmüller

Forschungs-Neutronenquelle Heinz Maier-Leibnitz (FRM II), Technical University of Munich, Garching, Germany

In 2018, the FRM II was in operation with 3 cycles (No. 44, 45, 46a) for a total of 150 days. We had originally planned to offer our users and clients 180 days of reactor operation, but had to reduce the number of days of operation, not for any technical reasons, but on account of a severe delay in fuel delivery by our French fuel supplier.

Supply with fresh fuel

For the year 2018, 180 operating days were scheduled with the overall operation plan having already been published at the end of July 2017. As no new fuel elements had been produced by summer 2018, leading to foreseeable delays in the supply of fresh fuel, the three planned full cycles were distributed more evenly over the year 2018 in order to provide neutrons for the first cycle of 2019, in the event of not a single fresh fuel element being available until the beginning of 2019.

Although the manufacturer was able to provide two fuel assemblies for final inspection in readiness for transport to the FRM II by mid-December 2018, it was not possible to carry out the transport planned for December. The reason for this was that the shipping company for such nuclear transports, or rather their French subcontractor, was unexpectedly denied permission by the French security authority to transport the fuel elements via a German security vehicle on French territory. As this established transport scheme had worked for the previous 15 years, this unexpected issue had to be resolved with the authorities involved at the beginning of 2019.

The fuel cycles in 2018

Cycle 44 was started on 23 January 2018 as scheduled. Owing to a misleading signal from the cooling tower water level sensor and the subsequent automatic switch-off of both tertiary cooling pumps, the personnel on duty stopped the reactor on 30 January 2018 via a manually initiated scram. This action was the deliberate and safety-oriented procedure followed by the shift manager in the event of evidence for, or proven loss of the external heat sink of the reactor. After clarifying the reason and cooling down the cold source again, the reactor was restarted on 5 February 2018 and continued in operation until 30 March 2018 when the control rod reached its upper end position at burnup of the fuel assembly of 1197.0 MWd.

Cycle 45 was started on 26 April 2018. The start-up was postponed for 3 days after the proposed schedule because of the failure of an electrical cabinet fan in the control system of the helium compressor of the cold source. Following repair, the cold source had to be made operational again, which caused the slight delay. The cycle was interrupted on 21 June 2018 by an automatic scram (RESA), which was caused by a transient in the external power grid. The reactor was restarted on 23 June 2018 and the cycle ended as planned on 28 June

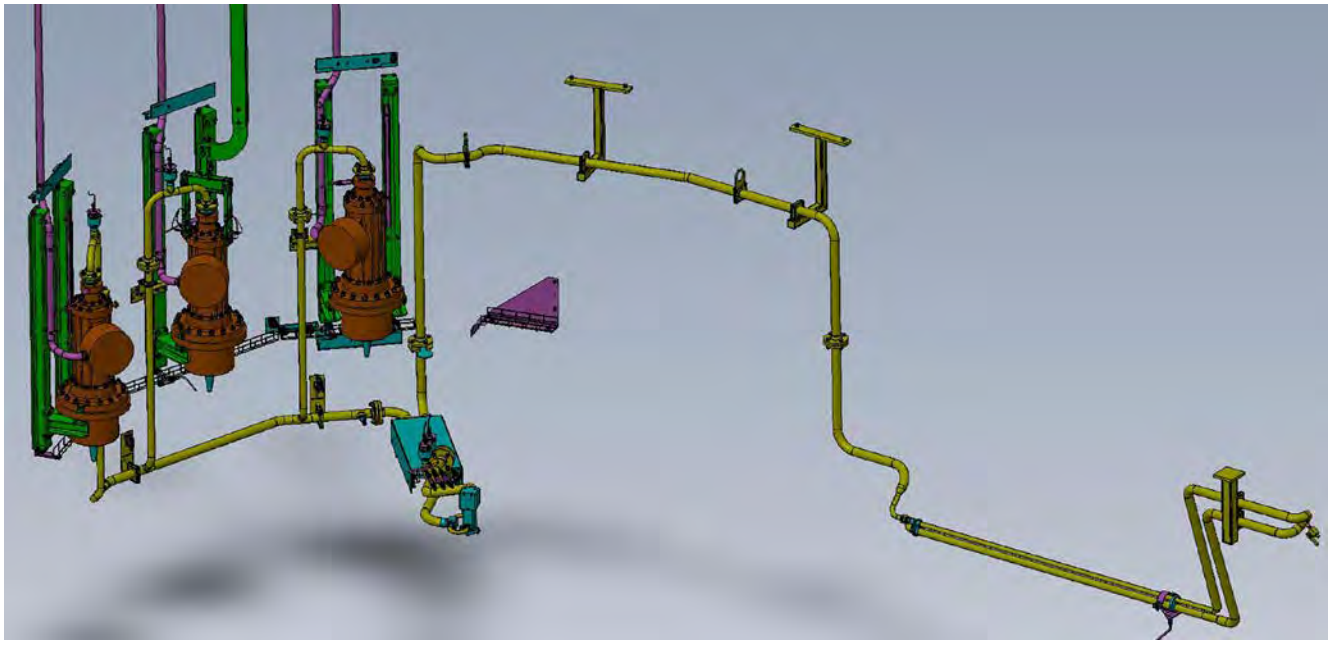

Figure 1: Drawing of the three new cooling pumps of the future ^{99}Mo-production facility.

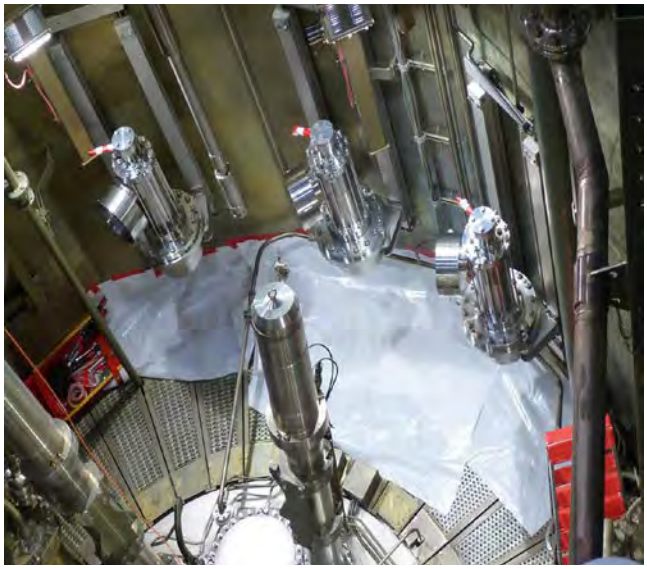

Figure 2: Photo of the three new cooling pumps in the reactor pool of the future ^{99}Mo-production facility.

2018 with the maximum licensed burnup of the fuel assembly of 1200 MWd.

The power operation of cycle 46 was started as planned on 3 September 2018. The reactor operated without interruption until 3 October 2018 and was deliberately switched off after a half cycle at a fuel element burnup of 593 MWd.

Through a total of 1862 periodic in-service inspections, onsite inspections by independent experts from the regulatory body covering 18 different subject areas, as well as 28 modifications to the facility that had to be referred to the regulatory body, it was ensured that the high technical and safety related standard of the FRM II could be sustained, or even further enhanced.

Follow-up of the periodic safety review (PSR)

In 2015, a periodic safety review (PSR) was carried out for the first time, 10 years after the start of routine operation, and the relevant extensive documents were submitted to the regulatory body on time. In 2018, further feedback and inquiries were received from the TSO experts on various parts of these documents, which had to be processed in part with the involvement of external companies. It is to be expected that time-consuming work on the completion of the PSR will still be necessary in 2019 in order to meet all the additional requirements of the TSO experts.

Continuation of various projects

The maintenance intervals between the operating cycles were used for the further implementation of various projects, in addition to the usual routine maintenance and recurring tests.

Detritiation of the D_2O moderator:
About 10 m^3 of the existing moderator (D_2O) was transported in dedicated drums to Canada for the removal of accumulated tritium from the heavy water. The FRM II received, in advance, the same amount of detritiated D_2O, to be reused as a moderator.

Installation of the ^{99}Mo isotope production facility:
The installation of the cooling system for the future ^{99}Mo-production facility continued in 2018. One major step was the mounting of the three new cooling pumps in the reactor pool and some pipes of the cooling circuit.

New buildings and dismantling activities

On 3 September 2018 there was a roofing ceremony of the new workshop and office building of the FRM II and the laboratory and office building of the FZJ. According to the current status, the workshop building UYW can be handed over to the FRM II at the end of June 2019. However, due to the much more complex laboratory infrastructure in the UYL building, this will be delayed by a few months.

At the same time, the staff of FRM II are also involved in other projects such as the dismantling of the old FRM and the preparations necessary for this, the dismantling of the cyclotron within the premises of FRM II, which began in September by the contracted companies, as well as additional tasks necessitated by the nuclear fuel development laboratory that is operated under license according to § 9 AtG.

The key issue: Human resources and recruiting

For the safe and reliable operation of the FRM II, the continuous adaption to new technical and regulatory requirements and the additional work load caused by the further growth of the scientific instrument suite and industrial usage require adequate human resources and a very skilled and experienced staff. Due to the disadvantageous conditions in the public sector as compared to private companies in the nuclear field and the limited flexibility of the human resources departments of the university, the recruitment of urgently needed skilled personnel is nearly impossible in the region around Munich. As a result, the staff of the FRM II reactor division currently consists of around 110 people while the organizational chart shows positions for around 135 staff members for only routine operation. This implies that some really key positions are also vacant without adequate replacement. If one takes additional projects such as the dismantling of the cyclotron accelerator and the old FRM, or the extension of the neutron guide halls into account, the lack of personnel is even more serious. In fact, our ability to act to realize the visions for the MLZ for the next years is largely limited by this human resources and recruiting issue.

Completion of the EMPIrE irradiation for lower-enriched U-Mo fuels

B. Baumeister, Ch. Reiter, Ch. Schwarz, Ch. Steyer, W. Petry

Forschungs-Neutronenquelle Heinz Maier-Leibnitz (FRM II), Technical University of Munich, Garching, Germany

In 2018, the EMPIrE experiment successfully completed the irradiation of new uranium-molybdenum (U-Mo) fuels. Part of the irradiated fuel was manufactured by FRM II scientists in the nuclear fuel laboratory. Important data and knowledge were gathered during the irradiation and the post-irradiation examinations at the Idaho National Laboratory. These will allow major steps to be made towards the comprehension of such fuel systems for the conversion of high-performance research neutron sources such as the FRM II to lower-enriched uranium fuels.

EMPIrE (European Mini-Plate Irradiation Experiment) is a joint European/US irradiation experiment, designed to gather important knowledge on high-density low-enriched uranium-molybdenum (U-Mo) fuels for research neutron sources such as the FRM II. Together with its sister experiment SEMPER-FIDELIS for full size plates, EMPIrE is part of the HERACLES comprehension phase – see www.heracles-consortium.eu – for these fuels and focuses mainly on the demonstration of different manufacturing techniques for the production of mini-size (82.5 mm x 19 mm) dispersion and monolithic fuel.

Overview

As part of the monolithic fuel branch, the FRM II high-density fuels group has developed, established and successfully applied a new PVD (physical vapor deposition) process for the deposition of µm thick diffusion barrier coatings (e.g. of zirconium, molydenum) between the U-Mo foil and the aluminum cladding of fuel plates. This step in the process occurs between the bare U-Mo foil fabrication by BWX Technologies Inc. (USA) and the final fuel plate manufacturing by Framatome-CERCA (France), followed by the irradiation test in the Advanced Test Reactor (ATR) at the Idaho National Laboratory (INL, USA). Disperse fuel plates were manufactured by Framatome-CERCA using various fabrication parameters such as a powder manufacturing process, coating technique, heat treatment and molybdenum content of the U-Mo powder. Part of the powder used for the production of these fuel plates originated from the European atomizing process, which was developed by FRM II scientists at Framatome-CERCA.

Production of monolithic irradiation fuel plates at FRM II

Of the 48 samples to be irradiated in EMPIrE, four represent monolithic U-Mo fuel. The application of the Zr layer onto the U-Mo foils was performed by FRM II in the nuclear fuel laboratory. All relevant processing steps, such as e.g. wet-chemical cleaning of the foils, took place in an individualised double glovebox system for the safe handling and treatment of nuclear fuel under an inert argon atmosphere. The Zr coating was applied by the newly-developed PVD process, automatically controlled by a PLC system which is optimised towards safe and stable operation for reproducible results.

Following two test sets with stainless steel surrogates and three test sets with depleted uranium, the final coating of the low-enriched uranium (LEU) foils with high-purity reactor-grade zirconium was successfully performed in mid-2016. Due to the high safety requirements for nuclear fuel, the whole production process was monitored by a comprehensive quality assurance program according to NQA-1, including materials procurement, pre-defined working routines and the documentation of all relevant data. Subsequently, the cladding was applied by the so-called C2TWP technique at Framatome-CERCA in fall 2016, where twice the required number of plates passed the final conformance test. By the time the LEU fuel plates were shipped to ATR at the end of 2016, the monolithic production program for the EMPIrE project has been completed successfully and on schedule, with only 18 months between the first tests and the specification-compliant fuel plates.

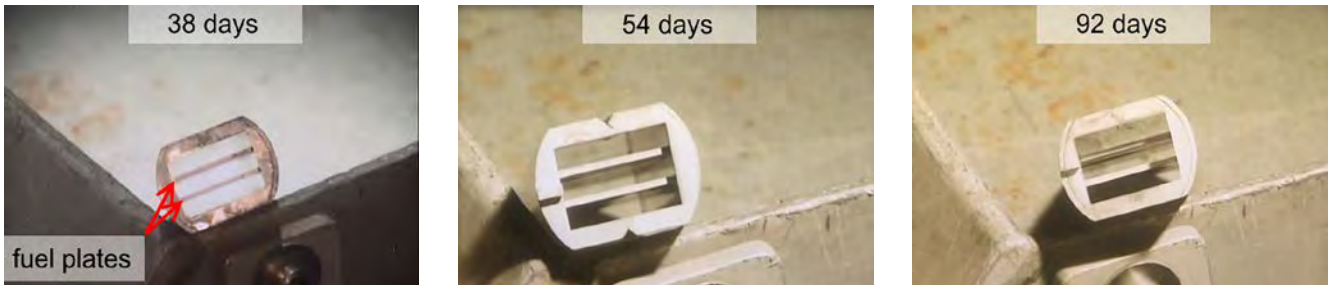

Figure 1: EMPIrE irradiation capsule with fuel plates after irradiation for 38, 54 and 92 days, respectively.

Figure 2: Christian Steyer loading uranium into the coating device inside the glovebox.

Figure 3: Burning plasma during the cleaning process of the uranium foil prior to coating.

Irradiation at ATR

Prior to the irradiation, a secondary comprehensive characterisation of all irradiation fuel plates using ultrasonic transmission, ultrasonic pulse-echo, thermography, optical and scanning electron microscopy with energy-dispersive x-ray spectroscopy was performed at INL. This characterisation confirmed the specification conformity of all fuel plates destined for irradiation. These plates were then loaded into irradiation capsules, designed for insertion into the ATR core. In March 2018, the irradiation of a total of 48 fuel plates (44 disperse and 4 monolithic) began, batches of 16 plates being irradiated for 38, 54 and 92 days, respectively. The irradiation conditions for the monolithic plates such as fission rate, burnup, heat flux were chosen to be most widely similar to the operating conditions of FRM II. In August 2018, the irradiation was successfully completed without any incident.

Post-irradiation examination

Post-irradiation examination (PIE) is an essential part of any irradiation experiment in order to determine the effect of the uranium burnup on the integrity and structure of the fuel, as well as to ensure that no irradiation-driven defects such as plate warping, bursting or excessive swelling have occurred. Thus, both non-destructive and destructive PIE are carried out on the irradiated fuel plates. The data obtained in PIE will further help to optimise the fuel system properties as well as the manufacturing processes.

A first visual inspection in hot cells at INL has detected no visible defects or abnormalities on any fuel plates so far. As part of the non-destructive PIE work, a more detailed characterisation by precision gamma scanning, neutron radiography and dimensional inspection is currently being performed. These characterisations will deliver localised profiles of fuel burnup, plate swelling and oxide layer thickness. Based on these results, a selection of irradiated fuel plates will then be sectioned and prepared for metallographic examination, e.g. by optical and scanning electron microscopy. There, U-Mo fuel, coating layers, aluminum matrices and the cladding will be thoroughly analysed and the possible formation of interlayers and new phases will have been investigated by the end of 2019.

Outlook

The successful completion of the EMPIrE irradiation experiment will deliver important data and knowledge on the disperse and monolithic U-Mo fuel systems. The respective European fuel manufacturing processes, including the FRM II PVD and Framatome-CERCA C2TWP processes, have been successfully demonstrated. Together with its sister experiment SEMPER-FIDELIS currently being carried out at the Belgian research reactor BR2, these irradiations allow major steps towards the comprehension of such fuel systems with respect to the conversion of high-performance research neutron sources such as FRM II to lower-enriched uranium fuels.

In parallel, the high-density fuels group at FRM II, in close collaboration with Framatome-CERCA, is currently working on the further enhancement of their fuel manufacturing processes. For example, the PVD coating process is being adapted to different coating materials such as molybdenum. Further, the process will be upscaled to the full-size geometry (762 mm x 45 mm) in preparation for the upcoming irradiation test – FUTURE MONO 1. This irradiation test will be part of the qualification process for lower-enriched monolithic U-Mo fuels.

This work was supported by a combined grant (FRM1318) from Bundesministerium für Bildung und Forschung (BMBF) and Bayerisches Staatsministerium für Wissenschaft und Kunst (StMWK). This work was supported by the European Commission within the framework of HORIZON 2020 through Grant Agreement 661935 in the HERACLES-CP project and Grant Agreement 754378 in the LEU-FOREvER project.

Filling lithium-ion cells faster

R. Gilles, A. Voit

Heinz Maier-Leibnitz Zentrum (MLZ), Technical University of Munich, Garching, Germany

Electro mobility and the urgent need to store electric energy are stimulating research on lithium ion cells. Industry partners are increasingly aware of the unique possibilities neutrons offer for a non-destructive, in-situ and operando investigation of batteries. Developers from the mobility and industrial technology company Bosch and scientists at the Technical University of Munich (TUM) are using neutrons to analyse the filling of lithium ion cells with electrolyte for hybrid cars. Their experiments show that electrodes are wetted twice as fast in a vacuum as under normal pressure.

Several hours of waiting for the wetting of the electrodes

One of the most critical and time-consuming processes in battery production is the filling of lithium-ion cells with electrolyte fluid following the placement of electrodes in a battery cell. While the actual filling process takes only a few seconds, battery manufacturers often wait several hours to ensure the liquid is fully absorbed into the pores of the electrode stack.

The fact that neutrons are barely absorbed by the metal battery housing makes them ideal for analyzing batteries. That is why Bosch employees, in collaboration with scientists from the TU Munich and the University of Erlangen-Nuremberg, investigated the filling process at the neutron imaging and tomography facility ANTARES at the MLZ.

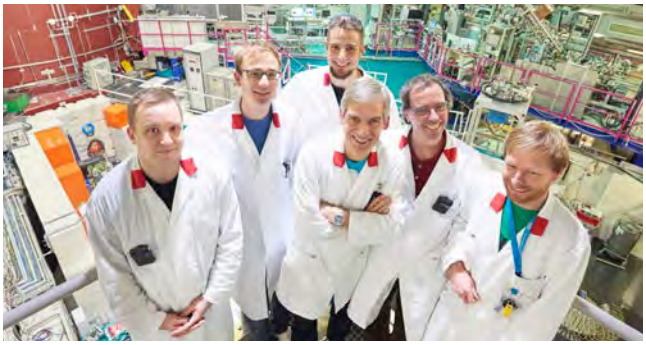

Figure 1: The scientists and developers of the project (from left): Andy Gottschalk (Bosch), Thomas Knoche (IWB, TUM), Hagen Reisenweber (FAU Erlangen-Nürnberg), Dr. Ralph Gilles (MLZ, TUM), Dr. Wolfgang Weydanz (Bosch) and Dr. Michael Schulz (MLZ, TUM).

Twice as fast in a vacuum

Manufacturers of lithium-ion cells often fill the empty cells in a vacuum. The process is monitored indirectly using resistance measurements. “To make sure that all the pores of the electrodes are filled with the electrolyte, manufacturers build in large safety margins,” says Bosch developer Wolfgang Weydanz. “That costs time and money.” Given the benefit of the neutrons, the scientists recognised that in a vacuum the electrodes were wetted completely in just over 50 minutes. Under normal pressure, this takes around 100 minutes (see fig. 2). The liquid spreads evenly in the battery cell from all four sides, from the outside in. In addition, the electrodes absorb ten percent less electrolyte than under normal pressure. The culprit is gases that hinder the wetting process, as the scientists were able to demonstrate for the first time using the neutrons.

[1] W. J. Weydanz et al., J. Power Sources 380, 126 (2018)

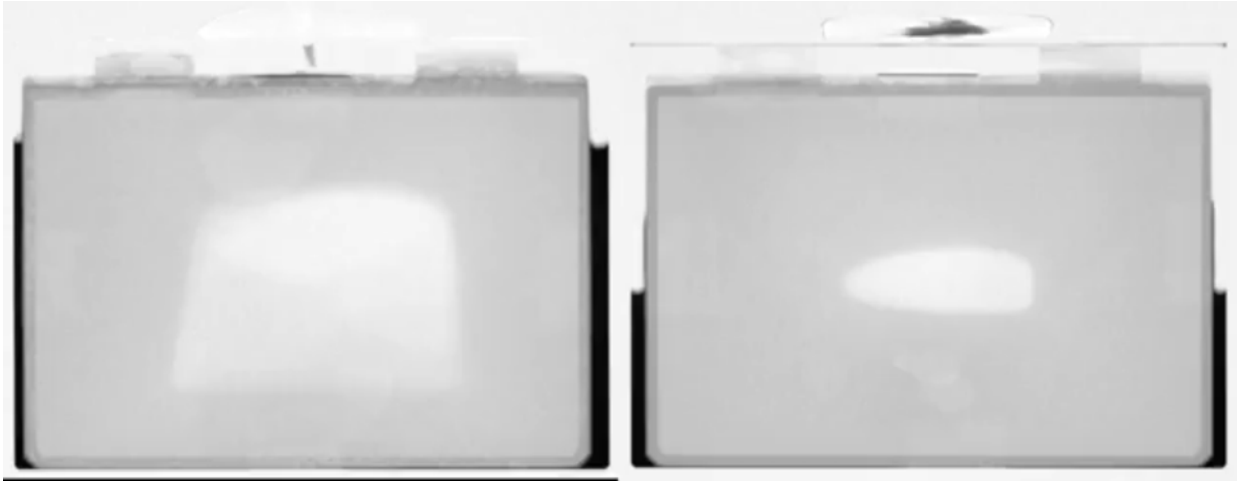

Figure 2: The tomography shows the difference between the electrode wetting at atmospheric pressure (left) and in a vacuum (right). A vacuum accelerates the wetting process by a factor of 2. The wetting of the electrode (dark area) proceeds evenly from all sides.

Testing electrolysis cells

I.Crespo, A. Voit

Heinz Maier-Leibnitz Zentrum (MLZ), Technical University of Munich, Garching, Germany

Thanks to the EU project SINE 2020 at ANTARES, the Danish company Haldor Topsøe has acquired interesting radiographies of its electrolysis cells.

Haldor Topsøe specialises in the development and manufacture of catalysts and the design of processing plants for the chemical and petrochemical industries. The production of hydrogen is important as it is a clean fuel that is easy to store.

With this in view, Haldor Topsøe is developing solid oxide electrolysis cells (SOECs) for hydrogen production. SOECs are a rather competitive solution for small-scale hydrogen production. The stacks available in the market may suffer from performance loss when used over prolonged periods. This is due to the physical stress that may weaken the connection between individual layers of a stack.

After consultation, the SINE2020 Industry Coordinators advised the team from Haldor Topsøe to use neutron imaging at the Maier-Leibnitz Zentrum (MLZ) in Germany. Neutron imaging is the most appropriate technique in this case as it is able to penetrate centimetres of metal without damaging it, and it can “see” hydrogenated materials.

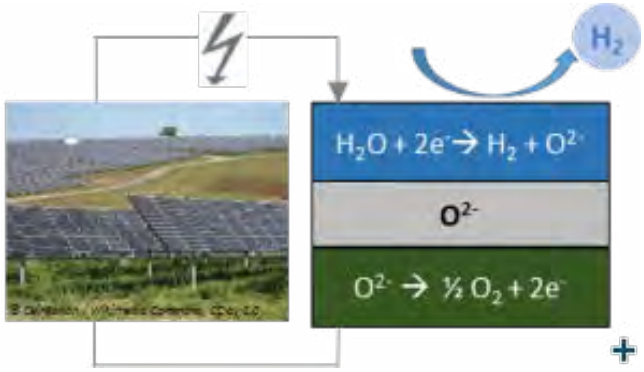

Figure 1: Electricity from renewable sources (such as solar energy) is used by SOECs to produce hydrogen (H_2). The hydrogen can then be stored for later use as a fuel. | © (left image) Ceinturion / Wikimedia Commons

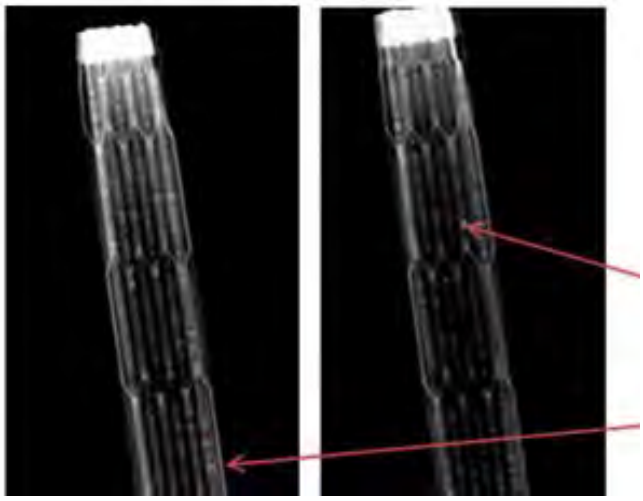

Figure 2: The experiment revealed interesting features that HALDOR-TOPSØE had not considered before seeing the results of neutron imaging. The arrows indicate the inhomogeneities identified within the stack.

Haldor Topsøe performed neutron radiography and tomography test measurements at the MLZ, through the SINE2020 Industry Activities. The researchers were able to identify hitherto unknown features within the stack.

Christoffer Tyrsted, Research Scientist at Haldor Topsøe, stated: “All the way through we received good and competent feedback from the parties. The experiments revealed other interesting features we had not considered before obtaining the data.”

Dr. Michael Schulz, scientist at the radiography station ANTARES at the MLZ says: „The test radiographies were also positive for us, as there might be follow-up-measurements.”

“Build your favourite chemical element”, the children at the ”open day with the mouse” were told. They were invited to use magnetic sticks for the electrons, and balls for neutrons and protons.

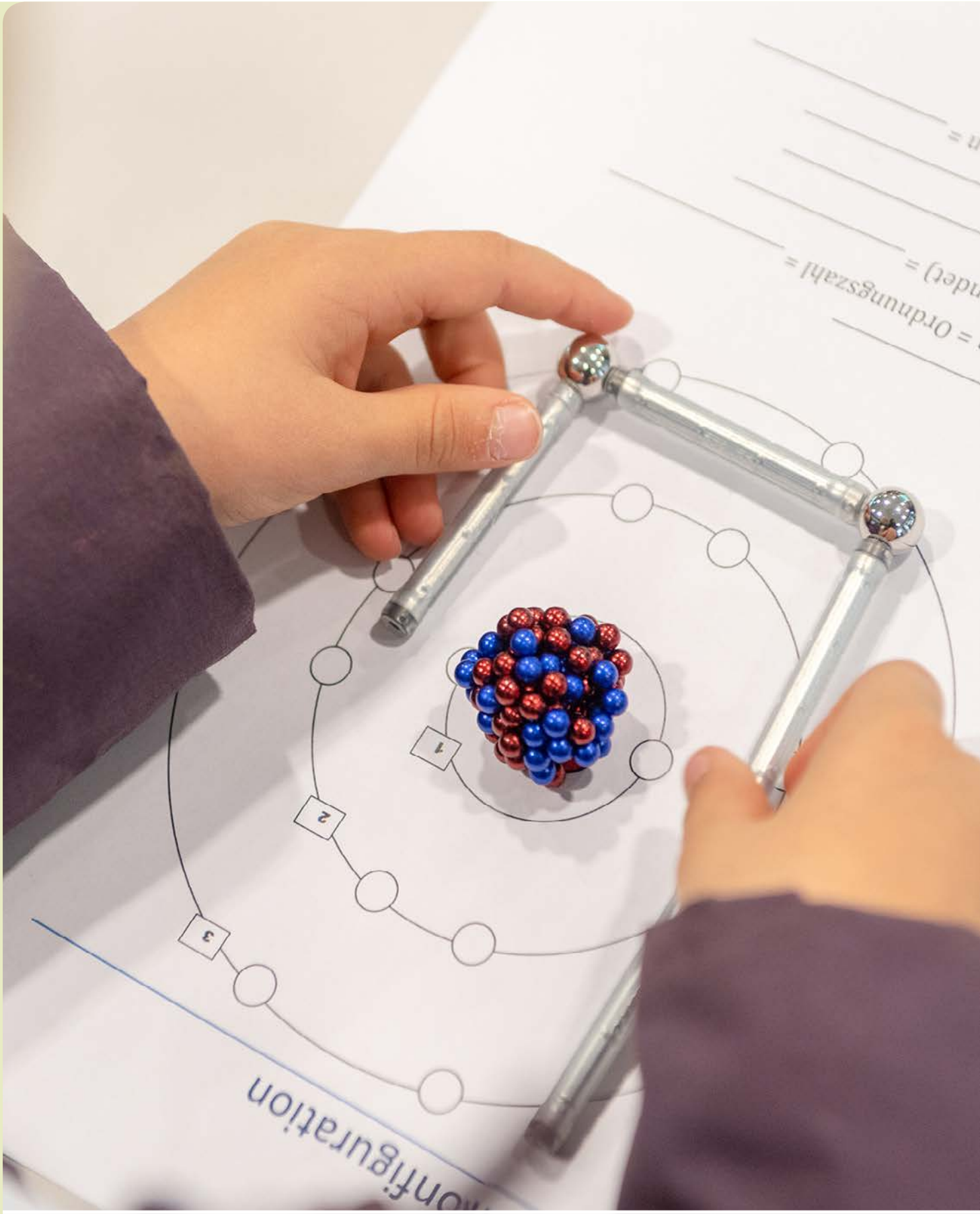

Facts & Figures

The year in pictures

January 11th

The district administrator of Freising, Josef Hauner (2nd from right), and departmental heads of the district office are initiated into the secrets of neutron spectroscopy by Scientific Director Prof. Dr. Winfried Petry.

January 21st

Visit from the funding body: Dr. Volkmar Dietz (3rd from right), Dr. Andrea Fischer, and Dr. Jürgen Kroseberg (3rd from left) of the Federal Ministry of Education and Research are on their way through the experimental hall accompanied by Prof. Dr. Sebastian Schmidt (Forschungszentrum Jülich, 2nd from left), Dr. Jürgen Neuhaus and Prof. Dr. Winfried Petry (both MLZ/TUM, right).

January 23rd

Impressed with the largest research facility of the district was Christoph Göbel (middle), when visiting the neutron source. FRM II Technical Director Dr. Anton Kastenmüller (2nd from left) and Adminstrative Director Johannes Nußbickel (left) escorted the district administrator of Munich and his departmental heads to the reactor pool.

April 1st

Baton change at the MLZ and FRM II: Prof. Dr. Peter Müller-Buschbaum has been appointed new Scientific Director of the FRM II and MLZ. He succeeds Prof. Dr. Winfried Petry who has headed FRM II since 2001.

April 18th

Stamping the egg: On the occasion of the 150th anniversary of the Technical University of Munich, the Atomic Egg features on the special issue stamp.

April 20th

From Argentina to Garching: Six engineers and scientists have been working at the MLZ in order to gain experience for the new research neutron source in Argentina RA-10, planned to be operational in 2021.

April 28th

Talks for teachers: The traditional Edgar-Lüscher seminar for teachers of the natural sciences presented “Big instruments for big questions”. The 42nd edition of the famous seminar in the Bavarian Forest was again organised by the FRM II and MLZ Scientific Director Prof. Dr. Peter Müller-Buschbaum (front row, left) and former Scientific Director Prof. Dr. Winfried Petry.

April 30th

Funding from Norway: The Norwegian Research Council granted 2 million Kroner for a Post-Doc position to design a sample holder for Li-ion coin cell batteries, which can be charged and discharged while being observed with neutrons. It will be used at the neutron powder diffractometer SPODI and the future fast neutron powder diffractometer ErwiN.

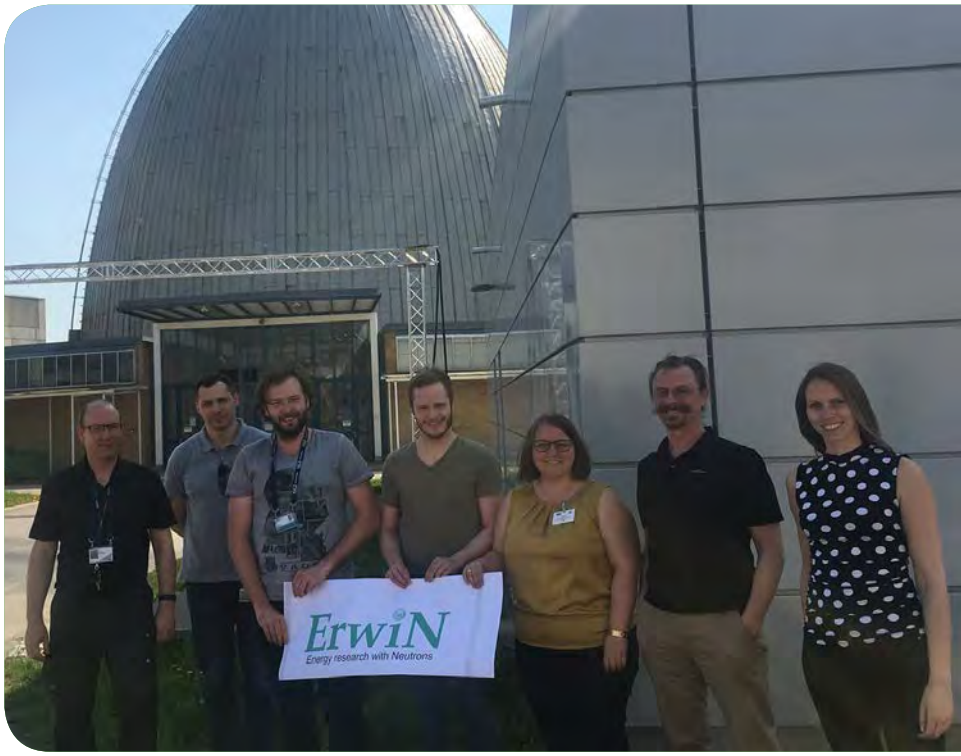

May 29th

Birth of a new instrument: The KOeln-Munich spectrometer specifically designed for polarisation analysis (KOMPASS) saw first neutron light with one of its fathers, instrument scientist Dr. Dmitry Gorkov (University of Cologne).

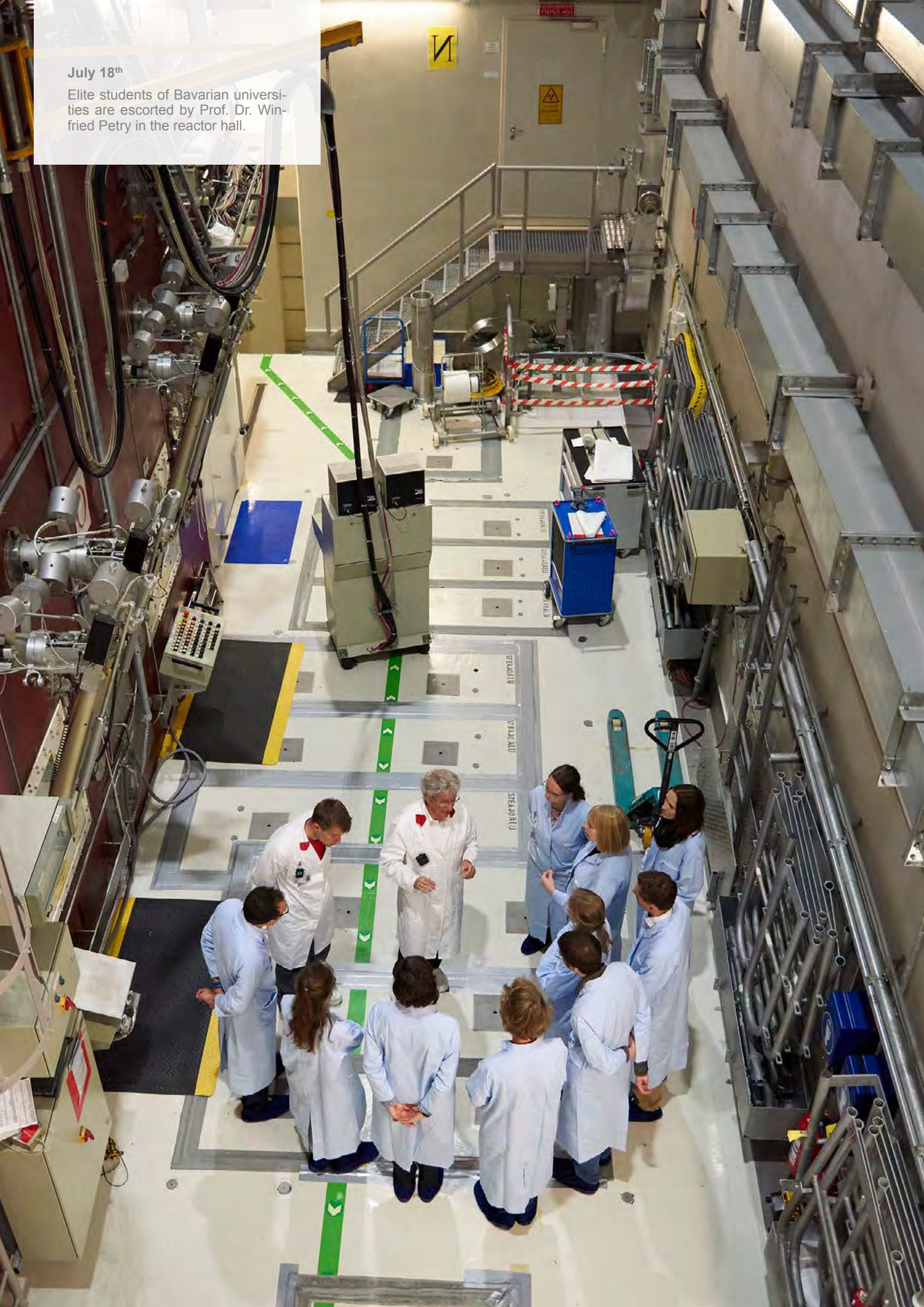

July 18th

Elite students of Bavarian universities are escorted by Prof. Dr. Winfried Petry in the reactor hall.

June 28th

The steering committee of the Institut Laue-Langevin meets on the premises of the Technical University of Munich in Garching.

July 17th

Science on the street: On the occasion of the Euroscience Open Forum in Toulouse, France, the MLZ organised a common booth with seven other European large scale facilities. 4600 visitors were able to take part in the “Olympic games of neutrons and photons”.

July 18th

Positrons on a bill board: Architectural students present their picture of the neutron- induced positron source underneath a bridge in Munich. One of the first visitors of the exhibition by the TUM Chair of Fine Arts was Dr. Christoph Hugenschmidt (2nd from left), leading scientist at the MLZ positron source.

July 18th

Exhibition of the egg: Three architectural students of the Technical University of Munich present their wooden atomic egg - a walking experience with audio information in an art gallery in Munich.

July 18th

Gift for the departing scientific directors: Prof. Dr. Winfried Petry (left) and Dr. Stefan Mattauch (representing Prof. Dr. Thomas Brückel) opening a picture of the MLZ staff on the occasion of the MLZ summer party.

July 27th

The total lunar eclipse viewed from the FRM II.

August 1st

Girls go tech: Seven girls had the opportunity to peer over the shoulders of the reactor drivers during their three-day course organised by the MLZ and the TUM physics department in the summer break.

August 28th

On the way into professional life: Four apprentices have successfully completed their training in specialised computer science and mechatronics at the FRM II.

September 3rd

Roofing ceremony for the two new office, workshop and laboratory buildings (from left): Doris Lackerbauer (Public Building Authority Rosenheim), Prof. Dr. Sebastian Schmidt (Forschungszentrum Jülich), Josef Zellmeier (Bavarian Ministry of Housing, Construction and Transport), Albert Berger, Professor Juliane Winkelmann (both Technical University of Munich), Dr. Anton Kastenmüller (FRM II, TUM), Dr. Gunter Henn (Henn Architekten GmbH), Dr. Dietmar Gruchmann (City of Garching), Prof. Dr. Stephan Förster (Forschungszentrum Jülich), Dr. Jürgen Neuhaus (FRM II, TUM).

October 3rd

Neutrons and ice cream on the ”day with the mouse”: More than 100 children above the age of 7 got a special tour and a cold surprise on a public holiday!

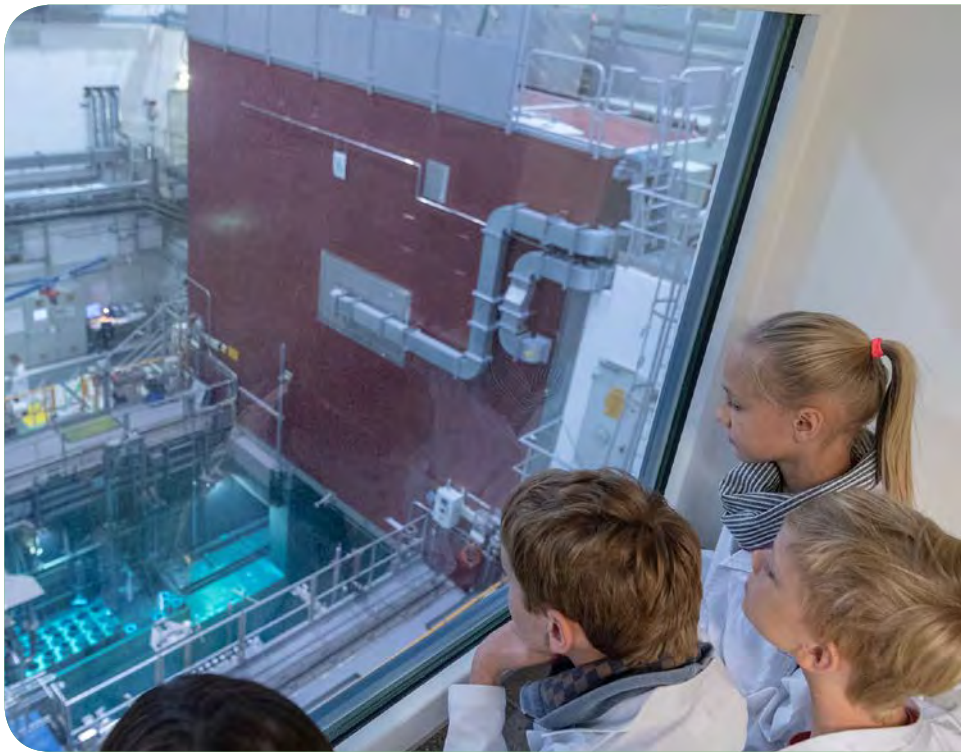

October 9th

Honorary title for Prof. Dr. Winfried Petry: TUM president Prof. Dr. Wolfgang Herrmann (right) bestowed the title of “Emeritus of Excellence” of the Technical University of Munich on the former scientific director of the MLZ and FRM II. Prof. Petry is one of 67 former professors to hold this honorary title.

October 13th

Looking for reactor drivers: On the open day, people tested their ability to run a nuclear reactor at the radiation protection booth. In addition to an MLZ booth and many talks, more than 500 visitors took the opportunity for a tour of the neutron source.

October 24th

Medal for professional training: Jens Krüger (right) received the August Föppl Medal from TUM president Prof. Dr. Wolfgang A. Herrmann. He was acknowledged for having trained 20 IT apprentices at the FRM II.

October 25th

Honorary colloquium for Prof. Petry (from left): Prof. Dr. Peter Müller-Buschbaum, Dr. Anton Kastenmüller, Prof. Dr. Marion Kiechle, Prof. Dr. Wolfgang Herrmann, Prof. Dr. Winfried Petry and Albert Berger.

November 21st

Reviewing the MLZ: MLZ directorate and science group coordinators together with external referees who evaluated the MLZ's scientific achievements and its plans for the future.

November 23rd

Women in Nuclear held their annual meeting at the research neutron source.

November 26th

Exchange on the interim storage in Ahaus (from left): Dr. Ewold Seeba (BGZ), Karola Voß (Mayor of Ahaus), Dr. Anton Kastenmüller (FRM II, TUM) and Hans-Georg Althoff (First deputy of Ahaus).

November 27th

Elevator with millimetre precision: Engineers of the Forschungszentrum Jülich accomplished the task of lifting a 20 metre long small angle scattering instrument by 10 centimetres. Now, KWS-2 can make full use of its new detector.

December 6th

The members of the Horizon2020 project ACCELERATE met in Garching. The goal of the project is to support the longterm sustainability of large scale research infrastructures.

Workshops, Conferences and Schools

①	Seminar: Neutrons in Research and Industry; Garching	January 8th - December 17th	TUM/ MLZ
②	F-Praktikum, Hands-on training for TUM physics students; Garching	January 29th - February 1st	TUM/ MLZ
③	RRFM European Research Reactor Conference; Munich	March 11th - 15th	FRM II/ TUM
④	CREMLIN Connecting Russian and European Measures for Large-scale Research Infrastructures Workshop; Peterhof, Russia	May 13th - 16th	TUM
⑤	PSND Workshop on Position Sensitive Neutron Detectors; Jülich	May 15th - 17th	JCNS/ MLZ
⑥	MLZ Conference: Neutrons for Culture and Art; Lenggries	June 19th - 22nd	MLZ

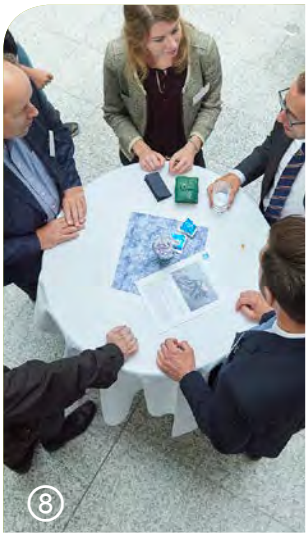

⑦	22nd Laboratory Course Neutron Scattering; Jülich and Garching	September 3rd - 14th	JCNS/ MLZ
⑧	VDI-TUM Expert Forum; Garching	September 13th	TUM
⑨	SNI 2018 – German Conference for Research with Synchrotron Radiation, Neutrons and Ion Beams at Large Facilities; Garching	September 17th - 19th	MLZ
⑩	JCNS Workshop 2018: Trends and Perspectives in Neutron Instrumentation; Tutzing	October 29th - November 1st	JCNS
⑪	2nd Born Again School and User Meeting; Garching	December 19th - 21st	JCNS/ MLZ


④

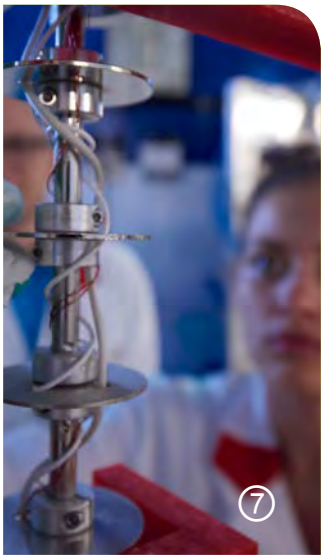
⑦

⑥

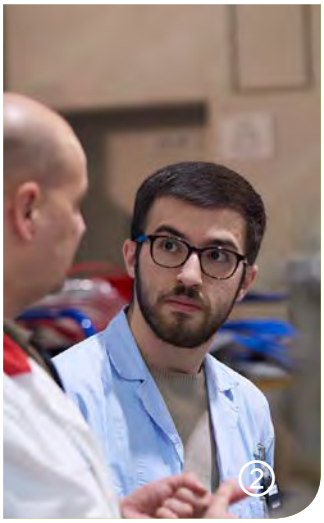
②


⑪

Science for everyone

A. Görg, C. Hönl, B. Tonin-Schebesta, A. Voit

Heinz Maier-Leibnitz Zentrum (MLZ), Technical University of Munich, Garching, Germany

In 2018, the FRM II and MLZ communications team sought to broaden its appeal to younger target groups and extend the spectrum of communication tools with the new format of storytelling on its MLZ-Webpage. The record number of visitors welcomed in 2017 was almost achieved again, with 3650 children and adults enjoying a guided tour through the neutron source. This year has also brought a new high in the number of articles published on the FRM II and MLZ.

Visitor magnet for children and adults

This year, many children profited from additional opportunities to tour the research neutron source and become acquainted with research using neutrons. For the first time, the MLZ offered a whole day experience with special tours for 100 children on the official "day with the mouse" on 3rd October. While the children were treated to a tour and invited to design their own chemical elements with magnetic sticks (Geomag), they were able to watch live experiments with liquid nitrogen and enjoyed freshly-made ice cream afterwards, and the parents learned more about the neutron source and its manifold applications in science, industry and medicine in talks by FRM II and MLZ staff.

A similar programme was offered to children on the open day, which also attracted many adults. In total, more than 500 visitors took one of the tours, which were still in high demand on the open day. Many more used the occasion to attend the talks and visit the booths of the MLZ and FRM II radiation protection teams as well as the walkable wooden atomic egg. A former staff member was there to provide a first-hand account of the early days of the first nuclear reactor in Germany. As the Technical University of Munich was celebrating its 150th birthday, the open day was not only held on the campus in Garching, but on all campuses of the TUM. For the third time, a group of girls spent three days immersed in physics during the summer holidays under the auspices of the TUM programme "Mädchen machen Technik". Dr. Marina Ganeva (Forschungszentrum Jülich / MLZ) regaled the young scientists for a whole day with their own experiments and a special tour of the neutron source.

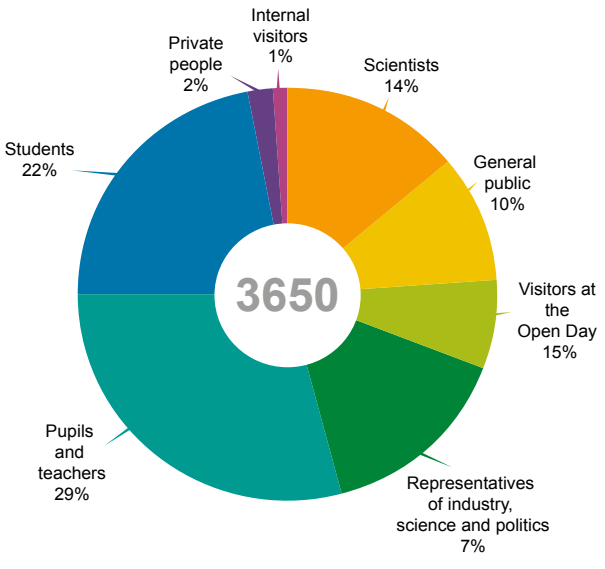

Figure 1: Number and categories of visitors during the year 2018 at the Research Neutron Source Heinz Maier-Leibnitz.

During 2018, 3650 visitors toured the FRM II. This is on a par with the record year 2017 (3692 visitors), reflecting the huge interest on the part of the public in getting to know the neutron source and its applications - thanks to the great engagement of the FRM II and MLZ staff members who conduct these tours.

Science communication in the market place

Within the framework of the Association of European-level Research Infrastructure Facilities (ERF-AISBL) the working group Research Infrastructures Communications and Engagement (RICE) met in April at the Rutherford Appleton Laboratories, UK, to devise common activities.

Only three months later, the RICE working group organized participation at the Science in the City Festival in Toulouse, France. More than 4600 visitors took part in the "Olympic Games of Neutrons and Photons" in July 2018. In addition to the MLZ press office team as the main organizer (see fig. 2), within a common event area there were booths from the Square Kilometre Array (SKA) in the UK, MAX IV laboratory in Sweden, Helmholtz-Zentrum Berlin, CERIC-ERIC in Italy, EUROfusion in Garching, Elettra Synchrotone in Italy, ESO in France and the EU project SINE2020 in Garching. The French science minister Frédérique Vidal (see fig. 3),amongst others, took the opportunity to become acquainted with scientific methods and research projects in a fun-filled and exciting way: they chose real research questions relating to such diverse topics as energy, environment, cultural heritage, astronomy, health and materials engineering. Depending on the topic, the visitors were then guided to

Figure 2: Together with other European research infrastructures, the MLZ organized a tent on the market place at the Science in the City Festival in Toulouse, France.

Figure 3: The French science minister Frédérique Vidal (4th from left) visited the Science in the City Festival in Toulouse.

different stations, where they had to prove their scientific and creative skills. At the end, the science enthusiasts, young and old, received a personalized "scientist's diploma" and a gold medal. The different activities proposed at the booth made the eyes of the kids sparkle especially: as an engineering activity, they built telescopes by using marshmallows and spaghetti, or proved their skills as engineers operating a tokamak fusion reactor at a computer game. As a souvenir, the young scientists were invited to take funny pictures in a photo booth.

Highest number of press articles in more than 10 years

241 media contributions about us over the year mark an all-time high since the restart of communication at the FRM II and MLZ in 2008. This is largely due to the high interest in the transport of the used fuel elements to the interim storage facility in Ahaus, North Rhine-Westphalia. More than 30 percent of the total media articles deal with the fuel elements of the FRM II.

However, science-driven topics, such as the batteries for electro-mobility analysed by the mobility and industrial developer company Bosch (see page 84), or the phase change memory material, attracted almost the same attention.

Storytelling to look behind the scenes

A new format, which was introduced on the MLZ Webpage (www.mlz-garching.de) generated many media articles: the stories "FRoM behind the SCiENcES". The concept of storytelling makes a person, be it a guest scientist, a technician or a MLZ researcher, the focal point of the article and portrays him or her. Seven stories were published in 2018 in addition to 46 news items on the webpages and 60 posts on the FRM II facebook-page. The post and story that attracted the most coverage was on our instrument scientist Dr. Markos Skoulatos, who has re-designed an ancient Greek calculating machine "Antikythera" for the prediction of planetary motion and solar and lunar eclipses. More than one thousand clicks and shares on the Facebook post and the story on the webpage were counted.

Figure 4: A journalist from Bayerischer Rundfunk (right) interviewing instrument scientist Dr. Malgorzata Makowska on the dinosaur eggs, which she analysed using neutron radiography at the NECTAR facility.

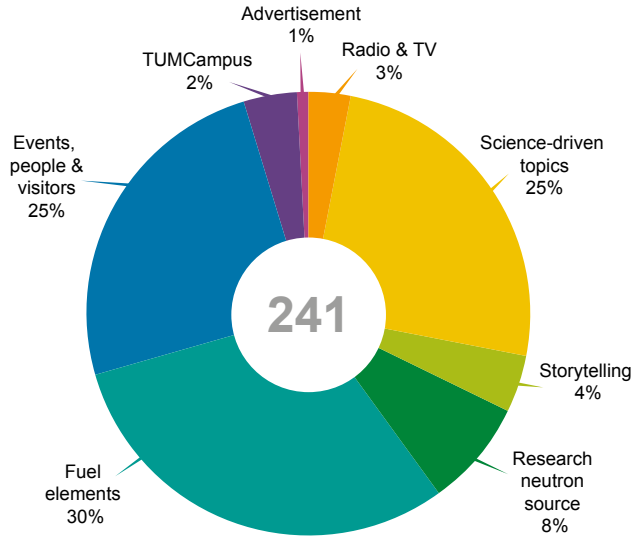

Figure 5: Media articles on FRM II and MLZ in 2018.

The User Office in 2018: Task Force SNI

R. Bucher[1], F. Carsughi[1], C. Hönl[2], I. Lommatzsch[2], G. Ogunbambi[2], B. Tonin[2]

[1]Jülich Centre for Neutron Science (JCNS) at MLZ, Forschungszentrum Jülich GmbH, Garching, Germany; [2]Heinz Maier-Leibnitz Zentrum (MLZ), Technical University of Munich, Garching, Germany

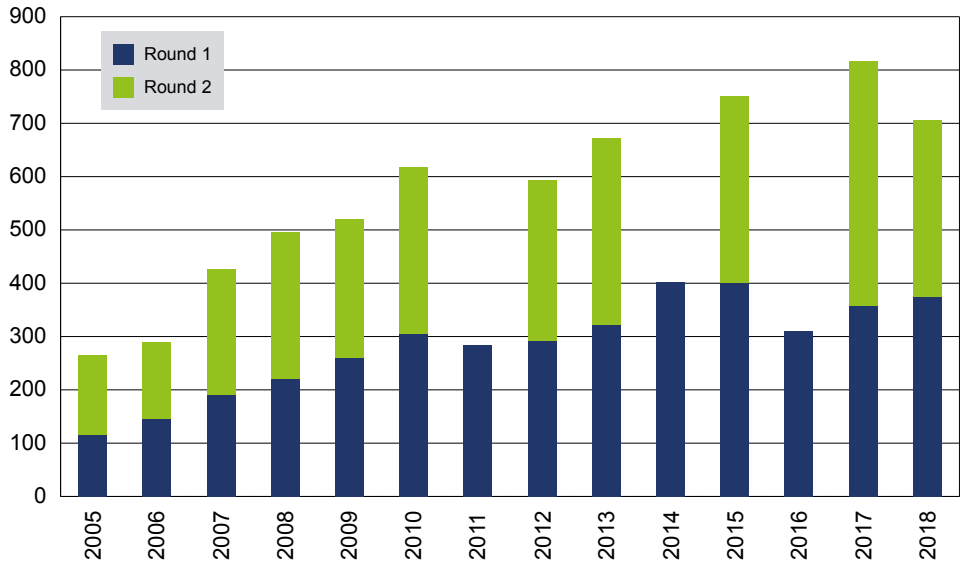

Proposals submitted since the start of user operation at FRM II.

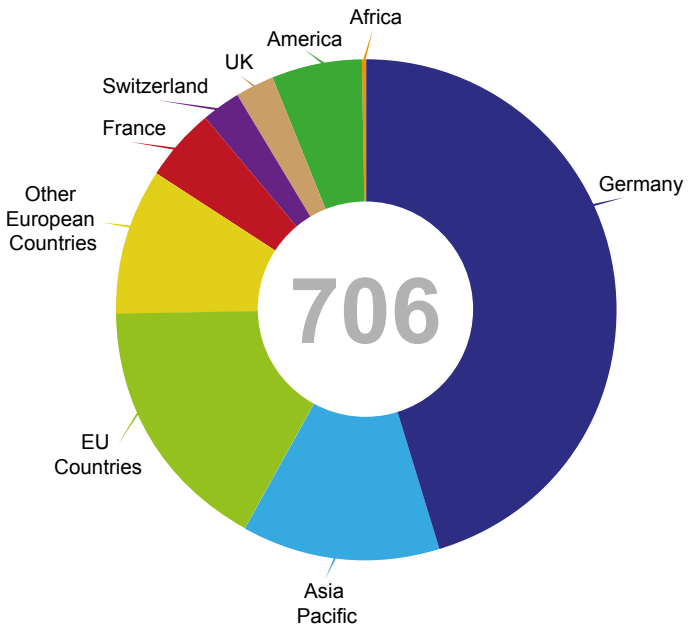

Where did the main proposers of all 706 proposals submitted in 2018 come from?

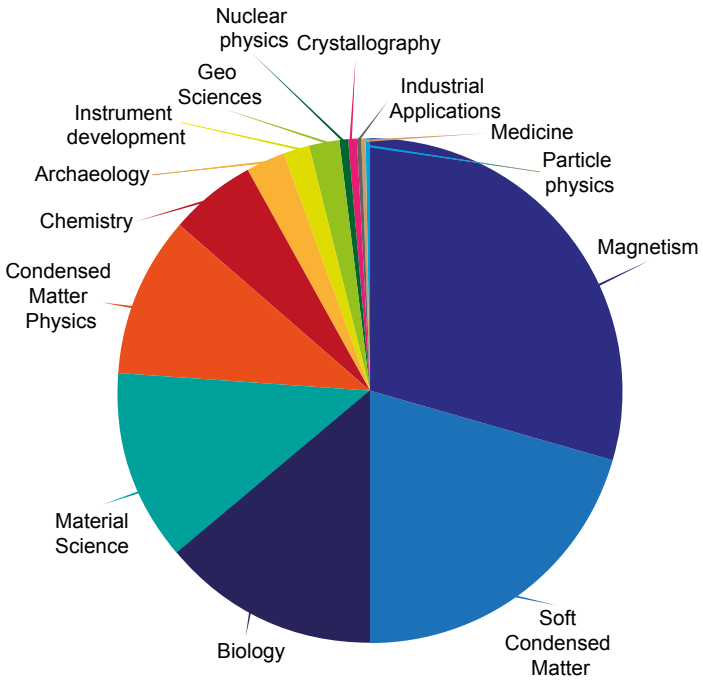

Which scientific fields did the proposals submitted in 2018 cover?

As usual, the User Office took care of all those users who visited us to carry out experiments (987 applied for an access badge via our Online System) following an email invitation from us to the main proposers of 663 proposals for their scheduled experiment. We dealt with 2818 email requests from users and booked almost 3000 nights at hotels in Garching.

Furthermore, we presented the MLZ at the DPG Spring Meeting in Berlin in March and were happy to answer many questions. Some of our visitors there accepted an invitation to participate in the MLZ Conference on Neutrons for Culture at the beautiful venue of Lenggries in June – we had a lot of fun organising and playing a part in this conference!

However, to come to the highlight: 2018 was the year of the German Conference for Research with Synchrotron Radiation, Neutrons and Ion Beams at Large Facilities, in a word: the SNI2018. We organised this quadriennal conference here in Garching for the Committees Research with Synchrotron Radiation, Neutrons and Ion Beams. The participants were for the most part from Germany but delegates from whole Europe and as far afield as Argentina, Japan, South Korea, and New Zealand gathered to present results and exchange ideas at this showcase for collaborative research at research centres and universities.

We present numbers bound to impress about this really big event!

Organisation

FRM II and MLZ

The Forschungs-Neutronenquelle Heinz Maier-Leibnitz (FRM II) provides neutrons for research, industry and medicine and is operated as a Corporate Research Center by the Technical University of Munich (TUM). The scientific use of the FRM II, with around 1000 user visits per year, is organised within the “Heinz Maier-Leibnitz Zentrum” (MLZ).

The chart below shows the overall network comprising the neutron source FRM II and the MLZ, as well as the funding bodies and the scientific users performing experiments at the MLZ addressing the grand challenges of our todays society.

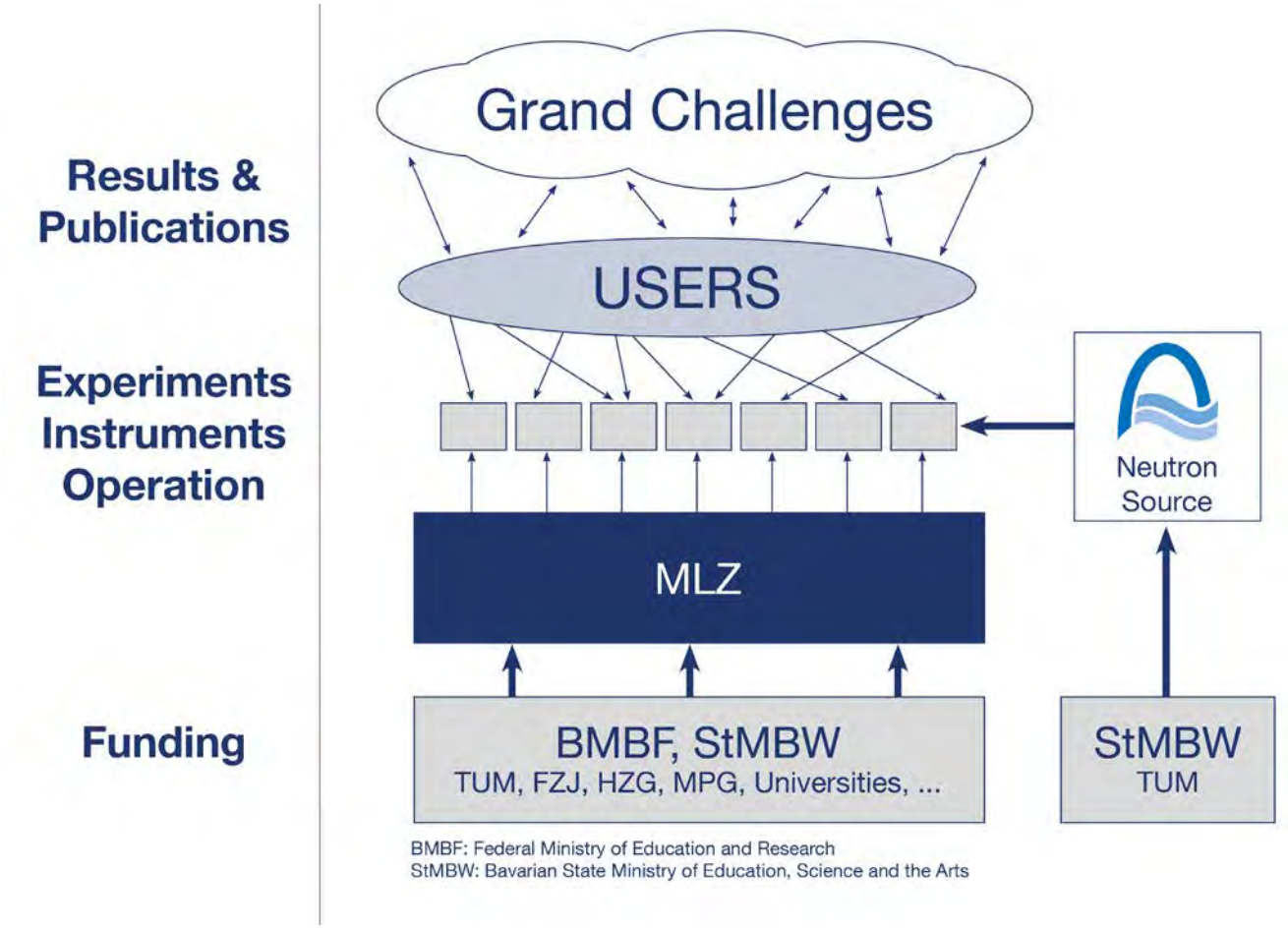

Figure 1: The neutron source FRM II and the user facility MLZ.

Scientific Director MLZ, HGF
Prof. Dr. Stephan Förster

Technical Director FRM II
Dr. Anton Kastenmüller

Scientific Director MLZ, FRM II
Prof. Dr. Peter Müller-Buschbaum

Administrative Director FRM II
Johannes Nußbickel

Scientific Cooperation at the Heinz Maier-Leibnitz Zentrum (MLZ)

The Heinz Maier-Leibnitz Zentrum with its cooperation partners Technische Universität München (TUM), Forschungszentrum Jülich (FZJ) and Helmholtz-Zentrum Geesthacht (HZG) is embedded in a network of strong partners including the Max Planck Society (MPG) and numerous university groups exploiting the scientific use of the Forschungs-Neutronenquelle Heinz Maier-Leibnitz. The organisational chart of the MLZ is shown below.

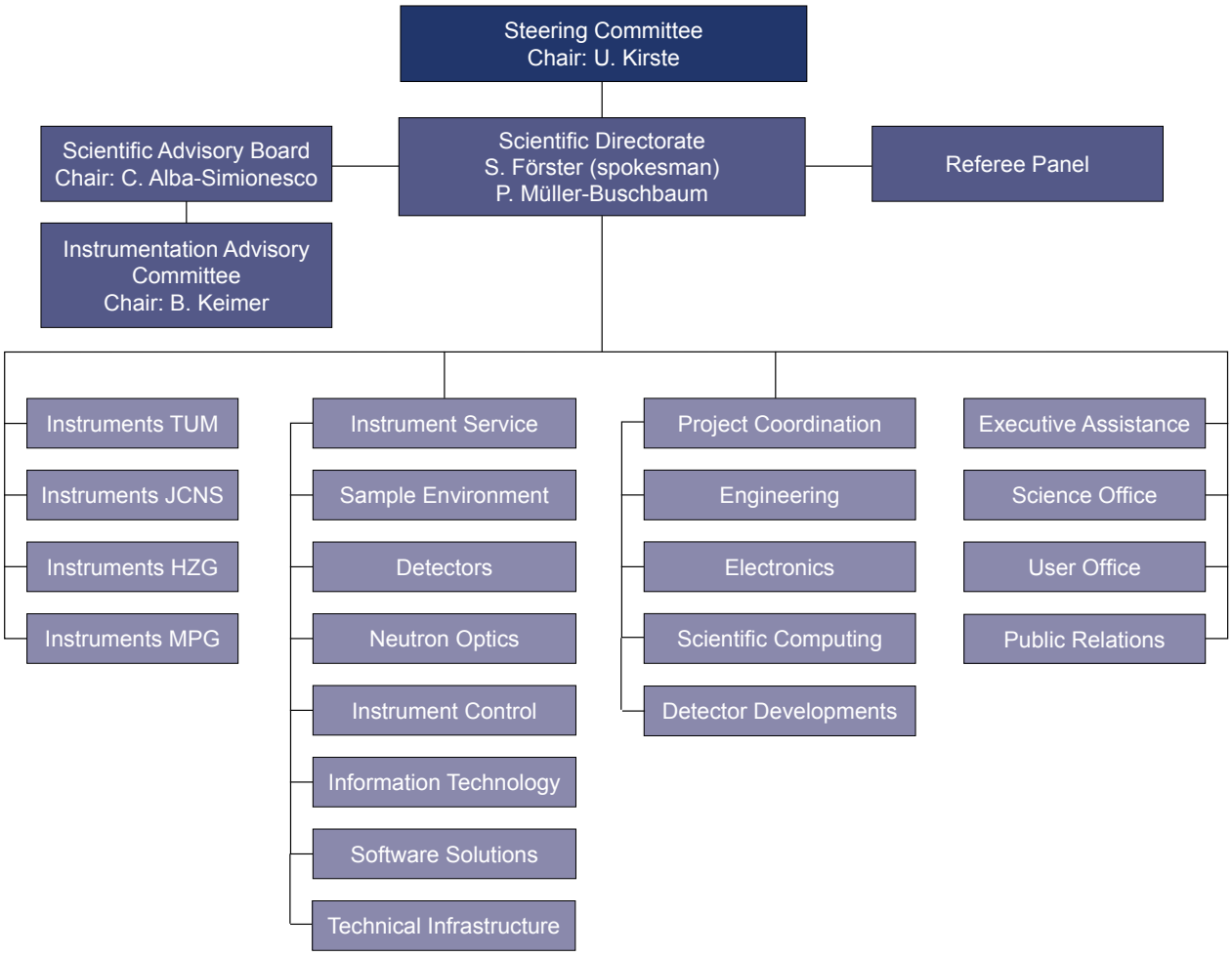

Figure 2: Organisational chart MLZ.

Staff

The charts below show the staff of MLZ and FRM II. The staff of MLZ according to its share among the partners with a detailed view according to the function within the MLZ is depicted as well.

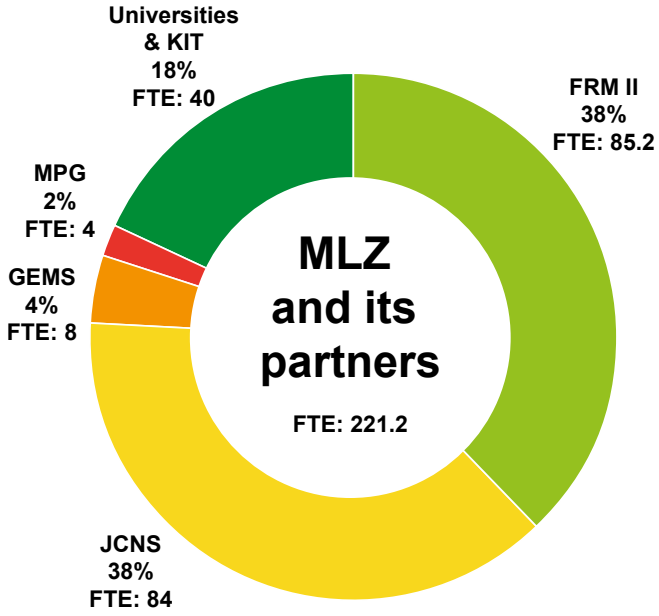

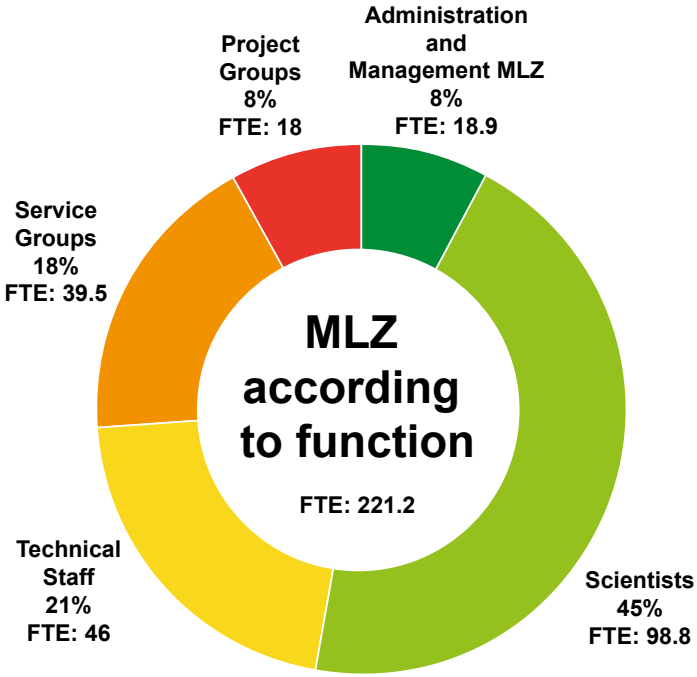

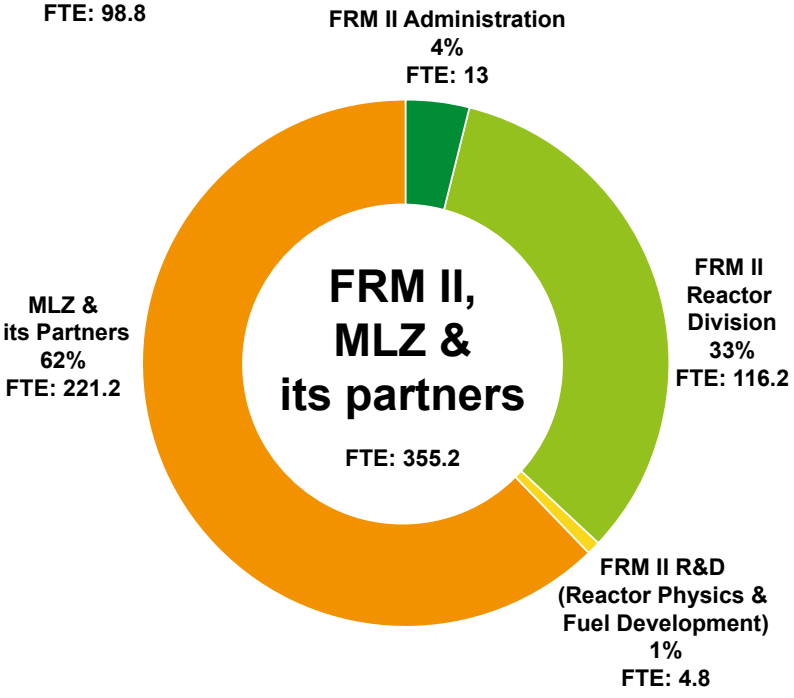

FTE = Full Time Equivalent

Budget

The tables and charts below show the revenue and expenses in 2018.

Revenue 2018

Federal Funding	16.700.000 €
Bavarian Funding	20.420.110 €
Contribution TUM (Planstellen)	10.271.728 €
Contribution FZJ	11.966.000 €
Contribution HZG	1.531.000 €
Total	**60.888.838 €**

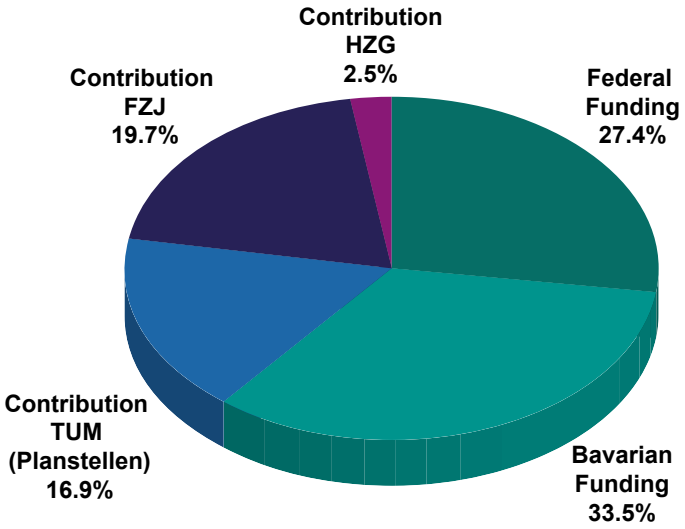

Expenses 2018

	TUM (€)	FZJ (€)	HZG (€)	**Total (€)**
Personnel costs	16.363.394 €	8.500.000 €	1.593.000 €	**26.456.393 €**
Consumables	22.062.864 €	2.416.000 €	461.000 €	**24.939.864 €**
Investment	1.333.426 €	2.600.000 €	342.000 €	**4.275.426 €**
Total	**39.759.684 €**	**13.516.000 €**	**2.396.000 €**	**55.671.683 €**

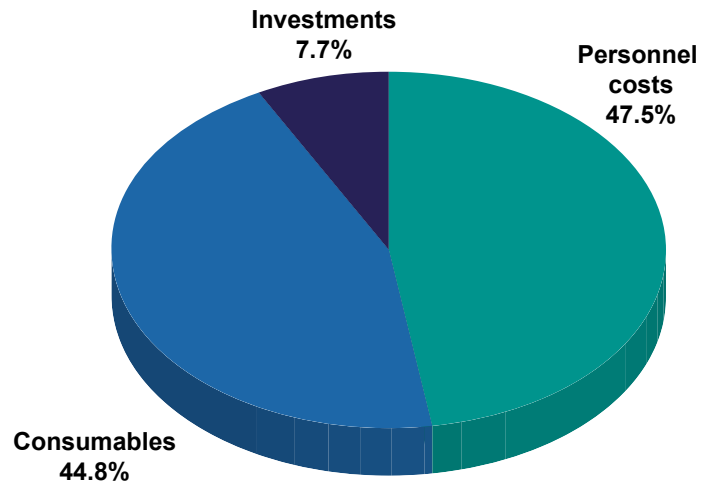

Publications & Theses

In 2018, we received notice of a total of 345 scientific publications, including journal articles, contributions to books and conference proceedings (https://impulse.mlz-garching.de/ and figure below). Furthermore, in total 76 theses supervised by staff of the MLZ and its partner institutions were completed in 2018.

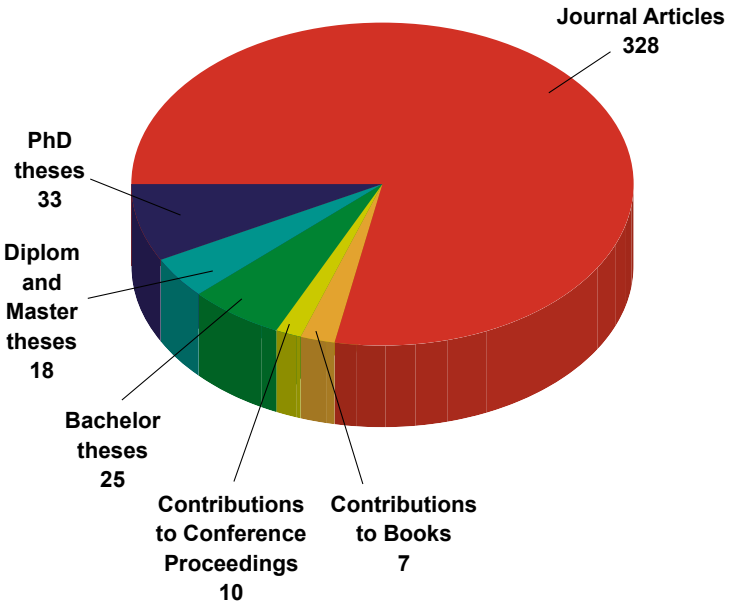

In 2018, more than 250 PhD theses, based on experiments at the MLZ or method and instrument developments for the MLZ, were either ongoing or completed. Of these, about 165 are under the direct supervision of staff at the MLZ and its collaboration partners while the others involve external users. Of all the doctoral students, around 82% come from German universities, 14% from other universities in Europe and 4% from the rest of the world.

The next figure shows the classification of the journal articles by Scientific Area (several tags per journal article are possible):

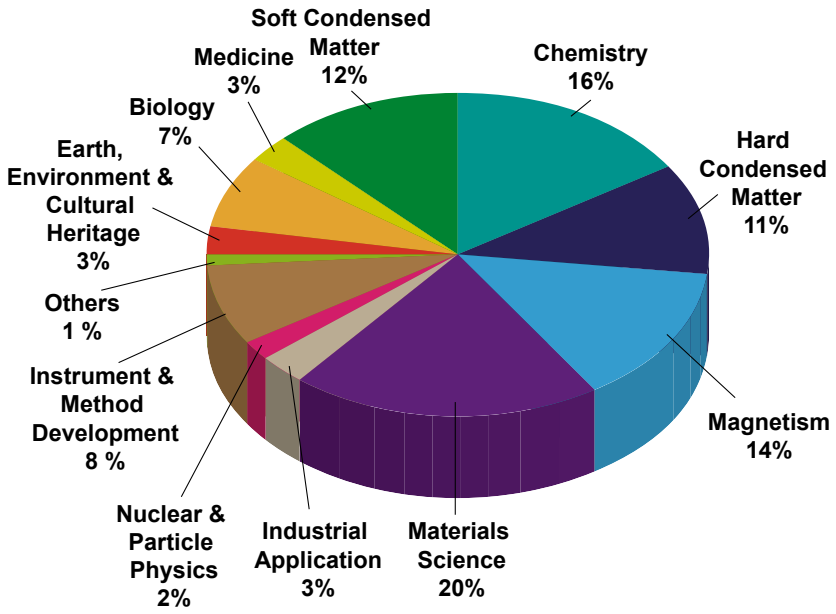

The journal articles at the MLZ can be pictured as a pyramid: Basic Research & Methods (20%) required to tackle the Key Technologies (47%) and articles that address directly the Grand Challenges of our society today (33%). The circular charts represent the individual subjects being dealt with within these three categories.

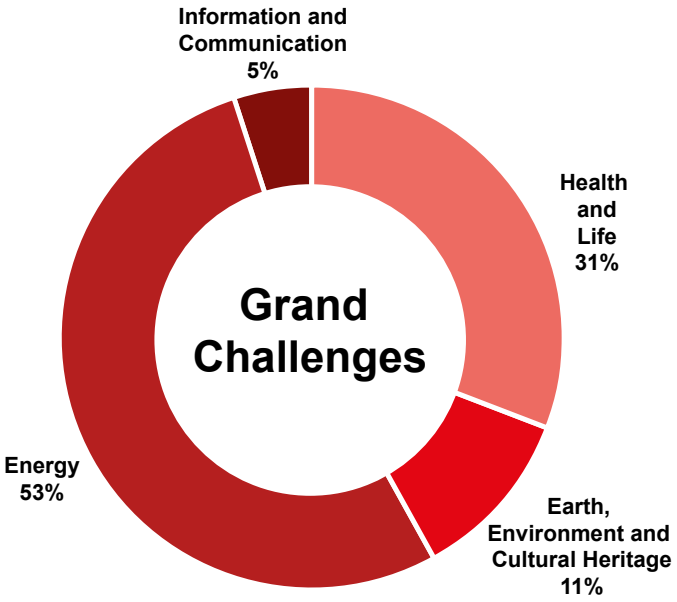

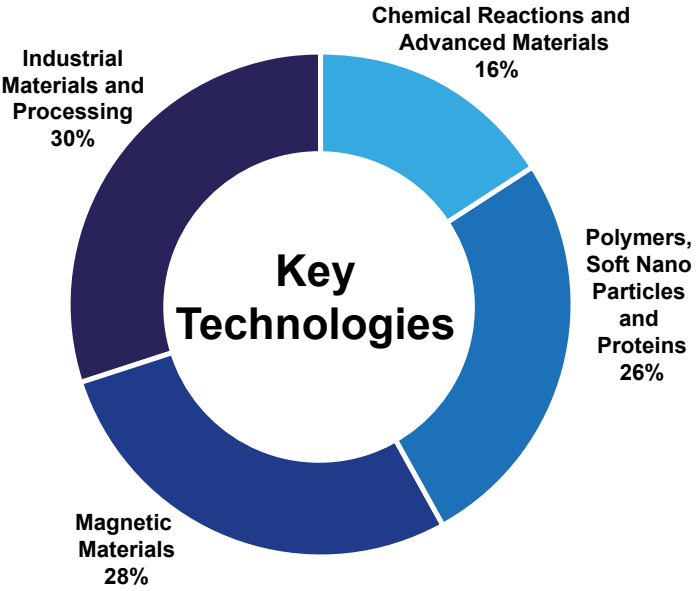

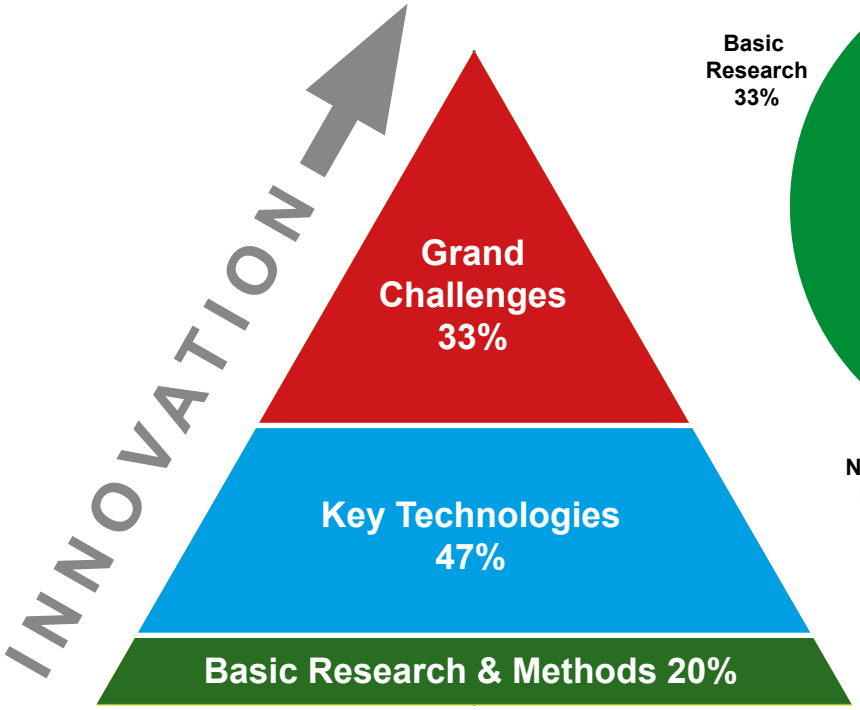

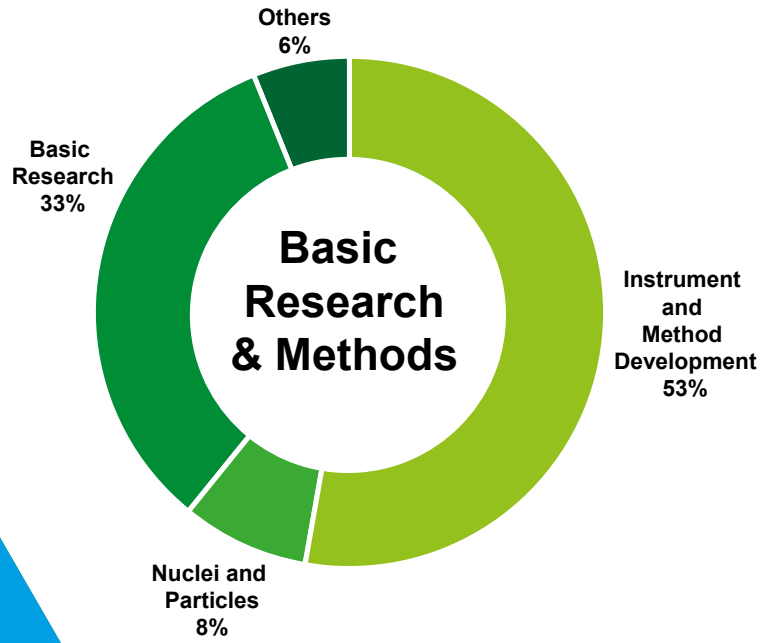

Organisation

Steering Committee

Chair
Dr. Ulrike Kirste
Bavarian State Ministry of Science and the Arts

Members
Prof. Dr. Sebastian Schmidt (Vice Chair)
Board of Directors of Forschungszentrum Jülich GmbH

Albert Berger
Senior Executive Vice-President
Technical University of Munich

Thomas Frederking
Member of the Executive Board
of Helmholtz-Zentrum Berlin GmbH

Prof. Dr. Dr. h.c. mult. Wolfgang A. Herrmann
President
Technical University of Munich
represented by Prof. Dr. Thomas Hofmann
Vice-President
Technical University of Munich

Prof. Dr. Wolfgang Kaysser
Member of the Executive Board
of Helmholtz-Zentrum Geesthacht GmbH

Dr. Jürgen Kroseberg
Federal Ministry for Education and Research

Prof. Dr. Jan Lüning
Scientific Management of Helmholtz-Zentrum Berlin GmbH

Prof. Dr. Stephan Paul
Technical University of Munich
Physics-Department E18

Guests
Prof. Dr. Stephan Förster
Scientific Director of the MLZ, representing HGF institutions

Prof. Dr. Peter Müller-Buschbaum
Scientific Director of the MLZ, representing TUM

Dr. Anton Kastenmüller
Technical Director ZWE-FRM II
Technical University of Munich

Johannes Nußbickel
Administrative Director ZWE-FRM II
Technical University of Munich

Dirk Schlotmann
Forschungszentrum Jülich GmbH

RD Petra Lörz
Technical University of Munich, FRM II

Figure 1: Steering Committee meeting December 2018 with S. Paul, D. Schlotmann, A. Berger, L. Arleth (chair of the MLZ Review Committee), S. Schmidt, J. Kroseberg, P. Müller-Buschbaum, U. Kirste, J. Nußbickel, S. Förster, W. Kaysser, A. Kastenmüller, and J. Lüning (from left to right).

Figure 2: Scientific Advisory Board (from left to right): R. Niewa, C. Rüegg, M. Müller. B. Keimer, C. Alba-Simionesco, H. Schober, S. Förster, P. Müller-Buschbaum, R. von Klitzing, W. Daum, A. Arbe, and W. Paul.

Scientific Advisory Board

Chair
Prof. Christiane Alba-Simionesco
Laboratoire Léon Brillouin, CEA, Saclay

Members
Prof. Dr. Hartmut Abele
Technische Universität Wien

Prof. Dr. Arantxa Arbe
Centro de Fisica de Materiales
Material Physics Center, San Sebastián

Alejandro Javier Guirao Blank
Volkswagen AG, Wolfsburg

Werner Daum
Bundesanstalt für Materialforschung
und -prüfung (BAM), Berlin

Prof. Dr. Bernhard Keimer
Max-Planck-Institut für Festkörperphysik, Stuttgart

Prof, Dr. Rainer Niewa
Institut für Anorganische Chemie
Universität Stuttgart

Prof. Dr. Wolfgang Paul
Martin Luther Universität Halle-Wittenberg

Prof. Dr. Joachim Rädler
Ludwig-Maximilians-Universität, München

Prof. Dr. Christian Rüegg
Paul Scherrer Institute, Villigen

Prof. Dr. Helmut Schober
Institut Laue Langevin, Grenoble

Prof. Dr. Regine v. Klitzing
Technische Universität Darmstadt

MLZ Instrumentation Committee

Chair
Prof. Dr. Bernhard Keimer
Max-Planck-Institut für Festkörperphysik, Stuttgart

Members
Maria Teresa Fernandez Diaz
Institut Laue Langevin (ILL), Grenoble

Dr. Eberhard Lehmann
Paul-Scherrer-Institut, Villigen

Dr. Frédéric Ott
Laboratoire Léon Brillouin, CEA, Saclay

Prof. Dr. Catherine Pappas
Delft University of Technology, Delft

Prof. Dr. Henrik Ronnøw
Ecole Polytechnique Fédérale de Lausanne

Dr. Margarita Russina
Helmholtz-Zentrum für Materialien und Energie, Berlin

Dr. Ulli Köster
Institut Laue Langevin, Grenoble

Evaluation of Beam Time Proposals: Members of the Review Panels

Prof. Dr. Arantxa Arbe
Centro de Fisica de Materiales,
Material Physics Center, San Sebastián

Prof. Dr. Lise Arleth
Niels Bohr Institute
University of Copenhagen

Prof. Piero Baglioni
Dipartimento di Chimica 'Ugo Schiff'
University of Firenze

Prof. Peter Battle
Department of Chemistry
University of Oxford

Dr. Matthew Blakeley
Institut Laue Langevin (ILL), Grenoble

Dr. Victor Bodnarchuk
Frank Laboratory of Neutron Physics, Dubna, Moscow reg.

Dr. Johann Bouchet
DAM
Commissariat à l'énergie atomique et
aux énergies alternatives (CEA), Arpajon

Dr. Philippe Bourges
UMR12 CEA-CNRS
Laboratoire Léon Brillouin, CEA Saclay

Dr. Daniel Clemens
Helmholtz Zentrum Berlin für Materialien und Energie

Dr. Robert Cubitt
Institut Laue Langevin (ILL), Grenoble

Dr. Sabrina Disch
Department Chemie
University of Cologne

Dr. Cecile Dreiss
Institute of Pharmaceutical Science
King's College London

Prof. Dr. Kristina Edström
Department of Chemistry
Uppsala University, Uppsala

Dr. Stephan Eijt
Delft University of Technology, Delft

Prof. Dr. Ulli Englert
Department of Inorganic Chemistry
RWTH Aachen

Prof. Dr. Bjorn Fak
Institut Laue Langevin (ILL), Grenoble

Dr. Bela Farago
Institut Laue Langevin (ILL), Grenoble

Dr. Peter Fouquet
Institut Laue Langevin (ILL), Grenoble

Prof. Dr. Rupert Gebhard
Abt. Vorgeschichte
Archäologische Staatssammlung, München

Dr. Anne-Caroline Genix
Laboratoire Charles Coulomb
Université Montpellier

Dr. Francesco Grazzi
Institute for Complex Systems
Consiglio Nazionale delle Ricerche, Sesto Fiorentino

Dr. Christian Grünzweig
Paul Scherrer Institute, Villigen

Prof. Dr. Thomas Hellweg
Physikalische und Biophysikalische Chemie
Universität Bielefeld

Prof. Paul Henry
ISIS Neutron and Muon Source
STFC Rutherford Appleton Laboratory, Didcot

Prof. Björgvin Hjörvarsson
Department of Astronomy and Space Physics
Uppsala University, Uppsala

Dr. Klaudia Hradil
Röntgenzentrum
Technische Universität Wien

Dr. Christy Kinane
ISIS Neutron and Muon Source
STFC Rutherford Appleton Laboratory, Didcot

Dr. Joachim Kohlbrecher
Paul-Scherrer-Institut, Villingen

Dr. Reinhard Kremer
Max Planck-Institut für Festkörperforschung, Stuttgart

Prof. Christian Krempaszky
Fakultät für Maschinenwesen
Technical University of Munich

Prof. Jeremy Lakey
Institute for Cell and Molecular Biosciences
University of Newcastle, Newcastle upon Tyne

Dr. Reidar Lund
Department of Chemistry
University of Oslo

Dr. Sandrine Lyonnard
Commissariat à l'énergie atomique et
aux énergies alternatives (CEA), Grenoble

Prof. Dr. Andreas Magerl
Kristallographie und Strukturphysik
Universität Erlangen-Nürnberg, Erlangen

Dr. Eric Mauerhofer
Institut für Energie- und Klimaforschung
Forschungszentrum Jülich GmbH

Prof. Andreas Michels
Faculté des Sciences, de la Technologie
et de la Communication
Université de Luxembourg

Dr. Gwilherm Nénert
PANalytical B.V., Almelo

Dr.-Ing. Thomas Nitschke-Pagel
Institut für Füge fund Schweißtechnik
Technische Universität Braunschweig

Prof. Dr. Thommy Nylander
Physical Chemistry
Lund University, Lund

Dr. Esko Oksanen
European Spallation Source (ESS ERIC), Lund

Dr. Alessandro Paciaroni
Dipartimento di Fisica
Università degli Studi di Perugia

Dr. Joe Paddison
Churchill College
University of Cambridge

Prof. Dr. Christine Papadakis
Soft Matter Physics
Technical University of Munich

Dr. Oleg Petrenko
Department of Physics
University of Warwick, Coventry

Dr. Thilo Pirling
Institut Laue-Langevin (ILL), Grenoble

Prof. Dr. Radosław Przeniosło
Institute of Physics
University of Warsaw

Prof. Dr. Diana Lucia Quintero Castro
Faculty of Science and Technology
University of Stavanger

Dr. Navid Qureshi
Institut Laue Langevin (ILL), Grenoble

Dr. Florin Radu
BESSY
Helmholtz Zentrum Berlin für Materialien und Energie, Berlin

Prof. Dr. Günther Redhammer
Materialforschung und Physik
Universität Salzburg

Dr. Sarah Rogers
ISIS Neutron and Muon Source
STFC Rutherford Appleton Laboratory, Didcot

Dr. Stephane Rols
Institut Laue Langevin (ILL), Grenoble

Dr. Emmanuel Schneck
Colloids and Interfaces Biomaterials
Max Planck Institute, Potsdam

Prof. Dr. Andreas Schönhals
Bundesanstalt für Materialforschung und -prüfung, Berlin

Dr. Romain Sibille
Laboratory for Neutron Scattering
Paul Scherrer Institute, Villigen

Dr. Thorsten Soldner
Institut Laue-Langevin, Grenoble

Prof. Dr. Wolfgang Sprengel
Institut für Materialphysik
Technische Universität Graz

Dr. Andreas Stark
Institute for Materials Research
Helmholtz Zentrum Geesthacht

Dr. Peter Staron
Institute of Materials Research
Helmholtz-Zentrum Geesthacht

Dr. Ross Stewart
ISIS Neutron and Muon Source
STFC Rutherford Appleton Laboratory, Didcot

Dr. Christopher Stock
School of Physics and Astronomy
University of Edinburgh

Dr. Pavel Strunz
Department of Neutron Physics
Nuclear Physics Institute, Rez near Prague

Dr. Anne Stunault
Institut Laue Langevin (ILL), Grenoble

Dr. Laszlo Szentmiklosi
Center for Energy Research
Hungarian Academy of Sciences, Budapest

Prof. Dr. Regine von Klitzing
Fachbereich Physik
Technische Universität Darmstadt

Dr. Ing. Frank Weber
Institut für Festkörperphysik
Karlsruher Institut für Technologie (KIT)

Jun. Prof. Dr. Hongbin Zhang
Theory of Magnetic Materials
Technische Universität Darmstadt

Figure 3: Venue of the MLZ Review Panels' meeting at Munich airport.

Figure 4: MLZ User Committee (from left to right): D. Keeble, J. Gibmeier, S. Combet, L. Paduano, R. Niewa, D. Quintero Castro, P. Müller-Buschbaum, A. Rennie and F. Carsughi.

MLZ User Committee

Chair
Prof. Adrian Rennie
Uppsala University, Uppsala

Members
Dr. Sophie Combet
Laboratoire Léon Brillouin, CEA Saclay

Dr.-Ing. Jens Gibmeier
Karlsruhe Institute of Technology (KIT)

Prof. David Keeble
University of Dundee, UK

Prof. Luigi Paduano
Università di Napoli

Prof. Diana Quintero Castro
Stavanger University Norway

Prof. Dr. Rainer Niewa (Observer on behalf of the KFN)
Universität Stuttgart

Partner institutions

Bavarian Research Institute of
Experimental Geochemistry and Geophysics
University of Bayreuth
www.bgi.uni-bayreuth.de

Georg-August-Universität Göttingen

- Institue of Physical Chemistry
  www.uni-pc.gwdg.de/eckold
- Geowissenschaftliches Zentrum
  www.uni-goettingen.de/de/125309.html

German Engineering Materials Science Centre GEMS
Helmholtz-Zentrum Geesthacht GmbH
www.hzg.de/institutes_platforms/gems/

Jülich Centre for Neutron Science JCNS
Forschungszentrum Jülich GmbH
www.jcns.info

Karlsruhe Institute of Technology

- Institute for Applied Materials – Energy Storage Systems (IAM-ESS)
  www.iam.kit.edu

Ludwig-Maximilians-Universität München

- Section Crystallography
  www.lmu.de/kristallographie
- Faculty of Physics
  www.softmatter.physik.uni-muenchen.de

Max Planck Institute for Solid State Research Stuttgart
www.fkf.mpg.de

RWTH Aachen University

- Institute of Crystallography
  www.xtal.rwth-aachen.de
- Institute of Inorganic Chemistry
  www.ac.rwth-aachen.de

TU Clausthal

Clausthal University of Technology

- Institute of Materials Science and Engineering
  www.iww.tu-clausthal.de

TECHNISCHE UNIVERSITÄT DRESDEN

Technische Universität Dresden

- Institute of Solid State Physics
  www.tu-dresden.de/mn/physik/ifp

Technical University of Munich

Department of Physics

- E13 - Institute for Functional Materials
  www.functmat.ph.tum.de
- E18 - Institute for Hadronic Structure and Fundamental Symmetries
  www.e18.ph.tum.de
- E21 - Research area Strongly Correlated Electron Systems
  www.sces.ph.tum.de
- RCM - Radiochemie München
  www.rcm.tum.de

MRI
Klinikum rechts der Isar

Technical University of Munich

- MRI - Klinikum Rechts der Isar
  www.mri.tum.de

Technical University of Munich

- Exzellenzcluster
  „Origin and Structure of the Universe“
  www.universe-cluster.de

Vienna University of Technology

- Neutron- and Quantum Physics
  Research area at the Atominstitut Vienna
  Abele Group
  http://ati.tuwien.ac.at/forschungsbereiche/nqp/home/

Universität der Bundeswehr München

- Institute of Applied Physics and Measurement Technology
  www.unibw.de/lrt2

University of Cologne

- Faculty of Mathematics and Natural Sciences
  Department of Physics
  www.ikp.uni-koeln.de

- Institute of Physics II
  www.ph2.uni-koeln.de

Imprint

Publisher

Technische Universität München
Forschungs-Neutronenquelle
Heinz Maier-Leibnitz (FRM II)
Lichtenbergstr. 1
85747 Garching
Germany

Phone: +49.89.289.14966
Fax: +49.89.289.14995
Internet: www.mlz-garching.de
www.frm2.tum.de
EMail: jahresbericht@frm2.tum.de

Editorial Office, Design and typesetting

Ramona Bucher
Ariane Fröhner
Anke Görg
Connie Hesse
Elisabeth Jörg-Müller
Andrea Voit

Editors

Rainer Bruchhaus
Henrich Frielinghaus
Robert Georgii
Michael Hofmann
Olaf Holderer
Christoph Hugenschmidt
Johanna Jochum
Peter Link
Wiebke Lohstroh
Andreas Ostermann
Björn Pedersen
Anatoliy Senyshyn
Olaf Soltwedel
Yixi Su

Photographic credits

BGZ Ahaus: 98 (bottom)

Uli Benz: 96 (bottom), 97 (middle)

Markus Garst, Karlsruhe Institute of Technology (KIT): front cover

Thomas Gigl: 95 (top)

Andreas Heddergott: 4 (bottom 1st from left), 87, 89 (top), 96 (middle), 97 (bottom)

Christoph Hohmann, NIM: 12 (bottom)

Ralf-Uwe Limbach: 4 (bottom 2nd from left)

Stephan Loibl: 90 (top),

Sebstian Mast: 13 (bottom)

Märl/ Dick/ Häberle: 10 (bottom)

Wenzel Schürmann, TUM: 4 (top, bottom 3rd and 4th from left), 9, 10/11 (background), 10 (top), 11 (bottom), 12/13 (background) 59, 79, 84 (top), 88, 89 (bottom), 90 (bottom), 91, 92 (top), 94, 96 (top), 98 (top, middle), 99, 100 (top left, bottom), 101 (bottom left, bottom right, top right), 103 (bottom left), 112, 113, back cover

Editors, authors or FRM II / TUM:
other images

Front page:
A lattice of magnetic vortices – so-called skyrmions – exists also at low temperatures in the chiral magnet. The arrows represent the direction of the local magnetisation.

Back page:
The staff of the Heinz Maier-Leibnitz Zentrum (MLZ) and Forschungs-Neutronenquelle Heinz Maier-Leibnitz (FRM II) in July 2018.

Heinz Maier-Leibnitz Zentrum (MLZ)

www.mlz-garching.de

DOI: 10.14459/2019md1474027

MLZ Instrument Suite

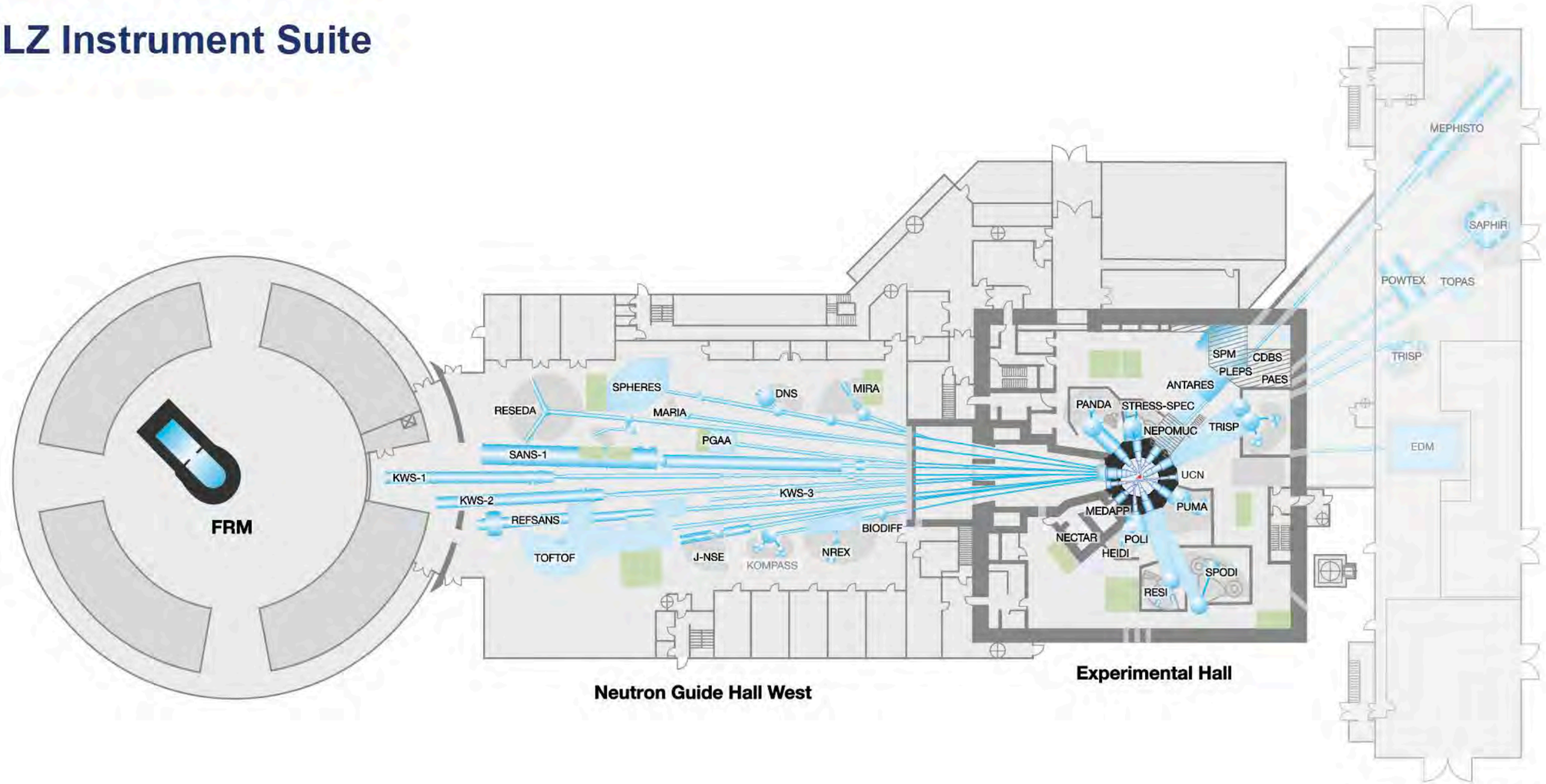

Instrument	Description	Neutrons	Operated by	Funding	Instrument group at MLZ
ANTARES	Radiography and tomography	cold	TUM	TUM	FRM II
BIODIFF	Diffractometer for large unit cells	cold	TUM, JCNS	TUM, FZJ	FRM II, JCNS
DNS	Diffuse scattering spectrometer	cold	JCNS	FZJ	JCNS
HEIDI	Single crystal diffractometer	hot	RWTH Aachen	FZJ	JCNS
J-NSE	Spin-echo spectrometer	cold	JCNS	FZJ	JCNS
KOMPASS	Three axes spectrometer	cold	Uni Köln, TUM	VF	FRM II
KWS-1	Small angle scattering	cold	JCNS	FZJ	JCNS
KWS-2	Small angle scattering	cold	JCNS	FZJ	JCNS
KWS-3	Very small angle scattering	cold	JCNS	FZJ	JCNS
MARIA	Magnetic reflectometer	cold	JCNS	FZJ	JCNS
MEPHISTO**	Instrument for particle physics, PERC	cold	TUM	TUM, DFG	FRM II
MIRA	Multipurpose instrument	cold	TUM	TUM	FRM II
MEDAPP	Medical irradiation treatment	fast	TUM	TUM	FRM II
NECTAR	Radiography and tomography	fast	TUM	TUM	FRM II
NEPOMUC	Positron source, CDBS, PAES, PLEPS, SPM	-	TUM, UniBw München	TUM	FRM II
NREX	Reflectometer with X-ray option	cold	MPI Stuttgart	MPG	MPI Stuttgart
PANDA	Three axes spectrometer	cold	JCNS	FZJ	JCNS

Instrument	Description	Neutrons	Operated by	Funding	Instrument group at MLZ
PGAA	Prompt gamma activation analysis	cold	Uni Köln	TUM	FRM II
PUMA	Three axes spectrometer	thermal	Uni Göttingen, TUM	VF, TUM	FRM II
POLI	Single-crystal diffractometer polarized neutrons	hot	RWTH Aachen	VF, FZJ	JCNS
POWTEX*	Time-of-flight diffractometer	thermal	RWTH Aachen, Uni Göttingen, JCNS	VF, FZJ	JCNS
REFSANS	Reflectometer	cold	GEMS	VF, HZG	GEMS
RESEDA	Resonance spin-echo spectrometer	cold	TUM	TUM	FRM II
RESI	Single crystal diffractometer	thermal	LMU	TUM	FRM II
SANS-1	Small angle scattering	cold	TUM, GEMS	TUM, HZG	FRM II, GEMS
SAPHIR*	Six anvil press for radiography and diffraction	thermal	Uni Bayreuth	VF	FRM II
SPHERES	Backscattering spectrometer	cold	JCNS	VF, FZJ	JCNS
SPODI	Powder diffractometer	thermal	KIT	VF, TUM	FRM II
STRESS-SPEC	Materials science diffractometer	thermal	TUM, TU Clausthal, GEMS	TUM, HZG	FRM II, GEMS
TOFTOF	Time-of-flight spectrometer	cold	TUM	TUM	FRM II
TOPAS*	Time-of-flight spectrometer	thermal	JCNS	FZJ	JCNS
TRISP	Three axes spin-echo spectrometer	thermal	MPI Stuttgart	MPG	MPI Stuttgart
UCN*	Ultra cold neutron source, EDM	ultra-cold	TUM	TUM, DFG	FRM II

*construction
**reconstruction
VF: instrument construction funded by "BMBF-Verbundforschung" (Collaborative Projects)